

7

**Constraints on the Petrogenesis of Lavas from Large Plumes:
Inferences from Geochemical Studies of Lavas from Mauna Kea,
Hawaii and Mt. Bureau, Kerguelen Archipelago**

by

Huai-Jen Yang

M.S. Geology, Taiwan University

(1986)

Submitted to the Department of
Earth, Atmospheric, and Planetary Sciences
in Partial Fulfillment of the Requirements
for the Degree of

DOCTOR OF PHILOSOPHY

at the MASSACHUSETTS INSTITUTE OF TECHNOLOGY

May 1996

© Massachusetts Institute of Technology, 1996. All rights reserved.

Signature of Author: _____
Department of Earth, Atmospheric and Planetary Sciences
May, 1996

Certified by: _____
Frederick A. Frey
Professor of Geochemistry
Thesis Supervisor

Accepted by: _____
Thomas H. Jordan
Department Head

MASSACHUSETTS INSTITUTE
OF TECHNOLOGY
WITHDRAWN
JUN 01 1996
MIT LIBRARIES

Constraints on the Petrogenesis of Lavas from Large Plumes: Inferences from Geochemical Studies of Lavas from Mauna Kea, Hawaii and Mt. Bureau, Kerguelen Archipelago

by

Huai-Jen Yang

Submitted to the Department of Earth, Atmospheric, and Planetary Sciences at the Massachusetts Institute of Technology in partial fulfillment of the requirements for the Degree of Doctor of Philosophy in Geochemistry

ABSTRACT

Lavas derived from large mantle plumes can provide important information about mantle composition and processes. However, the use of lavas to infer mantle composition requires an understanding of the processes which control the chemical variations of lavas, such as partial melting, crystal fractionation and accumulation, magma mixing, magma - wall rock interaction and postmagmatic alteration. In this thesis, I investigate the chemical effects of these processes using experimental constraints and the compositions of lavas and minerals from Mauna Kea volcano at Hawaii and Mt. Bureau in the Kerguelen Archipelago.

A model for calculating major element variations in basaltic magmas during crystal fractionation was developed based on experiments at 0.001-10 kb in simple and natural systems. Based on this algorithm, the high Fe-Ti basalts from the Mauna Kea volcano fractionated olivine, plagioclase and augite at pressures ranging from 0.001 to 10 kb. This method was also used to show that the coherent trends defined by Mt. Bureau group A lavas in MgO variation diagrams were dominated by crystal fractionation at low pressures.

Submarine lavas erupted on the east rift zone of Mauna Kea volcano have high MgO contents (11-20%) which resulted from olivine accumulation in evolved melts. The differences in Sr, Nd, and Pb isotopic ratios and abundance ratios of incompatible elements indicate a diversity in parental magma compositions. The mineral compositions of these lavas provide evidence for isolated magma chambers which had undergone distinct crystal fractionation and magma mixing histories. Similar to these submarine lavas, samples recovered from the Hawaiian Scientific Drilling Project (HSDP) also contain accumulated olivines. The compositions of primary magmas were estimated by adding equilibrium olivine into HSDP samples and subaerially exposed lavas with < 8 vol% olivine phenocrysts and > 7 wt% of MgO to reach 16 wt% MgO. The abundances of SiO₂ and FeO in these estimated primary magmas reflect the depth of magma segregation. The SiO₂-Nb correlation indicates that younger lavas were segregated at relatively higher pressures by lower extents of partial melting. This temporal trend reflects migration of Mauna Kea away from the Hawaiian Plume.

Mt. Bureau is an expression of the Kerguelen Plume. Lavas forming the upper part of Mt. Bureau have MgO contents ranging from 5.12 to 3.37% and relatively homogeneous isotopic compositions. Their compositional variations are consistent with crystal fractionation from parental magmas derived from different extents of melting. The chemical and isotopic compositions of lavas forming the lower subsection are interpreted as deriving from mixed sources with different proportions of MORB and plume components. The Mt. Bureau section represents a transition from a near ridge setting to an intraplate setting.

Thesis advisor: Frederick A. Frey

ACKNOWLEDGMENTS

I appreciate to having a section for what I would like to say but do. First, I thank Fred Frey, the #1 advisor in my heart, for guiding me into the field of geochemistry. Trace element geochemistry is the foundation of my thesis. The seminars on Th-U disequilibrium were solid from the basic principles to the geological applications. The MORB seminars extended my knowledge to a regime outside plume volcanism. Discussions during group meetings helped me to keep up with the current hot topics. Being the TA of 12.119 for three times gave me an unique chance to access and have a better understanding on these "state of art" analytical techniques. All these classes have been fun. Critical review ensured the quality of my thesis. In addition to the knowledge of geochemistry, I will carry Fred's attitude of doing science with me as I leave MIT.

I would like to thank Tim Grove for teaching me 1-atm isothermal experiments and initiating the OPAM study. Also, three semesters of igneous petrology classes have reinforced my thermodynamics and petrology background. Discussions with Tim and Ro Kinzler on OPAM study gave me the capability of applying phase diagrams to solve geological problems. I appreciate Sam Bowring's effort to guide me to use isotope data in a "right" way. I thank Tim Grove, Sam Bowring and Roberta Rudnick for being my committee members.

I give my special acknowledgments to two young experimental petrologists, Tom Wagner and Glenn Gaetani. They were always there to help me with experiments and answer my questions. Eiichi Takazawa and Alberto Saal have been my office mates for six years. I thank them for sharing all kinds of knowledge and their flexibility on "sample change". I also benefited from discussions with new generation on the 12th floor, Kirsten Nicolaysen and Steve Parman and the WHOI people, Deborah Hassler, Ken Koga and Kwok-Lin Lee.

Dominique Weis is acknowledged for sharing Mt. Bureau isotopic data, as are Mike Garcia and Dave Clague for providing thin sections of Mauna Kea submarine samples.

During six years, I have done many analyses that could not be accomplished without

these great lab managers : Pillalamarri Ila in the neutron activation lab; Mike Jercinovic and Neel Chatterjee in the electron microprobe lab; Jerzy Blusztajn, Dave Kammer, Bill Olszewski and Drew Coleman in clean room and mass spectrometer lab; Pete Dawson in XRF lab; Barry Grant in ICP-MS lab and Bill Olszewski and Dave Applegate in the CLAIR facility.

The three weeks in Hawaii for HSDP have generated another group of friends. I enjoyed the fantastic discussions on the cores with Mike Garcia, Dave Clague, Don DePaolo, Ed Stolper, Mike Baker, John Lassiter and Aaron Pietruzska. I will never forget Wayne Campbell for thousand miles ride and all the fun in Hawaii.

Finally, best regards to my dear wife and daughter who have suffered from the absence of husband and father for many years. Without their support and understanding, I would not be able to concentrate on my research. Moral and financial support from my parents kept me away from all kinds of difficulties. The concerns from the Huang family were also important encouragement. My only regret is that I can't share the pleasure of accomplishment with grandfather.

TABLE OF CONTENTS

Title page.....	1
Abstract.....	2
Acknowledgments.....	3
Table of contents.....	5
Introduction.....	8

Chapter 1: Experiments and Models of Anhydrous, Basaltic Olivine-Plagioclase-Augite Saturated Melts from 0.001 to 10 kbar.....13

Abstract.....	14
Introduction.....	15
Experiment	
Starting Material.....	16
Experimental Methods.....	17
Analytical Method.....	18
Experimental Results.....	18
Discussion	
Prediction of ol-plag-aug saturated melts.....	19
Melt composition as a thermobarometer.....	24
Predicting fractional crystallization paths.....	25
Comparison of predicted Fractional Crystallization Sequences (FCS).....	29
Glasses from EPR: an example of fractionation at 2 kbar.....	32
Summary.....	33
References.....	35
Tables.....	38
Figure Caption.....	48
Figures.....	52

Chapter 2: Submarine Lavas From Mauna Kea Volcano, Hawaii: Implications for Hawaiian Shield-Stage Processes.....67

Abstract.....	68
Introduction.....	69
Sampling.....	70
Petrography.....	71
Analytical.....	71
Results	
Mineral Composition.....	72
Major Element Compositi on	73
Trace Element Abundances.....	75
Sr, Nd, Pb and He isotopic ratios.....	76
Discussion	
Compositional variations in Group 1 samples: mixing of evolved melt and a magma with abundant olivine xenocrysts.....	76
Compositional variations in Group 2 samples: magma mixing and evidence for a highly evolved melt component.....	78
Diversity of Primary Magmas Represented in the Uppermost Mauna Kea Shield.....	79
Geochemical Comparisons With Other Hawaiian Shields.....	80
Conclusions.....	81

References.....	83
Tables.....	88
Figure Captions.....	92
Figures.....	97

Chapter 3: Mineral Chemistry of Submarine Lavas from Mauna Kea, Hawaii: Implications for processes at rift zones.....	112
Abstract.....	113
Introduction.....	114
Samples.....	115
Analytical Techniques.....	116
Petrography and mineral compositions.....	116
Discussion	
Magma mixing in isolated magma chambers.....	123
The compositions of the evolved magmas.....	125
The origin of olivine-cognate or exotic.....	126
Implications from olivine rim compositions.....	128
Evidence of high pressure fractionation.....	129
Comparison with Mauna Kea lavas recovered from. Hawaiian Scientific Drilling Project (HSDP).....	130
Conclusions.....	131
References.....	132
Tables.....	135
Figure Captions.....	150
Figures.....	153

Chapter 4: Evolution of Mauna Kea volcano: Inferences from lava compositions recovered in the Hawaii Scientific Drilling Project.....	169
Abstract.....	170
Introduction.....	171
Previous Studies of Mauna Kea Volcano.....	172
Results	
Major Elements.....	174
Incompatible Trace Elements.....	177
Discussion	
Compositional effects of post-eruptive alteration processes.....	180
Comparison of Tholeiitic to Alkalic Transition in HSDP Core and Subaerial Exposed Sections.....	181
Petrogenetic Inferences Resulting From Systematic Changes in Magma Composition as a Function of Depth in the HSDP Core.....	183
Implications For How the Hawaiian Plume "Works".....	192
Conclusions.....	193
References.....	194
Tables.....	200
Figure Captions.....	202
Figures.....	206

Chapter 5: The geochemistry of Mt. Bureau basalts: implications for the plume composition and plume-MORB interaction.....	221
Introduction.....	222

Samples.....	225
Petrographic Description.....	225
Analytical Methods.....	225
Results.....	226
³⁹ Ar/ ⁴⁰ Ar dating.....	226
Major elements	227
Trace elements	228
The effects of zeolitisation on chemical compositions.....	229
Sr, Nd, and Pb isotopes.....	230
Grouping of samples.....	232
Discussion.....	233
General geochemical variations in group A samples.....	233
<i>The role of crystal fractionation.....</i>	233
<i>Parental magmas for group A lavas.....</i>	236
<i>The scatter in the general MgO-SiO₂ correlation defined by</i>	
<i>group A samples: Evidence for control by partial melting.....</i>	238
<i>Compositional variations with stratigraphic height in the upper</i>	
<i>subsection</i>	239
<i>The Sr, Nd, and Pb isotopic compositions of group A lavas:</i>	
<i>implications for plume isotopic compositions.....</i>	241
The origin of the isotopic diversity of the Mt. Bureau lavas.....	242
<i>Kerguelen Plume -SEIR MORB interaction</i>	242
<i>Source mixing or melt mixing</i>	245
<i>Kerguelen Plume-Kerguelen Plateau interaction.....</i>	249
<i>Isotopic variations in the Mt. Bureau section: implications for</i>	
<i>plume-MORB interaction.....</i>	250
<i>Comparisons of ⁸⁷Sr/⁸⁶Sr ratios in volcanic and plutonic rocks:</i>	
<i>constraints on the time scale of heterogeneity.....</i>	252
Conclusions.....	253
References.....	255
Tables.....	260
Figure Captions.....	272
Figures.....	278

INTRODUCTION

Long-lived ocean islands are formed by partial melting of thermal plumes rising from boundary layers. Thermal plumes rise because of thermal instability which develops when the Rayleigh number Ra_δ ($Ra_\delta = \frac{\alpha g \Delta T \delta(t)^3}{\kappa \nu}$; where α is the thermal expansivity, g is gravity, ΔT is temperature difference between the top and bottom of the layer, $\delta(t)$ is the thickness of the layer which increases with time and is defined as $\delta(t) = (\pi \kappa t)^{1/2}$, κ is thermal diffusivity and ν is viscosity) of a thermal boundary layer reaches a critical value, for example 3000 (the Rayleigh number for mantle convection ranging from $5 \cdot 10^5 \sim 5 \cdot 10^7$) suggested by Howard (1964). The core-mantle boundary is a thermal boundary layer where plumes may develop. Plumes originating from core-mantle boundary were proposed in whole mantle convection models (Loper, 1985; Bercovici et al., 1989; Olson et al., 1989). Another possible region where plumes may form is the transition zone, where a significant temperature difference exists between upper and lower mantle (Jeanloz and Morris, 1986). Plumes initiation from the transition zone are suggested in layered mantle convection models (Richter and McKenzie, 1981; Kenyon and Turotte, 1983; O'Nions, 1987).

To the first order thermal plumes are fixed with respect to each other and the locations of these thermal plumes are referred as hot spots (Wilson, 1963). As a thermal plume ascends, adiabatic decompression (a temperature gradient of $1^\circ\text{-}2^\circ\text{C/kb}$) causes it to melt when its temperature becomes higher than the solidus temperature (a temperature gradient of $\sim 13^\circ\text{C/kb}$) generating basaltic magmas. Hot spot volcanism may initiate with a high magma production rate forming continental flood basalts, such as the Deccan Traps and Columbia River basalt province, and submarine oceanic plateaus, such as the Kerguelen Plateau, (Richard et al., 1989; White and McKenzie, 1989). As the magma production rate decreases, smaller seamounts and oceanic islands form (Richard et al., 1989). Because hot spots are relatively stationary, hot spot volcanism ceases when a volcano is carried away from the hot spot by the motion of the

lithospheric plate. This results in a chain of volcanoes with a progressive increase in ages as volcanoes move away from the hot spot; for example, the Emperor-Hawaiian chain in the Pacific Ocean and the Ninetyeast Ridge in the Indian Ocean (Wilson, 1963). These linear structures on the ocean floor indicate the direction of plate motion (Morgan, 1972).

Although the depth where plumes originate is an issue of debate, it is generally accepted that thermal plumes rise from deep mantle. Studies on ocean island basalts (OIB) show that the plume sources are distinct from the sources of mid-ocean ridge basalts (MORB) which are depleted in incompatible trace elements by previous partial melting events. Isotopic compositions indicate that OIB are derived from mixed sources with several possible components including primitive mantle, the depleted MORB source, recycled oceanic crust and sediments (Hofmann and White, 1982; Zindler and Hart, 1986; Weaver, 1991). To infer the chemical compositions of plume sources from basalts is difficult because of the complexities introduced during partial melting, and postmelting processes, such as crystal fractionation, magma mixing, wall rock interaction, and post-eruptive alteration.

In this thesis, I investigate the geochemical effects of these processes by studying lavas forming Mauna Kea volcano at Hawaii and Mt. Bureau in the Kerguelen Archipelago. Chapter one focuses on crystal fractionation. Empirical equations derived from 190 experiments were used to describe the compositions of olivine-plagioclase-augite saturated melts. Based on these equations, a method was developed to calculate the chemical variations during fractionation at 0.001-10 kb. This algorithm was used in chapter four to estimate the pressures at which high Fe-Ti basalts from Mauna Kea volcano formed and in chapter five to calculate the liquid line of descent of Mt. Bureau lavas. In chapter two, the compositional variations of submarine lavas dredged from the east rift of the Mauna Kea volcano were attributed to olivine accumulation. The variations in isotopic ratios and abundance ratios of trace elements indicate that these submarine lavas were not derived from a common source. The detailed mineral compositions of these submarine lavas were presented in chapter three. They provide evidence for magma

mixing and extensive fractionation in isolated magma chambers in the rift zone distant from the summit of the volcano. Chapter four is a study of drill core samples recovered by the Hawaiian Scientific Drilling Project (HSDP). The compositions of primary magmas were estimated by adding equilibrium olivine to the compositions of nearly aphyric lavas. The compositional variations in these estimated primary magmas reflect the extents of partial melting and the depths of magma segregation. From the variations in the abundances of incompatible elements in the estimated primary magmas, such as Nb, and abundance ratios, such as La/Yb, the variations in the extents of melting can be inferred. These HSDP samples were compared to the older submarine lavas and younger subaerially exposed lavas (Frey et al., 1990; Frey et al., 1991) to understand the evolution of Mauna Kea volcano. Chapter five is a study of Mt. Bureau lavas which are the surface expression of the Kerguelen Plume. The Mt. Bureau lava section is divided into two subsections based on their geochemical characteristics. There are no systematic variations in isotopic and chemical compositions with stratigraphic height, but lavas from the upper subsection are relatively homogeneous in chemical and isotopic compositions. They evolved from diverse parental magmas and reflect the geochemical characteristics the Kerguelen Plume. Lavas from the lower subsection were derived from mixed sources with different proportions of plume and MORB source components. The tectonic setting may have been an important factor in controlling the mixing process.

REFERENCES

- Bercovici D., Schubert G., and Glatzmaier G. A. (1989) Three-dimensional, large-scale convection in the Earth's mantle. *Science* 244, 950-955.
- Frey F. A., Garcia M. O., Wise W. S., Kennedy A., Gurriet P., and Albarede F. (1991) The evolution of Mauna Kea Volcano, Hawaii: Petrogenesis of tholeiitic and alkalic basalts. *J. Geophys. Res.* 96, 14,347-14,375.
- Frey F. A., Wise W. S., Garcia M. O., West H., Kwon S.-T., and Kennedy A. (1990)

- Evolution of Mauna Kea Volcano, Hawaii: Petrologic and geochemical constraints on postshield volcanism. *J. Geophys. Res.* 95, 1271-1300.
- Hofmann A. W. and White W. M. (1982) Mantle plumes from ancient oceanic crust. *Earth Planet. Sci. Lett.* 57, 421-436.
- Howard L. N. (1964) Convection at high Rayleigh number. *Proceedings of the 11th International Congress on Applied Mechanics, Munich.*, 1109-1115.
- Jeanloz R. and Morris S. (1986) Temperature distribution in the crust and mantle. *Ann. Rev. Earth Planet. Sci.* 14, 377-415.
- Kenyon P. M. and Turotte D. L. (1983) Convection in a two-layer mantle with a strongly temperature-dependent viscosity. *J. Geophys. Res.* 88, 6403-6414.
- Loper D. E. (1985) A simple model of whole mantle convection. *J. Geophys. Res.* 90, 1809-1836.
- Morgan W. J. (1972) Plate motions and deep mantle convection. *Geol. Soc. Am. Mem.*, 7-22.
- O'Nions R. K. (1987) Relationships between chemical and convective layering in the Earth. *J. Geol. Soc. Lond.* 144, 259-274.
- Olson P., Silver P. G., and Carlson R. W. (1989) The large-scale structure of convection in the Earth's mantle. *Nature* 344, 209-215.
- Richard M. A., Duncan R. A., and Courtillot V. E. (1989) Flood basalts and hot spot tracks: plume heads and tails. *Science*.
- Richter F. M. and McKenzie D. P. (1981) On some consequences and possible causes of layered mantle convection. *J. Geophys. Res.* 86, 6124-6133.
- Weaver B. L. (1991) The origin of ocean island basalt end-member compositions: trace element and isotopic constraints. *Earth Planet. Sci. Lett.* 104, 381-397.
- White R. and McKenzie D. P. (1989) Magmatism at rift zones: the generation of volcanic continental margins and flood basalts. *J. Geophys. Res.* 94, 7685-7730.
- Wilson J. T. (1963) A possible origin of the Hawaiian islands. *Can. J. Phys.* 41, 863-870.

Zindler A. and Hart S. R. (1986) Chemical Geodynamics. *Ann. Rev. Earth Planet. Sci.* 14, 493-571.

CHAPTER ONE

**Experiments and models of anhydrous, basaltic
olivine-plagioclase-augite saturated melts from 0.001
to 10 kbar**

ABSTRACT

A new method for modeling fractional crystallization processes that involve olivine (ol), plagioclase (plag) and augite (aug) is presented. This crystallization assemblage is the major control on the chemical variations in mid-ocean ridge basalts. The compositional and temperature variations in ol-plag-aug saturated basalts over a range of pressures are described using empirical expressions. A data base of 190 experiments in natural and basalt-analog chemical systems is used to describe temperature, Al, Ca and Mg molar fractions as functions of Si, Fe, Na, Ti and K molar fractions and pressure. The effects of minor components, such as Na, Ti and K, on major elements are evaluated using two methods: (1) investigating the differences between observed natural compositions and those predicted from equations developed from experiments in simple systems and (2) using equations developed in this paper to predict compositions of ol-plag-aug saturated melts. Increases in the abundances of Na and K cause Ca and Mg abundances to decrease and Al abundance to increase in ol-plag-aug saturated melts. The effects of variations of Ti are to increase Mg but decrease Al and Ca. The equations presented here can be used to evaluate the pressure and temperature at which a given melt can be saturated with ol-plag-aug, and thus provide a useful thermobarometer. A model is described to calculate ol-plag-aug fractional crystallization as a function of pressure and melt composition, using melt and augite models developed here, combined with existing models for olivine-melt and plagioclase-melt equilibria. I compare the fractional crystallization sequence of ALV-2004-3-1 predicted from the models presented in this paper, Langmuir et al. (1992) modified by Reynolds (1995), Ariskin et al. (1993), and Ghiorso and Sack (1995) at 0.001 and 4 kbar. As an example, I show that the glasses from the east flank of the East Pacific Rise at 11°45'N may have been derived by crystallization processes at 2 kbar.

INTRODUCTION

Phase diagrams have been used extensively in the investigation of the generation and evolution of basalts. Phase diagrams in the simple systems, such as CaO-MgO-Al₂O₃-SiO₂ (CMAS) and CMAS+Na₂O, are powerful because the limited variance of equilibria in these systems allows the phase boundaries to be depicted in one, two and three dimensions, and thus easily visualized. For example, Walter and Presnall (1994) determined the position of the boundary of olivine-orthopyroxene-clinopyroxene-an Al phase-melt in P-T-composition space by parameterizing the divariant equilibrium melting in the CMAS+Na₂O system from 7 to 35 kbar in terms of pressure and Na₂O abundance in the melt. Shi developed equations to describe the olivine (ol)-plagioclase (plag)-augite (aug)-melt (OPAM) boundary from experiments in the CMAS+FeO (Shi, 1992) and CMAS+FeO+Na₂O (Shi, 1993) system at 0.001 kbar. Phase diagrams relevant for natural system crystallization and melting processes have traditionally been less tractable due to the higher variance of equilibria in the natural system. The accumulation of relevant experimental data, however, has made possible the development of methods for predicting multi-variant phase boundaries (degree of freedom greater than three). Kinzler and Grove (1992), for example, compiled ~70 experimental data to develop equations to describe the phase boundaries defined by melts coexisting with ol, aug, low-Ca pyroxene and an Al phase in both the plagioclase and spinel stability fields.

In this study, the results of anhydrous experiments carried out at 0.001 kbar on a variety of basaltic compositions are presented. In order to explore the effects of minor components (Na, Ti, and K) on the OPAM boundary, these data and experiments in the natural system from the literature are predicted using equations derived from experiments in the CMAS+FeO (Shi, 1992) and CMAS+FeO+Na₂O systems (Shi, 1993). Differences between observed and predicted compositions are interpreted to be caused by the presence of minor components such as Na₂O, K₂O and TiO₂ in the natural system. I then develop empirical equations describing the

OPAM boundary in P-T-composition space, based on 190 experiments in the natural and simple systems over the pressure range of 0.001~10 kbar, which include new data as well as data from the literature. These equations resolve the individual effects of Na, K and Ti on Ca, Al and Mg in ol-plag-aug saturated melts. I also demonstrate how to use these equations as a thermobarometer to estimate the pressure and temperature at which a given melt can be saturated with ol, plag, and aug.

Empirical equations for predicting augite compositions as functions of pressure and their coexisting melt compositions are also presented. These empirical equations for describing melt and augite compositions are combined with the existing expressions for ol-melt and plag-melt equilibria to construct a model for calculating fractional crystallization paths for a range of basaltic compositions. The new model for predicting the OPAM boundary represents an improvement over the method described by Grove et al. (1992), because composition and pressure effects on both ol-plag-aug saturated melt and augite compositions are taken into account in the model presented here. The OPAM boundary is especially relevant for mid-ocean ridge basalts (MORB) as the dominant geochemical variations present in MORB have been attributed to ol-plag-aug fractionation (Walker et al., 1979; Stolper, 1980). A fractional crystallization path calculated from the model presented in this chapter is compared with those calculated from the programs of Langmuir et al. (1992) modified by Reynolds (1995), Ariskin et al. (1993), and Ghiorso and Sack (1995). Finally, the fractionation history of a suite of glasses from the east flank of East Pacific Rise (EPR) at 11°45'N is discussed by comparing the compositional trend defined by these glasses with 0.001 kbar experimental results and the fractionation path calculated at 2 kbar using the method presented here.

EXPERIMENTS

Starting Material

As high MgO lavas are potential parents for more evolved lavas, these were selected as

starting material. All six lavas used in the experiments consist of fresh glassy to aphyric pillow fragments. Four of the lavas, PROTEA-9-70-002, 67-032, 64-002 and 61-002, were dredged from 10~12°N on the EPR in 1984 (Thompson et al., 1985; 1989). The fifth, ALV-2004-3-1, was sampled by ALVIN dive 2004 at 11°45'N on the EPR. The sixth, RE-46, which has the highest MgO abundance coupled with an unusually low Na₂O abundance, is an Icelandic basalt. Table 1 provides chemical analyses of the starting material. PROTEA-9-70-002 was analyzed by electron microprobes at both Smithsonian and Massachusetts Institute of Technology (MIT).

Experimental Methods

Anhydrous isothermal experiments were carried out at 0.001 kbar. The freshest parts of the basalt pillows were reduced to powder by grinding in a SPEX shatter box for 3 minutes. 0.08~0.1 g of powdered sample were pressed into a pellet using elvanol as a binder. The pellet was sintered on a 0.008" diameter Fe-Pt alloy wire loop using a natural gas/oxygen torch. The loop and sample were suspended in the hot spot of a Deltech DT31VT quenching furnace. Temperature was monitored by a Pt-Pt₉₀Rh₁₀ thermocouple which was calibrated against the melting points of NaCl, Au and Pt on the IPTS 1968 temperature scale (Biggar, 1972). Oxygen fugacity was controlled near the quartz-fayalite-magnetite (QFM) oxygen buffer using a CO₂-H₂ gas mixture, and monitored by ZrO₂-CaO electrolyte cells. Experiments were terminated by quenching in water. Experimental run conditions are reported in Table 2.

Volatilization of sodium from the experimental charge and mass transfer of iron between the experimental charge and container (wire loop) can be significant problems in 0.001 kbar experiments. In order to minimize the iron exchange between the silicate charge and Pt wire loop, the loops used to hold the experimental charge were fabricated to contain about 8 wt % iron. This Fe-Pt alloy is in equilibrium with tholeiite at QFM over the temperature interval of 1400 to 1100 °C (Grove, 1981). Sodium volatilization is related to sample size, gas flow rate, oxygen fugacity, experimental duration, and experimental temperature (Tormey et al., 1987).

Larger sample size (100 mg), and low gas flow rate (0.1 mL/s) were used to reduce sodium volatilization.

Analytical Method

Phase compositions were analyzed with MIT 4-spectrometer JEOL 733 superprobe, using 15 Kev accelerating voltage and 10 nA beam current. Beam size is 10 μm for glass analyses and 1 μm for crystalline phases. Counting time were 20-40 seconds depending on elements. The data were reduced using Bence and Albee (1968) matrix correction with modification of Albee and Ray (1970). Olivine and glass are homogeneous while plagioclase and augite tend to be compositionally zoned. Only the rim compositions were analyzed for plagioclase and augite.

EXPERIMENTAL RESULTS

All the phase compositions in the experimental products are listed in Table 3. The Fe-Mg exchange distribution coefficients [$K_D = (X_{\text{Fe}}^{\text{xtl}} \cdot X_{\text{Mg}}^{\text{liq}}) / (X_{\text{Mg}}^{\text{xtl}} \cdot X_{\text{Fe}}^{\text{liq}})$] are 0.28 ± 0.01 for olivine-liquid and 0.24 ± 0.02 for augite-liquid. The plagioclase-liquid Ca-Na exchange distribution coefficients [$K_D = (X_{\text{Ca}}^{\text{xtl}} \cdot X_{\text{Na}}^{\text{liq}}) / (X_{\text{Na}}^{\text{xtl}} \cdot X_{\text{Ca}}^{\text{liq}})$] range from 0.75 to 1.30, most are within 1.15 ± 0.15 . The consistent K_D values do not prove equilibrium, but are good indicators of close attainment of exchange equilibrium. Mass balance between the bulk composition of starting material and experimental products was used to evaluate whether iron or sodium had been lost from the silicate charge. Na_2O loss was typically 1-5 % relative. Iron loss was typically less than 1-3 %. The crystallization sequence for sample RE-46 is olivine followed by plagioclase then augite in at 1198 °C (Fig. 1). Sample ALV-2004-3-1 has olivine-plagioclase near its liquidus followed by augite in at 1170 °C. Augite begins to crystallize in addition to olivine and plagioclase over the temperature interval of 1170-1150 °C in the other four starting compositions. Due to its higher $\text{CaO}/\text{Al}_2\text{O}_3$ ratio, RE-46 has a higher ol-plag-aug

saturation temperature than the other compositions (Fig. 1).

DISCUSSION

Prediction of ol-plag-aug saturated melts

Effects of Na₂O Since 85~90% of the chemical constituents in basalts and upper mantle are contained in the CMAS system, it constitutes a good analog system for studying partial melting and crystal fractionation (Presnall et al., 1978; Libourel et al., 1989). In the natural system behavior is more complex because at least four more components: FeO, Na₂O, TiO₂ and K₂O, are required to describe the compositional variations. Shi and Libourel (1991) carried out experiments in the CMAS+FeO system at 0.001 kbar to investigate the effects of FeO on the CMAS system. Shi (1992) developed empirical equations to describe the compositions of ol-plag-aug saturated melts in the CMAS+FeO system at 0.001 kbar (variance=2). He used temperature and Si molar fraction in melt (X_{Si} ; in later discussion X denotes molar fraction) as two independent variables to describe the molar fractions of Al, Ca, Fe and Mg (X_{Al} , X_{Ca} , X_{Fe} and X_{Mg}) in melts saturated with ol-plag-aug. In order to evaluate the effects of Na₂O, TiO₂ and K₂O on ol-plag-aug saturated melts, I used the equations of Shi (1992) to predict the experiments in the CMAS+FeO+Na₂O and natural systems. The data set used for evaluation is listed in Table 4. The comparisons between observed compositions and compositions predicted from the equations of Shi (1992) are shown in Fig. 2. Predicted compositions have higher X_{Fe} and X_{Ca} , and lower X_{Al} than observed compositions. Predictions X_{Mg} for are good for high-Mg melts but more scattered for low-Mg melts which contain greater abundances of Na₂O, TiO₂ and K₂O.

The differences between observed compositions and those predicted from the equations of Shi (1992) are attributed to the effects of the minor components present in the natural but not in CMAS+FeO system. Because Na is the most abundant of the minor components in the data set [1.32~8.43 wt % corresponding to 2~7 mole %, excluding the experiments on lunar

samples (Grove and Vaniman, 1978)], I plot Na_2O wt % versus the differences between predicted and observed compositions (i.e. $\Delta\text{Al} = \text{predicted } X_{\text{Al}} - \text{observed } X_{\text{Al}}$). Na_2O correlates with ΔAl , ΔCa and ΔFe (Fig. 3). Differences increase as Na_2O abundance in the melt increases. Based on Fig. 3, the addition of Na_2O increases Al and decreases Ca and Fe relative to the Na_2O -free system. The behaviors are consistent with the experimental results of Biggar and Humphries (1981). They showed that an increase in the abundance of Na_2O moves ol-plag-aug saturated melt compositions towards the plagioclase apex of the forsterite-diopside-plagioclase pseudoternary in the forsterite-diopside-anorthite-albite system. Shifting ol-plag-aug saturated melt compositions towards the plagioclase apex causes increases in the Al and Si abundances and decreases in the Fe, Ca and Mg abundances in the melt. However, this plagioclase effect is difficult to reconcile with the lack of Na_2O - ΔMg correlation for the experiments of Shi (1993) for which Na_2O is the only additional component. The Shi (1993) experiments were carried out at a constant temperature, 1100 °C, and thus temperature may be exercising an important control on the Na_2O - ΔMg systematics. Another striking feature of the ΔMg - Na_2O variation is that experiments on alkalic compositions (open triangles) and tholeiitic compositions (stars and open diamonds) do not show the systematic variation as defined by Na_2O versus ΔAl , ΔCa and ΔFe . For example, the differences between predicted and observed Al, Ca and Fe increase as Na_2O abundance increases from tholeiitic to alkalic compositions. In contrast, there is no systematic Na_2O - ΔMg variation from tholeiitic to alkalic compositions. This reflects the effects of other minor components and will be discussed in next sections.

Combined effects of TiO_2 and K_2O on ol-plag-aug saturated melts The combined effects of other minor components on ol-plag-aug saturated melts can be evaluated by comparing ΔCa , ΔFe , ΔMg and ΔAl between the natural and CMAS+FeO+ Na_2O systems again using the equations of Shi (1992). In Fig. 3 at a given Na_2O content, experiments on natural compositions (symbols other than open circle) have larger magnitudes of ΔCa , ΔFe and ΔAl than melts of the CMAS+FeO+ Na_2O compositions (open circles). These differences can be

inferred to reflect the combined effects of other minor components. As Ti_2O and K_2O are the next most abundant components after Na_2O , the discrepancies of ΔCa , ΔFe and ΔAl between the natural and CMAS+FeO+ Na_2O systems are attributed to the combined effects of these two elements. As Fig. 3 shows, the combined effects of Ti_2O and K_2O on Ca, Fe and Al abundances in ol-plag-aug saturated melts are similar to those of Na_2O , since the addition of TiO_2 and K_2O increases the magnitudes of ΔCa , ΔFe and ΔAl . This analysis does not, however, allow us to distinguish between the individual effects of Ti_2O and K_2O .

The equations of Shi (1992) tend to overestimate and underestimate X_{Mg} for nepheline (open triangles in Fig. 3) and hyperthene normative compositions (stars and open diamonds in Fig 3), respectively. In the experiments of Sack (1987), Na_2O and K_2O are the most abundant components in addition to CMAS components (Na: 5.1~12.6 mole %; K: 1.4~6.6 mole % , Ti: 1.1~3.3 mole % compare to Na: 2~7 mole %, K: 0.01~1.4 mole %, Ti: 0.4~4.2 mole % in tholeiitic compositions). High alkali abundances drive melt compositions towards the plagioclase apex and hence decrease X_{Mg} in the melts. This explains the overestimate of X_{Mg} for the experiments of Sack (1987) by the equation of Shi (1992). For tholeiitic compositions TiO_2 is the next abundant component after CMAS+FeO+ Na_2O . The negative correlation between TiO_2 and ΔMg exhibited by experiments on tholeiitic compositions indicates that the addition of TiO_2 to CMAS+FeO increases X_{Mg} (decreases ΔMg) in the melts (Fig. 4). This effect is opposite to the effects of Na_2O and K_2O discussed above. The effect of TiO_2 on X_{Mg} apparently overwhelms that of Na_2O in tholeiitic compositions because the equation of Shi (1992) underestimates ($\Delta\text{Mg} < 0$, Fig. 4) rather than overestimating X_{Mg} in the experiments for tholeiitic compositions. The relatively good TiO_2 - ΔMg correlation compared to the lack of Na_2O - ΔMg correlation for tholeiitic compositions (Figs. 4 and 3) also indicates that ΔMg in tholeiitic compositions is dominated by TiO_2 even though X_{Ti} is less than X_{Na} .

Shi (1993) also developed empirical equations for describing compositions of ol-plag-aug saturated melts and coexisting phases in the CMAS+FeO+ Na_2O system at 1100 °C

(variance=2). Therefore, the combined effects of TiO_2 and K_2O on melt composition can be evaluated by comparing the observations and predictions obtained using the equations of Shi (1993) for experiments on natural samples. However, large differences exist between observed compositions and those predicted with the equations of Shi (1993) (Fig. 5). The good correlations between temperature and ΔCa , ΔFe , ΔMg and ΔAl confirm that the differences are likely to be dominated by temperature (Fig. 6). At 1100 °C, temperature has no effect on the differences and thus the differences (indicated by the arrows in Fig. 6) should reflect the combined effects of TiO_2 and K_2O . Because the equations of Shi (1993) underestimate Al and overestimate Ca and Fe at 1100 °C, the combined effects of TiO_2 and K_2O are to increase Al and decrease Ca and Fe contents in melts (Fig. 6). This agrees with the inference from the Shi (1992) equations (Fig. 3). The equation of Shi (1993) underestimates and overestimates X_{Mg} in tholeiitic and alkalic melts, respectively, at 1100°C. Because TiO_2 and K_2O are the next abundant components after CMAS+ Na_2O in tholeiitic and alkalic compositions respectively, it is inferred that the effect of TiO_2 is to increase X_{Mg} and that of K_2O is to decrease X_{Mg} in ol-plag-aug saturated melts.

Estimating the compositions of ol-plag-aug saturated melts As discussed above, variations in the abundances of minor components such as Na_2O , TiO_2 and K_2O have systematic effects on the compositions of natural system melts saturated with ol-plag-aug, relative to melts saturated with this same mineral assemblage in the simple systems. I developed equations based on experiments in both the natural and simple systems to describe the compositions of ol-plag-aug saturated melts. Data from high pressure experiments (Grove et al., 1992; Grove et al., 1990; Baker and Egglar, 1987; Bender et al., 1978) were also included in the data set to parameterize equations for ol-plag-aug saturated melt compositions as functions of pressure, and bulk composition by multiple regression. This data set (Table 4) covers nepheline- and hyperthene-normative compositions and its compositional ranges are as following, Mg#: 0.15~1, Na_2O : 0~8.43 wt %, SiO_2 : 38.59~63.41wt %, TiO_2 : 0~5.63 wt %, K_2O : 0~5.45 wt % and pressure

ranges from 0.001 to 10 kbar. Eight components: SiO₂, TiO₂, Al₂O₃, FeO, MgO, CaO, Na₂O and K₂O; are required and sufficient to describe the basaltic compositions. The variance of a 4-phase equilibrium in an 8-component system is 6 ($F=C+2-P=8+2-4=6$; F is the variance, C is the number of components and P is the number of phases). To evaluate the effects of pressure and minor components on major components, pressure, X_{Na} , X_K and X_{Ti} are chosen as independent variables. Two more independent variables are required. Least squares multiple linear regression analysis was used to obtain equations that combined X_{Si} and X_{Fe} with X_{Na} , X_K , X_{Ti} and pressure to predict X_{Al} , X_{Ca} , X_{Mg} and temperature. Based on 190 experiments, the coefficients for the independent variables listed in Table 5 provide the best fits describing X_{Al} (eq. 1), X_{Ca} (eq. 2), X_{Mg} (eq. 3) and temperature (eq. 4). Pressure is in kbar and temperature is in °C. The values in parentheses are the standard errors of the coefficients. The ratio of a coefficient and its standard error (t-value) gives the degree of significance of its corresponding variable. The higher the absolute t-value is, the more significant the variable. For example, the absolute t-value of X_K in eq. 1 (Table 5) is 17.3 and removing the X_K term from eq. 1 decreases the square of the correlation coefficient (R^2) from 0.937 to 0.835. In the equations most of the variables have absolute t-value greater than 10. The predicted temperatures are within ± 20 °C for 170 experiments. Fifteen are greater than ± 20 °C but less than ± 30 °C. Five are greater than ± 30 °C (Fig. 7).

As equations 1-3 (Table 5) are first degree polynomials for P, X_{Na} , X_K and X_{Ti} , the individual effects of these independent variables on dependent variables can be predicted from the sign of the coefficient of that independent variable. For example, if X_K , X_{Ti} , X_{Si} , X_{Fe} and P are fixed, increasing X_{Na} will decrease X_{Ca} and X_{Mg} but increase X_{Al} . Following this approach, it is inferred that the effects of X_K on X_{Ca} , X_{Mg} and X_{Al} are the same as that of X_{Na} and the effects of X_{Ti} are to decrease X_{Al} and X_{Ca} . The effect of X_{Ti} on X_{Mg} cannot be predicted from eq. 3, because the absolute t-value of X_{Ti} is 2.925 which means X_{Ti} is insignificant. Removing X_{Ti} from eq. 3 only slightly decreases R^2 (from 0.989 to 0.987). In

order to better evaluate the effect of X_{Ti} on X_{Mg} , I tested combinations of other independent variables that give more significant t-value (~ 5.8) for X_{Ti} to predict X_{Mg} (Table. 6). Although these equations give slightly low R^2 , they all predict that increasing X_{Ti} will increase X_{Mg} if other independent variables are fixed. Therefore, the effect of X_{Ti} on X_{Mg} is opposite to that of X_{Na} and X_K . This result is consistent with the inferences drawn from the discussion above using the equations of Shi (1992, 1993). The overall effects of increasing the abundance of X_{Ti} are to increase X_{Mg} but decrease X_{Al} and X_{Ca} . These effects tend to move melt compositions away from the plagioclase apex. In summary, the effects of X_{Na} and X_K counterbalance the effect of X_{Ti} on X_{Mg} . This may explain the success of the simple system equation (Shi, 1992) in predicting X_{Mg} (Fig. 2) for natural system data even though they did not consider the effects of X_{Na} , X_K and X_{Ti} .

Melt composition as a thermobarometer The equations presented in Table 5 can be used to estimate the temperature and pressure at which a basaltic melt may have coexisted with olivine, plagioclase and augite from the melt composition. VG-360, a sample inferred to have been on the ol-plag-aug cotectic at 4 kbar (Gataeni et al., 1995), is taken as an example. The X_{Ca} , X_{Al} and X_{Mg} predicted from equations 1-3 at various pressures were combined with other observed components and recalculated into normative oxygen unit components (Grove et al., 1993). A series of "predicted" compositions were projected from plagioclase onto the ol-cpx-qtz plane. Comparison between observed composition and the predicted melts indicates that the best fit is at 4 kbar (Fig. 8). Projections from ol, cpx and qtz also give best fit at 4 kbar implying that VG-360 may have been ol-plag-aug saturated at 4 kbar. Thus, the method described here gives a similar result to that obtained by Gataeni et al. (1995). The predicted pressure and compositional variables were then used in equation 4 to predict temperature. The predicted temperature for VG-360 is 1184 °C, while prediction from olivine composition gives 1161 °C (Gaetani et al., 1995). Another example shown in Fig. 8 is RE-46, a starting composition in this study. The prediction is consistent with the experimental results presented

in this study which show that RE-46 is not ol-plag-aug saturated at 0.001 kbar (Fig. 8). The third example is the composition of the glassy matrix of SU-46-66, a dredged tholeiite from the east rift of Mauna Kea, Hawaii. Predicted and observed normative oxygen unit components match very well at 0.001 kbar (Fig. 8). SU-46-66 contains phenocrysts of olivine, plagioclase and augite.

Predicting fractional crystallization paths The equations presented in Table 5 also can be used to track the position of the OPAM boundary in pressure, temperature and composition space as fractional crystallization of a basaltic magma proceeds and therefore provide the basis for a model of fractional crystallization. The OPAM boundary has been previously modeled by Grove et al. (1992). They first predicted the ol-plag-aug-low Ca pyroxene-melt (OPALM) point with the equations of Kinzler and Grove (1992), and then extended a straight line from the predicted OPALM point towards the Ol-Cpx sideline in the olivine-clinopyroxene-quartz (Ol-Cpx-Qtz) pseudoternary with a slope parallel to the experimentally determined OPAM boundary of ALV-1690-20 at 0.001 kbar. This was a simplification of more complex relations that are sensitive to both composition and pressure. In this paper the OPAM boundary is modeled as a function of both bulk composition and pressure. Mineral-melt equilibrium expressions for ol, plag and aug are required in order to calculate fractionation paths for melts that will saturate with some combinations of these mineral phases. As both pressure and system composition may change as fractionation proceeds, these mineral-melt equilibrium expressions need to incorporate the controls of both pressure and system composition on the compositions of ol, plag and aug that crystallize from basaltic melts.

Based on experimental results, the geometric relation between the OPALM, OPAM and ol-plag (OPM) boundaries was simplified by Grove et al. (1992) in the following way. For a given pressure and bulk composition, the OPAM boundary projects as a line terminated by the OPALM point in the Ol-Cpx-Qtz pseudoternary (Fig. 9a). In the olivine-plagioclase-clinopyroxene (Ol-Plag-Cpx) pseudoternary, the OPAM line collapses as a point overlapping

with the OPALM point forming the end point of the OPM boundary (Fig. 9b). The OPM boundary projects as a line perpendicular to Ol-Plag sideline (Fig. 9b). I will adopt these geometric relations to predict fractionation paths. The Ol-Cpx-Qtz pseudoternary is chosen to demonstrate the OPAM boundary since the OPAM boundary appears as a prominent feature in this projection. In the following section I provide a method for predicting ol-plag-aug fractionation paths as functions of pressure and system composition.

Olivine Fractionation For MORB the most common fractionation sequence at low pressure is olivine followed by olivine-plagioclase then olivine-plagioclase-augite. A typical primitive MORB composition is in the olivine primary phase liquidus volume. Therefore, olivine is the liquidus phase. In each fractionation step, the olivine composition can be calculated from the melt composition and the olivine-liquid Fe-Mg exchange distribution coefficient [$K_D = (X_{Fe}^{ol} \cdot X_{Mg}^{liq}) / (X_{Mg}^{ol} \cdot X_{Fe}^{liq}) = 0.3 \pm 0.03$]. This exchange K_D is constant over the range of compositions and pressures considered in this study (Roeder and Emslie, 1970; Gee and Sack, 1988; Ulmer, 1989). Fractionation of olivine alone proceeds until the melt composition intersects the ol-plag boundary.

Olivine-Plagioclase Fractionation Plagioclase joins olivine as a crystallizing phase when the melt composition reaches the OPM boundary. In the Ol-Plag-Cpx pseudoternary the OPM boundary is extended from the OPALM point, which is predicted from the equations of Kinzler and Grove (1992), perpendicularly to the Ol-Plag sideline. The Ol-Plag sideline is bisected by the OPM boundary into two segments which give the relative proportions of olivine and plagioclase in the fractionating assemblage. The predicted OPM boundary shifts slightly as melt composition changes and the boundary is recalculated at each increment by recalculating the OPALM point for the fractionated liquid. The result is that the olivine proportions vary in a range from 30~26 wt %. Equilibrium plagioclase compositions are calculated using the composition and pressure dependent expressions for plag-melt equilibrium of Grove et al. (1992). Olivine-plagioclase fractionation proceeds until augite becomes stable.

Determining melt composition for augite saturation For each increment in the "modeled" ol-plag fractionation path, X_{Ca} , X_{Al} and X_{Mg} were predicted by eq. 1-3 (Table 5), combined with other components and recalculated to form a "predicted path" of ol-plag-aug saturated melt compositions in the Ol-Cpx-Qtz pseudoternary. When the "predicted" composition for the ol-plag-aug saturated melt matches the "modeled" composition of the ol-plag saturated melt (i.e. the intersection of "modeled" ol-plag fractionation path and "predicted path", Fig. 10), augite joins the fractionating assemblage of the modeled melt. Henceforth, the fractionation assemblage contains three phases: ol, plag and aug. As an example, the first ol-plag-aug saturated melts at various pressures are shown in Fig. 10 along with "modeled" and "predicted" paths using the most primitive glass dredged from the east flank of the overlapping spreading center at 11°45'N on the EPR, ALV-2004-3-1.

Prediction of augite compositions coexisting with olivine, plagioclase and a basaltic melt

Augite composition is required in order to model crystallization along the OPAM boundary. Clinopyroxene-melt equilibria is complex and difficult to model, relative to olivine-melt and plagioclase-melt equilibria. Nielsen et al. (1988) found correlations of $\ln K$ (equilibrium constant between pyroxene and melt) with reciprocal temperature for enstatite (en), ferrosilite (fs) and diopside (di) components in pyroxene at 0.001 kbar. Therefore, quadrilateral pyroxene compositions can be predicted from melt composition if the equilibrium temperature is known. However, en, fs and di components in Nielsen et al. (1988) equations were calculated from the model of Davidson (1985) and Davidson and Lindsley (1985), which neglected minor components such as Al, Ti and Na. Sack and Carmichael (1984) modeled Ti content in clinopyroxene. However, their equations require Mg and Fe molar fractions in the clinopyroxene, information we need as well. In addition to equations for ol-plag-aug saturated melts, Shi (1993) also developed empirical equations for describing augite compositions in the CMAS+FeO+Na₂O system. However, these equations cannot predict compositions of augite in the natural system, most likely due to the constant temperature in his calibration data set. In

order to predict augite composition from coexisting melt composition and take minor components into account, I have chosen to model experimentally produced augite compositions empirically. The calibration data set is limited to include only augite compositions that coexist with ol-plag-aug saturated melts. The data set for regression includes experiments on natural samples over the pressure range from 0.001 to 10 kbar (Table 4). Augite composition was parameterized in terms of the composition of its coexisting melt, temperature and pressure. Combinations of independent variables that yield the best fits to 102 experimental augites are provided in Table 7. X_{Fe} and X_{Mg} were combined as one dependent variable, X_{FeMg} , for regression. X_{Fe} and X_{Mg} were then determined from augite Fe-Mg exchange K_{D} . The experimentally determined K_{D} is 0.24 at 0.001 kbar (this study) and 0.27 at 8~10 kbar (Grove et al., 1992). X_{Al} in augite (eq. 10) is calculated from the other components in augite which are predicted from the melt compositions (eq. 5-9). Equation 10 is thus a structure constraint for augite composition.

Olivine, plagioclase and augite fractionation In addition to mineral compositions, phase proportions are also required to constrain crystallization along the OPAM boundary. Recognizing that the OPAM boundary, as simplified by Grove et al. (1992), projects to a point in the Ol-Plag-Cpx pseudoternary, and assuming that the OPAM boundary is linear in the compositional space, one approach to obtain the proportions of ol-plag-aug in the crystallizing assemblage from the position of this point, relative to the projected positions of the three crystallizing phases (ol, plag and aug) in the pseudoternary. The predicted first ol-plag-aug saturated melt gives the ol-plag-aug proportions for the first increment of ol-plag-aug fractionation. After removing this increment, the residual melt composition is projected again onto the Ol-Plag-Cpx pseudoternary in order to determine the proportions of crystallizing phases appropriate for the next fractionation increment. In each fractionation increment X_{Ca} , X_{Al} and X_{Mg} of residual melt were predicted by equation 1-3, then combined with other modeled components to recalculate into "predicted" compositions. The "predicted" and

"residual" compositions should match well for a self-consistent model of ol-plag-aug crystallization along the OPAM boundary, however, this is not always the case. The lack of correspondence indicates that the OPAM boundary in the Oliv-Plag-Cpx-Qtz pseudoternary is curved rather than linear. Thus, the tangent of a point on this curve does not intersect the Oliv-Plag-Cpx pseudoternary at the same position as the projection of that point (OPAM point), and furthermore, the positions of tangent intersection vary with melt composition along the OPAM boundary. Therefore, to obtain the proportions of ol-plag-aug crystallizing along the OPAM boundary I used an iterative technique. An initial estimate of ol-plag-aug proportions is chosen using the estimates of Grove et al. (1992). The compositions of residual melts are compared to predicted melts that are obtained using this first estimate of phase proportions. The proportions of ol, plag and aug are then varied until the difference between the "predicted" and "residual" compositions is minimized. The OPALM point was also predicted for each fractionation increment. The OPAM boundary terminates when it meets OPALM point. The OPAM boundary modeled from an experimentally produced ol-plag-aug saturated melt, ALV-2004-3-1-10, is shown in Fig. 11 with that predicted from the method of Grove et al. (1992). The new model provides a better fit to the experimentally determined OPAM boundary than the previous model (Grove et al., 1992).

Comparison of predicted Fractional Crystallization Sequences (FCS) The FCS of ALV-2004-3-1, a high MgO glass from East Pacific Rise (EPR), at 0.001 and 4 kbar, were calculated by the models presented in this chapter (YKG), Langmuir et al. (1992) (with modifications by Reynolds, 1995, referred as LR), Ariskin et al. (1993, COMAG) and Ghiorso and Sack (1995, MELTS). This composition was used for the experimental study, and some aspects of these isothermal experiments can be directly compared with the FCS models. In each model fractional crystallization began at the liquidus and ceased at 5.00 wt % MgO. Results are summarized in Figs. 12, 13 and Table 8. First I compare the phase appearance sequence and proportions of near liquidus phases. In the case of basalt melts that are near multi-phase

saturation on their liquidus (ol-plag and ol-plag-aug in the case of ALV-2004-3-1) the differences between isothermal mineral phase appearance compositions and proportions and those that occur during fractional crystallization are small, so a comparison with the experimental data is justified. Second, I compare experimentally produced mineral compositions in an ol-plag-aug saturated melt with the phase compositions predicted for that liquid by the models. Third, I compare the liquid compositional variations followed during the fractional crystallization. In this instance, the isothermal experiments on ALV-2004-3-1 are not comparable, and only the models will be compared.

The 0.001 kbar the crystallization sequences predicted from YKG, LR, COMAG and MELTS are illustrated in Fig. 12. ALV-2004-3-1 has ol+plag on the liquidus and YKG and COMAG also predict these as liquidus phases. MELTS (not shown in Fig. 9, because temperature interval is small) and LR predict ol as a liquidus phase. YKG, LR and COMAG predict that augite joins the fractionating assemblage when residual melt evolves to 7.24, 7.46 and 7.16 wt% MgO, respectively. However, MELTS predicts that augite crystallizes at 8.39 wt% MgO and orthopyroxene crystallizes at 6.07 wt% MgO. In contrast to the prediction of MELTS, orthopyroxene is not observed in the experiments, nor is it a stable phase on the FCS calculated by YKG, LR and COMAG. Similarly, magnetite is not stable, but is predicted by COMAG. In summary, the early crystallization sequence predicted by MELTS, YKG, LR and COMAG are generally similar to the experimentally determined crystallization sequence, but there are some differences in later phase appearances. At 4 kbar, YKG predicts that ol and plag are liquidus phases, and the residual liquid becomes augite saturated at 8.20 wt% MgO. LR predicts olivine as the liquidus phase (not shown in Fig. 12) followed by plagioclase after a 4 °C interval and augite appears at 8.39 wt% MgO. COMAG predicts ol +plag as the liquidus assemblage, augite crystallizes at 7.9 wt% MgO and magnetite appears at 6.29 wt% MgO. The crystallization sequence predicted by MELTS at 4 kbar is aug - aug+plag - aug+plag+opx - aug+plag+opx+sp. From the experiments of Grove et al. (1992), ALV-2004-3-1 is inferred to

saturate with ol+plag+aug on its 8 kbar liquidus. Thus, MELTS predictions that augite is on the liquidus and that olivine is absent as a crystallizing phase are incorrect. For this reason, the FCS modeled by MELTS at 4 kbar is not considered in the following discussion. In summary, the crystallization sequences at 4 kbar predicted by YKG, LR and COMAG are generally similar and they differ from that predicted by MELTS.

The ol:plag proportions predicted from the four models are slightly different, but close to the proportions measured in ALV-2004-3-1 (Fig. 12). The MELTS estimate is identical to that in the experiment, and the LR estimate is 6 wt% higher in olivine. The ol:plag:aug proportions at the first appearance of aug in ALV-2004-3-1 are 4:50:46. The COMAG estimate (6:50:44) comes closest at 0.001 kbar to the values measured in the isothermal experiment.

To compare the compositions of minerals that each model predicts as crystallizing phases I chose an experimental liquid, ALV-2004-3-1-60, produced at 0.001 kbar and saturated with ol, plag and aug (Table 3). YKG and LR predict ol, plag and aug as saturating phases. MELTS and COMAG do not predict olivine as one of the saturating phases for the ALV-2004-3-1-60 liquid. MELTS predicts aug + plag and COMAG predicts orthopyroxene as the saturating phase. YKG and LR predict the same olivine compositions (Table 8). Predicted anorthite (An) contents in plagioclase are 0.68 (YKG), 0.71 (LR) and 0.62 (MELTS) (Table 8). Compared to those predicted by YKG and LR, the augite composition at 0.001 kbar modeled by MELTS has higher Al₂O₃ and FeO, and lower SiO₂, TiO₂, and CaO (Table 8). Plagioclase and augite compositions calculated by YKG fall between those predicted by LR and MELTS and are closer to experimental results (Table 8).

FCS predicted from YKG, LR, COMAG and MELTS at 0.001 and 4 kbar are compared in Fig. 13. The different slopes defined by ol-plag saturated melts in the MgO-Al₂O₃ and MgO-SiO₂ plot reflect the slight differences in the ol-plag proportions predicted by the four models. More significant differences exist between the ol-plag-aug saturated compositions predicted by each model. The early appearance of augite in the FCS predicted by MELTS causes low CaO in

residual melts (Fig. 13). The high TiO_2 in ol-plag-aug saturated melts modeled by MELTS is due to the low TiO_2 contents in augite predicted by MELTS. In general, the FCS calculated from MELTS at 0.001 kbar differs significantly from those calculated from YKG, LR and COMAG. At a given MgO content YKG, COMAG and LR predict lower SiO_2 and CaO, and higher FeO at 4 kbar relative to their respective 0.001 kbar FCS. The V-shaped pattern produced by COMAG at 0.001 and 4 kbar (Fig. 13) is caused by the appearance of magnetite as a crystallizing phase. LR predicts higher Na_2O contents in augite at 4 kbar causing Na_2O in residual melts to increase less steeply (Fig. 13) relative to YKG and COMAG.

Glasses from EPR: an example of fractionation at 2 kbar Glasses were collected with the submersible ALVIN from the east limb of the overlapping spreading center at $11^{\circ}45'\text{N}$ on the EPR. Most of the samples have MgO ranging from 6~7 %. Detailed sampling localities and major element chemistry are described by Thompson et al. (1989). In the Ol-Cpx-Qtz pseudoternary most of the dredged glasses form a coherent trend parallel to but offset towards olivine from the 0.001 kbar OPAM boundary defined by experimental data (Fig. 14). Some glasses deviate from the coherent trend and plot even farther towards the olivine corner. These are potential parental compositions for glasses that fall on the trend paralleling the 0.001 kbar OPAM boundary. The first ol-plag-aug saturated melts predicted from 4 potential parental compositions at 2 kbar lie on the trend defined by most glasses (solid squares, Fig. 14). Therefore, the trend defined by most glasses can be explained by magmas evolving from different parents to the onset of ol-plag-aug crystallization at 2 kbar. Another possibility that can be tested is that these glasses were derived from a single parent. A group of three samples which lie close to the primitive end of the trend but offset towards Olivine are good candidates. The 2 kbar fractionation path predicted from a potential parent, ALV-2002-2-1, is shown on Ol-Cpx-Qtz pseudoternary (Fig. 15). Although the OPAM boundary predicted from ALV-2002-2-1 is consistent with the trend defined by most glasses, the modeled and observed compositions do not correspond. For example, the melt composition of the last increment of the fractionation

calculation plots close to the most evolved glass, Dr-19, in Ol-Cpx-Qtz pseudoternary. However, Dr-19 has higher MgO than the last modeled melt (6.75 vs. 4.26 %). Therefore, fractional crystallization cannot explain the compositional variations in these glasses. An alternative is that these glasses evolved through equilibrium crystallization rather than fractional crystallization. To evaluate equilibrium crystallization, I mass balance all the glass compositions and their coexisting olivine, plagioclase and augite compositions, which were predicted from glass compositions, against ALV-2002-2-1 at 2 kbar. Most of the sums of the squared residual are less than 0.15. Therefore, equilibrium crystallization at 2 kbar from a single parent can explain the glass compositional variations of the glasses from east EPR. In conclusion, glasses from east EPR evolved through crystallization of ol, plag and aug at 2 kbar. They evolved either from diverse parental compositions to the onset of ol-plag-aug crystallization through fractional crystallization, or from a more restricted set of parental compositions through equilibrium crystallization.

SUMMARY

Based on the differences between experimentally produced ol-plag-aug saturated melt compositions in the natural system and those predicted from equations developed from experimentally produced ol-plag-aug saturated melts in simple systems, it is inferred that the effects of Na are to increase Al but decrease Ca and Fe in ol-plag-aug saturated melts. Empirical equations derived from a data set including experiments in the natural and simple systems over the pressure range of 0.001~10 kbar further suggest that the effects of Na and K are to decrease Ca, and Mg but increase Al in ol-plag-aug saturated melts. The effects of Ti are to increase Mg but decrease Al and Ca. The empirical equations describe the position of ol-plag-aug saturated melts in pressure-temperature-composition space and thus can be used to estimate the equilibrium pressure and temperature at which a given basaltic melt can coexist with olivine, plagioclase and augite. A method is described for predicting the fractionation path of

tholeiitic basalts at various pressures. A fractional crystallization sequence calculated from this method is compared with those predicted from the models of Langmuir et al. (1992, with modification by Reynolds, 1995), Ariskin et al. (1993), and Ghiorso and Sack (1995). I applied the model to a suite of glasses from the east limb of the overlapping spreading center at 11°45' N on the EPR. The results indicate that the compositions of these glasses can be explained by crystallization from diverse parents to the onset of ol-plag-aug crystallization through fractional crystallization or from restricted parental compositions to more evolved ol-plag-aug compositions through equilibrium crystallization, at 2 kbar (the base of crust).

REFERENCES

- Albee AL, Ray L (1970) Correction factors for electron microprobe analysis of silicates, oxides, carbonates, phosphates and sulfates. *Anal Chem* 42: 1408-1414
- Ariskin AA, Frenkel MY, Barmina GS and Nielsen RL (1993) Comagmat: A FORTRAN program to model magma differentiation processes. *Comp Geosci* 19: 1155-1170.
- Baker DR, Eggler DH (1987) Composition of anhydrous and hydrous melts coexisting with plagioclase, augite, and olivine or low-Ca pyroxene from 1 atm to 8 kbar: Application to Aleutian volcanic center of Atka. *Am Mineral* 72: 12-28
- Bence AE, Albee AL (1968) Empirical correction factors for the electron microanalysis of silicates and oxides. *J Geol* 76: 382-403
- Bender J F, Hodges FN, Bence AE (1978) Petrogenesis of basalts from the project FAMOUS area: Experimental study from 0 to 15 kbar. *Earth Planet Sci Lett* 41: 277-302
- Biggar GM (1972) Diopside, lithium metasilicate and the 1968 temperature scale. *Mineral. Mag.* 38: 768-770
- Biggar GM, Humphries DJ (1981) The plagioclase, forsterite, diopside, liquid equilibrium in the system $\text{CaO-Na}_2\text{O-MgO-Al}_2\text{O}_3\text{-SiO}_2$. *Mineral Mag* 44: 309-314
- Davidson PM (1985) Thermodynamic analysis of quadrilateral pyroxene. Part I: Derivation of the ternary non-convergent site-disorder model. *Contrib Mineral Petrol* 91: 383-389
- Davidson PM, Lindsley DH (1985) Thermodynamic analysis of quadrilateral pyroxenes. Part II: Model calibration from experiments and applications to geothermometry. *Contrib Mineral Petrol* 91: 390-404
- Gaetani GA, DeLong SE, Wark DA (1995) Petrogenesis of basalts from the Blanco Trough, Northeast Pacific: inferences for off-axis melt generation. *J Geophys Res* 100: 4197-4214
- Ghiorso MS, Sack RO (1995) Chemical mass transfer in magmatic processes IV. A revised and internally consistent thermodynamic model for the interpolation and extrapolation of liquid-solid equilibria in magmatic systems at elevated temperatures and pressures. *Contrib Mineral Petrol* 119: 197-212
- Gee LL, Sack, RO (1988) Experimental petrology of melilite nephelinites. *J Petrol* 29: 1233-1255
- Grove TL, Vaniman DT (1978) Experimental petrology of very low Ti (VLT) basalts. *Mare Crisium: The View from Luna 24*, Pergamon Press (New York): 445-471
- Grove TL (1981) Use of FePt alloys to eliminate the iron loss problem in 1-atmosphere gas mixing experiments: Theoretical and practical considerations. *Contrib Mineral Petrol* 78: 298-304
- Grove TL, Bryan WB (1983) Fractionation of pyroxene-phyric MORB at low pressure: An experimental study. *Contrib Mineral Petrol* 84: 293-309

- Grove TL, Kinzler RJ, Bryan WB (1990) Natural and experimental phase relations of lavas from Serocki Volcano. *Ocean Drill Proc Scientific Results* 106/109: 9-17
- Grove TL, Kinzler RJ, Bryan WB (1992) Fractionation of mid-ocean ridge basalt (MORB). *AGU Geophysical Monograph* 71: 281-310
- Grove TL (1993) Corrections to equations for calculating mineral components in "Origin of calc-alkaline series lavas at Medicine Lake Volcano by fractionation, assimilation and mixing" and "Experimental petrology of normal MORB near the Kane Fracture Zone: 22°N-25°N, mid-Atlantic ridge". *Contrib Mineral Petrol* 114: 422-424
- Juster TC, Grove TL (1989) Experimental constraints in the generation of FeTi basalts, andesites, and rhyodacites at the Galapagos spreading center, 85°W and 95°W. *J Geophys Res* 94: 9251-9274
- Kinzler RJ, Grove TL (1992) Primary magmas of mid-ocean ridge basalts, 1. experiments and methods. *J Geophys Res* 97: 6885-6906
- Kinzler RJ (1991) Experimental constraints on the generation and evolution of mid-ocean ridge basalts MIT, PhD thesis, pp 244
- Langmuir CH, Klein EM, Plank T (1992) Petrological systematics of mid-ocean ridge basalts: constraints on melt generation beneath mid-ocean ridges. *AGU Geophysical Monograph* 71: 183-280
- Libourel G, Boivin P, Biggar GM (1989) The univariant curve liquid = forsterite + anorthite + diopside in the system CMAS at 1 bar: Solid solutions and melt structure. *Contrib Mineral Petrol* 102: 406-421
- Nielsen RL, Davidson PM, Grove TL (1988) Pyroxene-melt equilibria: An updated model. *Contrib Mineral Petrol* 100: 361-373
- Presnall DC, Dixon SA, O'Donnel TH, Brenner NL, Schrock RL, Dycus DW (1978) Liquidus phase relations on the join Diopside-Forsterite-Anorthite from 1 atm to 20 kbar: Their bearing on the generation and crystallization of basaltic magma. *Contrib Mineral Petrol* 66: 203-220
- Reynolds JR (1995) Segment-scale systematics of mid-ocean ridge magmatism and geochemistry, Columbia University, PhD thesis, pp483
- Roeder PL, Emslie RF (1970) Olivine-liquid equilibrium, *Contrib Mineral Petrol* 29: 275-289
- Sack RO, Carmichael ISE (1984) $Fe^{+2} = Mg^{+2}$ and $TiAl_2 = MgSi_2$ exchange reactions between clinopyroxene and silicate melts. *Contrib Mineral Petrol* 85: 103-115
- Sack RO, Walker D, Carmichael ISE (1987) Experimental petrology of alkalic lavas: Constraints on cotectics of multiple saturation in natural basic liquids. *Contrib Mineral Petrol* 96: 1-23
- Shi P, Libourel G (1991) The effect of FeO on the system CMAS at low pressure and

- implications for basalt crystallization processes. *Contrib Mineral Petrol* 108: 129-145
- Shi P (1992) Basalt evolution at low pressure: Implications from an experimental study in the system CaO-FeO-MgO-Al₂O₃-SiO₂. *Contrib Mineral Petrol* 110: 139-153
- Shi P (1993) Low-pressure phase relationships in the system Na₂O-CaO-FeO-MgO-Al₂O₃-SiO₂ at 1100°C, with implications for the differentiation of basaltic magmas. *J Petrol* 34: 743-762
- Stolper E (1980) A phase diagram for mid-ocean ridge basalts: Preliminary results and implications for petrogenesis. *Contrib Mineral Petrol* 74: 13-27
- Thompson G, Bryan WB, Ballard RD, Hamuro K, Melson WG (1985) Axial processes along a segment of the East Pacific Rise, 10-12°N. *Nature* 318: 429-433.
- Thompson G, Bryan WB, Humphris SE (1989) Axial volcanism on the East Pacific Rise, 10-12°N. *Magmatism in the oceanic basins*, Saunders AD and Norry MJ (eds), Geological Soc. Spec. Pub. 42.
- Tormey DR, Grove TL, Bryan WB (1987) Experimental petrology of normal MORB near the Kane Fracture Zone: 22°-25°N, mid-Atlantic ridge. *Contrib Mineral Petrol* 96: 121-139
- Ulmer P, (1989) The dependence of the Fe²⁺-Mg cation-partitioning between olivine and basaltic liquid on pressure, temperature and composition. An experimental study to 30 kbar. *Contrib Mineral Petrol* 101: 261-273
- Walker D, Shibata T, DeLong SE (1979) Abyssal tholeiites from the Oceanographer fracture zone. II. Phase equilibria and mixing. *Contrib Mineral Petrol* 70: 111-125
- Walter MJ, Presnall DC (1994) Melting behavior of simplified lherzolite in the system CaO-MgO-Al₂O₃-SiO₂-Na₂O from 7 to 35 kbar. *J Petrol* 35: 329-359

Table 1 Starting compositions used in 0.001 kbar melting experiments

Composition	SiO ₂	TiO ₂	Al ₂ O ₃	FeO	MgO	MnO	CaO	K ₂ O	Na ₂ O	P ₂ O ₅	Total
67-032 ^a	50.2	1.59	15.8	9.50	7.52	-	11.6	0.15	2.88	0.17	99.4
64-002 ^a	50.2	1.50	16.1	9.21	7.91	-	11.9	0.12	2.68	0.16	99.8
61-002 ^a	50.4	1.84	14.7	10.3	6.96	-	11.7	0.17	2.90	0.18	99.2
70-002 ^a	50.2	1.26	16.0	9.04	8.24	-	12.5	0.10	2.50	0.13	100.0
70-002 ^b	49.6(1)	1.20(2)	15.8(2)	8.98(7)	8.66(6)	0.17(3)	11.9(1)	0.10(1)	2.67(6)	0.12(4)	99.2
70-002 ^c	50.1	1.22	15.9	9.07	8.74	-	12.0	0.10	2.70	0.12	100.0
70-002 ^d	49.8	1.25	15.9	8.96	8.75	-	12.4	0.10	2.67	0.13	100.0
2004-3-1 ^e	49.1(2)	1.19(2)	16.3(2)	8.65(9)	9.13(5)	0.09(5)	11.7(2)	0.10(1)	2.66(14)	0.04(2)	99.0
RE-46	48.8	0.62	15.4	8.91	10.7	0.16	13.5	0.01	1.55	0.03	99.8

^a determined with the Smithsonian electron microprobe

^b average of 368 electron microprobe analyses collected with the MIT JEOL electron microprobe, numbers in parentheses represent 1 sigma deviation in terms of least units cited, thus 49.6(1) should be read as 49.6±0.1

^c 70-002^b normalized to 100%, excluding MnO

^d 70-002^a, after the following correction factors were applied: SiO₂: 0.9944; MgO: 1.0686; Na₂O: 1.076, and then renormalized to 100%; these correction factors were determined by comparing analyses of the same set of 8 natural glass chips collected on each microprobe, and applying corrections for oxides that were 2 sigma or greater outside of electron microprobe counting statistics.

^e as in b but average of 7 microprobe analyses

Table 2 Run conditions for melting experiments

	Run #	T °C	log fO ₂	Time (hrs)	Run products ^a	Phase proportion (wt%)	Σ R ² b
2004-3-1	50	1223	-8.25	18.6	gl,plag,ol	97:2:1	0.77
	40	1213	-8.36	46.0	gl,plag,ol	84:12:4	0.70
	20	1188	-8.72	77.8	gl,plag,ol	70:22:8	1.04
	10	1170	-8.95	164.2	gl,plag,ol,aug	57:28:13:2	1.11
	60	1152	-9.39	170.2	gl,plag,ol,aug	34:40:14:13	0.94
	70	1134	-9.24	166	gl,plag,ol,aug	26:43:14:17	0.69
70-002	110	1160	-8.58	93.5	gl,plag,ol		
	120	1152	-9.02	93.5	gl,plag,ol,aug	48:31:9:12	0.18
	130	1140	-9.20	142.3	gl,plag,ol,aug	41:34:10:15	0.13
	140	1128	-9.38	165	gl,plag,ol,aug	25:42:11:22	0.11
67-032	100	1191	-8.25	114.3	gl,plag,ol		
	110	1171	-8.58	93.5	gl,plag,ol,aug	73:20:4:3	0.27
	130	1140	-9.20	142.3	gl,plag,ol,aug	48:32:7:13	0.05
	140	1128	-9.38	165	gl,plag,ol,aug	40:36:8:16	0.19
	150	1110	-9.76	269.8	gl,plag,ol,aug	29:42:9:19	0.51
64-002	100	1190	-8.71	94.5	gl,plag,ol		
	110	1160	-8.95	99.8	gl,plag,ol,aug	59:28:6:7	0.13
	140	1128	-9.40	166.3	gl,plag,ol,aug	40:36:8:16	0.19
	150	1110	-9.66	218.5	gl,plag,ol,aug	23:47:10:20	0.34
61-002	100	1190	-8.71	94.5	gl,plag,ol		
	110	1160	-8.95	99.8	gl,plag,ol,aug	80:14:4:2	0.05
	130	1140	-9.14	146.5	gl,plag,ol,aug	64:22:3:11	0.07
	140	1128	-9.38	165	gl,plag,ol,aug	48:30:5:15	0.92
	150	1110	-9.66	218.5	gl,plag,ol,aug	35:36:6:22	0.13
RE-46	10	1251	-8.39	136.2	gl		
	15	1251	-7.90	6.5	gl		
	5	1245	-8.42	6.2	gl		
	4	1230	-8.53	23.5	gl,ol	99.:1	1.02
	9	1225	-8.44	121.5	gl,plag,ol	93:4:3	0.93
	14	1207	-8.48	95.8	gl,plag,ol	86:8:6	0.19
	8	1198	-8.80	164.3	gl,plag,ol,aug	71:16:8:4	0.51
	7	1170	-9.31	183	gl,plag,ol,aug	41:31:11:17	0.37

a abbreviations used: gl: glass, ol: olivine, plag: plagioclase, aug: augite

b sum of the residuals squared for an unweighted least squares fit of the run product compositions to the starting composition

Table 3 Compositions of experimental products.

Run	Phase	# of anals	SiO ₂	TiO ₂	Al ₂ O ₃	FeO	MgO	MnO	CaO	K ₂ O	Na ₂ O	P ₂ O ₅	Total
2004-3-1-50	gl	7	49.7(1)	1.18(2)	16.4(1)	8.78(12)	9.00(10)	0.15(2)	11.8(2)	0.10(1)	2.53(10)	0.04(1)	99.7
	ol	3	50.5(3)	0.0	0.09(2)	12.3(2)	46.9(5)	0.10(1)	0.50(1)	-	-	-	100.3
	plag	3	49.6(6)	-	31.8(6)	0.55(5)	0.30(6)	-	15.5(2)	0.02(1)	2.68(11)	-	100.4
2004-3-1-40	gl	7	50.2(2)	1.38(6)	15.4(2)	9.46(10)	8.35(7)	0.14(4)	12.0(1)	0.11(2)	2.63(11)	0.04(1)	99.7
	ol	3	39.9(4)	0.0	0.12(4)	14.1(2)	45.8(2)	0.17(1)	0.47(2)	-	-	-	100.6
	plag	4	49.3(1)	-	31.7(1)	0.65(4)	0.30(7)	-	15.7(1)	0.02(1)	2.59(6)	-	100.3
2004-3-1-20	gl	6	50.2(3)	1.58(4)	14.2(9)	9.84(13)	7.71(12)	0.19(7)	12.3(1)	0.14(1)	2.64(21)	0.04(1)	98.8
	ol	3	39.7(4)	0.03(1)	0.12(3)	15.3(1)	43.9(2)	0.28(1)	0.50(1)	-	-	-	99.7
	plag	4	50.3(9)	-	29.8(11)	0.95(22)	0.54(24)	-	14.9(4)	0.03(1)	2.91(21)	-	99.4
2004-3-1-10	gl	6	50.8(3)	2.17(10)	13.5(2)	11.0(1)	7.08(7)	0.27(2)	11.5(1)	0.17(2)	2.52(2)	0.11(5)	99.2
	ol	4	39.6(5)	0.05(1)	0.08(2)	18.1(6)	42.1(5)	0.31(3)	0.46(3)	-	-	-	100.7
	plag	4	50.7(4)	-	29.9(4)	0.71(11)	0.40(10)	-	14.4(2)	0.04(1)	3.23(8)	-	99.4
	aug	8	51.5(1.1)	0.72(21)	2.92(78)	6.36(88)	16.7(6)	0.16(4)	20.8(2)	-	0.21(6)	-	99.3
2004-3-1-60	gl	10	50.4(4)	3.33(20)	12.5(2)	12.9(3)	6.22(13)	0.22(3)	10.4(2)	0.25(1)	2.51(9)	0.48(6)	99.4
	ol	4	38.8(1)	0.07(4)	0.06(4)	22.8(2)	38.7(2)	0.36(3)	0.41(3)	-	-	-	101.2
	plag	3	52.3(5)	-	29.5(4)	0.75(4)	0.36(18)	-	13.5(3)	0.03(2)	3.83(17)	-	100.3
	aug	13	51.8(4)	0.94(14)	2.46(57)	7.94(36)	16.4(5)	0.12(4)	19.8(3)	-	0.26(6)	-	99.7
2004-3-1-70	gl	10	50.0(7)	4.14(44)	12.1(5)	13.4(7)	5.75(3)	0.23(3)	10.0(2)	0.28(3)	2.55(12)	0.54(5)	99.0
	ol	5	38.5(4)	0.10(1)	0.06(5)	24.9(12)	36.9(9)	0.38(1)	0.45(2)	-	-	-	101.3
	plag	3	52.3(5)	-	29.1(1)	0.78(8)	0.30(5)	-	13.4(3)	0.02(2)	3.88(22)	-	99.8
	aug	7	51.3(7)	1.28(29)	2.86(72)	8.89(81)	16.3(6)	0.18(6)	18.8(11)	-	0.32(13)	-	99.9
70-002-120	gl	9	50.1(4)	2.52(13)	13.4(1)	11.9(1)	6.30(6)	0.16(3)	10.8(1)	0.38(2)	3.31(9)	0.19(3)	99.1
	ol	6	38.9(3)	0.04(3)	0.38(26)	20.8(1)	39.9(3)	0.35(2)	0.53(6)	-	-	-	100.9
	plag	6	52.5(8)	-	29.2(6)	0.86(11)	0.32(5)	-	13.2(6)	0.11(3)	3.90(33)	-	100.1
	aug	10	51.7(1.1)	1.10(49)	2.84(82)	7.29(1.4)	15.7(1.2)	0.13(4)	20.6(4)	-	0.28(7)	-	99.6

Table 3 (cont.)

Run	Phase	# of anal	SiO ₂	TiO ₂	Al ₂ O ₃	FeO	MgO	MnO	CaO	K ₂ O	Na ₂ O	P ₂ O ₅	Total
70-002-130	gl	9	50.3(8)	2.80(3)	13.2(3)	12.2(6)	5.90(15)	0.28(11)	10.3(3)	0.45(4)	3.25(21)	0.25(7)	98.9
	ol	5	38.5(2)	0.00	0.19(4)	23.4(3)	38.0(2)	0.37(1)	0.29(17)	-	-	-	100.8
	plag	5	51.9(9)	-	29.4(2)	0.70(10)	0.27(4)	-	13.4(3)	0.10(1)	3.75(7)	-	99.5
	aug	8	52.1(2)	0.96(13)	2.48(3)	8.06(29)	16.3(4)	0.21(7)	19.5(4)	-	0.21(4)	-	99.8
70-002-140	gl	8	49.2(3)	4.17(26)	12.0(2)	14.3(3)	5.51(13)	0.30(5)	9.90(16)	0.32(6)	2.68(21)	0.37(5)	98.7
	ol	5	37.4(2)	0.03(3)	0.21(5)	26.4(3)	35.5(2)	0.41(2)	0.42(2)	-	-	-	100.4
	plag	3	53.2(3)	-	28.9(1)	0.73(9)	0.22(3)	-	12.8(2)	0.13(1)	4.07(22)	-	100.1
	aug	4	51.0(1.5)	1.27(27)	3.14(11)	9.70(1.4)	15.2(1.2)	0.24(5)	18.0(6)	-	0.31(8)	-	98.9
67-032-110	gl	8	50.4(6)	2.10(21)	13.5(2)	11.79(3)	7.05(18)	0.22(4)	11.5(3)	0.17(3)	2.66(21)	0.26(6)	99.6
	ol	5	38.8(3)	0.00	0.21(10)	19.6(4)	41.2(4)	0.29(4)	0.39(6)	-	-	-	100.5
	plag	4	50.9(3)	-	30.2(6)	0.75(22)	0.34(16)	-	14.6(3)	0.08(1)	3.11(15)	-	100.0
	aug	7	52.5(1)	0.74(25)	2.47(61)	6.59(70)	16.9(4)	0.17(5)	19.9(3)	-	0.21(5)	-	99.5
67-032-130	gl	7	50.4(5)	2.62(11)	13.0(2)	13.0(2)	5.85(17)	0.27(4)	10.4(2)	0.29(5)	3.16(18)	0.23(5)	99.2
	ol	5	38.1(2)	0.00	0.22(7)	22.8(3)	38.0(5)	0.39(4)	0.50(7)	-	-	-	100.0
	plag	4	53.7(7)	-	28.3(4)	0.88(10)	0.31(6)	-	12.4(4)	0.15(1)	4.26(23)	-	100.0
	aug	9	49.5(2.2)	1.74(77)	3.91(1.47)	9.43(1.37)	13.9 (1.9)	0.23(8)	20.2(4)	-	0.37(10)	-	99.3
67-032-140	gl	7	49.8(6)	3.56(14)	12.6(1)	13.4(2)	5.31(9)	0.31(7)	9.70(16)	0.57(8)	3.38(13)	0.34(7)	99.0
	ol	5	37.8(2)	0.08(5)	0.22(5)	25.8(4)	35.6(2)	0.43(1)	0.52(14)	-	-	-	100.5
	plag	3	53.8(1)	-	28.4(2)	0.63(2)	0.18(1)	-	12.0(2)	0.18(0)	4.54(1)	-	99.7
	aug	10	50.6(1.7)	1.42(46)	3.16(1.20)	9.47(1.42)	14.8(1.4)	0.22(5)	19.9(9)	-	0.31(6)	-	99.9
67-032-150	gl	9	49.8(4)	4.92(9)	11.7(2)	14.2(3)	4.70(3)	0.21(3)	8.88(17)	0.68(5)	3.32(13)	0.45(9)	98.9
	ol	5	37.1(2)	0.08(6)	0.21(7)	29.0(2)	33.3(3)	0.45(5)	0.45(14)	-	-	-	100.6
	plag	3	53.7(3)	-	27.9(5)	0.97(4)	0.66(60)	-	11.8(3)	0.17(1)	4.42(8)	-	99.6
	aug	8	51.2(6)	1.50(15)	2.28(38)	10.2(5)	15.6(5)	0.24(2)	18.1(6)	-	0.23(3)	-	99.4

Table 3 (cont.)

Run	Phase	# of anals	SiO ₂	TiO ₂	Al ₂ O ₃	FeO	MgO	MnO	CaO	K ₂ O	Na ₂ O	P ₂ O ₅	Total
64-002-110	gl	8	50.2(2)	2.30(29)	13.4(2)	11.9(5)	6.76(27)	0.22(6)	11.2(3)	0.22(2)	3.03(18)	0.26(4)	99.5
	ol	5	38.9(2)	0.00	0.21(8)	19.1(4)	41.4(2)	0.31(3)	0.45(3)	-	-	-	100.4
	plag	4	52.8(7)	-	28.3(5)	1.14(14)	0.53(7)	-	13.3(5)	0.10(1)	3.74(27)	-	99.9
	aug	17	51.8(8)	0.76(21)	2.83(66)	6.70(91)	16.6(7)	0.15(6)	20.1(5)	-	0.27(11)	-	99.2
64-002-140	gl	11	49.3(2)	3.92(7)	11.8(1)	14.0(1)	5.43(4)	0.28(1)	9.59(12)	0.35(1)	2.93(7)	0.36(1)	97.9
	ol	5	37.3(1)	0.06(4)	0.18(8)	26.6(3)	35.3(2)	0.41(5)	0.41(4)	-	-	-	100.3
	plag	4	53.3(2)	-	28.5(4)	0.80(20)	0.25(9)	-	12.6(2)	0.14(1)	4.14(7)	-	99.7
	aug	4	51.5(1.1)	1.17(25)	2.57(63)	9.16(69)	15.9(6)	0.18(5)	18.9(2)	-	0.25(5)	-	99.6
64-002-150	gl	7	48.4(5)	5.28(18)	11.2(2)	15.4(4)	4.99(3)	0.23(4)	9.40(4)	0.43(3)	2.76(13)	0.49(7)	98.6
	ol	5	36.8(3)	0.05(7)	0.20(4)	29.2(2)	33.2(2)	0.46(3)	0.44(1)	-	-	-	100.5
	plag	4	54.1(6)	-	27.8(1.0)	0.85(22)	0.47(41)	-	12.0(3)	0.17(2)	4.50(7)	-	99.9
	aug	9	51.4(3)	1.36(10)	2.05(23)	9.92(24)	15.6(2)	0.19(6)	18.4(4)	-	0.26(4)	-	99.2
61-002-110	gl	8	50.4(6)	2.27(18)	13.3(4)	11.9(6)	6.71(35)	0.23(7)	11.2(2)	0.19(3)	2.73(21)	0.26(8)	99.2
	ol	5	38.7(3)	0.00	0.17(4)	19.2(3)	41.2(5)	0.26(8)	0.44(3)	-	-	-	100.0
	plag	3	52.1(3)	-	28.4(5)	1.12(18)	0.56(10)	-	13.7(3)	0.10(1)	3.53(17)	-	99.5
	aug	8	52.3(5)	0.72(5)	2.50(29)	6.40(43)	17.0(1)	0.15(5)	20.2(3)	-	0.24(4)	-	99.5
61-002-130	gl	7	50.0(7)	2.98(48)	12.8(4)	13.1(5)	6.06(16)	0.28(6)	10.5(34)	0.31(3)	2.91(15)	0.26(4)	99.2
	ol	5	38.3(3)	0.00	0.20(6)	23.8(3)	37.9(3)	0.35(3)	0.45(4)	-	-	-	101.0
	plag	4	53.3(6)	-	28.7(7)	0.87(31)	0.29(14)	-	12.9(2)	0.12(0)	4.09(14)	-	100.3
	aug	8	52.6(8)	0.81(9)	2.29(44)	7.86(34)	16.8(3)	0.24(2)	19.2(4)	-	0.22(3)	-	100.0
61-002-140	gl	7	49.8(4)	3.33(31)	12.2(3)	14.3(4)	5.29(23)	0.25(6)	9.73(40)	0.37(4)	3.08(21)	0.32(6)	98.7
	ol	5	37.4(2)	0.10(5)	0.28(8)	27.5(4)	34.3(4)	0.44(2)	0.49(7)	-	-	-	100.5
	plag	4	54.8(4)	-	28.2(8)	0.94(31)	0.24(13)	-	12.2(2)	0.13(1)	4.38(14)	-	100.9
	aug	5	52.1(4)	0.94(7)	2.17(37)	8.91(27)	15.9(2)	0.18(2)	18.4(3)	-	0.27(2)	-	98.9

Table 3 (cont.)

Run	Phase	# of anals	SiO ₂	TiO ₂	Al ₂ O ₃	FeO	MgO	MnO	CaO	K ₂ O	Na ₂ O	P ₂ O ₅	Total
61-002-150	gl	8	49.2(2)	4.33(12)	11.4(1)	15.8(2)	4.74(3)	0.26(4)	9.16(10)	0.43(1)	3.02(11)	0.44(4)	98.8
	ol	5	36.7(4)	0.16(6)	0.24(6)	31.3(3)	31.5(4)	0.47(5)	0.45(1)	-	-	-	100.8
	plag	3	55.0(2)	-	27.9(2)	0.78(5)	0.16(2)	-	11.3(1)	0.17(1)	4.85(8)	-	100.2
	aug	20	50.8(1.0)	1.43(3)	2.69(94)	10.5(1.0)	14.7(9)	0.24(5)	18.7(7)	-	0.30(7)	-	99.4
RE 46-15	gl	6	49.1(2)	0.50(2)	15.1(1)	8.15(13)	10.6(1)	0.10(5)	13.7(2)	0.01(0)	1.48(9)	0.08(0)	98.9
Re 46-5	gl	5	49.3(2)	0.50(2)	15.1(2)	8.21(22)	10.6(1)	0.10(5)	13.8(1)	0.01(1)	1.47(9)	0.08(3)	99.2
Re 46-4	gl	7	49.3(2)	0.53(3)	15.1(1)	8.20(9)	10.4(1)	0.08(4)	13.9(2)	0.01(1)	1.46(11)	0.07(3)	99.1
	ol	4	40.4(4)	0.02(0)	0.06(0)	11.6(2)	47.6(5)	0.21(2)	0.40(2)	-	-	-	100.6
RE 46-9	gl	18	50.0(3)	0.55(3)	15.2(2)	8.52(14)	10.1(2)	0.18(4)	14.1(1)	0.01(1)	1.14(7)	0.12(2)	100.0
	ol	4	40.7(3)	0.03(6)	0.09(6)	11.4(2)	48.5(1)	0.15(2)	0.41(4)	-	-	-	101.5
	plag	3	46.8(3)	-	31.4(1.0)	1.31(40)	1.55(47)	-	17.8(3)	0.00	1.07(2)	-	99.9
RE 46-14	gl	6	50.1(2)	0.58(1)	14.8(1)	9.17(9)	9.43(6)	0.10(4)	14.1(1)	0.02(1)	1.42(5)	0.10(2)	99.9
	ol	4	40.0(4)	0.02(1)	0.05(0)	13.0(1)	46.1(4)	0.24(2)	0.46(2)	-	-	-	100.1
	plag	8	47.2(3)	-	33.4(5)	0.69(11)	0.45(13)	-	17.6(2)	0.00	1.37(7)	-	100.7
RE 46-17	gl	9	50.5(3)	0.68(2)	14.1(1)	9.57(13)	9.04(17)	0.14(4)	14.1(1)	0.03(1)	1.58(8)	0.12(3)	99.9
	ol	3	40.5(2)	-	0.04(0)	13.6(2)	45.2(3)	0.20(1)	0.51(3)	-	-	-	100.4
	plag	4	46.9(4)	-	32.8(3)	0.68(07)	0.51(16)	-	17.6(1)	-	1.32(7)	-	99.7
RE 46-8	gl	6	51.2(1)	0.80(5)	14.0(1)	10.1(1)	8.81(8)	0.19(6)	13.4(1)	0.03(1)	1.46(12)	0.11(3)	100.1
	ol	8	40.1(3)	0.01(1)	0.07(3)	14.8(3)	45.2(2)	0.19(4)	0.46(5)	-	-	-	100.9
	plag	5	47.2(4)	-	33.4(3)	-	0.36(3)	-	17.4(2)	0.03(2)	1.43(13)	-	100.4
	cpx	10	53.2(5)	0.21(2)	2.56(38)	4.87(21)	18.4(3)	0.13(2)	21.1(6)	-	0.15(2)	-	101.4

Table 3 (cont.)

Run	Phase	# of anals	SiO ₂	TiO ₂	Al ₂ O ₃	FeO	MgO	MnO	CaO	K ₂ O	Na ₂ O	P ₂ O ₅	Total
RE 46-16	gl	8	51.3(5)	0.85(4)	14.00(3)	11.0(2)	8.00(12)	0.21(4)	12.7(1)	0.04(1)	1.80(10)	0.12(2)	100.0
	ol	4	39.1(3)	0.03(1)	0.22(2)	17.5(2)	41.9(2)	0.31(2)	0.46(3)	-	-	-	99.9
	plag	4	48.4(7)	-	31.4(4)	1.08(07)	0.69(10)	-	16.6(4)	-	1.80(21)	-	99.9
	cpx	12	51.8(3)	0.27(4)	2.85(56)	6.41(69)	17.1(3)	0.15(2)	20.5(4)	-	0.16(4)	-	99.8
RE 46-7	gl	11	52.0(2)	1.15(3)	13.3(1)	12.2(2)	7.31(22)	0.22(7)	12.0(2)	0.02(1)	1.61(9)	0.14(9)	100.0
	ol	5	38.7(3)	0.02(1)	0.17(5)	20.0(2)	40.9(3)	0.30(3)	0.44(4)	-	-	-	100.7
	plag	10	48.9(1.2)	-	31.2(8)	0.95(9)	0.50(13)	-	15.9(6)	0.02(1)	2.18(34)	-	99.6
	cpx	8	51.7(8)	0.27(2)	2.38(56)	6.84(34)	17.6(4)	0.17(2)	19.7(5)	-	0.16(3)	-	99.1

Paranthesized units represent 1 sigma of replicate analyses in terms of least units cited. Thus, 49.7(1) should be read as 49.7±0.1.

Table 4 Source of the data set for multiple regression

source	system	P (kbar)	T (°C)	# of experiment
Grove et. al., 1992	natural	0.001	1161	1
		2	1126-1163	5
		8	1210-1265	10
		10	1235-1250	2
Tormey et. al., 1987	natural	0.001	1152-1171	7
Grove & Bryan, 1983	natural	0.001	1137-1193	22
Grove et. al., 1990	natural	0.001	1108-1152	4
		8	1189	1
Juster et. al., 1989	natural	0.001	1150-1180	4
Grove & Vanime, 1978	natural	0.001	1099-1155	4
Baker & Egglar, 1987	natural	0.001	1100-1175	6
		8	1200-1250	4
		2	1020-1060	3
Walker et.al., 1979	natural	0.001	1085-1235	11
Bender et. al., 1978	natural	8	1250	1
Sack et. al., 1987	natural	0.001	1064-1176	20
This study	natural	0.001	1110-1171	16
Presnall et. al., 1978	CMAS	0.001	1266-1272	2
Libourel et. al., 1989	CMAS	0.001	1244-1275	24
Shi & Libourel, 1991	CMAS+FeO	0.001	1160-1220	27
Shi, 1993	CMAS+FeO+Na ₂ O	0.001	1100	16

Only experiments at 0.001 kbar were used to investigate the effects of minor components on the compositions of ol-plag-aug saturated melts using the equations derived from the CMAS + FeO (Shi, 1992) and CMAS+FeO+Na₂O system (Shi, 1993). Experiments in the natural system were used to parameterizing equations for describing augite compositions coexisting with olivine, plagioclase and a basaltic melt.

Table 5 Coefficients of independent variables for describing XAl, XCa, XMg and T in ol-plag-aug saturated melt

eq.#		constant	P	XNa	XK	XTi	XFe	XSi	(XSi) ²	XSi*XTi	R ²
1	XAl	0.236 (0.005)	0.00218 (0.00016)	0.109 (0.014)	0.593 (0.034)	-0.350 (0.043)	-0.299 (0.008)	-0.130 (0.011)	0.0	0.0	0.937
2	XCa	1.133 (0.047)	-0.00339 (0.00021)	-0.569 (0.018)	-0.776 (0.046)	-0.672 (0.061)	-0.214 (0.010)	-3.355 (0.197)	2.830 (0.206)	0.0	0.982
3	XMg	-0.277 (0.031)	0.00114 (0.00014)	-0.543 (0.012)	-0.947 (0.030)	-0.117 (0.040)	-0.490 (0.007)	2.086 (0.131)	-2.400 (0.137)	0.0	0.989
4	T	581.7 (99.5)	5.858 (0.436)	-691.0 (39.2)	-848.9 (96.1)	11492 (1582)	3114 (416)	-574.3 (21.7)	-3529 (433)	-25679 (3352)	0.937

Table 6 Coefficients of independent variables for describing XMg in ol-plag-aug saturated melt

	constant	P	XNa	XK	XTi	XCa	XFe	(XCa) ²	(XNa) ²		R ²
XMg	0.061 (0.006)	0.00226 (0.00018)	-0.538 (0.054)	-0.702 (0.042)	0.355 (0.061)	1.204 (0.064)	-0.472 (0.009)	-3.139 (0.182)	1.639 (0.368)		0.981
	constant	P	XNa	XK	XTi	XCa	XAl	(XCa) ²	(XAl) ²	(XNa) ²	R ²
XMg	-0.389 (0.037)	-0.00095 (0.00034)	-0.716 (0.086)	-1.369 (0.095)	0.512 (0.096)	0.562 (0.103)	4.781 (0.462)	-1.405 (0.284)	-11.058 (1.514)	1.106 (0.585)	0.955
	constant	P	XNa	XK	XTi	XAl	XFe				R ²
XMg	0.036 (0.017)	-0.00015 (0.00036)	-0.686 (0.022)	-1.512 (0.082)	0.438 (0.080)	0.761 (0.094)	-0.261 (0.031)				0.955

Table 7 Coefficients of independent variables for describing augite compositions saturated with olivine, plagioclase and a basaltic melt.

eq.#		constant	P	T	XSi	XTi	XAl	XFe	XMg	XCa	XNa	XK	R ²
5	XCa ^{aug}	25.043 (1.473)	0 -	0 -	0 -	0 -	-0.617 (0.077)	-0.832 (0.047)	-0.953 (0.075)	1.624 (0.086)	0.446 (0.057)	0.446 (0.057)	0.873
6	XMgFe ^{aug}	-11.051 (4.304)	0 -	0 -	0.504 (0.044)	0 -	0.385 (0.103)	1.089 (0.067)	1.171 (0.071)	-1.058 (0.100)	0 -	0 -	0.878
7	XTi ^{aug}	-3.612 (0.557)	-0.0217 (0.0059)	0.00105 (0.00043)	0 -	0.320 (0.023)	0.108 (0.021)	0.0339 (0.0064)	0 -	0.0225 (0.0149)	0.0426 (0.0114)	0.0426 (0.0114)	0.904
8	XNa ^{aug}	-2.296 (0.384)	0 -	0.00221 (0.00040)	0 -	0 -	0 -	0 -	-0.0202 (0.0092)	0 -	0.082 (0.007)	0 -	0.826
9	XSi ^{aug}	116.08 (17.78)	0.204 (0.046)	-0.0111 (0.005)	-0.310 (0.144)	-1.374 (0.253)	-1.582 (0.210)	-0.533 (0.120)	0 -	-0.706 (0.190)	-0.418 (0.136)	0 -	0.803
10	XAl ^{aug}	98.236 (0.690)	0 -	0 -	-0.964 (0.015)	-0.799 (0.045)	0 -	-1.022 (0.016)	-0.998 (0.017)	-1.015 (0.014)	-0.932 (0.059)	0 -	0.998

Independent variables in eq. 5~9 are melt compositions whereas those in eq. 10 are augite compositions calculated from eq. 5~9. The values in parentheses are the standard errors of the coefficients.

FIGURE CAPTIONS

- Fig. 1 The crystallization sequence of experiments at 0.001 kbar
- Fig. 2. Observed ol-plag-aug saturated melt compositions versus those predicted from Shi's equations (1992). The solid lines indicate observed=predicted compositions.
- Fig. 3 Differences between predicted and observed ol-plag-aug saturated melt compositions versus Na₂O (wt %) in melt (Δ = predicted - observed). Predicted compositions are calculated from Shi's equations (1992). Symbols are the same as Fig. 2. In each panel the upper number is the R² for open circles, the experiments in the CMAS+FeO+Na₂O system (Shi, 1993), and the lower number is that for the other symbols including experiments in the natural system.
- Fig. 4 Δ Mg (predicted XMg - observed XMg) versus TiO₂ (wt %) for ol-plag-aug saturated melts in the natural system. Predicted XMg are calculated from the equation of Shi (1992). Symbols are the same as Fig. 2. The R² for tholeiitic compositions is 0.377, not including two experiments with Δ Mg greater than 0.03.
- Fig. 5 Observed ol-plag-aug saturated melt compositions versus those predicted from the equations of Shi (1993). Symbols are the same as Fig. 2.
- Fig. 6 Differences between predicted and observed ol-plag-aug saturated melt compositions (Δ = predicted - observed) versus temperature. Predicted compositions are calculated from the equations of Shi (1993). Symbols are the same as Fig. 2. Arrows indicated the discrepancies between predicted and observed compositions at 1100 °C. An arrow heads pointing up represents predicted composition greater than observed composition and vice versa.
- Fig. 7 Observed compositions and temperature versus those predicted from equations 1-4. Data source is listed in Table 4. Symbols for 0.001 kbar experiments are the same as Fig. 2. High pressure experiments of Grove et al., (1992) (diamond) and Baker and

Eggler (1987) (square with slash) are included. The solid square is the 8 kbar experiment of Bender et al. (1978). The dash lines in temperature plot indicate region wherein the data are fit to $\pm 20^{\circ}\text{C}$.

Fig. 8 Prediction of pressures on which melts coexisting with ol-plag-aug. Solid symbols are observed compositions. Open symbols are compositions predicted from equations 1-3 at various pressures. For all three samples the first predicted composition is at 0.001 kbar, then, 1 kbar, 2 kbar, 3 kbar and so on. The best fits between observed and predicted compositions are at 0.001, 4, and 9 kbar for SA-46-66, VG-360 and RE-46, respectively. The 2 sigma error ellipse (EMP error) is calculated as standard deviation of the mean of replicate electron microprobe analyses of ALV-1690-20 starting composition (Grove et al., 1992).

Fig. 9 Simplified geometric relation between the OPALM, OPAM and OPM boundaries by Grove et al. (1992). OPALM is predicted with the equations of Kinzler and Grove (1992). In Ol-Cpx-Qtz pseudoternary (A), OPAM is a line extended from OPALM towards Ol-Cpx sideline with a slope parallel to the experimentally determined OPAM of ALV-1690-20 at 0.001 kbar. In Ol-Cpx-Plag pseudoternary (B), OPAM plots as a point and overlaps with OPALM. OPM is a line extended from OPAM (also OPALM) perpendicular to Ol-Plag sideline.

Fig. 10 Prediction of the first ol-plag-aug saturated melt evolving from sample ALV-2004-3-1 at 0.001, 2 and 5 kbar. Modeled residual fractionation path and predicted path are described in text. The intersections of modeled residual fractionation path and predicted path indicate melt compositions first saturated with ol-plag-aug at various pressures. EMP error ellipse is described in Fig. 8.

Fig. 11 Predicting OPAM boundary from an experimentally produced ol-plag-aug saturated melt, ALV-2004-3-1-10 at 0.001 kbar. Each increment is 1 wt % fractionation. Methods for modeling are described in text. Open squares form the "residual" ol-plag-

aug fractionation path. Crosses form the "predicted" OPAM path and open circles form the predicted OPALM path (see text for discussion). Open diamonds are the augite compositions predicted from the coexisting residual ol-plag-aug saturated melts. Solid triangles and squares are experimentally produced ol-plag-aug saturated melts and coexisting augites. The proportions of ol-plag-aug in fractionating assemblage are 0.08-0.45-0.47 which minimize the difference between the "residual" and "predicted" paths. Arrows indicate the directions of fractionation. Ol-plag-aug fractionation terminates when the difference between "residual melt" and predicted OPALM is minimum. The EMP error ellipse is described in Fig. 8. The dash line is the OPAM boundary predicted by the method of Grove et al., (1992).

- Fig. 12 Comparison of predicted phase appearances with observed phase appearance for ALV-2004-3-1. Data for ALV-2004-3-1 are derived from Tables 2 and 3 and inferred from an 8 kbar experiment in Grove et al. (1992). For models and experiments the saturating phases are shown using the same symbols used in Fig. 1 with the exception of lower right boxes in MELTS (opx) and COMAG (spinel). Numbers next to each phase are the composition (on top; Fo of ol, An content of plag or MgO wt. % of pyroxene) and the weight fraction in crystallizing assemblage (below). MgO on vertical axis represents the MgO content of the experimental or predicted liquid.
- Fig. 13 Fractional crystallization sequences starting from ALV-2004-3-1 calculated by the models of YKG (this paper), LR (Langmuir et al., 1992, modified by Reynolds, 1995) and MELTS (Ghiorso and Sack, 1995). In YKG each increment is 1 wt % while in LR and MELTS each increment is 2 °C.
- Fig. 14 Comparison of glasses from east flank of EPR (crosses), experimentally produced ol-plag-aug saturated melts at 0.001 kbar (open triangles) and the first ol-plag-aug saturated melts predicted from five glasses, 2004-3-1, 2003-6-1, 2002-2-1, 2003-4-1 and 2004-2-1 at 2 kbar (solid squares). The first ol-plag-aug saturated melt at 0.001

kbar (open square) is predicted from 2004-3-1. Two straight lines are drawn by eye fit to the 0.001 kbar experimental results (Table 2 and 3) and the predicted first ol-plag-aug saturated melts at 2 kbar. EMP error ellipse is described in Fig. 8.

Fig. 15 Comparison of glasses from east flank of EPR (crosses) and the fractionation path at 2 kbar (solid line) modeled from a glass, 2002-2-1. The proportions of ol, plag and aug in ol-plag-aug saturated melts are 0.12, 0.32 and 0.56, respectively. Open circles and solid squares are the modeled and predicted compositions for the first and last ol-plag-aug saturated melts in the calculated FCS. Dr-19 is the glass plotted at the most evolved end. EMP error ellipse is described in Fig. 8.

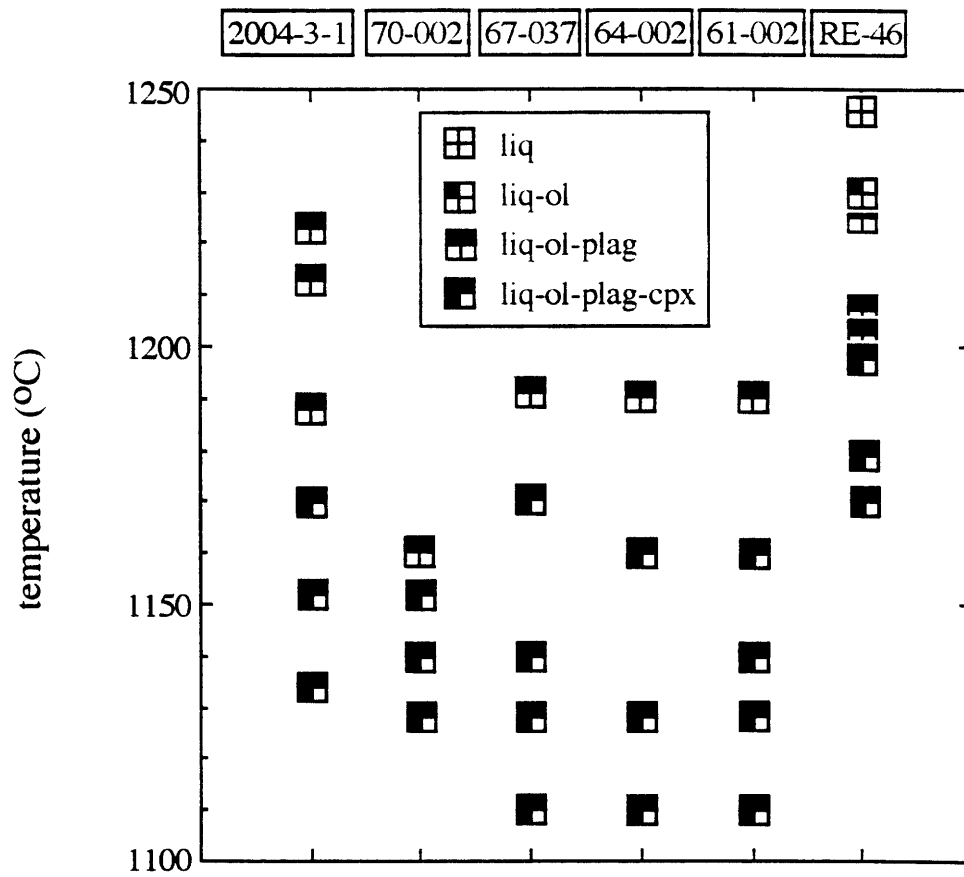
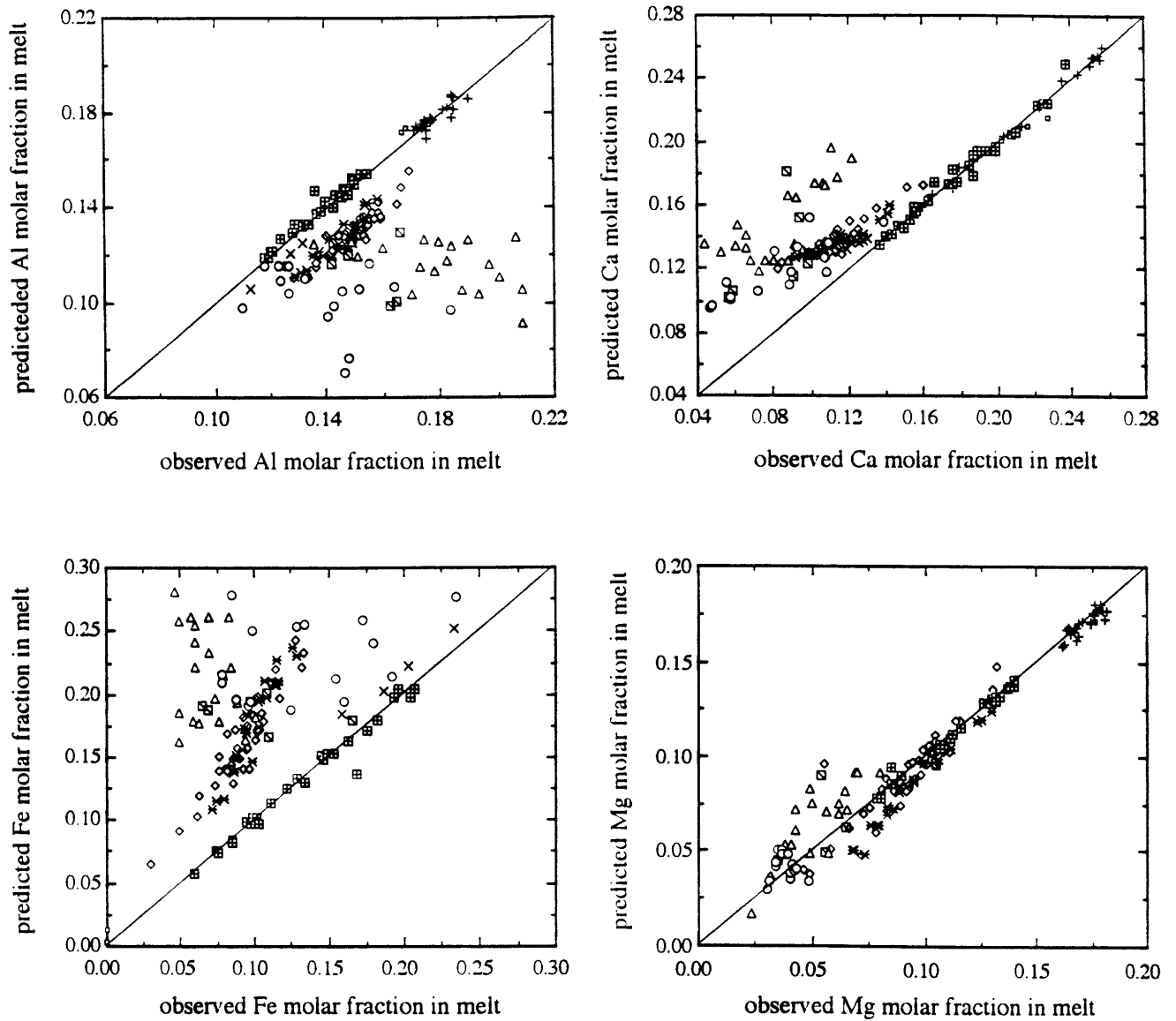


Fig. 1



Legend

simple system

- Shi, 1993
- Shi and Libourel, 1991
- + Libourel et al., 1989
- Presnall et al., 1979

natural system

- × this study
- ▣ Baker and Egglar, 1987
- △ Sack et al., 1987
- × Grove and Vaniman, 1978
- ◊ Grove et al, 1990
- ▣ Juster and Grove, 1989
- ◊ Tormey et al., 1987
- ◊ Grove and Bryan, 1983
- ◊ Walker et al., 1979

Fig. 2

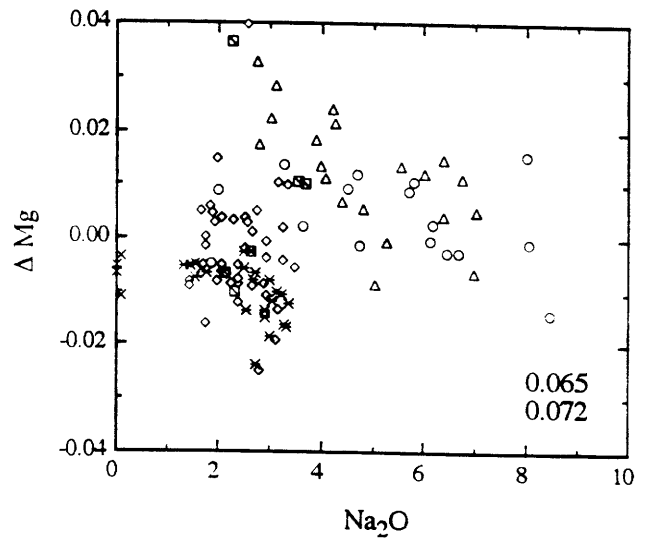
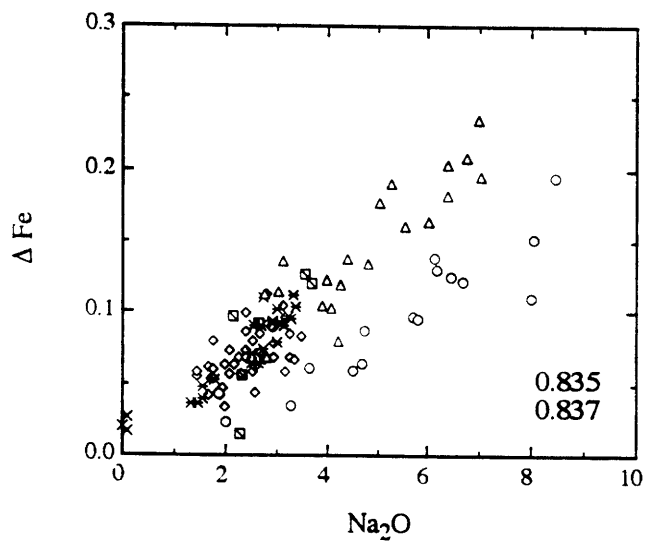
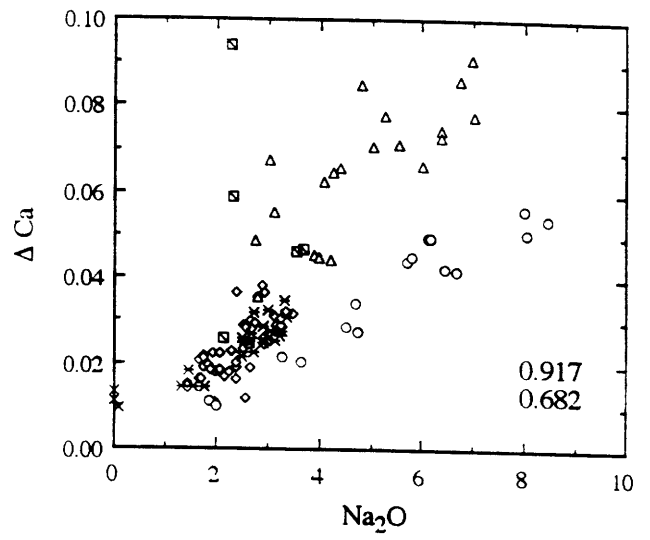
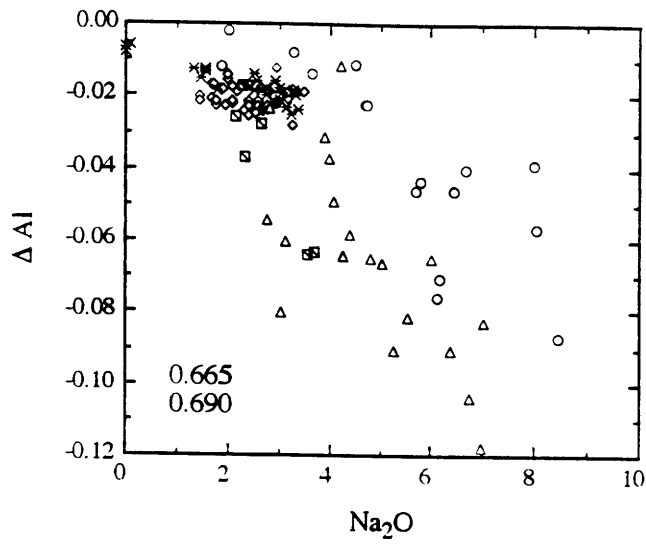


Fig. 3

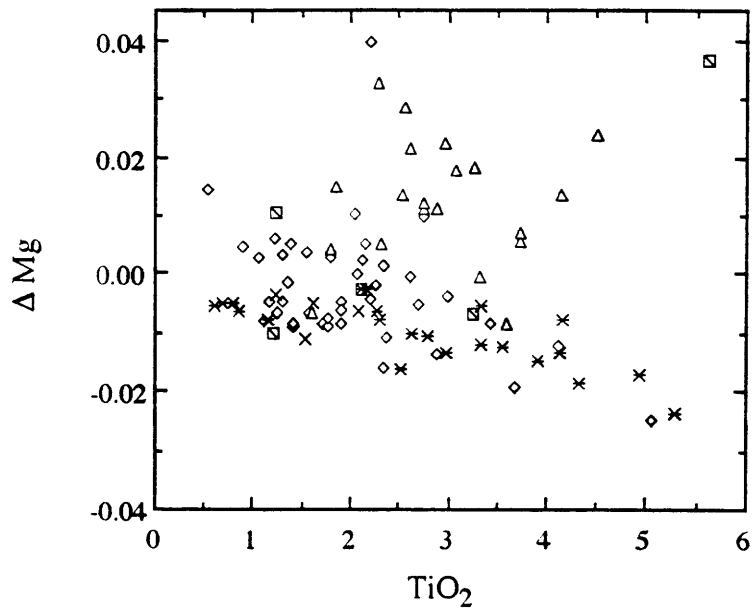


Fig. 4

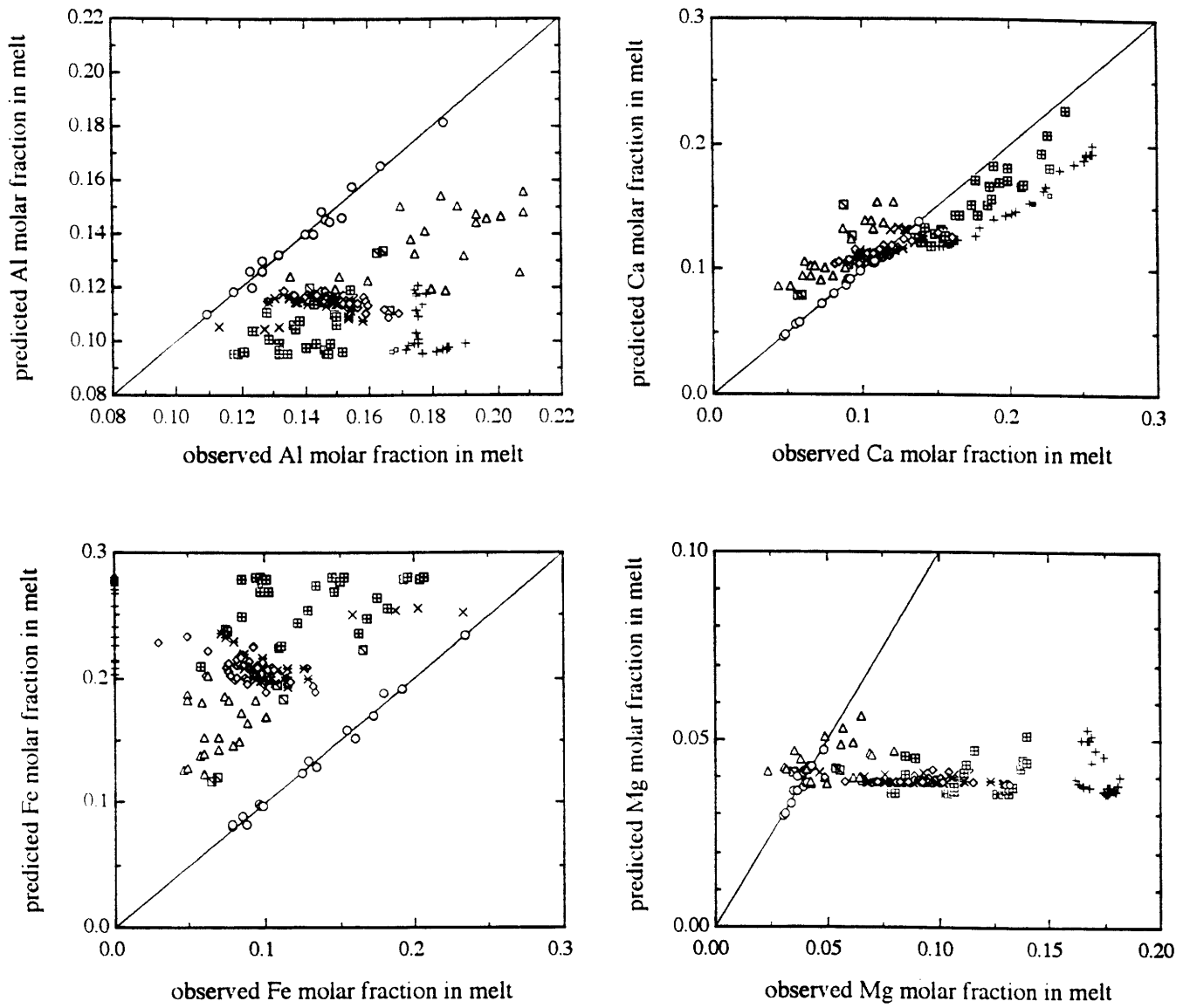


Fig. 5

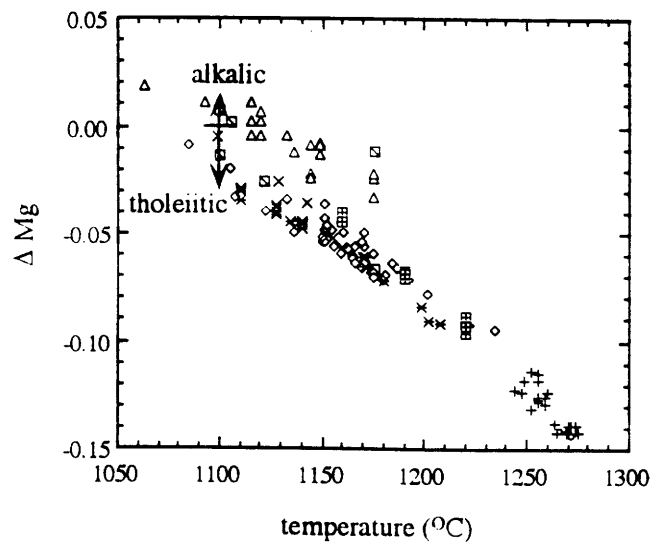
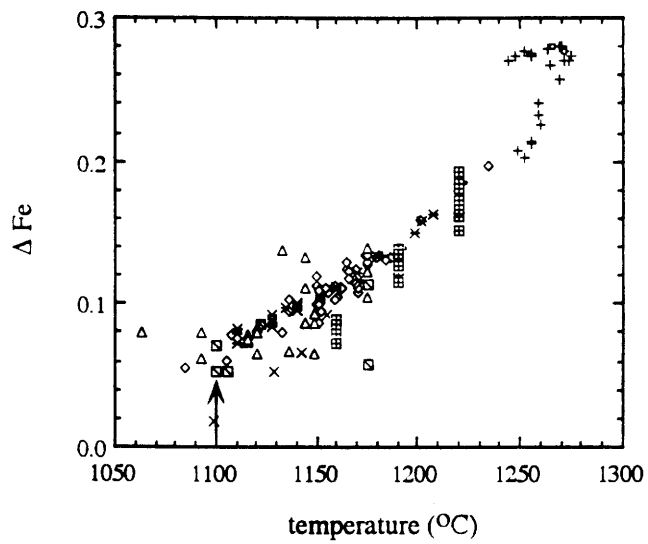
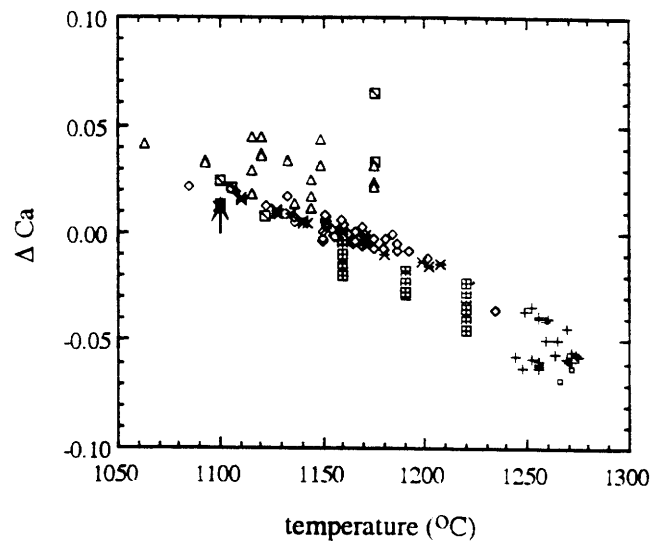
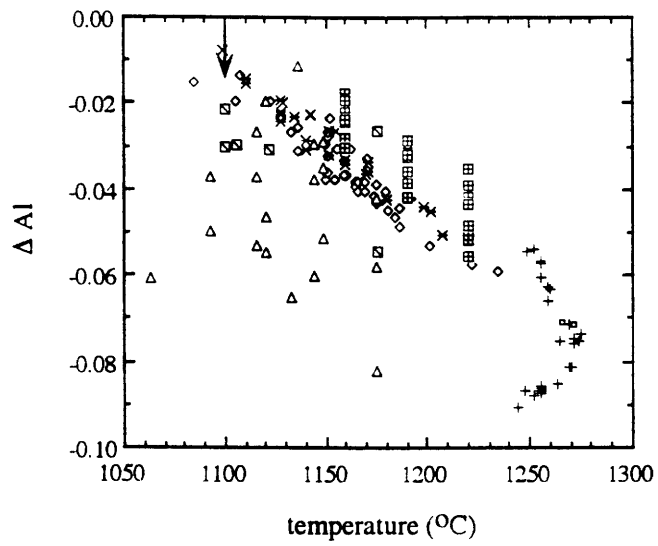


Fig. 6

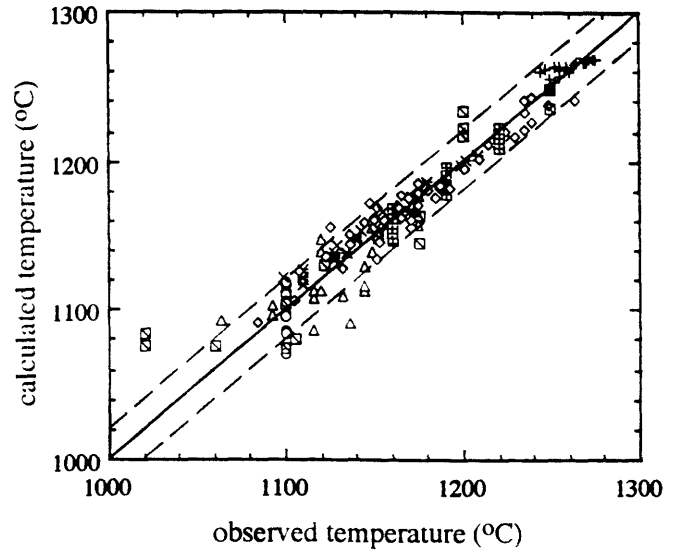
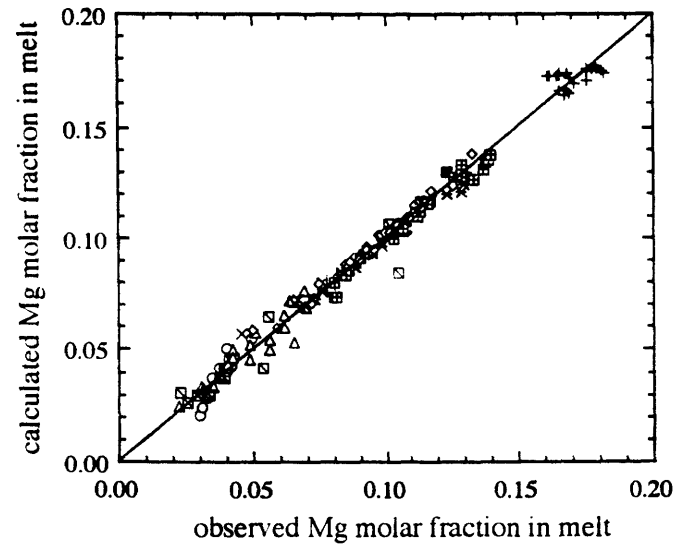
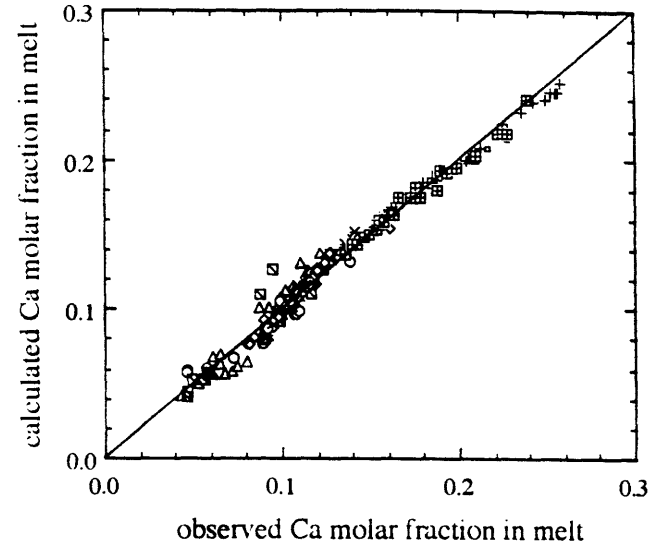
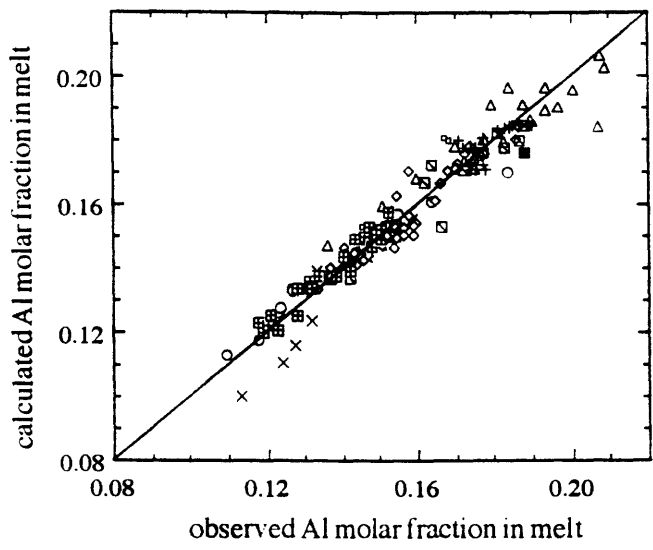


Fig. 7

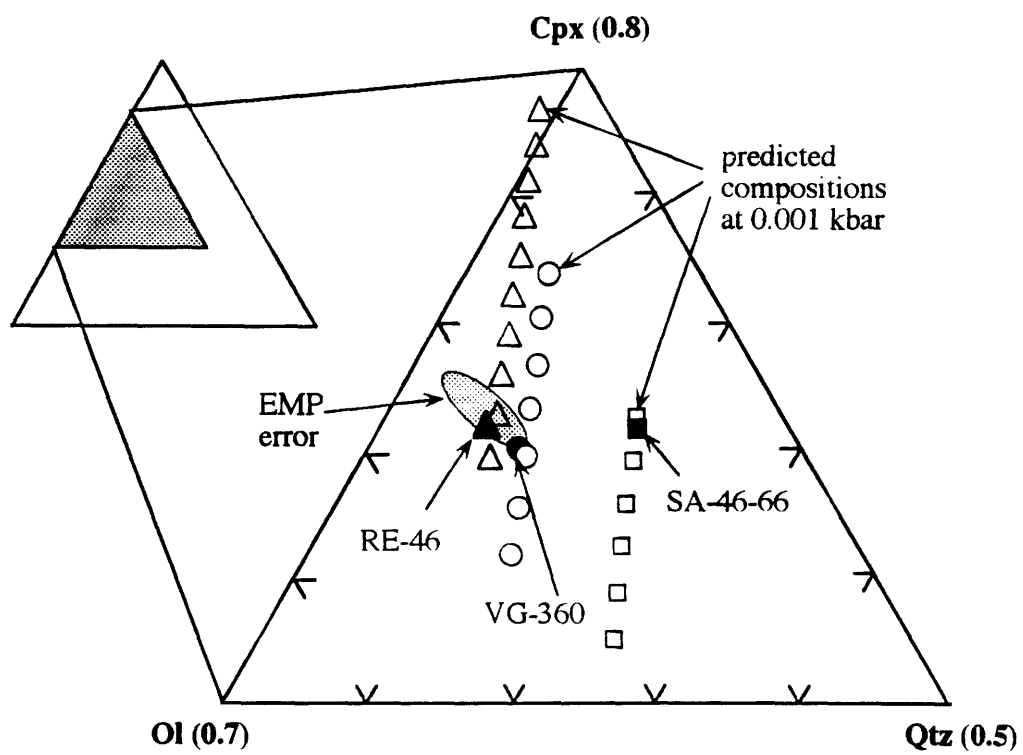


Fig. 8

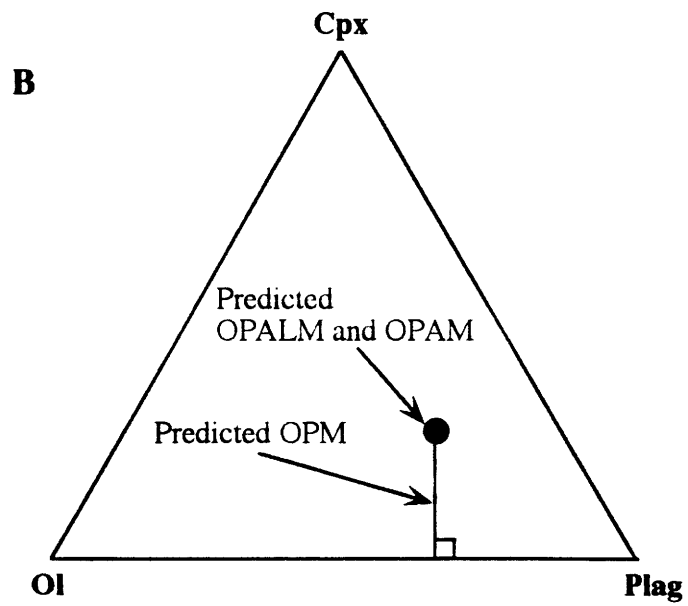
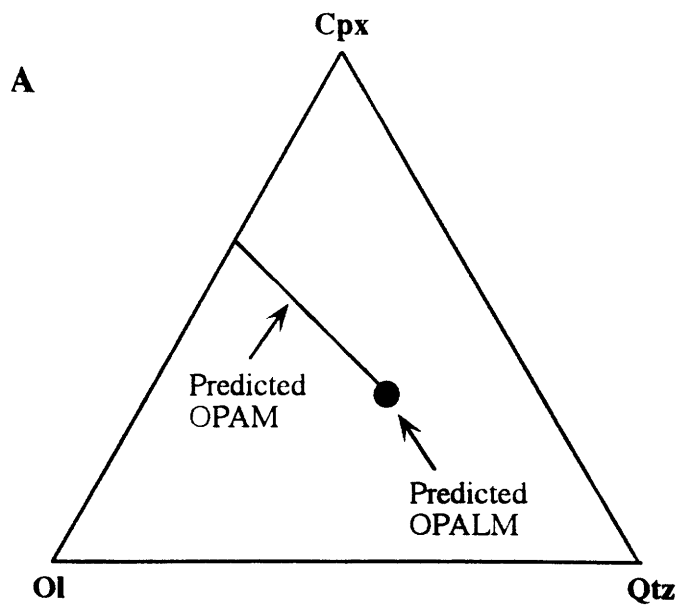


Fig. 9

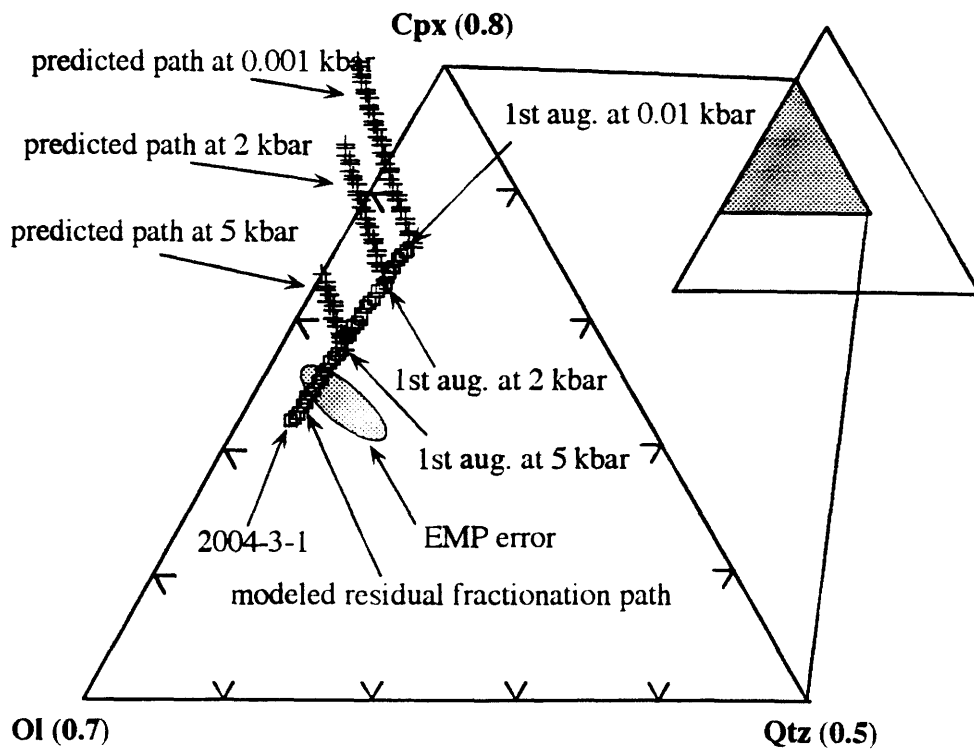


Fig. 10

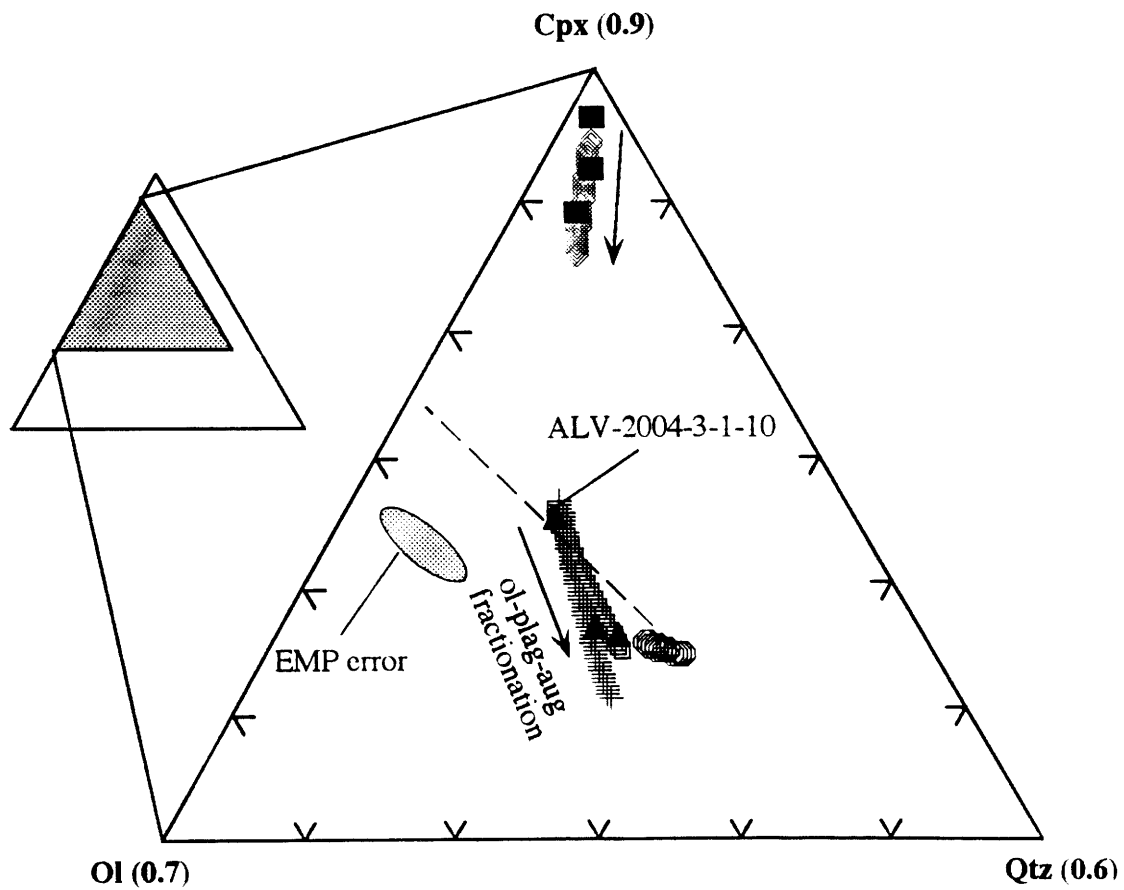


Fig. 11

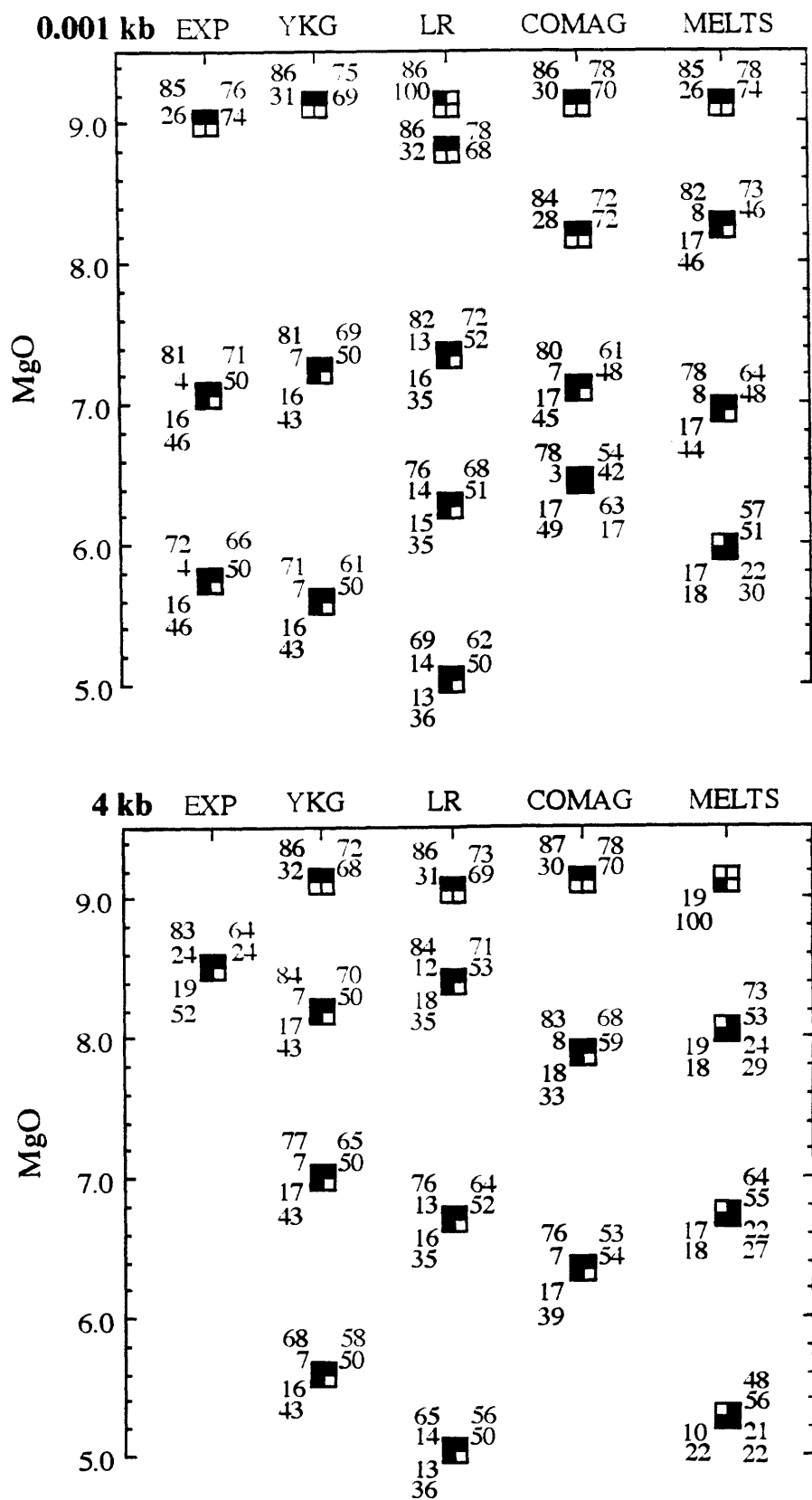


Fig. 12

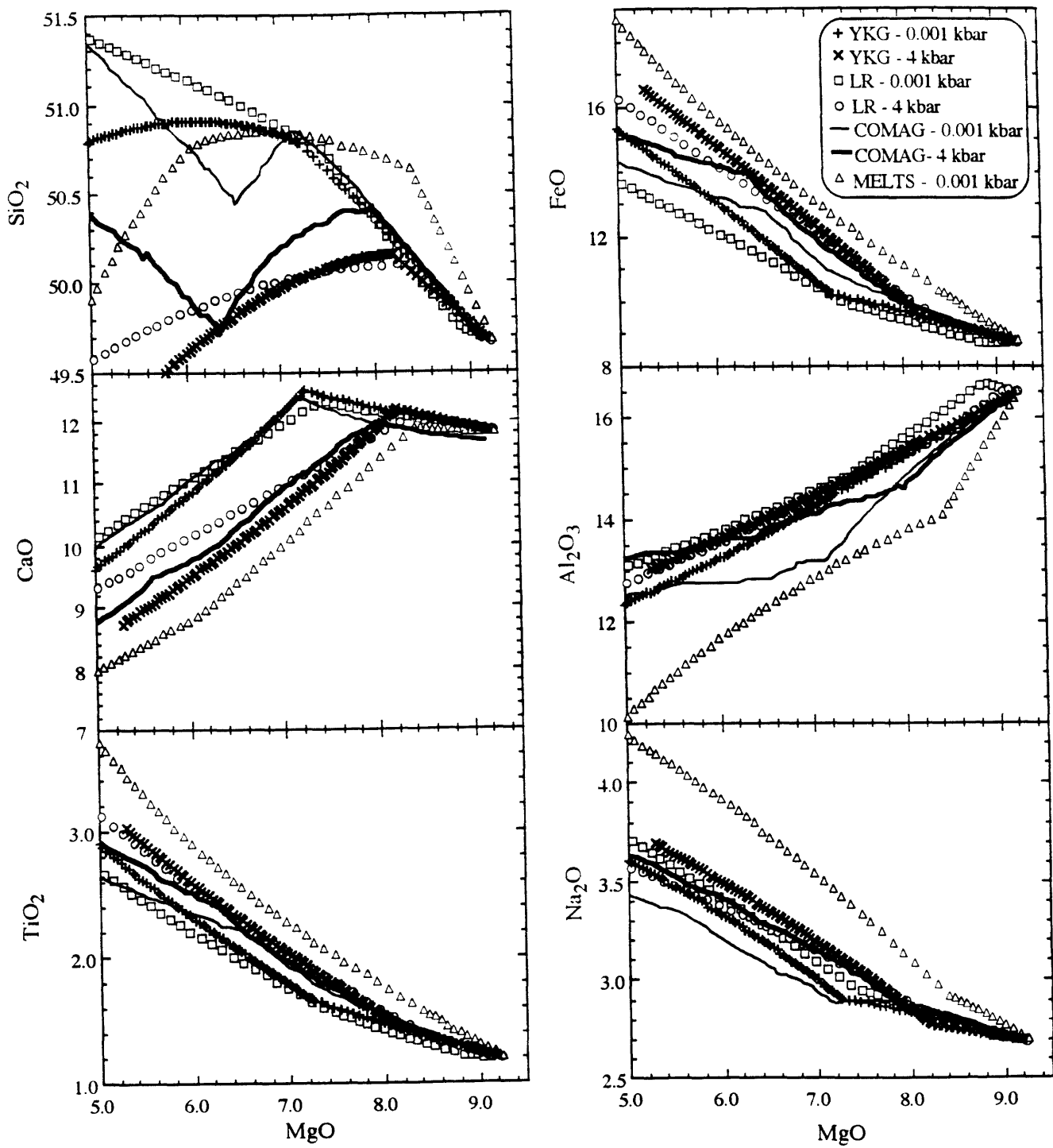


Fig. 13

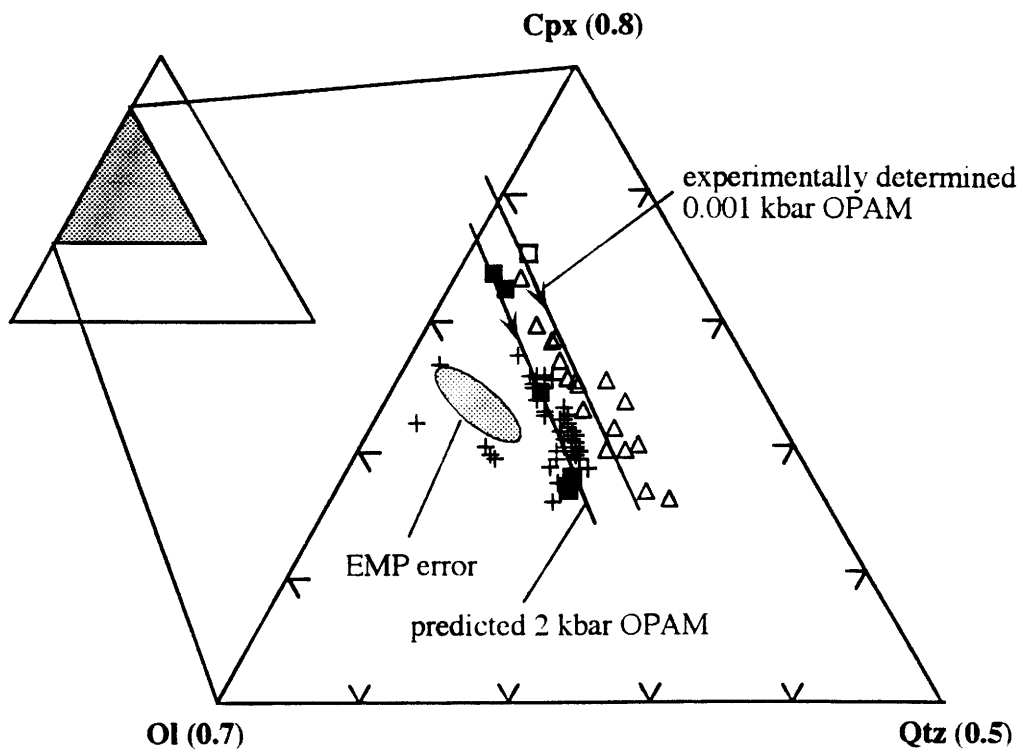


Fig. 14

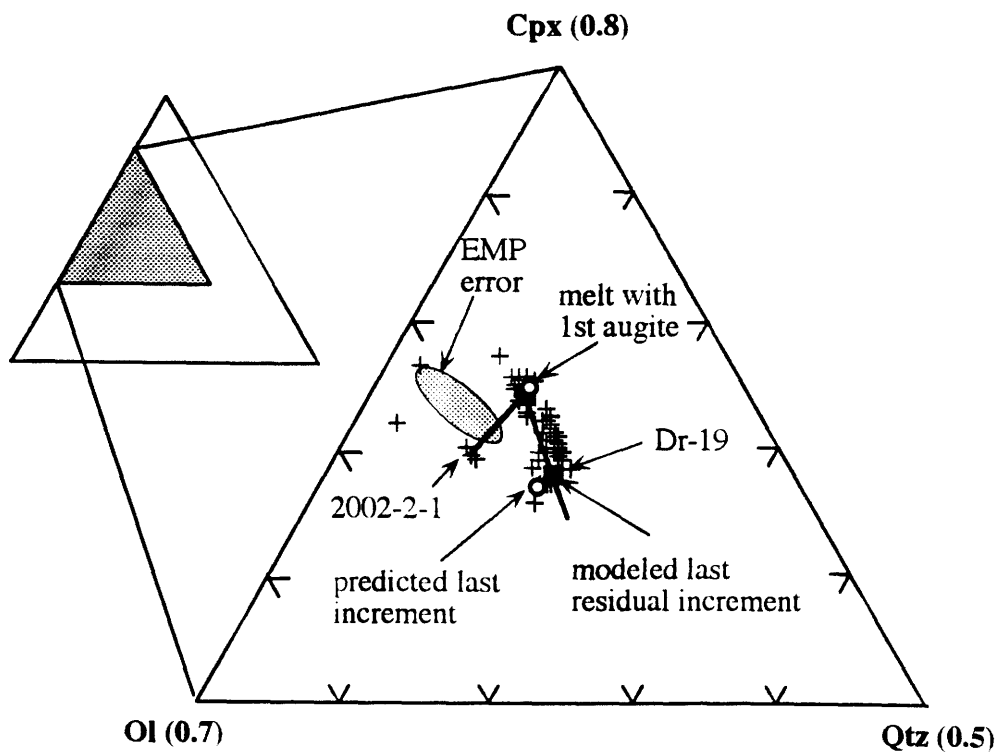


Fig. 15

CHAPTER TWO

Submarine Lavas From Mauna Kea Volcano, Hawaii: Implications for Hawaiian Shield-Stage Processes

ABSTRACT

The island of Hawaii is composed of five voluminous shields but only the youngest, active and well-exposed shields of Mauna Loa and Kilauea have been studied in detail. The shield lavas forming Kohala, Hualalai and Mauna Kea are largely covered by postshield lavas with geochemical characteristics that differ from the shield lavas. In order to determine the geochemical characteristics of the Mauna Kea shield which is adjacent to the Kilauea and Mauna Loa shields, twelve Mauna Kea shield basalts dredged from the submarine east rift were analyzed for major and trace element contents and isotopic (Sr, Nd and Pb) ratios. The lavas are MgO-rich (11 to 20%), submarine erupted, tholeiitic basalts, but they are not representative of crystallized MgO-rich melts. Their whole-rock and mineral compositions are consistent with mixing of three components: an evolved magma (<7% MgO), a mafic magma (>7% MgO) and olivine xenocrysts, probably disaggregated from a dunitic cumulate. At a given MgO content, some of the Mauna Kea whole-rocks have lower abundances of CaO and higher abundances of incompatible elements. The evolved melt component in these lavas reflects significant fractionation of plagioclase and clinopyroxene and in some cases even the late-crystallizing phases orthopyroxene and Fe-Ti oxide. Although these Mauna Kea lavas are not isotopically homogeneous, in general their Sr, Nd and Pb isotopic ratios overlap with the fields for lavas from Loihi and Kilauea volcanoes. Lavas from these three shields define the low $^{87}\text{Sr}/^{86}\text{Sr}$, high $^{206}\text{Pb}/^{204}\text{Pb}$ and low Zr/Nb ranges for Hawaiian shield lavas, and they may contain a larger proportion of a HIMU mantle component. Most of these Mauna Kea shield lavas, however, are distinguished from Kilauea and Loihi tholeiitic basalts by having lower La/Ce and La/Yb. These data provide additional evidence that each Hawaiian shield has distinctive geochemical characteristics.

INTRODUCTION

Hawaiian volcanos evolve through four distinct stages: preshield, shield, postshield, and rejuvenated (posterosional) (e.g., Clague and Dalrymple, 1987). The shield stage is the most voluminous and consists of tholeiitic basalt. Five volcanoes, Kohala, Hualalai, Mauna Kea, Mauna Loa and Kilauea, form the island of Hawaii, and two, Mauna Loa and Kilauea, are presently active and in the shield-building stage. Subaerial lavas forming these active and adjacent shields are geochemically distinct tholeiitic basalts, and these differences provide important constraints on the mantle sources of Hawaiian shield lavas and the magmatic processes associated with plume-related volcanism (e.g., Frey and Rhodes, 1993). However, the geochemical characteristics of the shield lavas forming the large adjacent volcano, Mauna Kea, are not well known because Mauna Kea is in the postshield stage, and its subaerial surface is covered by postshield lavas (Fig. 1). These lavas have been divided into a basaltic substage (Hamakua Volcanics, ~250 to ~70 ka) and a hawaiiite substage (Laupahoehoe Volcanics, ~65 to ~4 ka) (Porter, 1979; Frey et al., 1990; Wolfe et al., 1996). Although voluminous eruptions at Mauna Kea continued until ~130 ka (Moore and Clague, 1992), the oldest subaerial lavas of the Hamakua Volcanics are intercalated tholeiitic and alkalic basalts with rare picrites and ankaramites (Frey et al., 1991). A thick stratigraphic sequence of only tholeiitic lavas, analogous to the shield lavas of Kilauea and Mauna Loa, is not subaerially exposed on the flanks of Mauna Kea Volcano. In contrast, only tholeiitic lavas have been recovered from the submarine east rift of Mauna Kea (Garcia et al., 1989b; Frey et al., 1991; Moore and Clague, 1992).

We studied twelve lavas dredged from the east rift of Mauna Kea Volcano. Our objectives are to use petrologic, compositional and isotopic (Sr, Nd, Pb) data to infer the petrogenesis of these Mauna Kea lavas; to define and interpret the temporal geochemical changes during growth of Mauna Kea volcano; and to compare the geochemical characteristics of tholeiitic lavas forming the adjacent Mauna Kea, Kilauea and Mauna Loa shields (Fig. 1). The

temporal geochemical variations from late shield lavas to postshield lavas to rejuvenated lavas have provided significant constraints on the sources and processes occurring during the final growth stages of a Hawaiian volcano (e.g., Chen and Frey, 1985). Specifically for subaerial Mauna Kea lavas, Frey et al. (1991) concluded that the tholeiitic and alkalic basalts in the Hamakua Volcanics were derived from a garnet lherzolite source by different degrees of partial melting and that the phenocryst-rich picrites and ankaramites are products of phenocryst accumulation. In contrast to the diverse lava compositions in the basaltic substage (Hamakua Volcanics), the hawaiitic substage (Laupahoehoe Volcanics) contains only evolved lavas, such as hawaiites and mugearites, which are related to alkali basalts by clinopyroxene-dominated fractionation at moderate pressure (West et al., 1988; Frey et al., 1990). Our results show that the older submarine shield tholeiites are isotopically heterogeneous and some contain a component with relatively higher $^{87}\text{Sr}/^{86}\text{Sr}$ and lower $^{143}\text{Nd}/^{144}\text{Nd}$ than the subaerial lavas. Although this small suite of dredged shield lavas cannot be used to infer the long-term geochemical evolution of the Mauna Kea shield, this is the major goal of the Hawaii Scientific Drilling Project which began in late 1993 with a 1.1 km drill hole on the subaerial east flank of Mauna Kea Volcano (Thomas et al., 1993). Our results indicate that significant geochemical variations can be expected as deeper portions of the Mauna Kea shield are sampled.

Sampling

The dredge locations are shown in Fig. 1; samples designated MK were described by Garcia et al. (1989b) and samples designated SU were described by Moore (, 1966) Moore and Fiske (1969), and Moore and Clague (1992). All the samples analyzed in this study are pillow basalts dredged from 1.6 to 3.3 km water depth on the east rift (Fig. 1). They are inferred to be shield lavas because: (1) they are all tholeiitic basalt; (2) they were recovered from depths well below the 375m break in slope that Moore and Clague (1992) interpreted as marking the end of voluminous volcanism, and the high volatile contents of glasses associated with these dredged

rocks (e.g., S ranging from 0.029 to 0.123%) indicate that they are submarine eruptives (Garcia et al., 1989b; Moore and Clague, 1992); and (3) it is likely that volcanism at the distal end of a rift zone ceases before the end of the shield stage (Moore and Clague, 1992); therefore, these submarine lavas are likely to be much older than the subaerial lavas.

PETROGRAPHY

Olivine occurs as phenocrysts and microphenocrysts and is the most abundant mineral in these shield lavas (Table 1). They occur as undeformed and deformed grains; the latter exhibit planar extinction discontinuities or rectangular subgrain boundaries. Chromite and glass inclusions are abundant in both types of olivine. Except for samples MK 1-3 and 1-10, clinopyroxene and plagioclase also occur as phenocrysts and microphenocrysts (Table 1). Clinopyroxene usually occurs as microphenocrysts and forms aggregates with plagioclase laths; discrete phenocrysts of clinopyroxene are rare. Sample SU-22-64 is distinctive because it contains orthopyroxene phenocrysts and microphenocrysts (~2.7%, Table 1) surrounded by fine-grained clinopyroxene. Trace amounts of orthopyroxene were found in samples SU-20-64, SU-21-64 and MK 2-1. In sample MK 2-1 the orthopyroxene contains plagioclase inclusions. Microphenocrysts of a euhedral opaque mineral occur in sample MK 1-8.

ANALYTICAL

Abundances of major elements and the trace elements Rb, Sr, Ba, V, Cr, Ni, Zn, Ga, Y, Zr and Nb, were determined by X-ray fluorescence (XRF) at the University of Massachusetts. Abundances of the trace elements Sc, Hf, Ta, Th and REE were determined by instrumental neutron activation analysis (INAA) at MIT. For a discussion of accuracy and precision of the XRF and INAA procedures see Table 1d of Frey et. al. (1990).

Mineral compositions were analyzed with the MIT 4-spectrometer JEOL 733 superprobe, using 15 Kev accelerating voltage, 10 nA beam current, and a 10 μ m beam size. The data were reduced using Bence and Albee (1968) matrix corrections with the Albee and Ray

(1970) modification. Major element abundances of glasses were determined by electron microprobe at the U.S. Geological Survey in Menlo Park (SU samples), and at the University of Hawaii (MK samples).

Most of the isotopic data for Sr, Nd and Pb were obtained by mass spectrometry at the Woods Hole Oceanographic Institution using techniques adapted from Hart and Brooks (1977), Richard et al. (1976) and Barreiro (1983). Sr and Nd data for two samples were obtained at MIT. In order to remove the effects of alteration in seawater on isotopic ratios, all sample powders were leached in 6.2N HCl for 1 hour (100 °C) $^{87}\text{Sr}/^{86}\text{Sr}$ ratios were normalized to 0.70800 for E&A SrCO_3 , and during this study measured $^{87}\text{Sr}/^{86}\text{Sr}$ values for NBS 987 were 0.710234 ± 15 (n = 42). $^{143}\text{Nd}/^{144}\text{Nd}$ ratios are relative to 0.51264 for BCR-1 using $^{146}\text{Nd}/^{144}\text{Nd} = 0.72190$. Pb isotopic ratios were normalized for mass fractionation using average results for NBS 981, and during this study the mean values for NBS 981 were 16.902 ± 0.009 , 15.449 ± 0.011 and 36.567 ± 0.035 (n=17) for $^{206}\text{Pb}/^{204}\text{Pb}$, $^{207}\text{Pb}/^{204}\text{Pb}$ and $^{208}\text{Pb}/^{204}\text{Pb}$, respectively.

RESULTS

Mineral Compositions Olivine compositions were determined in all samples, and five samples were selected for detailed analyses of pyroxenes and plagioclase. These data are presented in chapter three, but here we summarize mineral composition data which are important in interpreting the whole-rock composition.

Olivine composition

A wide range of olivine compositions occurs in these Mauna Kea shield lavas with deformed and undeformed grains ranging from $\text{Fo}_{78.9}$ to $\text{Fo}_{90.6}$ in cores (Fig. 2a) and $\text{Fo}_{78.5}$ to $\text{Fo}_{93.3}$ in rims. Although Frey et al. (1991) found that some olivines in samples MK 1-3 and 5-13 are reversely zoned, all the olivines analyzed in this study are normally zoned. Abundances of CaO range from 0.15 to 0.33% in both types, which is consistent with crystallization from a

basaltic melt (Jurewicz and Watson, 1988). Although olivine cores with Fo = 87 to 90.6 are dominant (Fig. 2a), a wide range of olivine compositions occur in each sample (Fig. 2b). In each rock most of the olivines have compositions less forsteritic than olivine in equilibrium with a melt having the whole-rock composition, but all are more forsteritic than olivines in equilibrium with the glassy rims (Fig. 2b). A similar diversity of olivine types and compositions, up to Fo_{90.7}, occurs in submarine tholeiitic lavas dredged from the east rift zone of Kilauea Volcano (Clague et al., 1991; Clague et al., 1995).

Pyroxene Composition

We focus on results for sample SU-21-64 because it contains clinopyroxene and orthopyroxene, and their compositions provide the strongest evidence for magma mixing. Most of the relatively abundant clinopyroxene in this sample (Table 1) is reversely zoned with cores of Mg# [100Mg/(Mg+Fe)] = 71 to 79 and rims of Mg# 74 to 84 (Fig. 3). Similarly, the rare orthopyroxenes have cores of Mg# = 70 to 76 and rims of Mg# 82 to 83 (Fig. 3). If $(\text{Fe}/\text{Mg})_{\text{pyx}}/(\text{Fe}/\text{Mg})_{\text{melt}}$ is in the range of 0.23 to 0.27 (Tormey et al., 1987; Grove et al., 1992), pyroxenes of Mg# = 80 to 82 are in equilibrium with the glass in this sample (assuming $\text{Fe}^{+2} = 0.9$ total iron for glass and $\text{Fe}^{+2} = \text{total iron}$ for pyroxene). Therefore, the pyroxene cores are too Fe-rich to have formed in a melt with the glass composition.

Plagioclase Composition

Plagioclase in sample MK 1-8 is resorbed and relatively sodic (An_{55-59.5}). Like the pyroxenes, plagioclase in sample SU-21-64 is reversely zoned with cores of An₅₇₋₆₀ and rims of An₇₀₋₇₁ (Fig. 3).

Major Element Compositions

Whole rock All lavas dredged from the east rift of Mauna Kea are MgO-rich, tholeiitic basalts (Table 2, and Fig. 4). Relative to the subaerial Hamakua tholeiites, these submarine lavas, whole-rocks and associated glasses, define a total alkalis-SiO₂ trend which has lower total

alkalis at a given SiO₂ content (Fig. 4). An anomalous submarine sample, SU-22-64, is from the deepest dredge (3285m, Fig. 1); glass and whole-rock data for SU-22-64 reported by Moore and Clague (1992) (1992, Table B) indicate that it is transitional between tholeiitic and alkalic basalt. Our whole-rock analysis plots in the tholeiitic field; however, among the samples we studied, it is closest to the alkalic field and within the field of subaerial Hamakua tholeiites (Fig. 4). In contrast to many subaerial lavas from Mauna Kea (Frey et al., 1991), the high K₂O/P₂O₅ ratios (>1.56) of these submarine samples are similar to those of recent subaerial lavas from Kilauea and Mauna Loa [K₂O/P₂O₅ >1.5, (Wright, 1971)].

In MgO versus FeO (as total iron), CaO, TiO₂, Na₂O, K₂O and P₂O₅ plots (Fig. 5) these shield lavas form two distinct trends: one trend includes seven samples (referred to as Group 1); the other trend is defined by four samples (referred to as Group 2). At a given MgO content, Group 1 samples have higher CaO contents but lower abundances of FeO, TiO₂, Na₂O, K₂O and P₂O₅. Group 1 samples have a nearly constant Al₂O₃/CaO ratio (~1.23), whereas Group 2 samples have Al₂O₃/CaO ratios ranging from 1.32 to 1.41 (Fig. 5). In contrast to the linear MgO-SiO₂ trend defined by Groups 1 and 2, sample SU-22-64, has a distinctively low SiO₂ content (Fig. 5).

Glasses In contrast to the whole-rocks which have variable and relatively high MgO contents (10.8 to 20.3%, Table 2), the glassy rims of these pillow basalts have low MgO contents varying only from 5.3 to 6.9% (Table 3). Unlike the whole-rocks, these glasses define a positive trend of CaO vs. MgO and steep inverse K₂O-MgO and TiO₂-MgO trends (Fig. 5). These glass trends are consistent with control by fractionation of clinopyroxene and plagioclase in addition to olivine. Some of the whole-rock compositional differences between Groups 1 and 2 are also seen in the glass compositions; e.g., Group 2 glasses trend to higher TiO₂ and K₂O contents than Group 1 glasses. Also, the distinctly low SiO₂ content of the SU-22-64 whole-rock is also characteristic of glass in this sample (Fig. 5).

Trace Element Abundances Whole-rock abundances of incompatible elements such as Nb, La and Zr are positively correlated and the highest abundances are in Group 2 lavas and sample SU-22-64 (Table 2 and Fig. 6). Even abundances of Rb, a mobile element during post-magmatic alteration, are strongly correlated with Nb abundances. These submarine Mauna Kea lavas have Ba/Rb ratios, 13.6 ± 1.1 , typical of oceanic island basalts [12.5, (Hofmann and White, 1983)] thereby indicating that Rb abundances have not been affected by alteration. Although Group 2 lavas have higher abundances of highly incompatible elements, they are relatively depleted in Sr (Fig. 7), an element which is sensitive to fractionation of plagioclase. As MgO content increases, abundances of Ni and Cr increase, but abundances of V and Sc decrease (Fig. 6). At a given MgO content, abundances of Sc, an element sensitive to clinopyroxene fractionation, are lower in Group 2 lavas (Fig. 6).

The two groups of Mauna Kea shield lavas identified on the basis of major element trends are also distinct in some trace element abundance ratios; specifically, Group 2 lavas have higher La/Yb but lower Sr/Nb, Sr/Ce and Ti/Eu (Figs. 7 and 8). Relative to subaerial Hamakua tholeiites from the east flank of Mauna Kea, the dredged shield lavas have similar abundance ratios of La/Nb, Zr/Nb and Sr/Nb (Group 1 only), but most have lower La/Ce and La/Yb ratios (Fig. 8). These abundance ratios have been used as intershield discriminants (e.g., Rhodes et al., 1989; Frey and Rhodes, 1993; Roden et al., 1994). The range of La/Nb (0.74 to 0.90), and Sr/Nb (21.8 to 27.7 for Group 1) in the submarine Mauna Kea lavas overlaps with the field for Kilauea lavas; the range of Zr/Nb for Groups 1 and 2 (11 to 14) is intermediate between the fields of Kilauea and Mauna Loa lavas; and the range for La/Yb (4.3 to 5.7) for Groups 1 and 2 overlaps with the field for Mauna Loa lavas (Fig. 8). Among these Mauna Kea samples, SU-22-64 has the highest La/Yb (8.3) and lowest Zr/Nb (9.8) which is consistent with its more alkaline characteristics in major element composition (higher $\text{Na}_2\text{O} + \text{K}_2\text{O}$ at a given SiO_2 , Fig. 4).

Sr, Nd, Pb and He isotopic ratios The $^{87}\text{Sr}/^{86}\text{Sr}$ ratios of Group 1 samples range from 0.70350 to 0.70361 which largely overlaps with the ratios in postshield lavas (Kennedy et al., 1991), but most Group 2 samples and SU-22-64 have slightly higher $^{87}\text{Sr}/^{86}\text{Sr}$ ratios which exceed the ratios in postshield lavas (Table 2 and Fig. 9). Ratios of $^{143}\text{Nd}/^{144}\text{Nd}$ and $^{87}\text{Sr}/^{86}\text{Sr}$ are inversely correlated in these shield lavas; consequently, the $^{143}\text{Nd}/^{144}\text{Nd}$ ratios in most Group 2 lavas and SU-22-64 are lower than in postshield lavas (Fig. 9). Relative to postshield lavas, the shield tholeiitic basalts have a wider range of $^{206}\text{Pb}/^{204}\text{Pb}$, and the two compositional groups overlap in Pb isotopic ratios (Fig. 10).

Consistent with the relatively high $^3\text{He}/^4\text{He}$ ratios in other Hawaiian shield lavas, Graham et al. (1990) found that olivines from six samples of the MK dredge suite range from 12 to 14 R_a (R_a = atmospheric $^3\text{He}/^4\text{He}$). In contrast, the associated glasses have much lower and variable ratios of 2 to 9, apparently reflecting early degassing and subsequent ingrowth of ^4He .

DISCUSSION

Compositional variations in Group 1 samples: mixing of evolved melt and a magma with abundant olivine xenocrysts A possible explanation for the wide range of Group 1 lava compositions, e.g., MgO from 10.8 to 20.3% (Table 2a), is that they were derived by olivine fractionation and accumulation from a parental magma with intermediate MgO content (6~7 %). However, phenocryst compositions are inconsistent with this interpretation. In particular, the diversity of olivines in these lavas, i.e., deformed and undeformed grains with a wide compositional range (Fig. 2) and the presence of reversely zoned pyroxenes and plagioclase (Fig. 3) with core compositions that formed in a melt more evolved than the glass show that Group 1 lavas formed by magma mixing. Magma mixing is also an important process in the petrogenesis of rift magmas erupted on Kilauea Volcano (e.g., Wright and Fiske, 1971; Garcia et al., 1989a; Clague et al., 1995). Group 1 whole-rocks contain 9.8 to 33.2% olivine (Table 1), and the linear trends of MgO versus SiO_2 , Al_2O_3 , CaO, TiO_2 , Na_2O , and K_2O (Fig.

5) are consistent with mixing of forsterite olivine ($\sim\text{Fo}_{88}$ and 48% MgO) and the mafic end of the compositional range of Group 1 glasses (Fig. 11); thus, most of the olivines are xenocrysts.

The Ni-MgO trend defined by the whole-rocks intersects near the middle of the Ni-MgO field of the olivines (Fig. 6), and we infer that the whole-rock trend reflects control by addition of olivine with a mean composition of 48% MgO (F₈₈) and 2850 ppm Ni. Given the wide range of olivine compositions in each whole-rock (Fig. 2), it is surprising that the compositional variations of Group 1 whole-rocks are consistent with addition of olivine with the same mean composition, (Figs. 6 and 11). Clague et al. (1995) found a similar result for olivine-rich lavas dredged from the east rift of Kilauea volcano; that is, these lavas also contain olivines of diverse compositions, Fo ranging from 77.8-90.7, but their whole-rock compositions are consistent with addition of variable amounts of olivine with F₈₈ and 2840 ppm Ni. Apparently olivine-rich lavas in the submarine rift zones of Kilauea and Mauna Kea formed by similar processes. Clague et al. (1995) proposed that olivines in these Kilauea lavas were disaggregated from an olivine cumulate at the base of a magma chamber by an ascending melt, and subsequently this olivine-rich magma was mixed with low temperature, evolved magma formed in the rift zone. They also calculated that F₈₈ is the average composition of olivine crystallized as a primary Hawaiian magma, $\sim 16.5\%$ MgO, evolves to a melt with 7% MgO. Thus F₈₈ may be the average composition settled onto the floor of the magma chamber. Therefore, the average olivine composition required to explain the compositional variation in Group 1 lavas is consistent with incremental crystallization of a primary Hawaiian magma to a composition, $\sim 7\%$ MgO, typical of subaerial shield lavas.

In summary we conclude that the whole-rock compositions of Group 1 lavas are not representative of melts. They are mixtures of three components: (1) an evolved rift zone melt parental to the relatively low Mg# cores of pyroxenes and An-poor cores of plagioclase (Fig. 3); (2) disaggregated olivines from a cumulate layer which formed from relatively high MgO lavas; and (3) an olivine-bearing magma which disrupted the cumulate, incorporated xenocrystic

olivine and mixed with evolved magma in the rift zone. Phenocryst growth in this mixed magma resulted in reversely zoned pyroxene and plagioclase phenocrysts (Fig. 3). Because the glass compositions in these lavas are interpreted to be homogeneous mixtures of evolved melt formed in the rift zone and olivine-bearing melt, the whole-rock compositions are consistent with mixing of two components, the mixed melt, now represented by glass, and olivine xenocrysts.

Compositional variations in Group 2 samples: magma mixing and evidence for a highly evolved melt component Like Group 1 whole-rocks, the Group 2 whole-rocks have high MgO contents, 11-17%. However, the distinctive characteristics of Group 2 lavas, high $\text{Al}_2\text{O}_3/\text{CaO}$ (Fig. 5), relatively high abundances of incompatible elements and relative depletions in Sr and Sc (Figs. 6 and 7), indicate the presence of an evolved melt which has experienced significant fractionation of plagioclase and clinopyroxene. Sample MK 1-8 is most extreme in these characteristics: the glassy rim has the lowest MgO content (5.3%, Table 3); it contains a small amount of resorbed sodic, An_{58} , plagioclase [Table 4 of (Frey et al., 1991)], and it has anomalously low Sr/Nb, Sr/Ce and Ti/Eu ratios (Fig. 8) reflecting the effects of plagioclase and Fe-Ti oxide fractionation, respectively. Dredge MK-1 is far from the summit of Mauna Kea (Fig. 1); therefore, the highly evolved melt component in sample MK 1-8 may reflect enhanced fractionation resulting from the low magma supply to the distal end of rift zones.

As with Group 1 samples, the whole-rock compositions of Group 2 samples MK 1-8 and MK 1-10 can be explained by addition of olivine to a melt composition represented by the glassy margin (Fig. 11). Therefore some of the geochemical differences between Groups 1 and 2 reflect the more important role of an evolved melt in Group 2 lavas (Table 3). In contrast to Group 2 lavas from Dredge MK 1, samples SU-20-64 and SU-22-64 contain more than 15% phenocrysts and microphenocrysts of pyroxene and plagioclase (Table 1), and their whole-rock

compositions are determined by the proportions of olivine, plagioclase, pyroxenes and glass.

Diversity of Primary Magmas Represented in the Uppermost Mauna Kea Shield

Frey et al. (1991) suggested that the sequence submarine tholeiitic basalt-subaerial tholeiitic basalt-subaerial alkalic basalt reflected a decrease in extent of melting of a geochemically homogeneous source. This interpretation is viable for most of the Group 1 submarine lavas which are similar in Sr and Nd isotopic ratios to the subaerial lavas (Fig. 9). However, two Group 1 samples, MK 2-1 and MK 6-6, have different isotopic ratios (Figs. 9 and 10) and abundance ratios of incompatible elements (Sr/Nb, La/Nb and Zr/Nb in Fig. 8); therefore, all Group 1 samples were not derived from a common source. Moreover, sample SU-22-64 and Group 2 lavas, except for SU-20-64, have higher $^{87}\text{Sr}/^{86}\text{Sr}$ and lower $^{143}\text{Nd}/^{144}\text{Nd}$ than Group 1 lavas and subaerial Mauna Kea lavas (Fig. 9). These lavas from dredges MK-1 and SU-22-64 were recovered at the greatest distance from the summit of Mauna Kea (Fig. 1); therefore, the isotopically distinct samples from Dredges MK-1 and SU-22-64 may be older than the other submarine samples, and all the submarine lavas may be older than subaerially exposed Mauna Kea lavas. If the latter inference is correct, the Sr and Nd isotopic differences between Mauna Kea subaerial lavas and some of the submarine shield lavas (Fig. 9) are similar to the differences between postshield and shield lavas at other Hawaiian volcanoes [e.g., Haleakala-Chen and Frey (1985); Kohala-Hofmann et al., (1987); Lanphere and Frey, (1987)]. This trend has been interpreted as reflecting an increasing role for a depleted mantle source component as the volcano moves away from the plume source (e.g., Chen and Frey, 1985; West and Leeman, 1987). If the age of the dredged samples increases with distance from the Mauna Kea summit, the oldest shield lavas (Dredges MK-1 and SU-22-64) have the highest $^{87}\text{Sr}/^{86}\text{Sr}$ and lowest $^{143}\text{Nd}/^{144}\text{Nd}$ (Fig. 9). This inference of systematic temporal variations of Sr and Nd isotopic ratios among Mauna Kea shield lavas contrasts with the absence of systematic temporal variations in the postshield lavas (Kennedy et al., 1991), and it will soon be evaluated by studies of the recently

obtained 1.1 km drill core from Mauna Kea shield (Thomas et al., 1993). Finally, sample SU-22-64 which was dredged from the greatest depth and is most distant from the summit of Mauna Kea (Fig. 1), has distinctive compositional characteristics (i.e., transitional to alkalic composition (Fig. 4), relatively low SiO₂ content (Fig. 5), the highest La/Yb and lowest Zr/Nb (Fig. 8)) which are consistent with a relatively lower degree of melting.

Geochemical Comparisons With Other Hawaiian Shields There are remarkable similarities between the dredged Mauna Kea lavas (this paper) and lavas dredged from the submarine east rift of Kilauea (Clague et al., 1995). Submarine samples from both volcanoes have high MgO contents, 10-20%. In addition, they contain: abundant undeformed and deformed olivines which range widely in composition, (Fo₇₈₋₉₁), even in single flows; phenocryst phases such as plagioclase, clinopyroxene and orthopyroxene which are not near-liquidus phases of MgO-rich melts; and pillow rims of evolved glass, 5-7% MgO. These characteristics indicate that similar petrogenetic processes occurred in the east rift zones of Mauna Kea and Kilauea Volcanoes; in particular, accumulation of olivine followed by incorporation of these compositionally diverse olivines in an ascending magma and subsequent magma mixing with evolved, low temperature melt formed in a rift zone. A similar interpretation is applicable for a subaerial olivine-rich basalt from Haleakala volcano (Chen, 1993).

In a ⁸⁷Sr/⁸⁶Sr - ²⁰⁶Pb/²⁰⁴Pb plot Hawaiian shield lavas define a trend of increasing ⁸⁷Sr/⁸⁶Sr with decreasing ²⁰⁶Pb/²⁰⁴Pb (Fig. 12). Submarine Mauna Kea lavas are at the relatively low ⁸⁷Sr/⁸⁶Sr and high ²⁰⁶Pb/²⁰⁴Pb end of this trend. Most of these Mauna Kea shield lavas have ⁸⁷Sr/⁸⁶Sr and ²⁰⁶Pb/²⁰⁴Pb within the range defined by Loihi lavas; samples MK 6-6, MK 2-1 and SU-22-64 are exceptions (Fig. 12).

Frey and Rhodes (1993) and Roden et al. (1994) noted that there are important intershield differences in abundance ratios of La/Nb, Zr/Nb and Sr/Nb, and that these

differences in abundance ratios correlate with intershield differences in Sr and Nd isotopic ratios. As a whole the Mauna Kea shield lavas are like Kilauea and Loihi lavas in that they have relatively low La/Nb, Zr/Nb, Sr/Nb and $^{87}\text{Sr}/^{86}\text{Sr}$ (Fig. 13). Although the correlation for some individual Hawaiian shields is poor, the highest Zr/Nb ratios are in shield lavas which have relatively low $^{206}\text{Pb}/^{204}\text{Pb}$ (Fig. 14). Among the Mauna Kea shield lavas there is an inverse correlation between Zr/Nb and $^{206}\text{Pb}/^{204}\text{Pb}$ (except for sample MK-6-6, Fig. 14). The HIMU mantle component is characterized by relatively low Zr/Nb [<5 , (Weaver, 1991)] and high $^{206}\text{Pb}/^{204}\text{Pb}$ [>20 , (Hart, 1988)]. Therefore, the inverse Zr/Nb - $^{206}\text{Pb}/^{204}\text{Pb}$ trend defined by Hawaiian shield lavas may reflect small and variable amounts of a HIMU component with the largest proportion in some Kilauea lavas and Mauna Kea samples MK 2-1 and SU-22-64. Overall the correlations of Zr/Nb, La/Nb and Sr/Nb with isotopic ratios (Figs. 13 and 14) and the $^{87}\text{Sr}/^{86}\text{Sr}$ - $^{206}\text{Pb}/^{204}\text{Pb}$ correlation (Fig. 12) show that within shield geochemical heterogeneities are smaller than the geochemical differences between shields.

CONCLUSIONS

Lavas dredged from the east rift of Mauna Kea Volcano are MgO-rich, 10.8 to 20.3%, tholeiitic shield lavas erupted in a submarine environment. Their glassy rims represent evolved melts with 5.3 to 6.9% MgO. The MgO-rich whole-rock compositions are not representative of melt compositions, but they are mixtures of evolved melts and a magma containing abundant olivine xenocrysts. Similar rocks have been dredged from the east rift zone of Kilauea volcano, and Clague et al. (1995) conclude that they are mixtures of a magma containing xenocrystic olivine with diverse compositions and an evolved magma which had crystallized plagioclase, clinopyroxene, and in some cases, orthopyroxene. In chapter three, a detailed study on the mineral compositions of some of these submarine lavas provides evidence for isolated magma chambers containing very evolved magmas in the rift zone at large distances from the summit.

Although these submarine Mauna Kea lavas have Sr, Nd and Pb isotopic ratios and

abundance ratios of La/Nb, Sr/Nb and Zr/Nb which overlap with the fields defined by Kilauea and Loihi shield lavas (Figs. 12, 13 and 14), the Group 1 Mauna Kea lavas have lower La/Yb (Fig. 8). Consequently, these Mauna Kea shield lavas have distinctive geochemical characteristics. Nevertheless, as with other Hawaiian shields (Kurz, 1993), it is apparent that even the uppermost Mauna Kea shield lavas reflect multiple primary magma compositions. It is unknown, however, whether these geochemically distinct primary magmas represent long-lived heterogeneities in a plume source, varying contributions from physically different sources or if they reflect complexities in melting and magma ascent processes. In order to distinguish between these and other alternatives, it is essential to know how the geochemical characteristics of primary magmas at a given shield vary with eruption age. It is not possible, however, to use surficial subaerial and submarine shield lavas to obtain this information for a large fraction of the shield growth stage. In chapter four, the long term geochemical variations in Mauna Kea volcano will be investigated by studying the 776 meters drill core recovered from Hawaiian Scientific Drilling Project (HSDP).

REFERENCES

- Albee A. L. and Ray L. (1970) Correction factors for electron microprobe analysis of silicates, oxides, carbonates, phosphates and sulfates. *Anal. Chem.* 42, 1408-1414.
- Barreiro B. A. (1983) Lead isotopic compositions of South Sandwich Island volcanic rocks and their bearing on magma genesis in intra-oceanic arcs. *Geochim. Cosmochim. Acta.* 47, 817-822.
- BASALTIC VOLCANISM STUDY PROJECT (BVSP), Basaltic Volcanism on the Terrestrial Planets. (1981), Pergamon Press, New York.
- Bence A. E. and Albee A. L. (1968) Empirical correction factors for the electron microanalysis of silicates and oxides. *J. Geol.* 76, 382-403.
- Chen C.-Y. (1993) High-magnesian primary magmas from Haleakala Volcano, East Maui: Petrography, nickel, and major element constraints. *J. Volcanol. Geotherm. Res.* 55, 143-153.
- Chen C.-Y. and Frey F. A. (1985) Trace element and isotopic geochemistry of lavas from Haleakala volcano, East Maui, Hawaii: Implications for the origin of Hawaiian lavas. *J. Geophys. Res.* 90, 8743-8768.
- Chen C.-Y., Frey F. A., Garcia M. O., Dalrymple G. B., and Hart S. R. (1991) The tholeiitic to alkalic basalt transition at Haleakala Volcano, East Maui, Hawaii: Petrogenetic interpretations based on major and trace element and isotope geochemistry. *Contrib. Mineral. Petrol.* 106, 183-200.
- Clague D. A. and Dalrymple G. B. (1987) The Hawaiian-Emperor volcanic chain. Part 1, Geologic evolution. *U.S. Geol. Surv. Prof. Pap.* 1350, 5-54.
- Clague D. A., Moore J. G., Dixon J. E., and Friesen W. B. (1995) Petrology of submarine lavas from Kilauea's Puna Ridge, Hawaii. *J. Petrol.* 36(2), 299-349.
- Clague D. A., Weber W. S., and Dixon J. E. (1991) Picritic glasses from Hawaii. *Nature* 353, 553-556.
- Frey F. A. and Clague D. A. (1983) Geochemistry of diverse basalt types from Loihi Seamount, Hawaii : Petrogenetic implications. *Earth Planet. Sci. Lett.* 66, 337-355.
- Frey F. A., Garcia M. O., and Roden M. F. (1994) Geochemical characteristics of Koolau Volcano: Implications of intershield geochemical differences among Hawaiian volcanoes. *Geochim. Cosmochim. Acta.* 58, 1441-1462.
- Frey F. A., Garcia M. O., Wise W. S., Kennedy A., Gurriet P., and Albarede F. (1991) The evolution of Mauna Kea Volcano, Hawaii: Petrogenesis of tholeiitic and alkalic basalts. *J. Geophys. Res.* 96, 14,347-14,375.

- Frey F. A. and Rhodes J. M. (1993) Intersield geochemical differences among Hawaiian volcanoes: Implications for source compositions, melting process and magma ascent paths. *Phil. Trans. R. Soc. Lond. Ser. A*, 342, 121-136.
- Frey F. A., Wise W. S., Garcia M. O., West H., Kwon S.-T., and Kennedy A. (1990) Evolution of Mauna Kea Volcano, Hawaii: Petrologic and geochemical constraints on postshield volcanism. *J. Geophys. Res.* 95, 1271-1300.
- Garcia M. O., Ho R. A., Rhodes J. M., and Wolfe E. W. (1989a) Petrologic constraints on rift-zone processes. *Bull. Volcanol.* 52, 81-96.
- Garcia M. O., Jorgenson B. A., Mahoney J. J., Ito E., and Irving A. J. (1993) An evaluation of temporal geochemical evolution of Loihi summit lavas: Results from Alvin submersible dives. *J. Geophys. Res.* 98, 537-550.
- Garcia M. O., Muenow D., and Aggrey K. E. (1989b) Major element, volatile, and stable isotope geochemistry of Hawaiian submarine tholeiitic glasses. *J. Geophys. Res.* 94, 10,525-10,538.
- Graham D., Lupton J., and Garcia M. O. (1990) He isotopes in olivine phenocrysts from submarine basalts of Mauna Kea and Kohala, island of Hawaii (abstract). *EOS (Am. Geophys. Union Trans.)* 71, 657.
- Grove T. L., Kinzler R. J., and Bryan W. B. (1992) Fractionation in mid-ocean ridge basalts (MORB). In *Mantle Flow and Melt Generation at Mid-Ocean Ridges*. Geophys. Monogr. Ser., Vol. 71, edited by J. P. Morgan, D. K. Blackman, and J. M. Sinton, pp. 281-310, AGU, Washington, D.C.
- Hart S. R. (1988) Heterogeneous mantle domains: Signatures, genesis and mixing chronologies. *Earth Planet. Sci. Lett.* 90, 273-296.
- Hart S. R. and Brooks C. (1977) The geochemistry of Early Precambrian mantle. *Contrib. Mineral. Petrol.* 61, 109-128.
- Hofmann A. W., Feigenson M. D., and Raczek I. (1987) Kohala revisited. *Contrib. Mineral. Petrol.* 95, 114-122.
- Hofmann A. W. and White W. M. (1983) Ba, Rb and Cs in the Earth's mantle. *Z. Naturforsch* 38a, 258-266.
- Jurewicz A. J. G. and Watson E. B. (1988) Cations in olivine, 1, Calcium partitioning and calcium-magnesium distribution between olivines and coexisting melts, with petrologic applications. *Contrib. Mineral. Petrol.* 99, 176-185.
- Kennedy A. K., Kwon S.-T., Frey F. A., and West H. B. (1991) The isotopic composition of postshield lavas from Mauna Kea Volcano, Hawaii. *Earth Planet. Sci. Lett.* 103, 339-

- Kurz M. D. (1993) Mantle heterogeneity beneath oceanic islands - Some inferences from isotopes. *Phil. Trans. R. Soc. Lond.* 342, 91-103.
- Kurz M. D. and Kammer D. P. (1991) Isotopic evolution of Mauna Loa volcano. *Earth Planet. Sci. Lett.* 103, 257-269.
- Lanphere M. A. and Frey F. A. (1987) Geochemical evolution of Kohala Volcano, Hawaii. *Contrib. Mineral. Petrol.* 95, 100-113.
- Leeman W. P., Gerlach D. C., Garcia M. O., and West H. B. (1994) Geochemical variations in lavas from Kahoolawe volcano, Hawaii: Evidence for open system evolution of plume-derived magma. *Contrib. Mineral. Petrol.* 116, 62-77.
- Macdonald G. A. and Katsura T. (1964) Chemical compositions of Hawaiian lavas. *J. Petrol.* 5, 82-133.
- Moore J. G. (1966) Rate of palagonitization of submarine basalt adjacent to Hawaii. *U.S. Geol. Surv. Prof. Pap.* 550-D, 163-171.
- Moore J. G. and Clague D. A. (1992) Volcano growth and evolution of the island of Hawaii. *Geol. Soc. Am. Bull.* 104, 1471-1484.
- Moore J. G. and Fiske R. S. (1969) Volcanic substructure inferred from dredge samples and ocean-bottom photographs, Hawaii. *Geol. Soc. Am. Bull.* 80, 1191-1202.
- Porter S. C. (1979) Quaternary stratigraphy and chronology of Mauna Kea, Hawaii. *Geol. Soc. Am. Bull.* 90, 980-1093.
- Rhodes J. M., Wenz K. P., Neal C. A., Sparks J. W., and Lockwood J. P. (1989) Geochemical evidence for invasion of Kilauea's plumbing system by Mauna Loa magma. *Nature* 337, 257-260.
- Richard P., Shimizu N., and Allegre C. J. (1976) $^{143}\text{Nd}/^{144}\text{Nd}$, a natural tracer: an application to oceanic basalts. *Earth Planet. Sci. Lett.* 31, 269-278.
- Roden M. F., Trull T., Hart S. R., and Frey F. A. (1994) New He, Sr, Nd and Pb isotopic constraints on the constitution of the Hawaiian plume: Results from Koolau Volcano, Oahu, Hawaii. *Geochim. Cosmochim. Acta.* 58, 1431-1440.
- Staudigel H., Zindler A., Hart S. R., Leslie T., Chen C.-Y., and Clague D. A. (1984) The isotope systematics of a juvenile intraplate volcano: Pb, Nd, and Sr isotope ratios of basalts from Loihi Seamount, Hawaii. *Earth Planet. Sci. Lett.* 69, 13-29.
- Stille P., Unruh D. M., and Tatsumoto M. (1983) Pb, Sr, Nd and Hf isotopic evidence of multiple sources for Oahu, Hawaii basalts. *Nature* 304, 25-29.
- Stille P., Unruh D. M., and Tatsumoto M. (1986) Pb, Sr, Nd and Hf isotopic constraints on the

- origin of Hawaiian basalts and evidence for a unique mantle source. *Geochim. Cosmochim. Acta.* 50, 2303-2319.
- Sun S.-S. and McDonough W. F. (1989) Chemical and isotopic systematics of oceanic basalts: Implications for mantle composition and processes. In *Magmatism in the Ocean Basins.* 42, edited by A. D. Saunders and M. J. Norry, pp. 313-345, Geol. Soc. Spec. Pub., London.
- Tatsumoto M. (1978) Isotopic composition of lead in oceanic basalt and its implication to mantle evolution. *Earth Planet. Sci. Lett.* 38, 63-87.
- Tatsumoto M., Hegner E., and Unruh D. M. (1987) Origin of the West Maui volcanic rocks inferred from Pb, Sr and Nd isotopes and a multicomponent model for oceanic basalt. *U.S. Geol. Surv. Prof. Pap.* 1350, 723-744.
- Thomas D. M., DePaolo D. J., and Stolper E. M. (1993) Results of the Hawaii Pilot Hole: Stratigraphic section through the Mauna Loa-Mauna Kea interface (abstract). *EOS (Am. Geophys. Union Trans.)* 74(43), 642.
- Tormey D. R., Grove T. L., and Bryan W. B. (1987) Experimental petrology of normal MORB near the Kane Fracture Zone: 22oN-25oN, mid-Atlantic ridge. *Contrib. Mineral. Petrol.* 96, 121-139.
- Weaver B. L. (1991) The origin of ocean island basalt end-member compositions: trace element and isotopic constraints. *Earth Planet. Sci. Lett.* 104, 381-397.
- West H. B., Garcia M. O., Frey F. A., and Kennedy A. (1988) Nature and cause of compositional variation among the alkalic cap lavas of Mauna Kea Volcano, Hawaii. *Contrib. Mineral. Petrol.* 100, 383-397.
- West H. B., Garcia M. O., Gerlach D. C., and Romano J. (1992) Geochemistry of tholeiites from Lanai, Hawaii. *Contrib. Mineral. Petrol.* 112, 520-542.
- West H. B., Gerlach D. C., Leeman W. P., and Garcia M. O. (1987) Isotopic constraints on the origin of Hawaiian lavas from the Maui Volcanic Complex, Hawaii. *Nature* 330, 216-219.
- West H. B. and Leeman W. P. (1987) Isotopic evolution of lavas from Haleakala Crater, Hawaii. *Earth Planet. Sci. Lett.* 84, 211-225.
- Wolfe E. W., Wise W. S., and Dalrymple G. B. (1996) Geology and petrology of Mauna Kea volcano, Hawaii: A study of postshield volcanism. *U.S. Geol. Surv. Prof. Pap.* 1557, in press.
- Wright T. L. (1971) Chemistry of Kilauea and Mauna Loa lava in space and time. *U.S. Geol. Surv. Prof. Pap.* 735, 40.

Wright T. L. and Fiske R. S. (1971) Origin of differentiated and hybrid lavas of Kilauea Volcano, Hawaii. *J. Petrol.* 12, 1-65.

Table 1. Modes for dredged shield lavas from the East Rift Zone of Mauna Kea Volcano, Hawaii

	<u>Olivine</u>		<u>Clinopyroxene</u>		<u>Plagioclase</u>		<u>Orthopyroxene</u>		Groundmass
	ph	mph	ph	mph	ph	mph	ph	mph	
<i>Group 1</i>									
MK 2-1	14.0	5.4	0.0	3.4	0.2	5.2		Tr.	71.8
MK 5-3	9.3	1.0	0.0	2.2	0.2	3.0			84.3
MK 5-13	14.0	3.2	0.0	0.2	0.2	6.8			75.8
MK 6-6	22.0	1.8	0.2	4.2	0.4	9.6			61.8
MK 6-18	5.2	4.6	0.0	0.6	0.0	2.4			87.2
SU-21-64	30.7	2.5	1.8	3.8	2.0	4.6		Tr.	54.6
SU-46-66	14.2	1.3	0.1	3.9	0.0	2.7			77.7
<i>Group 2</i>									
MK 1-3	13.8	8.6	0.0	0.0	0.0	0.0			77.6
MK 1-8	16.4	2.1	0.6	1.6	0.8	2.4			76.1
MK 1-10	16.8	11.0	0.0	0.0	0.0	0.0			72.2
SU-20-64	19.7	1.2	1.6	4.8	4.0	4.9		Tr.	64.0
SU-22-64	11.2	6.3	1.3	4.5	0.5	6.7	2.6	0.1	66.8

Except for MK 5-3, data for MK samples are from Frey et al. [1991]. Modes based on 1000 counts per sample except SU-22-64 which is based on 2200 counts. The grain sizes for phenocrysts (ph), microphenocrysts (mph) and groundmass are > 0.7 mm, 0.1-0.7 mm and < 0.1 mm, respectively. The two groups are defined by differences in major element composition. Tr. indicates 1-3 grains in a 35x20 mm thin section.

Table 2a. Major and trace element contents and Sr, Nd and Pb isotopic ratios of the dredged group 1 shield samples from the East Rift Zone of Mauna Kea, Hawaii

	MK 2-1	MK 5-3	MK 5-13	MK 6-6	MK 6-18	SU-21-64	SU-46-66
SiO ₂	48.68	49.62	49.33	47.98	49.70	47.39	49.00
TiO ₂	2.01	2.07	1.97	1.76	2.06	1.49	1.90
Al ₂ O ₃	10.86	12.47	11.67	10.28	12.28	9.34	11.38
Fe ₂ O ₃	12.18	11.82	11.94	12.29	11.83	12.00	11.76
MnO	0.17	0.17	0.16	0.17	0.17	0.16	0.17
MgO	14.61	10.79	13.23	16.85	11.33	20.32	14.15
CaO	9.12	9.93	9.32	8.11	9.76	7.40	9.04
Na ₂ O	1.69	2.19	1.92	1.69	2.04	1.35	1.86
K ₂ O	0.32	0.34	0.31	0.28	0.33	0.25	0.30
P ₂ O ₅	0.18	0.21	0.19	0.18	0.20	0.15	0.19
Total	99.82	99.58	100.04	99.59	99.70	99.85	99.75
Rb	5.2	5.2	4.9	4.6	4.9	3.6	4.9
Sr	249	267	260	225	274	194	240
Ba	76	69	63	61	63	50	66
Sc	27.4	28.4	27.6	24.7	28.9	22.3	27.0
V	231	255	240	217	246	183	242
Cr	846	627	705	1015	583	1100	727
Co						79.8	62.6
Ni	619	361	533	804	415	1017	620
Zn	113	108	111	114	110	104	112
Ga	17.0	18.6	17.7	15.7	17.9	13.6	17.7
Y	21.4	23.1	21.8	19.8	22.8	17.7	20.5
Zr	126	135	122	110	129	95	121
Nb	11.4	10.0	9.6	9.7	10.2	7.0	9.3
Hf	3.0	3.1	3.1	2.8	3.2	2.24	3.01
Ta						0.36	0.62
Th						0.18	0.49
La	8.48	8.47	8.12	7.47	8.66	5.85	7.75
Ce	23.3	22.5	22.2	19.8	23.2	16.6	22.3
Nd	16.1	16.2	15.1	13.4	16.3	11.9	15.2
Sm	4.17	4.52	4.2	3.98	4.42	3.14	4.03
Eu	1.50	1.54	1.48	1.36	1.57	1.13	1.44
Tb	0.78	0.68	0.78	0.72	0.79	0.53	0.70
Yb	1.72	1.79	1.75	1.73	1.92	1.30	1.62
Lu	0.25	0.26	0.25	0.22	0.27	0.18	0.28
⁸⁷ Sr/ ⁸⁶ Sr	0.703614	0.703578	0.703573	0.703500	0.703545	0.703556	0.703525
¹⁴³ Nd/ ¹⁴⁴ Nd	0.512957	0.512979 ^M	0.512974	0.513006	0.512989	0.512989	0.512980
²⁰⁶ Pb/ ²⁰⁴ Pb	18.555	18.309	18.300	18.169	18.326	18.311	18.299
²⁰⁷ Pb/ ²⁰⁴ Pb	15.477	15.449	15.445	15.470	15.468	15.452	15.488
²⁰⁸ Pb/ ²⁰⁴ Pb	38.123	37.897	37.888	37.801	37.948	37.909	37.993

Major element contents are in weight percent and trace element contents are in parts per million.

Table 2b. Major and trace element contents and Sr, Nd and Pb isotopic ratios of the dredged group 2 shield samples from the East Rift Zone of Mauna Kea, Hawaii

	MK 1-3	MK 1-10	MK 1-8	SU-20-64	SU-22-64
SiO ₂	48.76	48.99	50.76	48.18	47.28
TiO ₂	2.11	2.14	2.70	2.02	2.44
Al ₂ O ₃	10.10	10.27	11.34	10.17	11.58
Fe ₂ O ₃	12.42	12.44	12.86	12.46	13.07
MnO	0.17	0.17	0.17	0.17	0.17
MgO	15.76	15.43	10.93	16.85	13.61
CaO	7.68	7.77	7.95	7.52	8.98
Na ₂ O	1.86	1.90	2.29	1.85	2.02
K ₂ O	0.42	0.43	0.63	0.39	0.58
P ₂ O ₅	0.24	0.24	0.34	0.25	0.28
Total	99.52	99.78	99.97	99.86	100.01
Rb	7.0	6.8	11.1	5.7	9.2
Sr	241	249	273	235	351
Ba	90	87	133	85	147
Sc	24.0	24.3	25.4	23.3	25.4
V	232	236	276	231	242
Cr	927	939	593	862	675
Co				73.1	67.7
Ni	729	716	441	821	521
Zn	122	121	145	119	129
Ga	16.6	16.9	19.4	16.5	19.0
Y	25.4	25.7	34.6	26.1	24.0
Zr	159	160	234	157	180
Nb	13.2	13.4	18.8	11.2	18.3
Hf	3.8	3.7	5.6	3.73	4.21
Ta				0.61	1.09
Th				0.5	0.99
La	10.8	10.9	16.2	10.1	14.6
Ce	29.6	30.0	41.1	29.9	41.0
Nd	19.0	19.6	27.5	19.4	24.3
Sm	5.02	4.99	7.22	5.05	5.89
Eu	1.71	1.72	2.44	1.71	1.95
Tb	0.78	0.84	0.98	0.88	0.83
Yb	1.99	2.04	2.83	2.01	1.76
Lu	0.26	0.27	0.40	0.29	0.26
⁸⁷ Sr/ ⁸⁶ Sr	0.703680	0.703701	0.703660	0.703615 ^M	0.703694
¹⁴³ Nd/ ¹⁴⁴ Nd	0.512936	0.512944	0.512938	0.512986	0.512954
²⁰⁶ Pb/ ²⁰⁴ Pb	18.418	18.396	18.367	18.244	18.542
²⁰⁷ Pb/ ²⁰⁴ Pb	15.505	15.465	15.443	15.440	15.472
²⁰⁸ Pb/ ²⁰⁴ Pb	38.174	38.034	37.967	37.824	38.132

Major element contents are in weight percent and trace element contents are in parts per million. See text for discussion of accuracy and precision. Co and Ta data are not reported for MK samples because they were ground in tungsten carbide. Superscript M indicates isotopic data obtained at MIT. All other isotopic data were obtained at Woods Hole Oceanographic Institution.

Table 3a. Major element contents of the glasses in dredged group 1 shield samples from the East Rift Zone of Mauna Kea, Hawaii

	MK 2-1	MK 6-6	MK 6-18	SU-46a-66	SU-46b-66	SU-46c-66	SU-46d-66	SU-21-64
SiO ₂	51.00	51.98	51.84	51.40	50.60	51.60	51.20	52.80
TiO ₂	2.95	2.69	2.44	2.33	2.37	2.40	2.36	2.86
Al ₂ O ₃	13.61	13.69	14.13	14.10	14.20	14.00	14.10	13.40
FeO	11.92	10.79	10.87	10.50	10.50	10.50	10.60	11.20
MnO				0.16	0.15	0.16	0.16	0.18
MgO	6.31	6.49	6.68	6.90	6.75	6.90	6.89	6.05
CaO	10.64	10.90	10.70	10.90	10.90	11.30	11.10	10.00
Na ₂ O	2.36	2.37	2.28	2.44	2.55	2.52	2.49	2.16
K ₂ O	0.45	0.42	0.38	0.36	0.37	0.37	0.37	0.45
P ₂ O ₅	0.32	0.33	0.29	0.21	0.20	0.21	0.21	0.31
S	0.103	0.029	0.114	0.042	0.034	0.048	0.045	0.123
Total	99.66	99.69	99.72	99.34	98.62	100.01	99.53	99.53

In weight percent

Table 3b. Major element contents of the glasses in dredged group 2 shield samples from the East Rift Zone of Mauna Kea, Hawaii.

	MK 1-8	MK 1-10	SU-20-64	SU-22a-64	SU-22b-64
SiO ₂	52.49	52.58	52.50	49.40	49.50
TiO ₂	3.18	2.79	3.19	3.36	3.67
Al ₂ O ₃	13.66	13.72	13.80	14.80	13.60
FeO	10.87	10.28	11.20	11.30	11.80
MnO			0.16	0.17	0.16
MgO	5.26	6.70	5.38	5.60	5.44
CaO	9.22	10.41	9.40	10.10	9.90
Na ₂ O	2.87	2.45	2.90	3.00	3.03
K ₂ O	0.75	0.51	0.59	0.83	0.79
P ₂ O ₅	0.41	0.35	0.36	0.40	0.41
S	0.074	0.101	0.081	0.099	0.102
Total	98.78	99.89	99.56	99.06	98.40

In weight percent. Data for MK samples from Garcia et al. [1989b]. Data for SU samples from Table B of Moore and Clague [1992]. Multiple analyses for SU-46-66 and SU-22-64 are separate glass chips.

Figure Captions

- Fig. 1. Dredge locations (+) on the submarine east rift (dashed line) of Mauna Kea Volcano. Bathymetric contour interval is 1 km. On the subaerial surface of Mauna Kea the unshaded region indicates outcrops of the postshield basaltic Hamakua Volcanics and the shaded region indicates outcrops of Laupahoehoe Volcanics which are dominantly composed of evolved postshield alkalic lavas such as hawaiites and mugearites. Open triangles indicate volcano summits. Inset shows location of volcanos on the island of Hawaii. Also indicated is the drill hole location of the Hawaiian Scientific Drilling Project (HSDP).
- Fig. 2a. Frequency distribution of olivine core compositions in dredged Mauna Kea basalts. Each square represents one grain and is an average of 2-5 analyzed points.
- Fig. 2b. Forsterite content of olivine cores from Mauna Kea dredged basalts (open circles). Note the wide range of compositions in each rock. Ranges shown by dashed lines at relatively low Fo content are for olivines calculated to be in equilibrium with the glass (glass analyses are not available for samples 1-3, 5-3 and 5-13); ranges shown by solid lines at relatively high Fo content are for olivines calculated to be in equilibrium with a melt having the whole rock composition (ranges indicate $K_D^{\text{Fe/Mg}} = 0.3 \pm 0.03$ with $\text{Fe}^{+2} = 0.9 \times \text{total iron}$).
- Fig. 3. Core to rim compositional zoning of clinopyroxene, orthopyroxene and plagioclase phenocrysts in Group 1 sample SU-21-64. $\text{Mg\#} = 100 \text{ Mg}/(\text{Mg}+\text{Fe})$ with all iron as Fe^{+2} . Distances are measured from the core at 0.00 mm. Except for the outermost rim these phenocrysts are reversely zoned; in fact the cores formed in equilibrium with melts that were more evolved than the glass in this sample. Analytical uncertainty in electron microprobe determinations of Mg# and An% are similar to the symbol size. Data from Yang, in preparation.

Fig. 4. Total alkalis versus SiO₂ content (all in wt.% with all iron as FeO) for Mauna Kea lavas. All the submarine shield lavas (whole rocks and glasses, open and filled squares, respectively) are tholeiitic basalts. The solid lines connect analyses of the same whole-rock samples (SU-20-64, SU-21-64 and SU-22-64) analyzed in different laboratories, (Table 2, this paper and table B of Moore and Clague, 1992). In each case, our data are higher in SiO₂ and lower in Na₂O + K₂O. Glass data from Garcia et al. (1989) and Moore and Clague (1992, Table B). The two glasses on the alkalic-tholeiitic dividing line are analyses of SU-22-64 which is transitional to alkalic basalt. The subaerial, postshield, basaltic substage (Hamakua Volcanics) includes tholeiitic and alkalic basalts (Frey et al., 1991). The youngest Mauna Kea lavas form the postshield hawaiitic substage (Laupahoehoe Volcanics). The ALKALIC-THOLEIITIC boundary line is from Macdonald and Katsura (1964).

Fig. 5. MgO variation diagram (wt.%) for Mauna Kea shield lavas and associated glasses dredged from the east rift. Whole-rock data for Groups 1 and 2 and sample SU-22-64 are in table 2. Groups 1 and 2 have distinct trends on the Na₂O, CaO, TiO₂, K₂O and FeO panels. Glass data are from Garcia et al. (1989) and Table B of Moore and Clague (1992).

Fig. 6. Left: Abundance of Nb versus Zr, La and Sr contents (all in ppm). Symbols are as in Fig. 5. Note that Group 2 lavas have lower Sr/Nb.

Right: MgO (wt.%) versus Ni and Sc contents (ppm). Symbols are as in Fig. 5. Relative to Group 1 lavas, Group 2 lavas have low Sc contents. The MgO-Ni trend defined by the whole-rocks intersects the MgO-Ni trend of olivine core compositions (+) in these rocks at ~3000 ppm Ni and 48% MgO.

Fig. 7. Primitive mantle-normalized trace element abundances. Normalizing values from Sun and McDonough (1989). Group 2 samples and SU-22-64 connected by solid lines have higher abundances of the most highly incompatible elements, but they have

relative depletions in Sr.

Fig. 8. Abundance ratios of incompatible elements (La/Yb, Sr/Nb, La/Nb, Zr/Nb, La/Ce and Ba/Nb) which have been used as intershield discriminants. Submarine samples from the east rift of Mauna Kea are indicated by the same symbols as in Fig. 5. Except for La/Yb, the Group 1 and 2 submarine lavas overlap with the subaerial tholeiites exposed on the east flank of Mauna Kea (data from Frey et al., 1991). Fields for Kilauea and Mauna Loa from BVSP (1981). The Ti/Eu-Sr/Ce panel indicates that Group 2 lavas trend to low Ti/Eu and Sr/Ce; a trend consistent with fractionation of plagioclase and Fe-Ti oxides. Distinctive samples discussed in the text are labelled. Error bars indicate one standard deviation. In the left panels error bars are similar to the symbol size.

Fig. 9. $^{143}\text{Nd}/^{144}\text{Nd}$ versus $^{87}\text{Sr}/^{86}\text{Sr}$ comparing Mauna Kea submarine shield lavas (symbols are as in Fig. 5) with Mauna Kea subaerial lavas (Hamakua and Laupahoehoe). The subaerial Hamakua tholeiitic and alkalic basalts have similar $^{87}\text{Sr}/^{86}\text{Sr}$ and $^{143}\text{Nd}/^{144}\text{Nd}$ (Kennedy et al., 1991). The submarine Group 1 lavas define a negative trend which overlaps with the Hamakua field, but Group 2 lavas and SU-22-64 extend to lower $^{143}\text{Nd}/^{144}\text{Nd}$ and higher $^{87}\text{Sr}/^{86}\text{Sr}$. Error bars in lower left are ± 1 sigma.

Fig. 10. $^{207}\text{Pb}/^{204}\text{Pb}$ and $^{208}\text{Pb}/^{204}\text{Pb}$ versus $^{206}\text{Pb}/^{204}\text{Pb}$ for Mauna Kea submarine shield lavas (symbols are as in Fig. 5). The two groups overlap in Pb isotopic ratios, and they encompass the $^{206}\text{Pb}/^{204}\text{Pb}$ and $^{208}\text{Pb}/^{204}\text{Pb}$ range in Mauna Kea subaerial lavas, (Hamakua and Laupahoehoe) (Kennedy et al., 1991). As in incompatible element abundance ratios (Fig. 8) and isotopic ratios of Sr and Nd (Fig. 9) Group 1 samples MK 2-1 and MK 6-6 are distinct from other Group 1 samples. Error bars in upper left are ± 1 sigma.

Fig. 11. Expanded MgO variation diagrams (wt.%) showing that the compositions of Group 1 whole-rocks (open squares) are consistent with addition of olivine in variable amounts

(dashed line) to the most mafic Group 1 glasses (shaded field). Symbols as in Fig. 5. This olivine has a composition (MgO content of ~48% and SiO₂ content of 40% (~Fogg)), similar to the mean olivine composition in these whole-rocks (Fig. 2a). Similarly, the compositionally most extreme Group 2 rock, sample 1-8, has a whole-rock composition that is consistent with addition of olivine (~Fogg) to the evolved 1-8 glass (solid line labelled MK 1-8). In contrast, the whole-rock compositions of samples SU-22-64 cannot be explained by addition of olivine to the coexisting glass (solid line labelled SU-22-64).

Fig. 12. ⁸⁷Sr/⁸⁶Sr versus ²⁰⁶Pb/²⁰⁴Pb plot comparing data for Mauna Kea submarine shield lavas with data for other Hawaiian shields: Koolau (Stille et al., 1983; Roden et al., 1994), Lanai (West and Leeman, 1987), Kahoolawe (West and Leeman, 1987; Leeman et al., 1994), Haleakala (Chen et al., 1991), West Maui (Tatsumoto et al., 1987), Mauna Loa (Kurz and Kammer, 1991), Kilauea (Tatsumoto, 1978; Stille et al., 1986) Kurz, unpublished) and Loihi (Staudigel et al., 1984; Garcia et al., 1993). Also shown in dashed fields are data for Mauna Kea subaerial lavas, Hamakua and Laupahoehoe (Kennedy et al., 1991). Group 1 samples MK 2-1 and MK 6-6 discussed in text are labelled.

Fig. 13. ⁸⁷Sr/⁸⁶Sr versus Sr/Nb and La/Nb comparing data for Mauna Kea shield lavas with fields for other Hawaiian shields: Koolau (Frey et al., 1994; Roden et al., 1994), Lanai (West et al., 1987; West et al., 1992), Kahoolawe (Leeman et al., 1994), Haleakala (Chen et al., 1991), Mauna Loa (1981; Kurz and Kammer, 1991), Kilauea (BVSP, 1981; Stille et al., 1986; Kurz, unpublished) and Loihi (Frey and Clague, 1983; Staudigel et al., 1984; Garcia et al., 1993). Rectangular fields are shown for Lanai, Mauna Loa and Kilauea because the same lavas have not been analyzed for trace elements and isotopic ratios. The relatively low Sr/Nb in sample SU-22-64 and Group 2 Mauna Kea lavas reflects an evolved melt component which has fractionated

plagioclase.

Fig. 14. $^{206}\text{Pb}/^{204}\text{Pb}$ versus Zr/Nb plot for Hawaiian shield tholeiites: Koolau (Frey et al., 1994; Roden et al., 1994), Kahoolawe (Leeman et al., 1994), Haleakala (Chen et al., 1991), Mauna Kea (this study), Mauna Loa (Rhodes and Hart, unpublished), Kilauea (Chen et al., 1996; Rhodes and Hart, unpublished) and Loihi (Frey et al., 1983; Staudigel et al., 1984; Garcia et al., 1993). A general inverse trend is defined by the entire data set and by most of the submarine Mauna Kea samples. Inset shows in detail the variation of Mauna Kea submarine lavas (symbols as in Fig. 5). Sample MK 6-6 is not on the trend defined by other samples.

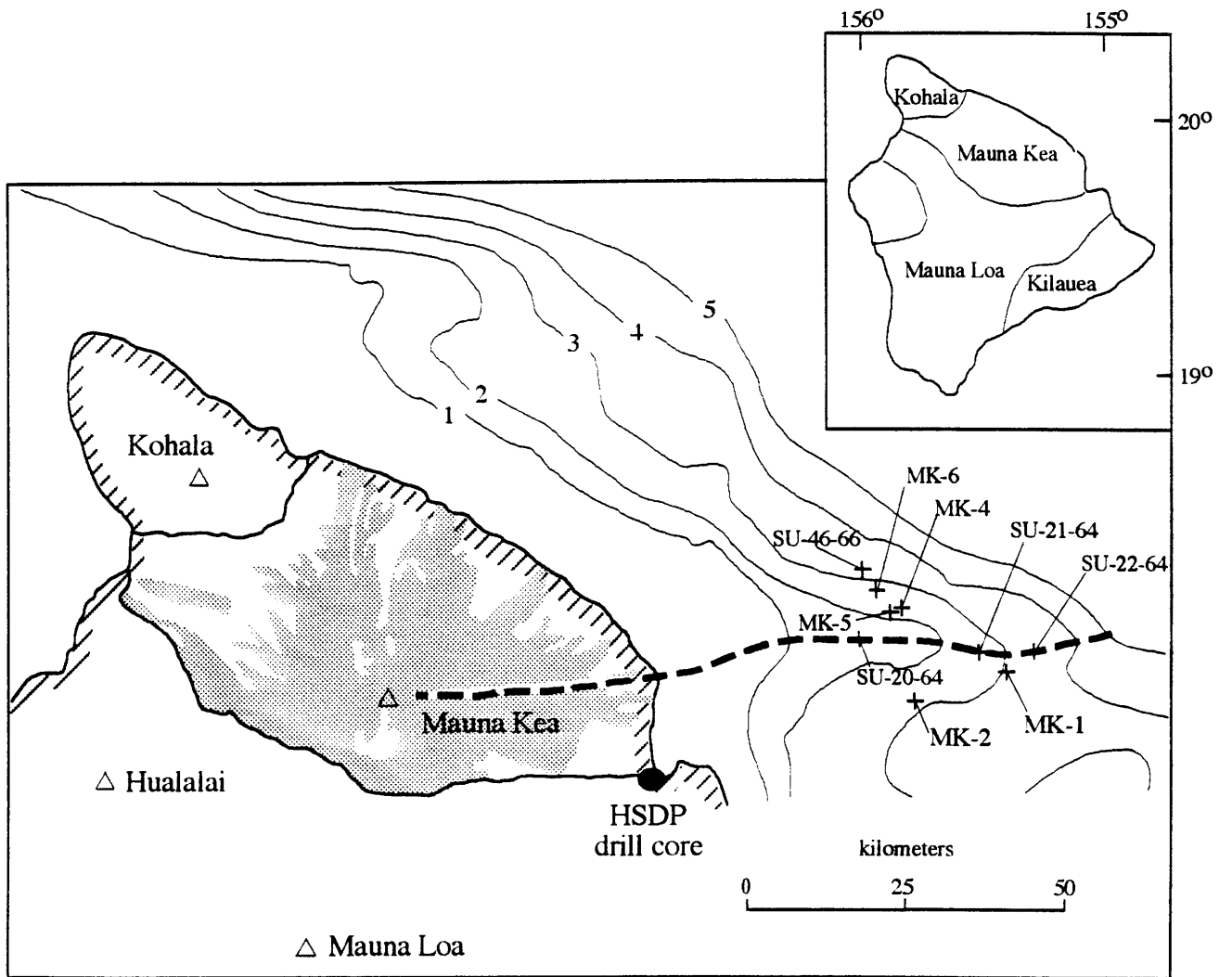


Fig. 1

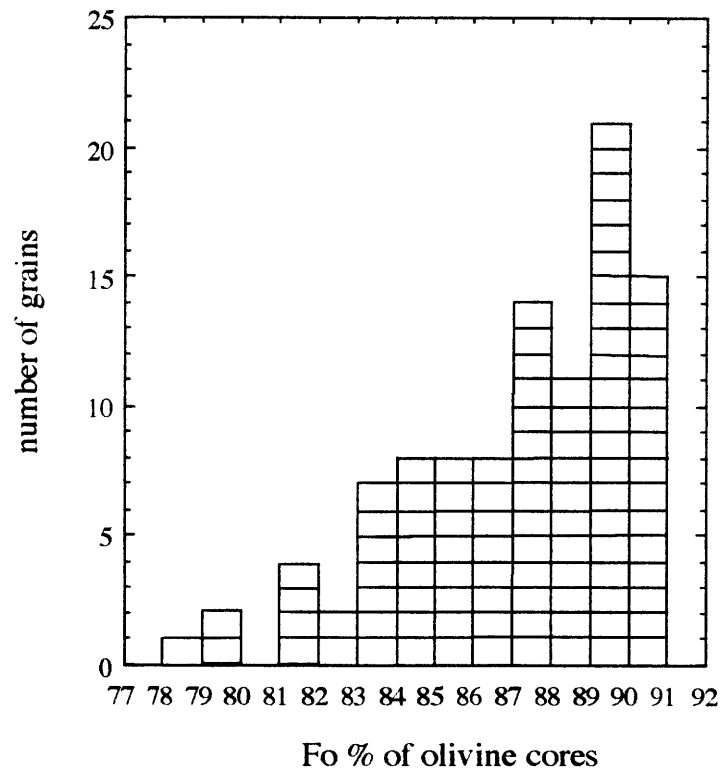


Fig. 2a

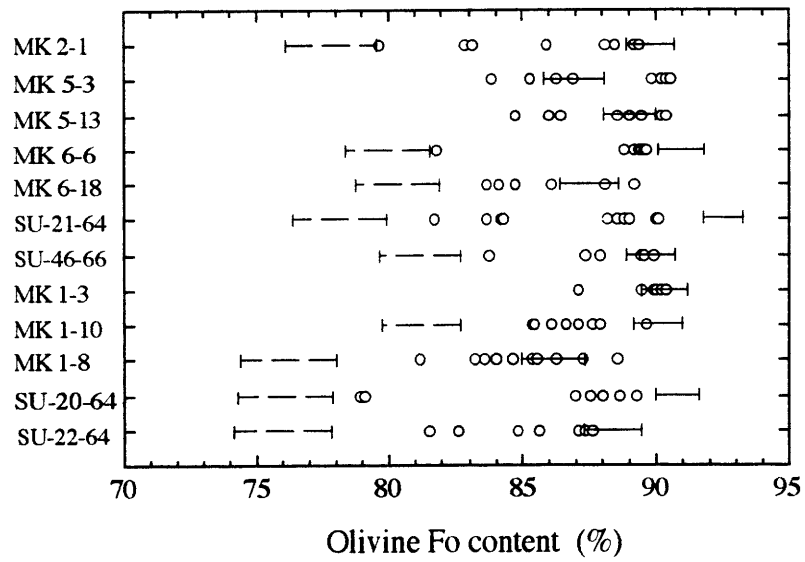


Fig. 2b

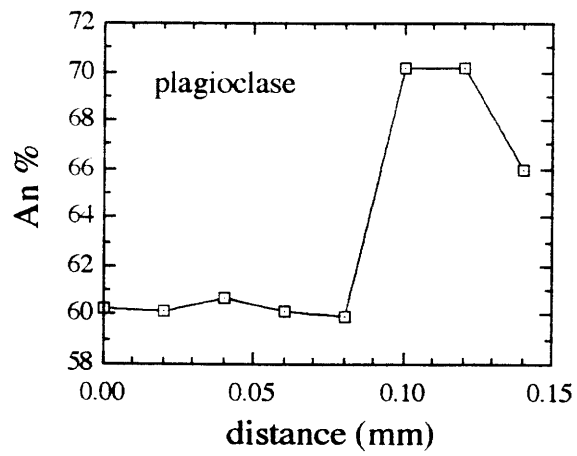
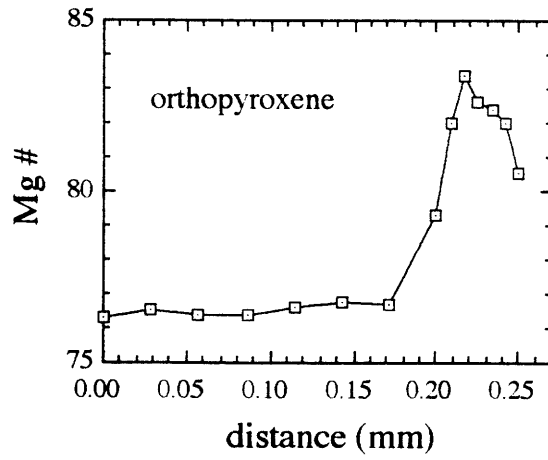
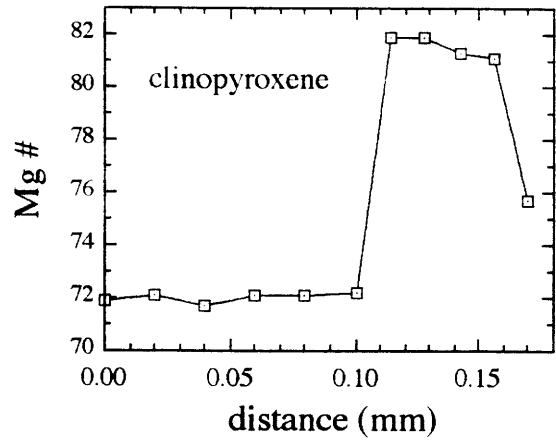


Fig. 3

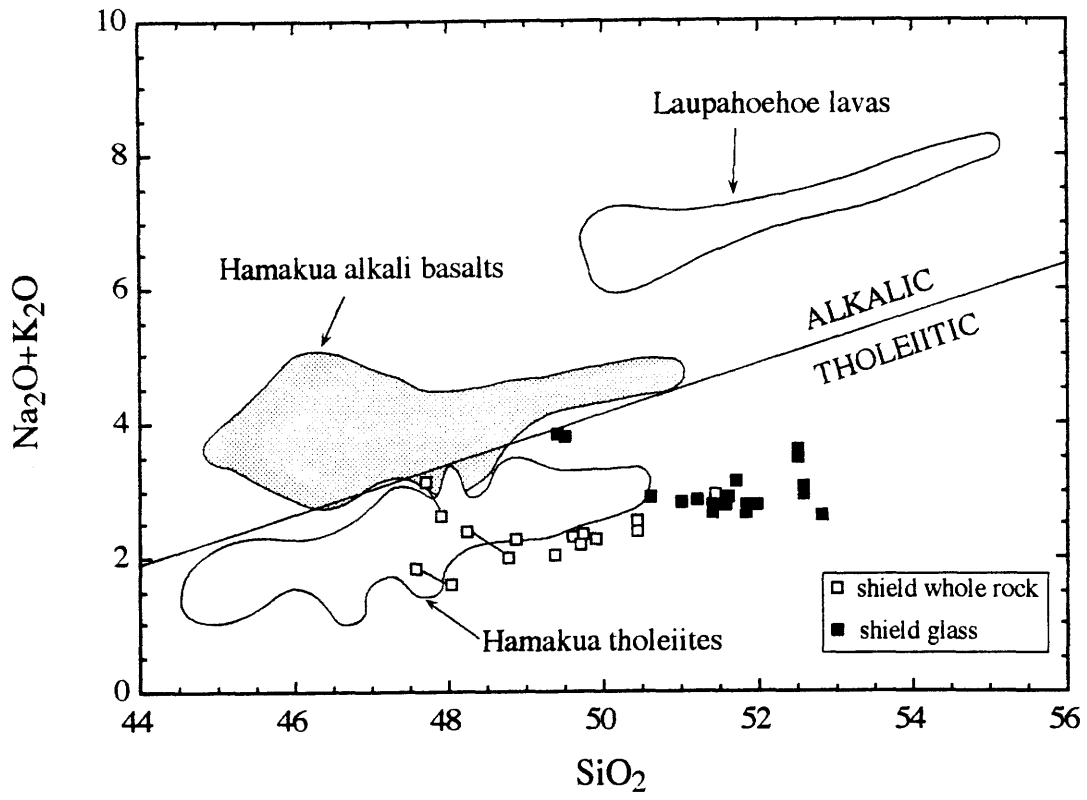


Fig. 4

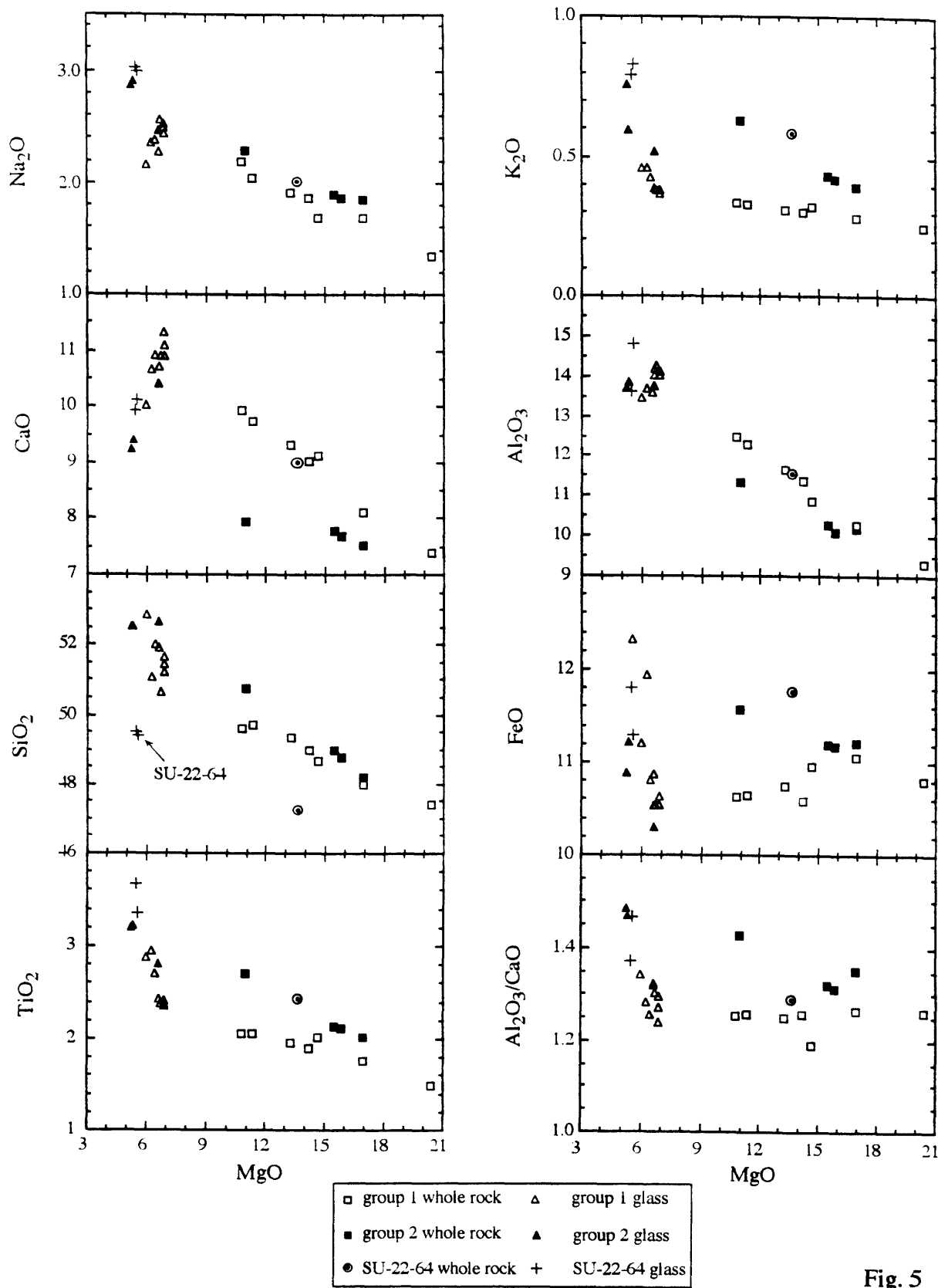


Fig. 5

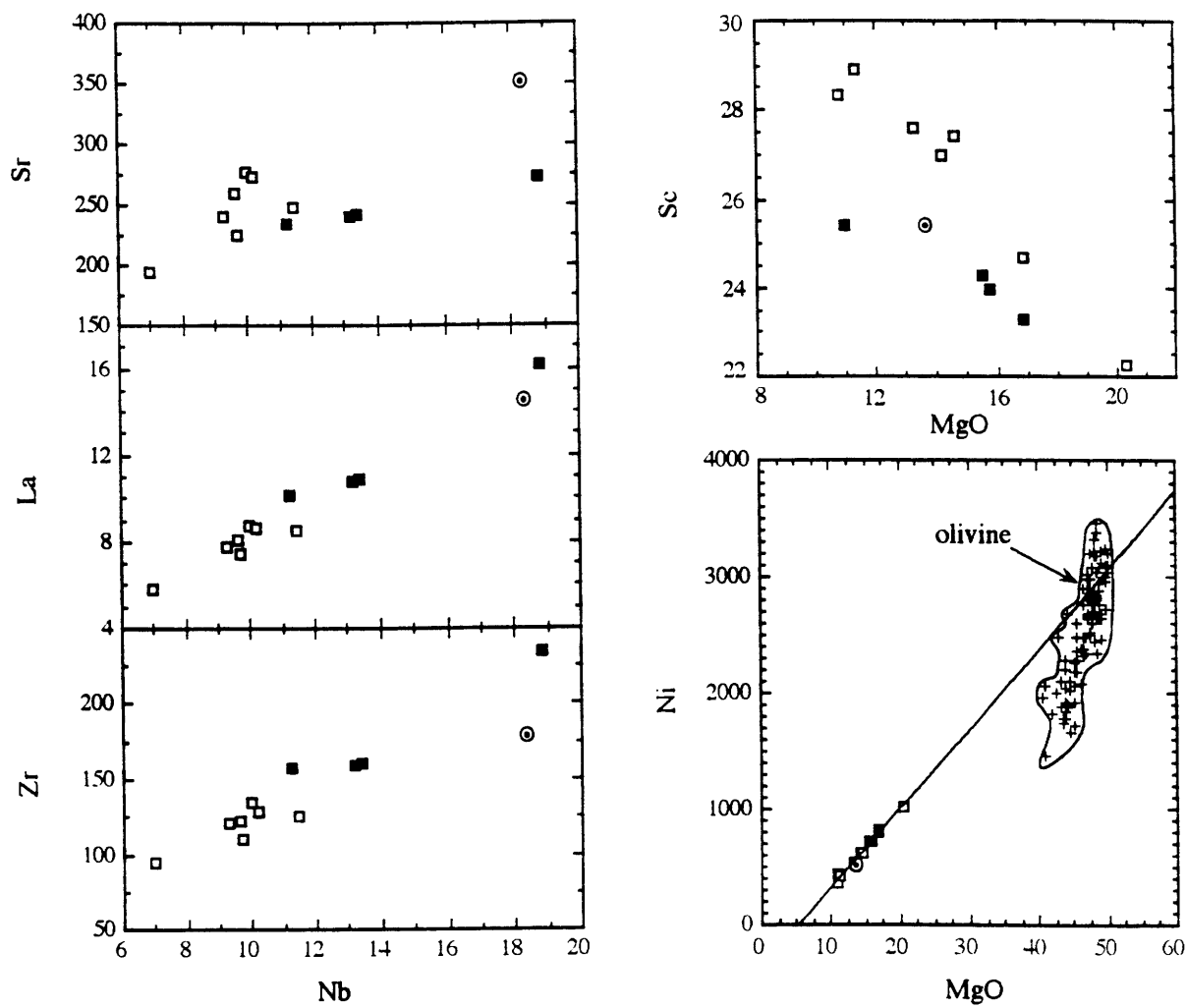


Fig. 6

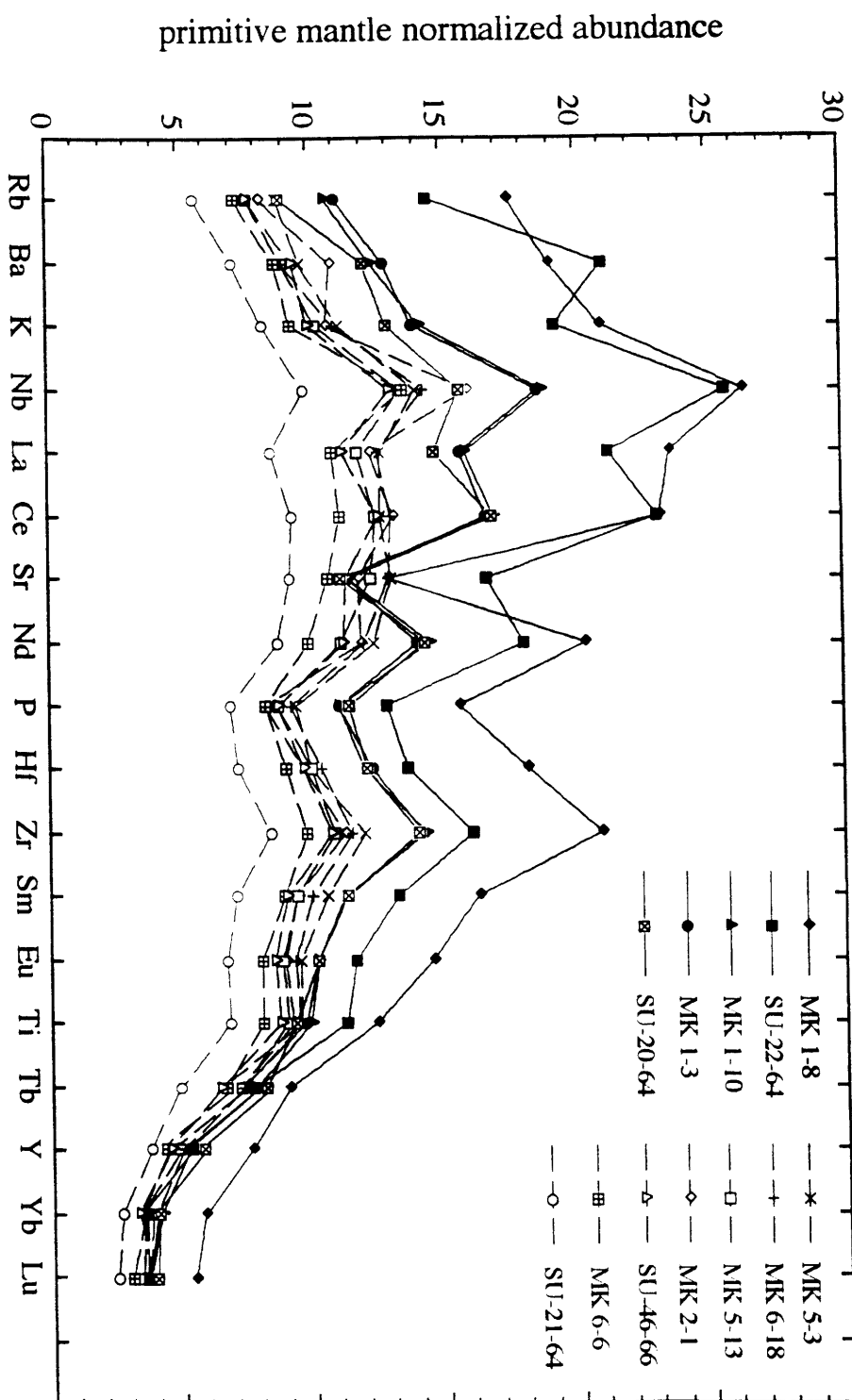


Fig. 7

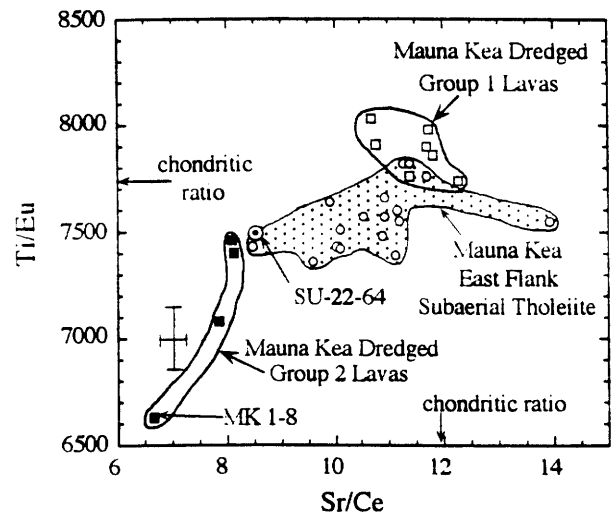
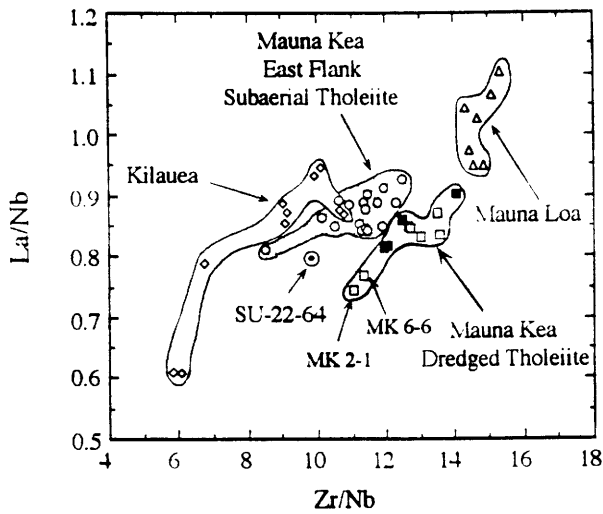
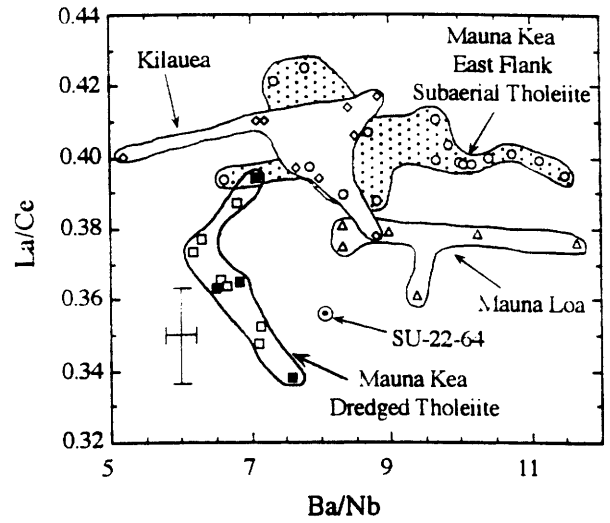
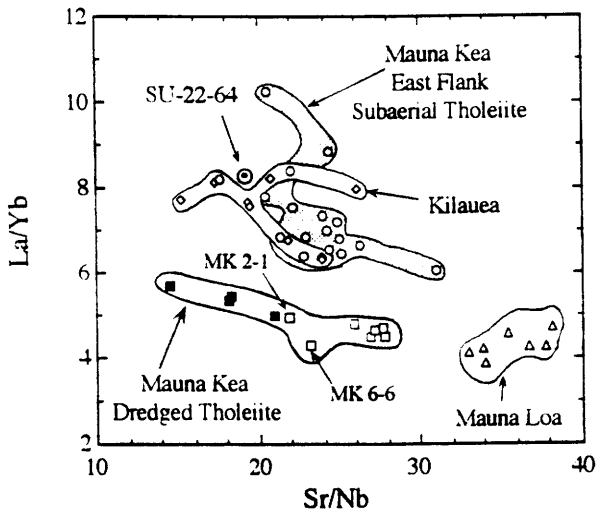


Fig. 8

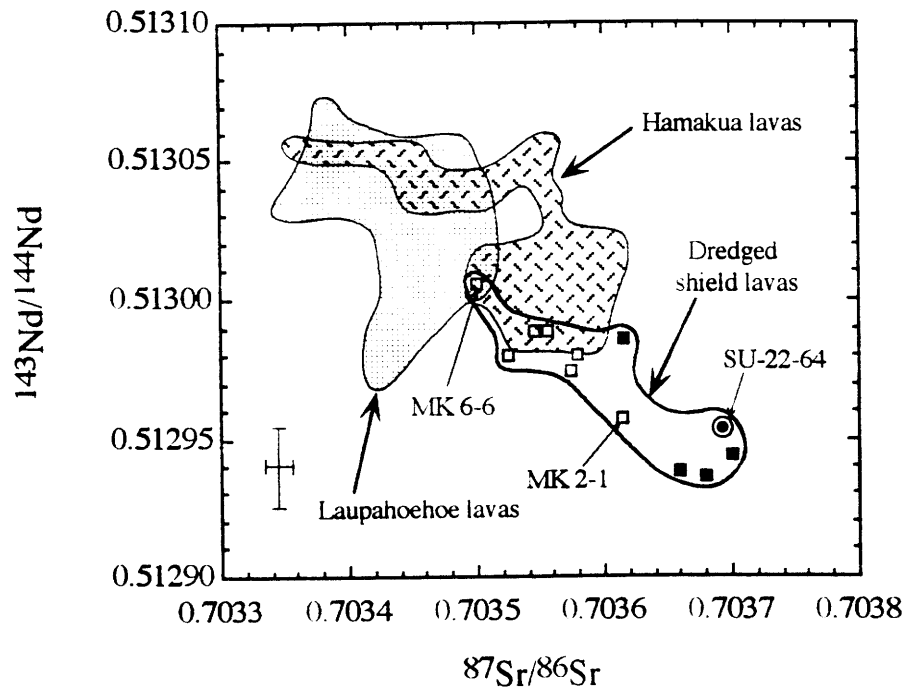


Fig. 9

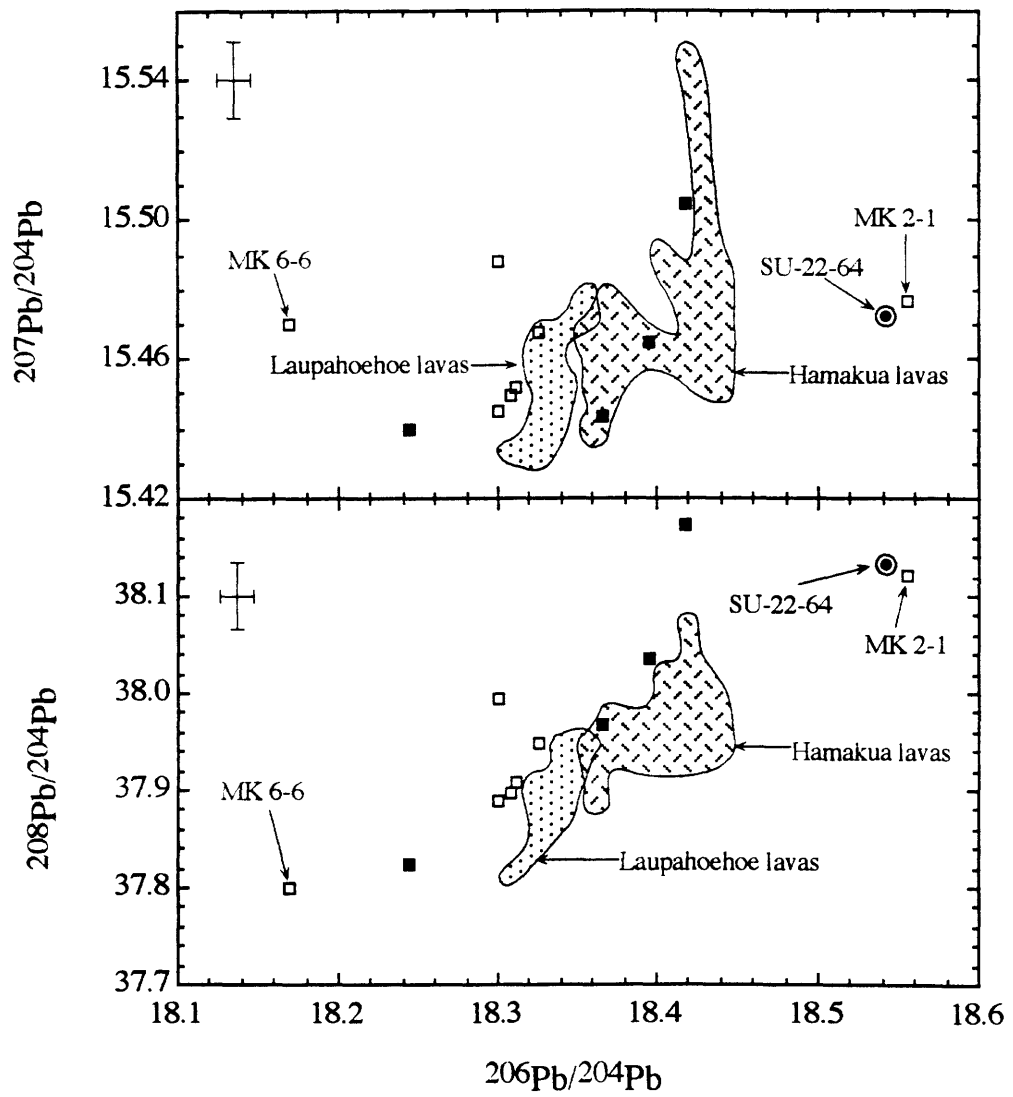


Fig. 10

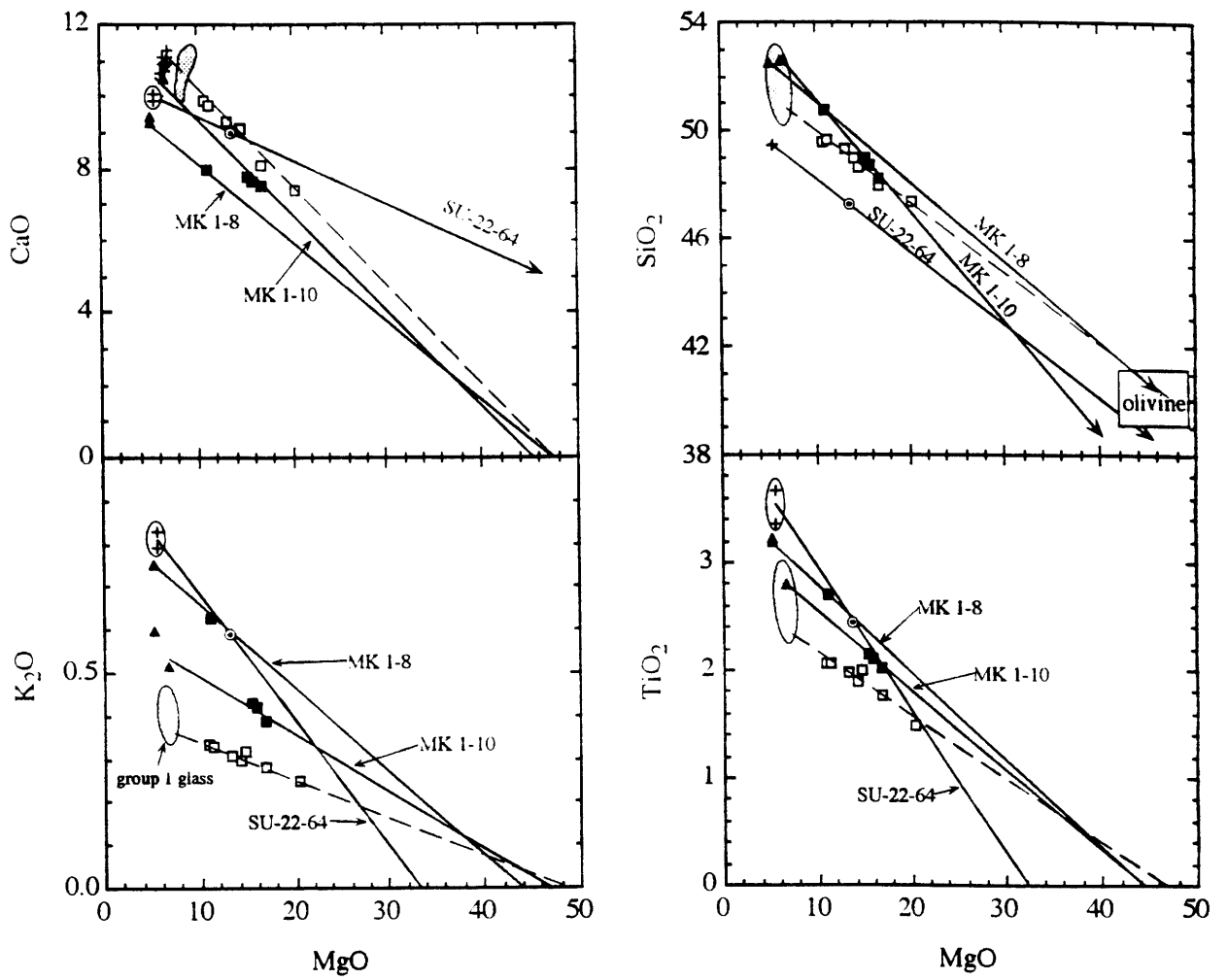


Fig. 11

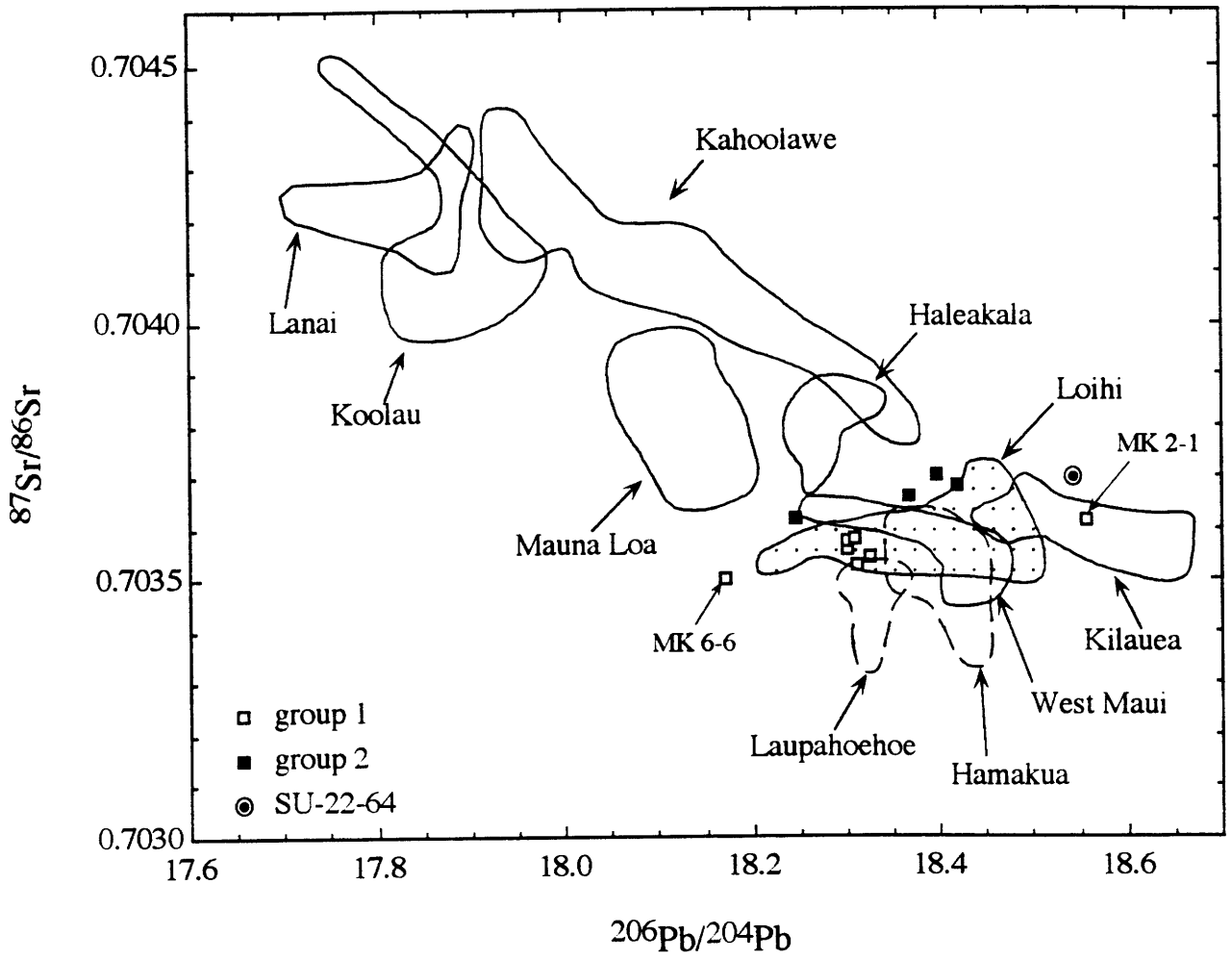


Fig. 12

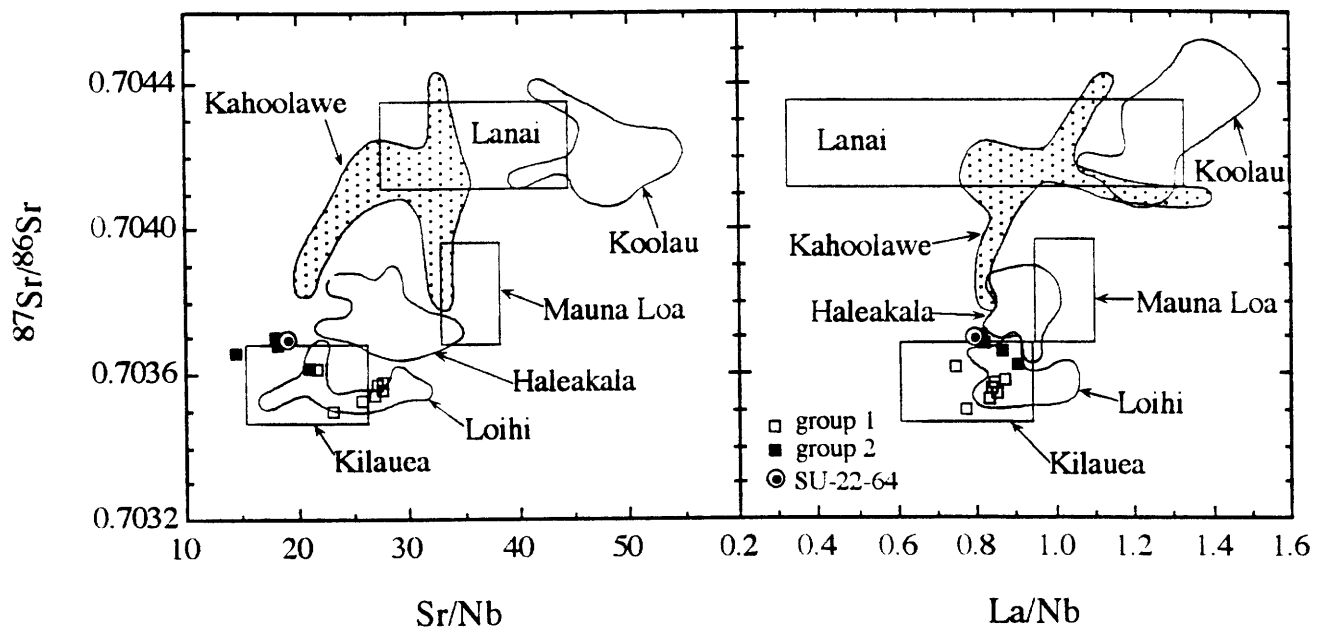


Fig. 13

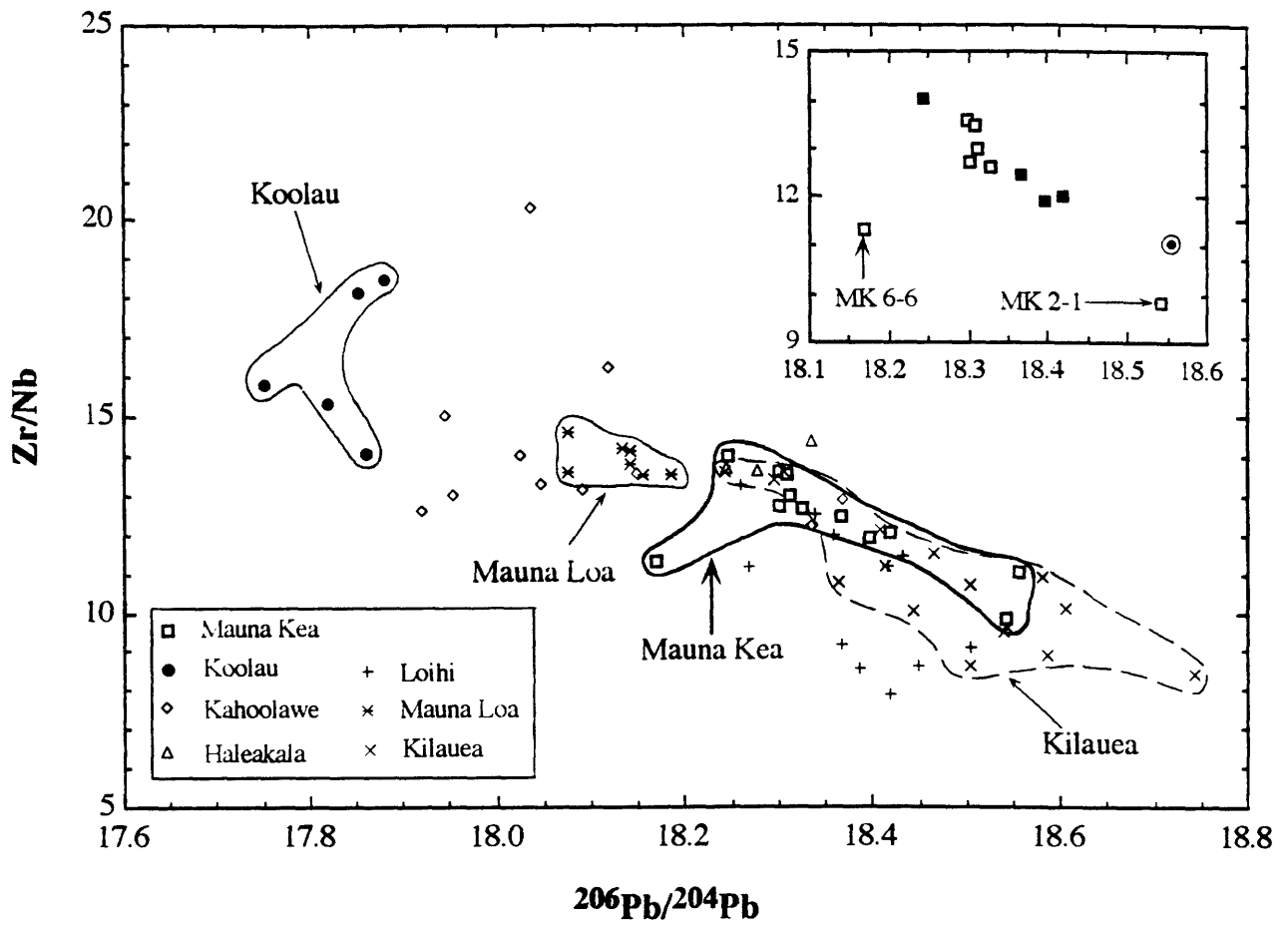


Fig. 14

CHAPTER THREE

Mineral Chemistry of Submarine Lavas from Mauna Kea, Hawaii: Implications for processes at rift zones

ABSTRACT

Submarine lavas erupted at the east rift of the Mauna Kea volcano, Hawaii contain olivine (ol), plagioclase (plag), augite (aug) and orthopyroxene (opx) crystals. All the olivines are normally zoned. In contrast, plagioclase, augite and orthopyroxene have more than one episode of reverse zoning. A mixing model of evolved magma chambers containing plagioclase, augite and orthopyroxene replenished by more mafic magmas with only olivine crystals can explain the difference in zonation between olivine and other crystals. Plagioclase and pyroxenes in each samples have distinct zoning profiles and compositional ranges indicating that these samples were derived from isolated magmas chambers which had undergone distinct fractionation and mixing histories. Some magma chambers were buffered at the $ol+melt \rightleftharpoons plag+aug+opx$ reaction point by constant intrusions of more mafic magmas. Some magma chambers evolved beyond this reaction point due to low magma supply rate. The most Fe-rich augite composition are in equilibrium with an evolved melt containing Mg# of 33 which are rarely erupted during shield building stage. Mass balance between whole-rock, glass and olivine compositions shows that these lavas contain cumulated olivine. The difference in the petrographic texture between these submarine lavas and HSDP cores are explained by the difference in magma supply rate. The magma reservoirs at the distal end of the rift zones have lower magma supply rate than those close to the summit of the volcano.

INTRODUCTION

Hawaiian shields grow by summit and rift eruptions. During the main shield stage, a shallow magma chamber fed by a central conduit is maintained at depths of 2~4 km (Ryan et al., 1981). After varying periods of storage in this chamber, magmas are erupted at the summit or injected into the prominent rift zones that radiate from the summit. Subsequently, magmas are erupted along these rift zones from localized vents at varying distances, often tens of kilometers from the summit. Within this magma plumbing system there are abundant opportunities for magma mixing (Fig. 1). For example, Rhodes (1988) inferred that the compositional homogeneity of summit lavas erupted at Mauna Loa indicates eruption from a long-lived, steady state summit magma reservoir with buffering of the erupted magma composition at the reaction point of $ol+melt=opx+cpx+plag$. This buffering reflects a balance between differentiation and frequent magma replenishment of the reservoir. Magma mixing is also an important rift zone process. Because shield-stage magmatism is episodic, there are periods of decreasing magma supply when pockets of magma become isolated at various depths within the rift zones. Evolved magma compositions with relatively low MgO contents form as these pockets cool and differentiate. Some of these evolved magmas may proceed beyond the reaction point involving olivine and melt. When magma supply rate increases, new magma migrates from the summit reservoir or conduit into rift zones where it can mix with residual evolved magmas (Murata and Richter, 1966; Wright and Fiske, 1971; Garcia et al., 1992; Helz and Wright, 1992; Clague et al., 1995). Also in apparently rare instances, mixing occurs between shield magmas associated with different but adjacent shields, such as Kilauea and Mauna Loa (Rhodes et al., 1989).

Most of the well documented cases of magma mixing among Hawaiian lavas are for lavas erupted at the active volcanoes, Kilauea and Mauna Loa. Because older shields are not well exposed, there are few combined studies of lavas and mineral compositions for shield stage lavas from other Hawaiian volcanoes. In the future, however, the best long-term

recorded of shield growth will emerge from the Hawaiian Scientific Drilling Project (HSDP). To date, drilling has penetrated to a depth of 776 meters into the Mauna Kea shield, and future drilling is planned to reach depths of 4 to 5 km. Apparently, lavas dredged from the submarine east rift of Mauna Kea are slightly older and geochemically distinct from the oldest Mauna Kea lavas recovered during phase 1 of HSDP (chapter four; Eiler et al., 1996; Lassiter et al., 1996; Sharp et al., 1996). In addition, the submarine dredged lavas erupted more distant (~30-50 km) from the summit than the HSDP site. In chapter two, the bulk compositions of these dredged lavas and preliminary compositional data of their minerals show that although these lavas have high MgO contents (10.79 to 20.32%), they formed by complex magma mixing processes. In this chapter, I use petrography and the complex compositional zonation of pyroxenes and plagioclase in these submarine lavas dredged from the east rift of Mauna Kea, Hawaii to document evidence for replenishment of magma reservoirs containing highly evolved lavas by multiple intrusions of more mafic magmas. Evidence for highly evolved magmas are augite core compositions which equilibrated with andesitic (Mg# ~ 33) even rhyolitic (Mg# ~ 30) melts. Abundances and compositions of olivine indicate that the whole rocks are mixtures of melts and exotic olivine. Sample SU-22-64 with an unusually low SiO₂ content contains the most abundant orthopyroxene (3%), and it reflects mixing and fractionation at relatively higher pressure. In this sample, the augite and olivine that rim orthopyroxene crystallized when melt ascended to lower pressure. The distinct petrographic textures in these submarine lavas and HSDP Mauna Kea lavas may reflect different magma recharging rates in magma reservoirs on the east rift which were located at different distances from the summit of the volcano.

SAMPLES

Sampling localities, abundances of major and trace elements and Sr, Nd and Pb isotopic ratios of twelve samples dredged from the east rift of Mauna Kea volcano, Hawaii are reported in chapter 2. These submarine samples are pillow lavas with quenched glassy rims. They were

classified into two groups based on their chemical and isotopic compositions. These two groups define distinct trends in MgO variation diagrams and were explained by olivine accumulation into geochemically different melts. This chapter presents new data for olivine compositions from six samples. Five of these six samples, including two group 1 samples, SU21-64 and MK2-1, two group 2 samples, SU20-64 and MK1-8, and a sample with an unusually low SiO₂ content, SU-22-64, were selected for detailed study of mineral compositions.

ANALYTICAL TECHNIQUES

Olivine, plagioclase, augite and orthopyroxene were analyzed with the 4-spectrometer JEOL 733 Superprobe at MIT, using 15 keV accelerating voltage, 10 nA beam current and a beam size of 1 μ m. Data were reduced using Bence and Albee (1968) matrix corrections with the modifications of Albee and Ray (1970). Compositions were determined on core to rim traverses across orthopyroxene, augite and plagioclase. The typical distance between two analysis points was usually $\leq 10 \mu$ m. Because olivine is not complexly zoned, only the cores and rims were analyzed. Analytical precision for the oxides of major elements were reported in Juster and Grove (1989). The reproducibilities were within ± 0.2 for the Mg# of pyroxenes and ± 0.3 for the An content in plagioclase. All analyses are consistent with mineral stoichiometry. For example, pyroxene analyses have cation numbers within a range of 4.00 ± 0.02 , mostly within 4.00 ± 0.01 , on a 6 oxygen basis.

PETROGRAPHY AND MINERAL COMPOSITIONS

The five studied samples contain olivine, spinel, plagioclase, augite and orthopyroxene. The proportions of phenocryst (> 0.7 mm) and microphenocryst (0.7~0.1 mm) in these samples are listed in the Table 1 of chapter 2. Olivine is the most abundant phenocryst and microphenocryst (18-33 vol%). Plagioclase and augite usually occur as microphenocrysts with plagioclase (3-9 vol%) slightly more abundant than augite (2-6 vol%). Orthopyroxene is rare,

1-5 grains in each sample, except for SU-22-64 which has 3% orthopyroxene.

Olivine occurs as a variety of crystal forms, from euhedral to resorbed and skeletal; most are euhedral to subhedral (Table 1). Although crystallized as single grains, multigrain aggregates are common. In 7 of 12 samples, 15 to 36% of the olivine grains are deformed showing kink bands or rectangular subgrain boundaries (Table 1). Most deformed olivines are subhedral to anhedral while undeformed grains are usually euhedral to subhedral (Table 1). Spinel and melt inclusions are common in olivine. Except for one reversely zoned grain (Fo_{80.0}-Fo_{80.5}) in SU-46-66, all analyzed olivines are normally zoned with compositionally homogeneous cores. Frey et al (1991) also reported two reversely zoned olivines in MK1-3 (Fo_{78.5}-Fo_{82.2} and Fo_{80.1}-Fo_{82.9}) and one in MK5-13 (Fo_{82.6}-Fo_{84.2}). Most of the olivine cores range from Fo₈₂ to Fo₉₁ and the rims vary from Fo₇₅ to Fo₈₄ (Fig. 2). In general, the olivine rims are in equilibrium with the glass compositions of the pillow rims (Fig. 2). There is no correlation between core composition, crystal form, or size.

Augite appears as euhedral to rounded phenocrysts and microphenocrysts. They usually occur as single crystals or form aggregates with plagioclase (Fig. 3A). Augite-olivine clots are only found in SU-22-64, where they are associated with orthopyroxene. Except for MK2-1, augites also form rims enclosing orthopyroxenes. In contrast to augite in Kilauea lavas (Helz and Wright, 1992; Clague et al., 1995) and Mauna Loa submarine lavas (Garcia et al., 1995), sector-zoned augite was not found in Mauna Kea submarine lavas. Plagioclase phenocrysts are locally resorbed, sometimes deeply embayed (Fig. 3B) and microphenocrysts are usually euhedral. Orthopyroxenes are anhedral except for those in MK1-8 which are euhedral. All orthopyroxenes are associated with augite and/or plagioclase. Representative analyses of olivine, plagioclase, and pyroxenes are listed in Tables 2, 3, 4 and 5. Because the zoned plagioclase and pyroxene in each sample have distinct compositional ranges (Figs. 4, 5 and 6) and zonation pattern, each sample is described separately.

SU-21-64

Plagioclase Plagioclases are reversely zoned ranging from An₅₅ to An₇₄ (Fig. 4). The most An-rich compositions are in equilibrium with the glass (Fig. 4). An euhedral phenocryst (pl-110) exhibits two episodes of reverse zoning (Fig. 7). It has a homogeneous core of An₆₀ with the outer part of the core decreasing to An₅₈ followed by reverse zoning to An₆₃. The second episode of reverse zoning increases from An₆₀ to An₇₂, then decreases to An₆₉ at the outermost edge (Fig. 7). Other phenocrysts are complexly zoned like pl-110, but they have slightly different compositions. Typically, they have ~An₅₆ in the cores and increase to An₅₈ in the first region of reverse zoning and to An₇₀ in the second region of reverse zoning. Several plagioclase grains record simple reverse zoning with cores of An₆₀ and rims of An₇₀; i.e., their zoning profiles correspond to the second episode of reverse zoning in pl-110. Some euhedral microphenocrysts are also reversely zoned with An contents decreasing from An₇₀ to An₆₅ in cores which are enclosed by rims of ~An₆₇ (inset in Fig. 7). This episode of reverse zoning is not observed in phenocrysts and probably corresponds to the reverse zoning in pyroxene outermost rims (Fig. 7). These microphenocrysts record detailed compositional variation occurring during the last stage of magmatism.

Augite All of the seven analyzed augite grains in SU-21-64 are reversely zoned (Fig. 3B). They have core compositions varying from Mg#=72 to 78, but the rims with Mg# ~82 are in equilibrium with the glass (Fig. 5). Based on compositional variations in cores, the seven analyzed augite grains in this sample are grouped into 3 types.

TYPE 1 Four grains are characterized by homogeneous cores with Mg # = 72 which are enclosed by more magnesium-rich rims whose Mg# decrease from 83 to 80. The outermost edges of two of these four grains have low Mg# of 74 which is not in equilibrium with glass and may reflect post-eruptive crystallization. When magmas were stored in a reservoir, the diffusion rates were relatively high due to high temperatures; therefore, crystals formed were able to maintain equilibrium with melt. For augite, the Fe-Mg exchange distribution coefficient

$[K_D = (X_{Fe}^{xtl} \cdot X_{Mg}^{liq}) / (X_{Mg}^{xtl} \cdot X_{Fe}^{liq})]$ is ~0.23-0.27 reflecting a higher Mg/Fe ratio in augite than in the melt. After magmas erupted to the surface, the rapid decrease in temperature led to increases in crystal growth rates and decrease in diffusion rates of elements in the melt causing disequilibrium between magma and crystals, that is, the augite crystallized has a Mg/Fe ratio close to that of the melt which is lower than the equilibrium Mg/Fe ratio of augite. The width of these outermost edges with disequilibrium compositions are usually < 10 μm . These disequilibrium compositions are not plotted in Figs. 4, 5, and 6.

TYPE 2 Two grains differ from type 1 augites in that the cores are normally zoned with Mg# ranging from ~79 to 77 with abrupt increases to ~Mg#=83 near the margin (Fig. 7). Generally, the Mg-rich rims show an episode of reverse zoning with a small contrast in Mg# (Fig. 7). This zoning pattern is similar to those in plagioclase microphenocrysts and pyroxene rims that enclose orthopyroxenes. In summary, there are two episodes of reverse zoning recorded in this type of augite.

TYPE 3 The composition and zonation of the high magnesium rim are similar to those of type 2 augites. The core, however, is reversely zoned instead of normally zoned, i.e. Mg# from 70.5 to 78.2. Only one (cpx-6 in Table 4) of the seven analyzed augites belongs to this type.

Finally, the augite rims which enclose orthopyroxenes have compositions and zonation similar to those of type 2 and 3 augite rims (Fig. 5).

Orthopyroxene Four orthopyroxene grains occur in a 4 cm by 2 cm thin section. Three were analyzed in detail. Two of the three are anhedral orthopyroxenes rimmed by more magnesium orthopyroxene and augite (Fig. 3C). The orthopyroxene rims are truncated by augite rims. In each of these orthopyroxene grains, the rim has higher Mg# than the core (Fig. 6). In detail, one orthopyroxene core is compositionally homogeneous with a Mg# of 76.5 ± 0.2 , while the other two orthopyroxene cores are normally zoned with Mg# decreasing from 75 to 74 and from 73 to 70 (Fig. 6). In the orthopyroxene with a normally zoned core, Mg# from 73 to 70, the high Mg# rim first decreases from 82.1 to 80.5, then slightly increases to 81.0, and then

decreases to 73 at the outermost edge (Fig. 7). Although the difference of 0.5 in Mg# is only slightly beyond analytical error (± 0.2), this reversal within the rim also appears in the augites that surround orthopyroxenes and some individual augite and plagioclase crystals (Fig. 7). The Mg# of 73 at the outermost edge resulted from disequilibrium crystallization after eruption as discussed earlier. The orthopyroxene grain with a homogeneous core (Mg# = 76.5) encloses a plagioclase and an augite with a Mg# of 76.8. The fourth orthopyroxene has a Mg# of 83.7 in the core. This single analysis is not shown in Fig. 6.

MK 2-1

The compositions of pyroxenes and plagioclase in MK2-1 show only small compositional ranges relative to those in SU-21-64 (Figs. 4, 5, 6, and 8). Five analyzed plagioclases range only from An₆₆ to An₇₁ (Fig. 4), but they show four episodes of reverse zoning (Fig. 8). The Mg# of augites vary from 77 to 84, most are from 80 to 83 (Fig. 5). Detailed analyses of one augite show that it has a complex compositional variation similar to that in plagioclase and orthopyroxene (Fig. 8). A rounded orthopyroxene occurs in this sample. Like an orthopyroxene in SU-21-64, it has a plagioclase inclusion. However, this orthopyroxene is not rimmed by augite (Fig. 3D). Its composition fluctuates between Mg# of 80 and 81.5 (Fig. 8).

SU-20-64

As in SU-21-64, plagioclase and pyroxenes show significant compositional variations which extend to lower An content and Mg# than the other samples (Figs 4, 5 and 6).

Plagioclase Plagioclase ranges from An₅₁ to An₆₈ (Fig. 4). Two locally resorbed phenocrysts, pl-126 and pl-180 (Fig. 3A), were analyzed in detail. Plagioclase pl-180 exhibits two episodes of reverse zoning (Fig. 9). Its core decreases from An₅₇ to An₅₃, then gradually increases to An₅₇ followed by a rapid increase to An₆₅. The second episode of reverse zoning is an abrupt increase from An₅₉ to An₆₆ near the rim (Fig. 9). An₆₆ is in equilibrium with glass

(Fig. 4). Relative to the equilibrium composition, An₆₆, the outermost edge has An₅₆ with a Al/Si ratio closer to that in the melt reflecting post-eruptive disequilibrium crystallization (Fig. 9). Another phenocryst, pl-126, has slightly different core composition and only one episode of reverse zoning recorded in the rim perhaps reflecting a growth rate that was unable to record the rapid changes in melt composition. Plagioclase microphenocrysts have normally zoned cores decreasing from An₆₇ to An₆₁ enclosed by reversely zoned rims with An contents increasing to An₆₇ (Fig. 9). The zonation and composition of microphenocrysts are comparable to the second episode of reverse zoning in phenocryst pl-180 (Fig. 9).

Augite Some analyzed augites also have two episodes of reverse zoning while others have only one episode. The Mg# in the cores vary from ~64 to ~79 (Fig. 5). In contrast, the rims have Mg# varying from 80 to 81.7, and they are in equilibrium with the glassy rim (Fig. 5).

Orthopyroxene Four anhedral orthopyroxene grains are enclosed in a augite rim. Some plagioclase laths are in the outer parts of the augite rim. The Mg# in orthopyroxene vary from 70.6 to 71.2 which are the lowest among those in five analyzed samples.

MK 1-8

Plagioclase Only one plagioclase grain was analyzed. It varies from An₅₅ to An₆₀ and is reversely zoned.

Augite The Mg # of eight analyzed augite cores are in the range of 70 to 83.5 (Fig. 5). The most complex augite shows an abrupt increase in Mg# from 73 at the outer part of the core to ~81 at the rim. The center part of the core has Mg# varying from 77.5 to 80.5 with two possible reversals superimposed on the general normal zoning (Fig. 10). At least one small reversal occurs in the rim (Fig. 10).

Orthopyroxene Three orthopyroxene grains were found. They have similar core compositions with Mg# ranging from 74 to 80 (Fig. 6). One grain shows two episodes of reverse zoning (Fig. 10).

SU-22-64

In contrast to SU-21-64, SU-20-64, and MK1-8, most of the core compositions of plagioclase and pyroxenes are in equilibrium with glass compositions (Figs. 4, 5 and 6). Because the compositional ranges of plagioclase and pyroxenes in this sample are small relative to SU-21-64, SU-20-64 and MK1-8, the compositional differences are not apparent in back-scattered electron images from scanning electron microscope (SEM). In Figs. 4, 5, and 6, they are all indicated as core compositions, although the variations include rim compositions.

Plagioclase The most complex plagioclase phenocrysts show three episodes of reverse zoning with the first increasing from $\sim\text{An}_{65}$ to $\sim\text{An}_{71}$, the second from $\sim\text{An}_{68}$ to $\sim\text{An}_{76}$ and the third from $\sim\text{An}_{65}$ to $\sim\text{An}_{69}$ (Fig. 11). The outermost edges with An_{55} reflects post-eruptive crystallization. Although the last episode of reverse zoning is defined by only one analysis, it is confirmed by analyses of microphenocrysts which record the detailed compositional variation during the last episode of reverse zoning.

Augite Augite occurs either as single crystals or associated with orthopyroxene. Despite the difference in texture, they have similar Mg# ranging from 80 to 85, most are between 80 and 83 (Fig. 5). Both individual augite crystals and those associated with orthopyroxene have two types of compositional variations. One type shows normal zoning; the other type exhibits one episode of reverse zoning (Fig. 10).

Orthopyroxene Among these 12 dredged basalts, SU-22-64 has the most abundant orthopyroxene (chapter 2). Eight of the ten analyzed orthopyroxene have Mg# ranging from 78 to 83. The Mg# of the other two are 72.7 ± 0.2 and 77.0 ± 0.5 (Fig. 5). Three grains are slightly normally zoned (Mg# from 78.2 to 79.7, from 82.4 to 83.2 and from 81.2 to 82.6), the other eight are compositionally homogeneous (the variations in Mg# are less than 0.3). All orthopyroxene grains are associated with augite. Their textures can be classified into four types:
TYPE 1: Five euhedral to subhedral orthopyroxene phenocrysts are surrounded by fine-grain augites and olivines (Fig. 3E). Two are slightly normally zoned with Mg# decreasing from

79.7 to 78.2 (opx-1) and 83.2 to 82.4 (opx-10). The other three are compositionally homogeneous with Mg# of 79.6 ± 0.3 (opx-2), 72.6 ± 0.2 (opx-5), and 82.1 ± 0.2 (opx-6).

TYPE 2: Subhedral to anhedral orthopyroxenes are rimmed by embayed augite rims (Fig. 3F). Orthopyroxenes are compositionally homogeneous, but the embayed augites are normally zoned.

TYPE 3: Anhedral orthopyroxenes are enclosed by fine-grain augites, and mantled by euhedral augite (Fig. 3G). Orthopyroxene and fine-grain augites are homogeneous and the outermost euhedral augite is reversely zoned.

TYPE 4: This is the most complex type. An anhedral augite microphenocryst is mantled by anhedral orthopyroxene, then surrounded by fine-grain augites and olivines, and finally enclosed by fine-grain olivines (Fig. 3H). Only one grain (opx-3) belongs to this type. The augite core and orthopyroxene are homogeneous with Mg# of 81.8 ± 0.3 and 81.4 ± 0.3 , respectively. The fine-grain augites are reversely zoned with Mg# varying from 82.1 to 77.8

Olivines in olivine-augite clots are Fo_{78} - Fo_{81} and are either homogeneous or normally zoned.

DISCUSSION

Magma mixing in isolated magma chambers The reversely zoned augite, orthopyroxene and plagioclase in these submarine lavas provide strong evidence for magma mixing. The occurrence of orthopyroxene crystals rimmed by augite is consistent with magma mixing. Experimental studies of Kilauea lavas, which have lower SiO_2 contents than Mauna Loa lavas (Frey and Rhodes, 1993), show that orthopyroxene is a late crystallizing phase forming after augite and plagioclase (Helz and Thornber, 1987). Because these submarine glasses and glasses recovered from the HSDP core have compositions similar to Kilauea glasses (Garcia, 1996), it is inferred that orthopyroxene is also a late crystallizing phase in Mauna Kea lavas. Therefore, augite rims enclosing orthopyroxene grains reflect a change from

more evolved (orthopyroxene saturated) to less evolved (orthopyroxene unsaturated) melt compositions, a result that is consistent with replenishment of a partially crystallized magma chamber by a mafic magma.

The crystals with the most complex zonation provide the most detailed information on the magma evolution, because the cores of some crystals are not intersected in the plane of the thin section. All five of the studied samples require at least three episodes of magma recharge. Although the textures, compositional ranges and zonation of minerals (except for olivine) in each sample are generally similar, there are significant differences between samples. For example, orthopyroxene in SU-22-64 is either homogeneous or slightly normally zoned (Fig. 11) and associated with augite and olivine (Figs. 3E, F, G, and H) while that in MK2-1 is not associated with augite (Fig. 3D) and shows a complex zonation with small compositional contrasts (Fig. 8). Most of the augites in SU-21-64 and SU-20-64 exhibit large compositional contrast in single grains while those in SU22-64 and MK2-1 have relative uniform compositions (Figs. 4, 5 and 6). If the growth rates of crystals in different magma chambers are similar, the different zonation patterns, for example, abrupt or gradual change in slope, reflect differences in the duration of mixing events. The abrupt compositional contrasts in the zoned pyroxenes and plagioclase in SU-21-64 (Fig. 7) indicate that mixing occurred in a short time interval, while the gradational reverse zoning of plagioclase pl-180 in SU-20-64 (Fig. 9) suggests that the magma chamber was continuously replenished by small amounts of mafic magma prior to the mixing event that preceded eruption. Apparently, minerals in each sample grew from magmas with distinct evolutionary history, thereby providing evidence for isolated magma chambers. This conclusion that lavas erupted along the east rift of Mauna Kea were derived from several different magma chambers which contained evolved magmas that were mixed with more mafic magmas is similar to the model proposed for the east rift of Kilauea (Garcia et al., 1992; Helz and Wright, 1992; Clague et al., 1995).

Derivation of these submarine lavas from the isolated magma chambers is consistent

with whole-rock trace element and isotopic characteristics. Although the abundances of major elements in whole rocks of group 1 submarine lavas (including MK2-1 and SU-21-64) were interpreted as reflecting olivine accumulation in a melt, MK2-1 and SU-21-64 have different $^{206}\text{Pb}/^{204}\text{Pb}$, Sr/Nb, La/Nb and Zr/Nb ratios indicating that they were not derived from a common parent (chapter 2). Two group 2 samples, SU-20-64 and MK1-8 have similar glass rim compositions. However, their distinct Sr and Pb isotopic ratios (chapter 2) also require different parental magmas.

The compositions of the evolved magmas An important question is what were the compositions of the mixing components? As the glassy rims (mixed melts) contain 5.31 to 6.26% MgO (chapter 2), the evolved components must have MgO less than this range. However, no evolved glasses or lavas with < 5% MgO have been recovered from the Mauna Kea shield (Garcia, 1996; Rhodes, 1996); therefore, the core compositions of plagioclase and pyroxenes, which are typically too enriched in Na and Fe to be in equilibrium with the glass (Figs. 4, 5 and 6), provide the only clues for the compositions of evolved components.

If the crystallization sequence of the evolved magmas is similar to that determined for Kilauea tholeiites, orthopyroxene crystallized after augite. In three samples, SU-20-64, SU-21-64 and MK1-8, orthopyroxenes are rimmed by augites indicating that orthopyroxene was stable in the evolved magmas before mixing but not in the hybrid magma. Their variable core compositions (Figs. 4, 5 and 6) imply that the compositions of the coexisting melts were not buffered at the ol+melt = augite+orthopyroxene+plagioclase reaction point. In other words, the differentiated magmas had reacted out olivine and evolved beyond this reaction point. This inference is supported by the absence of reversely zoned olivine in the five studied samples. On the other hand, orthopyroxene in MK2-1 is not rimmed by other phases. Also, compared to other samples it has more homogeneous plagioclase and augite compositions (Fig. 8). These observations are consistent with the melt composition in MK2-1 being buffered at the ol+melt =

augite+ orthopyroxene+plagioclase reaction point by multiple intrusions of more mafic magmas.

The MgO contents of melts coexisting with augite can be inferred from the Fe-Mg exchange coefficient- K_D . The lowest Mg# of augite in SU-21-64 and MK1-8 is ~70, corresponding to Mg# of 34-38 in melts (Fig. 12), using the Fe-Mg exchange K_D of 0.25 ± 0.2 (Tormey et al., 1987; Grove et al., 1992). An augite in SU-20-64 has Mg# of 63-65 which is in equilibrium with a melt containing Mg# of 28-33. Lavas with such iron-rich compositions are rarely erupted during the shield-building stage of Hawaiian volcanoes. A sample from the west rift of Kilauea contains 3.9% MgO with a Mg# of 40 (Wright and Fiske, 1971). Although not erupted, a lava with 2.26% MgO (Mg# = 33) and 59% SiO₂ is required for the mixing calculation to model Kilauea Yellow Cone lavas (Wright and Fiske, 1971). Highly evolved tholeiitic lavas with SiO₂ ranging from 66.1 to 72.5% and MgO ranging from 1.66 to 0.11% were also found at the Kuwale Ridge and Kauaopuu Ridge of the Waianae volcano on Oahu Island, Hawaii (Bauer et al., 1973; Fodor et al., 1977). The composition of pyroxenes in Mauna Kea submarine lavas provide evidence that such highly evolved melts were also present in the east rift zone of Mauna Kea. On the other hand, the highest Mg# in orthopyroxene, 81-83, which occurs in MK2-1, MK1-8, SU-21-64 and SU-22-64, represents the composition of orthopyroxene that first crystallized from the melt and can be used to infer the melt composition that was buffered at the reaction point of olivine+melt = orthopyroxene+plagioclase+augite. Orthopyroxene with Mg# of 81-83 is equilibrated with the glasses from MK2-1 and SU-21-64 (Fig. 6) which contain 6.05~6.31% MgO with Mg# of 52.

The origin of olivine-cognate or exotic In contrast to the reverse zoning in pyroxenes and plagioclase, all olivines, except three grains including two reported by Frey et al. (1991), are normally zoned indicating that they are from the mafic component. Olivine is abundant in Hawaiian picrites and the origin of the olivine, cognate or exotic, is critical in assessing if the

picritic lavas are representative of primary melts.

Three arguments are commonly used to identify exotic olivine; deformation textures, wide compositional ranges and Mg# that are not in equilibrium with whole rock or glass compositions. However, none of these arguments are conclusive. It is commonly hypothesized that deformation features formed in olivine cumulates (Clague et al., 1995), but deformation textures, such as kink bands and rectangular subgrain boundaries were experimentally produced at high temperature and pressure [see summary in (Helz, 1987b)]. They may also develop when magma flows through narrow conduits at high pressure (Wilkinson and Hensel, 1988). Olivines with diverse compositions crystallize as magmas evolve. These diverse compositions can persist in the magma without being reequilibrated, because the growth rate is greater than the diffusion rate. For example, olivines with 0.25 cm in length will grow in 4-7 days (using the growth rates of $2.2-4.3 \times 10^{-7}$ cm/sec, (Donaldson, 1975), but will not reequilibrate with residual melt in a year (Jurewicz and Watson, 1988). Although these olivines with diverse compositions are cognate in origin, their compositions are not in equilibrium with whole rocks or glasses. Since deformation textures and compositions are ambiguous indications for origin of olivine, I consider another approach to this problem; specifically, the volume of olivine and the MgO content of host melt.

Although very high MgO contents (> 20%) have been suggested for Hawaiian primary magmas (Wright, 1984), the highest MgO content of melt estimated from the most forsteritic olivine in lavas from Mauna Kea volcano is ~17% (Baker et al., 1996; Garcia, 1996). Therefore, whole rock compositions with MgO > 17%, especially those with MgO > 20%, probably contain cumulate olivine. Whether a lava with MgO < 17% contains accumulate olivines can be evaluated from the proportion of olivine in the whole rock. If the whole rock represents a crystallized melt and olivine is the only crystalline phase, the amount of olivine crystallized can be calculated by mass balancing whole rock composition with the compositions of olivine and residual melt, provided that the average composition of olivine is known. Based

on the linear trends in the MgO variation diagrams, the average olivine composition in Mauna Kea and Mauna Loa tholeiites are suggested to be \sim Fo₈₆ (Rhodes, 1996). With Fo₈₆, Figure 13 illustrates the relation between the MgO contents of parental melts (represented by whole rock composition) and residual melts (represented by glass composition) and the amount of olivine crystallized. A 13% MgO parental melt will crystallize 10.7 wt% olivine to form 9% MgO residual melt. Therefore, a 13% MgO whole rock with a 7% MgO glassy rim and more than 10.7 wt% olivine is likely to contain exotic olivine.

A similar mass balance calculation was carried out for magma mixing using the compositions of mixed melts and inferred mixing components. For these dredged samples, the glassy rim compositions represent mixed melts. The two mixing end-members are (1) evolved melts with 3-5% MgO and no olivine crystals and (2) mafic components containing 7-11% MgO melts evolved from a 17% MgO parent and olivine crystals. To estimate the maximum olivine proportion, it is assumed that the mafic component has not segregated any olivine; i.e. the bulk rock composition of the mafic component has 17% MgO. Olivine wt% in the mixture are calculated from mass balancing mixed melt (glassy rim) against various combinations of evolved and mafic components. The combination of 3% MgO evolved melt and 7% MgO mafic melt results in a maximum amount of olivine in the mixture (Fig. 14), because an evolved component with lower MgO content requires a greater amount of mafic component and a mafic component with lower MgO melt contains a larger amount of olivine. The maximum proportions of calculated olivine are less than the proportions of olivine in the whole-rocks (Fig. 14); therefore, all of these dredged lavas contain cumulate olivine.

Implications from olivine rim compositions In contrast to the wide ranges of core compositions, most olivines have rim compositions in equilibrium with the glassy rims thereby indicating that the rims crystallized after mixing. The typical rim width, 100 microns, grew within 6~13 hours, if the growth rates of $2.2\text{-}4.3 \times 10^{-7}$ cm/sec (Donaldson, 1975) are

considered. This implies that eruption occurred very quickly after mixing. It is suggested that the intrusion of new magma triggered eruption. With a magma ascent rate of 0.6-0.8 cm/sec estimated for Kilauea, (Helz, 1987a), the maximum distance that magma can travel during 6-13 hours is less than 400m, thereby providing evidence for very shallow magma chambers.

Evidence of high pressure fractionation Among these dredged lavas, SU-22-64 is unique in having a low SiO₂ content and a low Zr/Nb ratio and a high La/Yb ratio. These geochemical characteristics are consistent with melt segregation at relatively high pressure and low extent of melting (chapter 2). This sample also contains the most abundant orthopyroxene, a mineral that usually crystallizes from melts with high SiO₂ contents. A plausible explanation for this contradiction (i.e. orthopyroxene in a low SiO₂ melt) is that SU-22-64 was saturated with orthopyroxene at high pressure. Based on the experimental studies (Stolper, 1980), the olivine primary field shrinks at high pressure and multiple saturation boundaries move away from silica corner (Fig. 15), therefore, decreasing the SiO₂ content of the multiple saturated melts. During ascent to lower pressure, a low SiO₂ melt saturated with olivine, augite and orthopyroxene (point A in Fig. 15) became saturated with olivine and augite but not orthopyroxene (Fig. 15; point A lies on the olivine-augite cotectic at a lower pressure). Although a mixing process is required for the reverse zoning in plagioclase (Fig. 10) and can also explain orthopyroxene being rimmed by fine-grain augites and olivines, mixing at low pressures cannot readily explain orthopyroxene rimmed with only fine-grain olivines in the outermost edge (Fig. 3H), especially given the low MgO contents (5.60-5.44%) of the glasses which are unlikely to crystallize only olivine. These olivine rims may have formed after further ascent to lower pressure, where a melt will be in the olivine primary field and crystallize only olivine (Fig. 15; at the lowest pressure, point A is in the olivine primary field). Note that most of the pyroxenes in SU-22-64 have Mg# varying in a small range, similar to that of MK2-1 (Figs. 4 and 5). Although plagioclase compositions are more variable, their An contents are

generally higher than those in SU-21-64 and SU-20-64. Like MK2-1, this sample may also have been buffered at the ol+melt=augite+orthopyroxene+plagioclase reaction point but at a higher pressure. The complex textures associated with orthopyroxene developed while it ascended to lower pressure.

Comparison with Mauna Kea lavas recovered from Hawaiian Scientific Drilling Project (HSDP)

The initial phase of Hawaiian Scientific Drilling Project (HSDP) recovered 776 meters of Mauna Kea lavas. There are compositional differences between these HSDP lavas and submarine lavas. For example, at a given MgO content, submarine lavas have higher SiO₂ contents than HSDP Mauna Kea lavas (Chapter 4). Baker et al (1996) reported that "pigeonite rims on many olivine phenocrysts in the more evolved lavas" and used this texture to propose that the residual liquids (now represented by the groundmasses) had evolved to the olivine + liquid = pigeonite + augite + plagioclase reaction point. In contrast, orthopyroxenes in submarine lavas are surrounded by augite, and in some cases, augite and olivine. The texture in HSDP Mauna Kea lavas may indicate that the residual melt did not evolved beyond the reaction point because olivine was not reacted out. On the other hand, the evolved component in most of the studied submarine lavas evolved beyond this reaction point as discussed earlier. This difference can be explained by their different locations along the east rift. Relative to submarine lavas, HSDP lavas are located closer to the summit of the volcano (Fig 1 of chapter 2). They may have erupted from the summit reservoir (Fig. 1) or magma chambers close to the summit reservoir which were constantly replenished by mafic magmas with abundant olivine that prevented the mixed melts from evolving beyond the reaction point. As these submarine lavas are more distant from the summit, the extensive amount of fractionation reflected by the evolved mixing component is consistent with the low magma supply rate that is expected at the distal ends of rift zones.

CONCLUSIONS

The compositions of plagioclase and pyroxenes indicate the presence of evolved lava compositions which were not erupted. During the shield-building stage, evolved magmas with < 5% MgO may be common at the distal ends of rift zones. The differences in the mineral compositions and zoning profiles between samples provide evidence that these samples were derived from isolated magma chambers which had undergone distinct fractionation and mixing histories. Each magma chamber was recharged several times before eruption. Based on the width of olivine rims, the magma chambers were at shallow level (~400 m). However, high pressure fractionation also occurred as reflected in the composition and textures of SU-22-64. The difference in the petrographic texture between submarine lavas and HSDP core indicates that magma reservoirs at the distal ends of rift zones have lower magma supply rate than those close to the summit of the volcano. Finally, the complex petrogenesis indicated by the compositional zoning of crystals shows that interpretations based only on whole-rock analyses of MgO-rich Hawaiian lavas may be erroneous .

REFERENCES

- Albee A. L. and Ray L. (1970) Correction factors for electron microprobe analysis of silicates, oxides, carbonates, phosphates and sulfates. *Anal. Chem.* 42, 1408-1414.
- Baker M. B., Alves S., and Stolper E. M. (1996) Petrography and petrology of the Hawaiian Scientific Drilling Project lavas: Inferences from olivine phenocryst abundances and compositions. *J. Geophys. Res.*, in press.
- Bauer G. R., Fodor R. V., Hustler J. W., and Keil K. (1973) Contributions to the mineral chemistry of Hawaiian rocks. III. Composition and mineralogy of a new rhyodacite occurrence on Oahu, Hawaii. *Contrib. Mineral. Petrol.* 40, 183-194.
- Bence A. E. and Albee A. L. (1968) Empirical correction factors for the electron microanalysis of silicates and oxides. *J. Geol.* 76, 382-403.
- Clague D. A., Moore J. G., Dixon J. E., and Friesen W. B. (1995) Petrology of submarine lavas from Kilauea's Puna Ridge, Hawaii. *J. Petrol.* 36(2), 299-349.
- Donaldson C. H. (1975) Calculated diffusion coefficients and the growth rate of olivine in basalt magma. *Lithos* 8, 163-174.
- Eiler J. M., Farley K. A., Valley J. W., Hofmann A. W., and Stolper E. M. (1996) Oxygen isotope constraints on the sources of Hawaiian volcanism. *Earth Planet. Sci. Lett.*, submitted.
- Fodor R. V., Keil K., and Bauer G. R. (1977) Contributions to the mineral chemistry of Hawaiian rocks. V. Compositions and origin of ultramafic nodules and megacrysts in a rhyodacite from Oahu, Hawaiian Islands. *Pacific Sci.* 31, 211-222.
- Frey F. A., Garcia M. O., Wise W. S., Kennedy A., Gurriet P., and Albarede F. (1991) The evolution of Mauna Kea Volcano, Hawaii: Petrogenesis of tholeiitic and alkalic basalts. *J. Geophys. Res.* 96, 14,347-14,375.
- Frey F. A. and Rhodes J. M. (1993) Intershield geochemical differences among Hawaiian volcanoes: Implications for source compositions, melting process and magma ascent paths. *Phil. Trans. R. Soc. Lond. Ser. A*, 342, 121-136.
- Garcia M. O. (1996) Petrography, olivine and glass chemistry of lavas from the Hawaii Scientific Drilling Project. *J. Geophys. Res.*, in press.
- Garcia M. O., Hulsebosch T. P., and Rhodes J. M. (1995) Olivine-rich submarine basalts from the southwest rift zone of Mauna Loa Volcano: Implications for magmatic processes and geochemical evolution. In *Mauna Loa Revealed: Structure, Composition, History, and Hazards*. Geophys. Monogr. Ser., Vol. 92, edited by J. M. Rhodes and J. P. Lockwood, pp. 219-239, AGU, Washington, D.C.

- Garcia M. O., Rhodes J. M., Wolfe E. W., Ulrich G. E., and Ho R. A. (1992) Petrology of lavas from episodes 2-47 of the Puu Oo eruption of Kilauea volcano, Hawaii: Evaluation of magmatic processes. *Bull. Volcanol.* 55, 1-16.
- Grove T. L. and Juster T. C. (1989) Experimental investigations of low-Ca pyroxene stability and olivine-pyroxene-liquid equilibria at 1-atm in natural basaltic and andesitic liquids. *Contrib. Mineral. Petrol.* 103, 287-305.
- Grove T. L., Kinzler R. J., and Bryan W. B. (1992) Fractionation in mid-ocean ridge basalts (MORB). In *Mantle Flow and Melt Generation at Mid-Ocean Ridges*. Geophys. Monogr. Ser., Vol. 71, edited by J. P. Morgan, D. K. Blackman, and J. M. Sinton, pp. 281-310, AGU, Washington, D.C.
- Helz R. T. (1987a) Differentiation behavior of Kilauea Iki lava lake, Kilauea Volcano, Hawaii: An overview of past and current work. In *Magmatic Processes: Physicochemical Principles*, edited by B. O. Mysen, pp. 241-258, Geochem Soc Spec Publ, .
- Helz R. T. (1987b) Diverse olivine types in lava of the 1959 eruption of Kilauea Volcano and their bearing on eruption dynamics. *U.S. Geol. Surv. Prof. Pap.* 1350, 691-722.
- Helz R. T. and Thornber C. R. (1987) Geothermometry of Kilauea Iki lava lake, Hawaii. *Bull. Volcanol.* 49, 651-668.
- Helz R. T. and Wright T. L. (1992) Differentiation and magma mixing on Kilauea's east rift zone: A further look at the eruptions of 1955 and 1960. Part I. The late 1955 lavas. *Bull. Volcanol.* 54, 361-384.
- Jurewicz A. J. and Watson E. B. (1988) Cations in olivine, Part 2: Diffusion in olivine xenocrysts, with applications to petrology and mineral physics. *Contrib. Mineral. Petrol.* 99, 186-201.
- Juster T. C. and Grove T. L. (1989) Experimental constraints in the generation of Fe-Ti basalts, andesites, and rhyodacites at the Galapagos spreading center, 85oW and 95oW. *J. Geophys. Res.* 94, 9251-9274.
- Lassiter J. C., DePaolo D. J., and Tatsumoto M. (1996) Isotopic evolution of Mauna Kea volcano: Results from the initial phase of the Hawaii Scientific Drilling Project. *J. Geophys. Res.*, in press.
- Murata K. J. and Richter D. H. (1966) Chemistry of the lavas of 1959-1960 eruption of Kilauea Volcano, Hawaii. *U.S. Geol. Surv. Prof. Pap.* 537-A, 66.
- Rhodes J. M. (1988) Geochemistry of the 1984 Mauna Loa eruption: Implication for magma storage and supply. *J. Geophys. Res.* 93, 4453-4466.
- Rhodes J. M. (1996) The geochemical stratigraphy of lava flows sampled by the Hawaii

- Scientific Drilling Project. *J. Geophys. Res.*, in press.
- Rhodes J. M., Wenz K. P., Neal C. A., Sparks J. W., and Lockwood J. P. (1989) Geochemical evidence for invasion of Kilauea's plumbing system by Mauna Loa magma. *Nature* 337, 257-260.
- Ryan M. P., Koyanagi R. Y., and Fiske R. S. (1981) Modeling the three-dimensional structure of macroscopic magma transport systems: application to Kilauea volcano. *J. Geophys. Res.* 86, 7111-7129.
- Sharp W. D., Turrin B. D., Renne P. R., and Lanphere M. A. (1996) The $^{40}\text{Ar}/^{39}\text{Ar}$ and K/Ar dating of lavas from the Hilo 1-km core hole, Hawaiian Scientific Drilling Project. *J. Geophys. Res.*, in press.
- Stolper E. (1980) A phase diagram for mid-ocean ridge basalts: preliminary results and implications for petrogenesis. *Contrib. Mineral. Petrol.* 74, 13-27.
- Tormey D. R., Grove T. L., and Bryan W. B. (1987) Experimental petrology of normal MORB near the Kane Fracture Zone: 22°N-25°N, mid-Atlantic ridge. *Contrib. Mineral. Petrol.* 96, 121-139.
- Wilkinson J. F. G. and Hensel H. D. (1988) The petrology of some picrites from Mauna Loa and Kilauea volcanos, Hawaii. *Contrib. Mineral. Petrol.* 98, 326-345.
- Wright T. L. (1984) Origin of Hawaiian tholeiite: A metasomatic model. *J. Geophys. Res.* 89, 3233-3252.
- Wright T. L. and Fiske R. S. (1971) Origin of differentiated and hybrid lavas of Kilauea Volcano, Hawaii. *J. Petrol.* 12, 1-65.

Table 1 Percentage of deformed and undeformed olivine

sample #	undeformed			deformed			total counted
	euohedral	subhedral	anhedral	euohedral	subhedral	anhedral	
SU-21-64	38.6	17.0	11.3	5.7	15.9	11.4	88
MK2-1	60.3	14.2	10.6	3.5	3.5	7.8	141
SU-20-64	35.2	35.2	5.5	5.5	10.9	7.8	128
MK1-8	31.2	24.7	7.5	4.3	11.8	20.4	93
SU-22-64							
MK5-13	57.5	15.0	3.9	9.8	11.1	2.6	153
MK6-6	60.4	12.5	6.3	10.4	8.3	2.1	96
SU-46-66	17.0	54.7	11.3	0.0	9.4	7.5	53

Olivine crystals include phenocrysts (> 0.7mm) and microphenocrysts (0.1~0.7 mm).

Table 2-1 Olivine compositions of SU-21-64

sample #	SiO ₂	FeO	MnO	MgO	CaO	NiO	total	Fo (%)
SU-21-64								
53-c	39.88	13.15	0.20	46.73	0.28	0.36	100.60	86.4
53-r	38.99	18.16	0.25	42.49	0.31	0.24	100.43	80.7
52-c	39.41	14.37	0.26	46.16	0.26	0.34	100.80	85.1
52-r	38.96	18.01	0.26	42.94	0.29	0.26	100.72	81.0
49-c	39.53	14.03	0.24	45.77	0.27	0.33	100.17	85.3
49-r	38.90	18.73	0.26	42.82	0.30	0.19	101.19	80.3
45-c	39.36	14.26	0.23	45.37	0.27	0.30	99.78	85.0
45-r	39.16	18.29	0.27	42.58	0.29	0.20	100.79	80.6
40-c	39.57	14.63	0.22	44.91	0.29	0.37	99.99	84.5
40-r	38.87	18.61	0.25	42.17	0.28	0.14	100.31	80.2
38-c	40.66	9.70	0.16	49.28	0.24	0.41	100.45	90.1
38-r	38.55	18.56	0.29	42.03	0.28	0.12	99.83	80.1
39-c	40.51	9.86	0.04	48.28	0.27	0.38	99.34	89.7
39-r	39.14	18.39	0.32	41.97	0.30	0.21	100.33	80.3
35-c	39.90	13.63	0.20	45.79	0.29	0.35	100.16	85.7
35-r	38.89	19.20	0.29	42.47	0.30	0.14	101.28	79.8
19-c	40.60	9.71	0.05	48.41	0.24	0.42	99.41	89.9
19-r	38.89	18.89	0.24	40.49	0.28	0.16	98.94	79.3
18-c	39.68	12.94	0.21	45.53	0.27	0.33	98.96	86.3
18-r	38.94	18.50	0.31	42.16	0.30	0.24	100.44	80.2
22-c	40.47	9.85	0.18	47.83	0.25	0.33	98.91	89.6
22-r	39.23	18.08	0.33	42.58	0.32	0.25	100.78	80.8
23-c	40.52	9.51	0.17	49.25	0.23	0.42	100.11	90.2
23-r	39.16	19.01	0.26	42.04	0.30	0.14	100.90	79.8
93-c	40.18	12.37	0.20	47.20	0.25	0.36	100.55	87.2
93-r	39.12	19.29	0.34	42.17	0.31	0.21	101.44	79.6
4-c	40.67	9.53	0.19	48.34	0.23	0.41	99.38	90.0
4-r	38.94	19.30	0.31	41.77	0.29	0.17	100.77	79.4
5-c	40.56	9.60	0.18	48.17	0.22	0.44	99.18	89.9
5-r	39.62	18.38	0.27	42.50	0.29	0.28	101.34	80.5
6-c	40.58	9.95	0.18	49.40	0.23	0.46	100.80	89.9
6-r	39.06	18.37	0.30	42.28	0.30	0.25	100.56	80.4
8-c	40.77	10.95	0.21	48.50	0.24	0.36	101.02	88.8
8-r	39.27	18.72	0.27	42.35	0.29	0.25	101.15	80.1
2-c	40.75	9.55	0.14	49.39	0.24	0.45	100.52	90.2
2-r	39.47	16.20	0.21	44.46	0.26	0.26	100.86	83.0
1-c	40.72	10.84	0.18	48.90	0.26	0.42	101.31	88.9
1-r	39.20	18.57	0.27	42.26	0.33	0.23	100.85	80.2

Table 2-2 Olivine compositions of MK2-1

sample #	SiO ₂	FeO	MnO	MgO	CaO	NiO	total	Fo (%)
MK 2-1								
19-c	40.49	10.26	0.19	47.19	0.25	0.42	98.80	89.1
19-r	38.99	18.62	0.27	42.00	0.31	0.18	100.36	80.1
26-c	40.36	10.25	0.17	48.92	0.26	0.18	100.14	89.5
26-r	39.16	18.57	0.28	42.54	0.31	0.21	101.08	80.3
28-c	40.35	11.23	0.20	48.07	0.27	0.39	100.50	88.4
28-r	38.96	20.19	0.32	41.21	0.36	0.19	101.23	78.4
31-c	40.65	10.30	0.17	48.88	0.24	0.42	100.65	89.4
31-r	39.11	18.97	0.26	42.16	0.31	0.25	101.06	79.8
74-c	40.40	11.64	0.20	47.84	0.27	0.41	100.76	88.0
74-r	38.99	19.34	0.26	41.69	0.30	0.15	100.72	79.4
75-c	39.40	17.28	0.26	43.64	0.31	0.23	101.10	81.8
75-r	38.95	19.21	0.26	41.85	0.34	0.21	100.80	79.5
79-c	40.30	11.47	0.18	47.61	0.25	0.38	100.20	88.1
79-r	38.33	18.87	0.29	41.64	0.32	0.20	99.64	79.7
84-c	40.53	11.32	0.20	48.45	0.25	0.39	101.13	88.4
84-r	38.89	19.09	0.29	42.49	0.30	0.14	101.21	79.9
91-c	39.87	12.06	0.22	47.28	0.27	0.30	100.00	87.5
91-r	38.39	18.98	0.30	42.38	0.31	0.20	100.56	79.9
94-c	38.81	17.55	0.28	43.31	0.27	0.27	100.49	81.5
94-r	38.27	19.49	0.31	42.07	0.32	0.19	100.66	79.4
99-c	40.26	10.08	0.19	48.56	0.25	0.41	99.77	89.6
99-r	39.01	18.22	0.29	43.00	0.29	0.13	100.93	80.8
98-r	39.38	18.36	0.28	42.51	0.30	0.19	101.00	80.5
98-c	40.85	10.11	0.17	49.14	0.24	0.42	100.92	89.7
100-c	39.35	17.33	0.29	43.66	0.31	0.23	101.17	81.8
100-r	38.96	18.93	0.26	42.10	0.32	0.23	100.80	79.9
103-c	39.21	15.60	0.24	44.44	0.29	0.24	100.02	83.5
103-r	39.19	16.98	0.32	43.45	0.31	0.23	100.48	82.0
102-c	39.31	15.70	0.26	44.49	0.28	0.24	100.28	83.5
102-r	38.50	18.81	0.26	41.57	0.31	0.17	99.62	79.8
101-c	39.01	15.59	0.23	44.00	0.32	0.23	99.37	83.4
101-r	38.81	19.06	0.33	41.43	0.34	0.21	100.19	79.5
104-c	39.74	13.11	0.22	45.77	0.31	0.32	99.47	86.2
104-r	38.74	17.97	0.28	42.45	0.31	0.25	99.99	80.8

Table 2-2 Continued

sample #	SiO ₂	FeO	MnO	MgO	CaO	NiO	total	Fo (%)
114-c	39.36	15.09	0.22	45.36	0.29	0.30	100.61	84.3
114-r	38.71	18.93	0.25	42.25	0.32	0.23	100.67	79.9
116-c	40.24	10.88	0.19	48.56	0.26	0.36	100.49	88.8
116-r	38.51	18.46	0.28	42.23	0.33	0.24	100.04	80.3
115-c	39.23	16.05	0.27	44.35	0.33	0.19	100.41	83.1
115-r	38.56	19.30	0.27	41.98	0.32	0.19	100.61	79.5
117-c	39.24	17.31	0.28	43.37	0.26	0.25	100.70	81.7
117-r	38.94	18.74	0.31	42.43	0.29	0.22	100.92	80.1
131-c	39.53	14.66	0.28	46.04	0.30	0.25	101.07	84.8
131-r	39.52	19.18	0.28	42.14	0.33	0.18	101.63	79.7
128-c	38.66	19.17	0.32	41.04	0.25	0.19	99.62	79.2
128-r	38.43	18.72	0.29	40.73	0.32	0.22	98.71	79.5
131-c	39.51	14.55	0.29	46.02	0.30	0.16	100.82	84.9
131-r	38.80	19.01	0.30	42.45	0.31	0.20	101.07	79.9
1-c	39.60	14.04	0.19	45.29	0.26	0.37	99.75	85.2
1-r	38.64	20.20	0.32	41.63	0.34	0.19	101.32	78.6
4-c	40.38	10.49	0.06	48.42	0.25	0.39	99.99	89.2
4-r	39.07	18.31	0.27	42.67	0.35	0.18	100.85	80.6
6-c	40.57	10.21	0.17	48.54	0.25	0.42	100.16	89.4
6-r	38.82	18.70	0.28	42.56	0.34	0.22	100.92	80.2
24-c	40.61	10.30	0.19	48.78	0.26	0.36	100.50	89.4
45-c	39.34	16.68	0.28	43.26	0.29	0.27	100.12	82.2
45-r	38.64	18.75	0.27	42.11	0.32	0.22	100.30	80.0
41-c	40.47	10.12	0.16	48.17	0.27	0.42	99.61	89.5
60-c	39.27	16.35	0.29	43.87	0.28	0.22	100.29	82.7
60-r	38.77	19.09	0.30	41.92	0.33	0.18	100.58	79.7
140-c	39.43	13.57	0.20	45.16	0.36	0.15	98.86	85.6
140-r	39.05	19.37	0.28	41.75	0.36	0.23	101.04	79.4
92-c	39.40	16.91	0.27	43.49	0.31	0.22	100.59	82.1

Table 2-3 Olivine compositions of SU-20-64

sample #	SiO ₂	FeO	MnO	MgO	CaO	NiO	total	Fo (%)
SU-20-64								
20-c	39.93	10.45	0.15	49.27	0.22	0.36	100.38	89.4
20-r	38.62	20.45	0.20	41.78	0.25	0.25	101.55	78.5
21-c	39.96	9.84	0.08	48.55	0.23	0.36	99.02	89.8
21-r	38.39	20.64	0.29	40.41	0.27	0.25	100.25	77.7
22-c	40.07	10.28	0.14	48.27	0.25	0.35	99.35	89.3
22-r	38.61	19.54	0.25	41.50	0.26	0.23	100.38	79.1
23-c	40.01	10.42	0.13	48.35	0.21	0.32	99.45	89.2
23-r	38.66	19.69	0.21	41.18	0.26	0.23	100.22	78.9
24-c	39.60	13.22	0.21	47.03	0.24	0.32	100.62	86.4
24-r	38.03	20.26	0.30	40.34	0.26	0.21	99.39	78.0
25-c	39.85	12.07	0.15	47.96	0.25	0.31	100.57	87.6
25-r	37.88	22.81	0.26	39.05	0.27	0.20	100.46	75.3
26-c	39.53	13.40	0.10	46.85	0.24	0.34	100.46	86.2
26-r	38.56	21.05	0.26	40.31	0.28	0.20	100.66	77.3
31-c	40.02	11.05	0.16	48.35	0.23	0.35	100.14	88.6
31-r	38.57	20.77	0.25	40.16	0.28	0.21	100.25	77.5
32-c	39.69	13.85	0.19	46.63	0.26	0.31	100.93	85.7
32-r	39.04	17.45	0.21	43.59	0.26	0.27	100.81	81.7
33-c	40.04	10.98	0.09	48.92	0.23	0.39	100.65	88.8
33-r	38.22	20.15	0.26	40.80	0.27	0.20	99.89	78.3
51-c	39.35	13.61	0.18	46.15	0.24	0.29	99.82	85.8
51-r	38.38	20.85	0.26	41.00	0.28	0.26	101.02	77.8
56-c	40.13	10.12	0.14	49.04	0.24	0.41	100.08	89.6
56-r	38.58	21.75	0.28	40.46	0.27	0.23	101.56	76.8
176-c	39.60	14.49	0.18	46.08	0.24	0.30	100.88	85.0
176-r	38.34	21.02	0.21	40.66	0.30	0.24	100.76	77.5
177-c	38.58	17.82	0.24	43.02	0.26	0.26	100.19	81.1
177-r	37.96	21.42	0.28	40.33	0.29	0.21	100.48	77.1
178-c	38.95	18.02	0.26	43.06	0.26	0.26	100.80	81.0
178-r	38.09	21.60	0.29	39.48	0.32	0.22	100.00	76.5

Table 2-3 Continued

sample #	SiO ₂	FeO	MnO	MgO	CaO	NiO	total	Fo (%)
58-c	39.38	15.44	0.20	45.40	0.25	0.30	100.97	84.0
58-r	38.48	20.90	0.26	41.28	0.27	0.25	101.43	77.9
61-c	39.65	12.77	0.15	46.98	0.28	0.34	100.17	86.8
61-r	38.42	21.19	0.30	39.62	0.30	0.22	100.04	76.9
123-c	40.01	11.46	0.14	48.49	0.24	0.30	100.64	88.3
123-r	38.32	19.84	0.25	40.62	0.27	0.22	99.51	78.5
113-c	38.17	20.55	0.24	40.81	0.26	0.22	100.24	78.0
113-r	38.33	20.29	0.20	40.57	0.27	0.19	99.86	78.1
135-c	39.45	14.31	0.16	45.57	0.25	0.27	100.01	85.0
135-r	37.92	20.60	0.29	40.52	0.29	0.23	99.85	77.8
133-c	40.33	10.76	0.14	48.80	0.23	0.34	100.60	89.0
133-r	37.88	20.92	0.23	40.62	0.27	0.19	100.11	77.6
134-c	40.09	11.97	0.13	48.14	0.22	0.26	100.82	87.8
134-r	38.36	20.66	0.26	40.45	0.28	0.20	100.22	77.7
130-c	40.16	11.10	0.15	47.88	0.24	0.35	99.88	88.5
130-r	38.24	20.05	0.24	40.63	0.25	0.21	99.62	78.3
129-c	39.70	12.91	0.21	46.79	0.27	0.27	100.15	86.6
129-r	38.10	20.05	0.29	39.77	0.29	0.21	98.71	78.0
127-c	40.14	10.75	0.13	48.96	0.24	0.35	100.57	89.0
127-r	38.22	19.94	0.25	40.22	0.25	0.21	99.08	78.2
148-c	38.86	17.37	0.23	43.33	0.24	0.26	100.29	81.6
148-r	38.22	20.73	0.25	40.89	0.27	0.24	100.60	77.9
147-c	40.17	11.20	0.14	48.41	0.22	0.37	100.50	88.5
147-r	38.46	20.29	0.27	40.61	0.30	0.20	100.13	78.1
149-c	40.32	9.37	0.15	49.53	0.22	0.40	99.99	90.4
149-r1	38.14	20.28	0.27	40.30	0.29	0.21	99.49	78.0
151-c	39.75	13.18	0.21	46.12	0.24	0.30	99.80	86.2
153-c	39.35	15.62	0.20	45.51	0.25	0.28	101.21	83.9
154-r	38.17	19.78	0.24	40.73	0.28	0.23	99.43	78.6
154-c	40.29	10.39	0.17	48.90	0.22	0.35	100.32	89.4
155-c	40.19	10.74	0.15	49.14	0.22	0.34	100.77	89.1
155-r	38.48	20.42	0.24	40.62	0.26	0.25	100.27	78.0
110-c	40.32	9.95	0.13	49.06	0.23	0.38	100.06	89.8
110-r	38.18	19.60	0.27	40.19	0.28	0.21	98.73	78.5

Table 2-5 Olivine compositions of SU-22-64

sample #	SiO ₂	FeO	MnO	MgO	CaO	NiO	total	Fo (%)
SU-22-64								
1-c	39.97	13.82	0.22	45.99	0.24	0.34	100.59	85.6
1-r	38.70	19.71	0.26	41.29	0.31	0.18	100.43	78.9
2-c	39.71	16.95	0.22	43.57	0.25	0.27	100.98	82.1
2-r	39.12	18.64	0.23	42.59	0.27	0.24	101.08	80.3
3-c	39.76	14.64	0.22	45.78	0.23	0.34	100.96	84.8
3-r	39.22	17.60	0.25	42.97	0.28	0.22	100.53	81.3
4-c	39.95	12.66	0.18	47.26	0.26	0.43	100.72	86.9
4-r	39.20	18.32	0.25	42.53	0.33	0.21	100.83	80.5
5-c	40.23	12.82	0.16	46.81	0.29	0.32	100.62	86.7
5-r	38.31	20.31	0.26	40.67	0.30	0.16	99.99	78.1
8-c	39.76	15.77	0.20	44.84	0.30	0.27	101.14	83.5
8-r	38.75	19.93	0.31	41.05	0.32	0.18	100.54	78.6
6-c	41.16	9.25	0.12	49.48	0.22	0.46	100.69	90.5
6-r	38.87	20.19	0.30	41.32	0.30	0.22	101.19	78.5
7-c	40.53	11.05	0.14	48.52	0.24	0.47	100.96	88.7
7-r	38.99	20.52	0.27	40.84	0.33	0.21	101.16	78.0
9-1-c	38.75	19.04	0.23	41.76	0.44	0.18	100.39	79.6
9-1-r	39.39	19.11	0.22	41.42	0.40	0.16	100.70	79.4
9-2-c	39.03	18.16	0.20	42.30	0.43	0.21	100.32	80.6
9-2-r	39.21	18.08	0.25	42.32	0.39	0.17	100.41	80.7
9-3-c	38.83	17.78	0.24	42.50	0.46	0.19	99.99	81.0
9-4-c	39.23	18.46	0.25	42.36	0.39	0.18	100.88	80.4
9-5-c	40.23	17.80	0.19	41.84	1.15	0.16	101.37	80.7
9-6-c	38.66	18.87	0.25	41.99	0.42	0.18	100.36	79.9
10-c	38.73	21.22	0.26	40.42	0.24	0.26	101.12	77.3
10-r	38.83	20.25	0.28	41.11	0.32	0.20	100.99	78.4
11-c	39.69	14.42	0.18	46.00	0.19	0.25	100.72	85.0
11-r	38.96	19.39	0.28	42.04	0.31	0.17	101.15	79.4
12-c	39.82	14.64	0.20	45.62	0.28	0.25	100.80	84.8
12-r	39.29	19.92	0.24	41.38	0.35	0.15	101.31	78.7
15-1-c	39.44	19.57	0.29	42.02	0.31	0.16	101.78	79.3
15-1-r	38.66	20.76	0.32	40.96	0.35	0.16	101.21	77.9
15-2-c	39.20	18.79	0.28	42.32	0.30	0.12	101.02	80.1
15-2-r	39.15	20.09	0.26	41.37	0.30	0.17	101.33	78.6
15-3-c	39.05	19.00	0.29	42.00	0.33	0.16	100.83	79.8
15-3-r	39.02	20.61	0.31	40.91	0.32	0.20	101.35	78.0
15-4-c	38.73	19.28	0.27	42.59	0.30	0.17	101.34	79.8
15-4-r	39.40	19.34	0.32	42.14	0.32	0.22	101.75	79.5
18-c	41.09	9.72	0.14	49.81	0.22	0.45	101.42	90.1
18-r	39.05	20.34	0.30	40.84	0.29	0.21	101.04	78.2
19-c	41.31	9.18	0.13	49.80	0.24	0.47	101.12	90.6
19-r	38.82	20.61	0.32	40.82	0.31	0.14	101.02	77.9
20-c	41.10	9.16	0.10	50.07	0.22	0.40	101.05	90.7
20-r	39.38	19.13	0.28	42.37	0.31	0.19	101.67	79.8

Table 2-5 Continued

sample #	SiO ₂	FeO	MnO	MgO	CaO	NiO	total	Fo (%)
21-r	51.45	7.28	0.15	16.64	20.30	0.00	95.81	80.3
21-2-c	39.44	17.59	0.19	43.35	0.24	0.36	101.17	81.5
21-2-r	39.77	17.41	0.28	43.16	0.32	0.29	101.23	81.5
21-4-c	39.44	17.33	0.21	43.17	0.25	0.28	100.69	81.6
21-4-r	39.52	17.41	0.25	43.28	0.30	0.33	101.08	81.6
22-c	40.75	10.70	0.16	48.61	0.25	0.33	100.81	89.0
22-r	38.94	20.67	0.25	40.72	0.32	0.18	101.08	77.8
23-c	39.96	15.54	0.26	44.58	0.28	0.23	100.85	83.6
23-r	39.33	18.95	0.26	42.06	0.30	0.19	101.08	79.8
25-c	40.47	11.79	0.18	47.40	0.25	0.30	100.38	87.8
25-r	39.25	19.15	0.26	41.94	0.31	0.19	101.10	79.6
26-c	40.28	14.12	0.18	46.19	0.26	0.29	101.32	85.4
26-r	39.59	17.71	0.24	43.40	0.29	0.23	101.45	81.4
27-c	39.96	14.98	0.22	45.73	0.27	0.24	101.39	84.5
27-r	39.17	18.92	0.25	42.32	0.30	0.20	101.16	80.0
28-c	40.15	14.78	0.20	45.27	0.28	0.27	100.95	84.5
28-r	39.77	15.94	0.25	44.41	0.28	0.29	100.95	83.2
29-c	40.77	11.01	0.18	48.52	0.24	0.37	101.09	88.7
29-r	39.15	19.45	0.27	41.49	0.30	0.20	100.85	79.2
31-c	39.74	17.22	0.26	43.70	0.24	0.27	101.43	81.9
31-r	39.27	19.28	0.30	41.84	0.30	0.17	101.15	79.5
32-c	39.92	15.22	0.19	45.24	0.26	0.28	101.12	84.1
32-r	39.35	19.05	0.26	42.13	0.30	0.19	101.28	79.8

Table 2-6 Olivine compositions of MK 6-6

sample #	SiO ₂	FeO	MnO	MgO	CaO	NiO	total	Fo (%)
MK 6-6								
2-c	40.03	9.97	0.14	48.10	0.24	0.36	98.83	89.6
2-r	38.53	17.27	0.23	42.91	0.31	0.23	99.49	81.6
37-c	40.20	9.81	0.14	48.84	0.23	0.36	99.59	89.9
37-r	38.45	17.22	0.19	42.92	0.32	0.24	99.34	81.6
36-c	39.21	14.91	0.17	44.79	0.29	0.28	99.64	84.3
36-r	38.40	16.80	0.21	42.07	0.30	0.20	97.97	81.7
42-c	40.56	9.73	0.14	49.22	0.23	0.37	100.25	90.0
42-r	38.97	15.95	0.22	42.26	0.31	0.23	97.93	82.5
44-c	38.64	16.00	0.21	43.20	0.31	0.22	98.58	82.8
44-r	38.64	17.88	0.22	41.58	0.36	0.23	98.90	80.6
47-c	40.20	9.37	0.13	48.23	0.22	0.36	98.51	90.2
47-r	38.98	17.00	0.25	42.36	0.32	0.24	99.14	81.6
50-c	38.64	14.85	0.18	43.76	0.29	0.28	98.00	84.0
50-r	39.06	14.56	0.19	43.87	0.29	0.26	98.23	84.3
49-c	39.87	10.12	0.13	48.48	0.24	0.35	99.19	89.5
49-r	38.16	18.39	0.26	40.81	0.37	0.23	98.22	79.8
53-c	39.17	14.01	0.17	44.42	0.29	0.28	98.35	85.0
53-r	38.68	16.96	0.22	42.46	0.32	0.23	98.87	81.7
60-c	39.76	10.51	0.14	47.51	0.23	0.32	98.46	89.0
60-r	38.97	17.33	0.24	42.76	0.33	0.22	99.85	81.5
62-c	39.04	13.60	0.19	45.11	0.25	0.27	98.45	85.5
62-r	38.79	17.18	0.19	42.45	0.32	0.21	99.13	81.5
18-c	38.83	14.62	0.19	43.76	0.28	0.24	97.92	84.2
18-r	38.68	16.34	0.19	42.14	0.33	0.23	97.90	82.1
19-c	39.31	12.71	0.13	45.69	0.26	0.25	98.35	86.5
19-r	38.26	18.53	0.20	41.10	0.37	0.21	98.66	79.8
20-c	39.14	15.17	0.18	44.84	0.29	0.30	99.91	84.0
20-r	38.20	16.81	0.23	41.81	0.35	0.23	97.62	81.6
21-c	39.03	14.59	0.16	43.69	0.28	0.28	98.03	84.2
21-r	38.41	16.85	0.19	42.07	0.33	0.21	98.05	81.7
99-c	39.11	14.28	0.18	44.00	0.31	0.24	98.13	84.6
99-r	39.06	17.30	0.21	42.56	0.34	0.21	99.68	81.4
94-c	39.86	9.46	0.14	48.01	0.24	0.34	98.04	90.1
94-r	38.14	16.81	0.20	42.25	0.31	0.23	97.94	81.8
118-c	38.72	14.12	0.19	44.05	0.25	0.30	97.63	84.8
118-r	38.44	16.77	0.19	42.66	0.33	0.23	98.61	81.9
121-c	39.76	10.53	0.16	47.50	0.24	0.34	98.52	88.9
121-r	38.57	16.25	0.22	42.22	0.29	0.22	97.77	82.2
122-c	39.89	9.75	0.13	48.44	0.21	0.39	98.81	89.9
122-r	38.53	15.90	0.24	42.66	0.33	0.22	97.87	82.7

Table 2-1 Continued

sample #	SiO ₂	FeO	MnO	MgO	CaO	NiO	total	Fo (%)
80-r	39.11	19.26	0.30	41.57	0.34	0.22	100.81	79.4
80-c	40.72	10.93	0.17	48.58	0.23	0.37	100.99	88.8
86-c	40.14	13.50	0.26	46.85	0.25	0.36	101.35	86.1
86-r	39.21	18.81	0.29	42.38	0.30	0.20	101.20	80.1
87-c	41.02	9.13	0.14	49.61	0.25	0.43	100.58	90.6
87-r	39.30	18.33	0.25	42.74	0.28	0.23	101.12	80.6
89-c	40.56	11.05	0.14	48.56	0.26	0.39	100.96	88.7
89-r	39.44	17.02	0.30	43.60	0.28	0.27	100.90	82.0
90-c	40.43	10.22	0.15	48.80	0.24	0.36	100.20	89.5
90-r	39.00	19.46	0.28	41.73	0.35	0.24	101.06	79.3
92-c	40.20	13.37	0.24	47.08	0.29	0.34	101.52	86.3
92-r	40.00	18.89	0.29	41.65	0.35	0.22	101.39	79.7
72-c	38.60	18.90	0.28	41.89	0.28	0.17	100.12	79.8
72-r	39.25	18.23	0.29	42.56	0.30	0.24	100.87	80.6
65-r	39.61	17.12	0.22	43.05	0.29	0.29	100.57	81.8
65-c	40.18	12.07	0.24	47.05	0.26	0.39	100.19	87.4
58-c	40.70	9.85	0.20	48.36	0.21	0.42	99.75	89.7
58-r	39.03	18.67	0.27	41.42	0.29	0.25	99.94	79.8
96-c	39.30	13.85	0.20	44.54	0.28	0.32	98.48	85.1
96-r	39.26	18.19	0.29	41.88	0.28	0.23	100.14	80.4
57-c	40.64	9.79	0.13	48.54	0.22	0.40	99.72	89.8
57-r	39.35	17.99	0.25	42.00	0.25	0.25	100.10	80.6
14-c	39.59	15.35	0.18	43.69	0.29	0.17	99.26	83.5
14-r	39.05	18.96	0.32	42.17	0.27	0.22	100.98	79.9

In the column of sample #, c indicates core composition and r indicates rim composition.

Table 3 Representative plagioclase compositions

		SiO ₂	Al ₂ O ₃	FeO	MgO	CaO	Na ₂ O	K ₂ O	total	An (%)
SU-21-64										
pl-1	core	55.10	27.97	0.79	0.13	11.32	4.67	0.14	100.12	56.8
	rim	52.44	29.77	0.87	0.29	13.49	3.48	0.09	100.43	67.8
pl-2	core	54.08	29.06	0.86	0.19	12.05	4.37	0.14	100.76	59.9
	rim	51.75	30.56	0.75	0.19	13.87	3.21	0.07	100.40	70.2
pl-3	core	52.26	30.81	0.84	0.23	14.11	3.19	0.08	101.52	70.7
	rim	53.64	29.46	0.80	0.21	12.52	4.05	0.12	100.80	62.7
pl-101	core	51.91	30.29	0.63	0.07	13.39	3.47	0.17	99.93	67.4
	core	50.30	31.33	0.59	0.07	14.37	2.86	0.12	99.62	73.0
pl-98	core	55.12	28.23	0.63	0.04	11.19	4.65	0.28	100.15	56.2
	rim	53.82	29.06	0.68	0.05	11.97	4.33	0.21	100.12	59.7
pl-99	core	53.47	29.16	0.62	0.05	12.10	4.22	0.29	99.91	60.3
	rim	52.94	29.55	0.65	0.05	12.91	3.88	0.23	100.21	63.9
pl-104	core	54.59	28.28	0.61	0.05	11.18	4.65	0.33	99.69	56.0
	rim	51.96	30.52	0.60	0.07	13.82	3.28	0.15	100.40	69.4
pl-110	core	54.26	28.89	0.68	0.05	11.91	4.48	0.30	100.59	58.5
	rim	50.62	30.88	0.62	0.08	14.04	2.94	0.18	99.35	71.8
pl-s-1	core	52.49	29.51	0.79	0.09	13.01	3.67	0.18	99.71	65.5
	rim	51.26	30.50	0.69	0.08	13.90	3.10	0.16	99.69	70.6
pl-s-2	core	51.18	30.84	0.71	0.07	13.89	3.18	0.21	100.09	69.8
	rim	50.92	29.88	0.77	0.08	13.51	3.96	0.19	99.31	64.7
pl-s-3	core	53.18	28.45	0.92	0.16	12.76	3.86	0.23	99.56	63.8
	rim	51.17	30.72	0.66	0.08	14.09	3.03	0.17	99.91	71.3
MK2-1										
pl-1	core	52.68	29.47	0.83	0.32	13.18	3.58	0.12	100.19	66.6
	rim	51.63	29.84	0.75	0.31	13.58	3.16	0.09	99.36	70.0
pl-2	core	52.42	30.02	0.77	0.29	13.44	3.57	0.10	100.62	67.2
	rim	51.25	30.74	0.85	0.31	14.15	3.17	0.08	100.55	70.9
pl-3	core	51.41	30.74	0.54	0.24	13.78	3.27	0.09	100.06	69.6
	rim	51.95	30.48	0.92	0.25	13.59	3.44	0.08	100.71	68.3
pl-s-1	core	51.59	30.77	0.80	0.11	14.15	3.02	0.22	100.65	71.2
	rim	52.75	29.53	0.89	0.13	13.15	3.55	0.26	100.25	66.2
pl-s-2	core	52.54	29.52	0.87	0.14	13.19	3.49	0.27	100.01	66.6
	rim	51.93	30.51	0.75	0.11	13.69	3.05	0.27	100.30	70.2

Table 3 Continued

		SiO ₂	Al ₂ O ₃	FeO	MgO	CaO	Na ₂ O	K ₂ O	total	An (%)
SU-20-64										
pl-0	core	53.46	29.16	0.80	0.05	12.21	4.23	0.44	100.35	59.9
	rim	53.91	29.38	0.82	0.07	12.58	3.91	0.39	101.06	62.6
pl-126	core	54.46	28.29	0.75	0.04	11.36	4.48	0.53	99.91	56.6
	rim	53.03	29.57	0.69	0.09	12.71	3.72	0.29	100.11	64.3
pl-19	core	53.44	29.59	0.65	0.08	12.63	3.87	0.36	100.62	63.0
	rim	52.70	30.12	0.63	0.09	13.41	3.45	0.18	100.58	67.5
pl-109	core	52.00	29.63	0.77	0.11	12.51	3.90	0.37	99.29	62.5
	rim	51.76	30.50	0.71	0.08	13.80	3.19	0.16	100.21	69.9
pl-180	core	56.49	27.41	0.65	0.02	10.20	5.06	0.47	100.28	51.3
	rim	52.79	29.11	0.77	0.08	13.10	3.53	0.38	99.76	65.7
pl-s-1	core	53.59	28.95	0.71	0.10	12.21	3.96	0.32	99.83	61.8
	rim	51.84	30.00	0.79	0.10	13.65	3.50	0.27	100.15	67.2
pl-s-2	core	53.46	29.15	0.79	0.09	12.21	3.97	0.26	99.91	62.0
	rim	52.51	29.92	0.84	0.08	13.10	3.58	0.33	100.35	65.6
pl-1	core	53.38	29.25	0.74	0.09	12.30	4.18	0.12	100.05	61.5
pl-2	core	53.34	29.30	0.77	0.22	12.39	4.07	0.13	100.22	62.2
	rim	52.53	30.11	1.00	0.21	13.16	3.74	0.12	100.85	65.6
pl-3	core	55.22	27.53	1.12	0.30	11.18	4.71	0.14	100.21	56.3
	rim	56.62	27.91	1.11	0.32	11.16	3.00	0.13	100.25	66.7
SU-22-64										
pl-2	core	50.79	31.30	0.60	0.17	14.29	3.09	0.10	100.35	71.5
	rim	52.68	29.91	0.70	0.22	12.89	3.72	0.16	100.28	65.1
pl-3	core	52.54	29.65	0.77	0.22	12.97	3.65	0.10	99.90	65.9
	rim	50.60	31.25	0.79	0.17	14.67	2.84	0.07	100.39	73.8
pl-4	core	52.23	30.47	0.64	0.19	13.12	3.56	0.14	100.35	66.5
	rim	49.60	31.02	0.57	0.16	12.92	3.01	0.16	97.44	69.7
pl-1-1	core	52.14	30.05	0.46	0.08	13.52	3.73	0.19	100.17	66.0
	rim	49.24	31.64	0.54	0.07	15.14	2.62	0.12	99.36	75.7
pl-5	core	51.59	30.71	0.58	0.06	13.29	3.28	0.26	99.77	68.1
	rim	53.07	28.98	0.80	0.07	12.40	4.17	0.37	99.85	60.9
pl-6	core	51.01	30.64	0.58	0.06	13.80	3.28	0.27	99.64	68.8
	rim	52.85	29.60	0.64	0.06	12.93	3.88	0.32	100.27	63.6
pl-7	core	51.81	30.08	0.63	0.06	13.41	3.53	0.34	99.86	66.4
	rim	53.03	29.26	0.70	0.06	12.34	4.06	0.37	99.83	61.3
pl-8	core	51.92	30.27	0.53	0.06	13.36	3.40	0.29	99.83	67.3
	rim	50.43	31.06	0.54	0.06	14.22	2.99	0.22	99.51	71.6
pl-9	core	52.16	30.17	0.61	0.07	13.07	3.72	0.27	100.07	65.0
	rim	52.81	29.01	0.84	0.08	12.70	3.93	0.34	99.70	62.9
pl-10	core	51.99	29.89	0.57	0.06	12.97	3.62	0.28	99.38	65.4
	rim	52.56	29.99	0.61	0.06	12.49	3.70	0.33	99.74	63.8
	rim	51.17	30.61	0.62	0.07	13.80	3.24	0.25	99.76	69.2

Table 4 Representative augite compositions

		SiO ₂	TiO ₂	Al ₂ O ₃	Cr ₂ O ₃	FeO	MnO	MgO	CaO	Na ₂ O	total	Mg#
SU-21-64												
cpx-1	core	51.49	1.00	2.06	0.01	10.57	0.27	15.33	18.50	0.27	99.49	72.1
	rim	53.08	0.65	1.99	0.56	6.35	0.12	17.92	19.32	0.22	100.22	83.4
cpx-2	core	51.42	1.08	2.28	0.02	10.61	0.27	15.35	18.62	0.34	99.99	72.1
	rim	51.93	0.75	2.80	0.79	7.20	0.18	18.34	17.92	0.23	100.15	81.9
cpx-3	core	51.83	1.06	2.20	0.02	10.62	0.28	15.33	18.90	0.36	100.59	72.0
	rim	52.14	0.86	3.35	0.92	6.86	0.20	17.29	18.80	0.23	100.65	81.8
cpx-5	core	52.95	0.72	2.15	0.09	8.07	0.22	17.07	19.09	0.23	100.59	79.0
	core	51.50	0.95	2.29	0.15	8.78	0.21	16.61	18.90	0.27	99.65	77.1
	rim	52.17	0.68	2.88	0.97	6.16	0.16	17.46	19.75	0.24	100.47	83.5
cpx-6	core	51.80	1.07	2.40	0.18	9.99	0.30	15.81	18.76	0.28	100.60	73.8
	core	51.97	0.90	2.41	0.23	8.31	0.20	16.73	18.90	0.24	99.88	78.2
	rim	51.91	0.77	3.11	0.92	6.53	0.17	17.49	18.84	0.30	100.04	82.7
cpx-7	core	51.97	1.07	2.75	0.14	9.29	0.19	17.11	17.51	0.24	100.26	76.7
	core	51.84	0.98	2.52	0.13	9.61	0.24	16.14	18.48	0.30	100.25	75.0
	rim	52.00	0.80	3.24	0.87	6.78	0.18	17.27	19.26	0.28	100.68	82.0
cpx-9	core	51.74	0.97	2.17	0.00	10.97	0.32	15.20	18.73	0.27	100.37	71.2
	rim	53.08	0.67	1.93	0.66	6.30	0.19	18.07	19.28	0.18	100.37	83.6
cpx-10*	rim	52.79	0.66	2.00	0.69	6.36	0.17	18.06	18.79	0.26	99.79	83.5
	rim	51.88	1.08	3.75	0.63	8.76	0.23	18.53	15.59	0.27	100.69	79.0
cpx-11*	rim	51.34	1.01	3.80	0.76	8.50	0.23	18.47	16.25	0.27	100.64	79.5
MK2-1												
cpx-1	core	51.66	0.97	3.50	1.05	7.41	0.22	17.99	16.97	0.20	99.97	81.2
	rim	53.24	0.64	1.81	0.64	6.65	0.17	18.51	17.91	0.20	99.76	83.2
cpx-2	core	50.84	1.41	3.90	0.59	8.68	0.25	17.47	16.47	0.23	99.84	78.2
	rim	52.87	0.76	2.24	0.49	7.79	0.21	17.89	17.55	0.21	100.00	80.4
cpx-3	core	50.50	1.41	3.58	0.33	9.17	0.22	17.57	16.46	0.20	99.45	77.4
	rim	51.70	0.80	2.67	0.65	7.01	0.17	17.54	18.35	0.23	99.13	81.7
cpx-5	core	50.37	1.56	4.19	0.63	7.36	0.20	16.31	18.89	0.22	99.72	79.8
	rim	51.73	0.85	3.07	1.06	6.45	0.19	17.26	18.52	0.20	99.32	82.7
cpx-6	core	52.05	0.91	2.86	0.78	6.64	0.18	16.77	19.54	0.20	99.93	81.8
cpx-7	core	52.13	0.75	2.80		6.65		17.45	18.90	0.23	98.89	82.4

Table 4 Continued

		SiO ₂	TiO ₂	Al ₂ O ₃	Cr ₂ O ₃	FeO	MnO	MgO	CaO	Na ₂ O	total	Mg#
SU-20-64												
cpx-1	core	51.52	1.06	2.43	0.15	9.65	0.22	15.88	18.79	0.27	99.96	74.6
	rim	51.25	1.02	3.22	0.72	7.46	0.21	16.80	19.03	0.29	99.99	80.1
cpx-2	core	52.49	0.86	2.25	0.48	8.81	0.28	18.33	16.49	0.26	100.24	78.8
cpx-3	core	51.63	1.00	3.29	0.73	8.39	0.23	17.57	17.27	0.32	100.43	78.9
cpx-5	core	51.15	1.30	2.88	0.05	11.00	0.29	15.37	18.13	0.32	100.49	71.4
	rim	51.62	1.09	3.36	0.73	7.64	0.22	16.91	18.89	0.30	100.75	79.8
cpx-6	core	51.41	1.09	2.46	0.17	11.22	0.29	14.92	18.72	0.32	100.60	70.3
	rim	51.28	1.20	3.41	0.21	7.81	0.18	16.87	18.75	0.26	99.97	79.4
cpx-15	core	51.88	1.05	2.24		9.13		16.22	19.00	0.36	99.88	76.0
	core	52.19	0.87	1.98		8.62		16.52	18.91	0.31	99.39	77.4
	rim	52.84	0.63	1.89		7.09		17.79	18.75	0.30	99.28	81.7
cpx-16	core	51.55	1.11	2.77		8.40		16.67	18.97	0.28	99.74	78.0
	rim	53.27	0.64	1.58		8.66		19.62	15.41	0.29	99.46	80.2
cpx-17	core	51.20	0.71	1.50		14.20		14.08	17.23	0.32	99.24	63.9
	rim	51.20	1.00	2.85		7.86		17.46	17.81	0.21	98.39	79.8
MK1-8												
cpx-1	core	52.66	0.65	1.54	0.47	7.29	0.21	18.66	16.99	0.17	98.64	82.0
	rim	51.22	1.19	2.89	0.63	8.09	0.18	17.16	17.21	0.30	98.87	79.1
cpx-3	core	51.01	1.30	3.71	0.95	6.56	0.19	16.16	19.95	0.27	100.09	81.5
cpx-5	core	52.10	0.91	2.57	0.81	7.37	0.16	17.71	17.91	0.26	99.79	81.1
cpx-131	core	51.01	1.05	2.59		9.05		17.41	17.26	0.17	98.53	77.4
	core	50.33	1.43	3.13		10.02		15.43	18.55	0.35	99.23	73.3
	rim	51.51	0.99	2.70		7.19		16.94	19.14	0.31	98.77	80.8
cpx-129	core	52.89	0.74	1.84		8.52		18.59	16.34	0.24	99.16	79.6
	rim	52.85	0.71	1.69		6.49		17.65	19.12	0.17	98.67	82.9
cpx-132	core	50.21	1.54	2.98		11.47		15.16	18.29	0.41	100.06	70.2
	rim	51.88	1.06	2.41		7.97		16.78	18.57	0.20	98.88	79.0
cpx-133	core	50.70	1.48	2.95		9.89		15.46	18.40	0.41	99.28	73.6
	rim	52.02	0.97	2.31		8.16		17.02	17.83	0.27	98.58	78.8
cpx-136	core	51.83	1.15	2.13		10.09		15.72	18.66	0.21	99.78	73.5
	rim	52.26	0.98	2.42		7.34		17.55	17.92	0.33	98.80	81.0
SU-22-64												
cpx-2	core	52.36	0.92	2.69	0.97	5.91	0.15	17.44	19.58	0.33	100.35	84.0
cpx-1	core	52.29	0.78	2.76	1.03	5.55	0.07	17.28	20.16	0.29	100.21	84.7
cpx-3	core	50.28	1.30	3.97	0.98	5.86	0.13	15.17	21.83	0.31	99.83	82.2
cpx-5	core	51.55	1.10	3.19	0.55	7.05	0.11	15.98	20.54	0.32	100.39	80.2
cpx-6	core	51.77	1.15	2.60	0.71	7.60	0.11	16.54	19.49	0.34	100.30	79.5
cpx-7	core	51.97	0.70	2.76	1.08	5.23	0.10	17.02	20.25	0.23	99.34	85.3

* indicates augite rims enclosing orthopyroxene.

Table 5 Representative orthopyroxene compositions

		SiO ₂	TiO ₂	Al ₂ O ₃	Cr ₂ O ₃	FeO	MnO	MgO	CaO	Na ₂ O	total	Mg#
SU-21-64												
opx-8	core	54.45	0.55	1.33	0.02	15.55	0.32	26.16	2.04	0.03	100.45	75.0
	core	54.09	0.55	1.30	0.05	16.17	0.30	25.80	2.07	0.03	100.36	74.0
	rim	55.68	0.33	1.22	0.27	11.19	0.21	29.24	2.36	0.02	100.52	82.3
opx-1	core	53.79	0.57	1.39	0.12	16.34	0.35	25.46	1.94	0.06	100.01	73.5
	rim	55.01	0.45	1.94	0.47	11.11	0.23	28.69	2.50	0.02	100.41	82.1
opx-2	core	54.63	0.45	1.17	0.07	14.76	0.29	26.95	2.19	0.03	100.52	76.5
	rim	55.34	0.34	1.05	0.21	11.36	0.19	29.10	2.36	0.03	99.98	82.0
MK2-1												
opx-1	core	54.68	0.55	1.51	0.26	12.00	0.24	28.43	2.21	0.07	99.94	80.9
		55.19	0.50	1.38	0.25	11.65	0.22	28.62	2.09	0.03	99.91	81.4
SU-20-64												
opx-1	core	53.25	0.59	1.43	0.07	18.01	0.41	24.59	2.02	0.07	100.43	70.9
MK1-8												
opx-110	core	52.67	0.72	1.36	0.15	15.84	0.33	25.49	2.32	0.05	98.93	74.2
	core	53.69	0.44	0.84	0.09	15.34	0.27	26.47	2.15	0.08	99.37	75.5
	rim	54.15	0.60	1.20	0.26	13.21	0.23	26.63	2.37	0.00	98.65	78.2
opx-36	core	54.02	0.48	1.07	0.16	14.43	0.31	26.97	2.08	0.06	99.58	76.9
	core	53.90	0.50	1.33	0.18	13.27	0.29	27.59	2.15	0.03	99.24	78.8
	rim	52.73	0.68	1.67	0.26	14.66	0.26	25.72	2.52	0.03	98.53	75.8
opx-126	rim	54.04	0.45	1.74	0.50	12.15	0.20	28.15	2.42	0.05	99.70	80.5
	core	53.01	0.68	1.48	0.19	15.03	0.26	26.36	2.59	0.03	99.63	75.8
SU-22-64												
opx-1	core	54.54	0.58	1.36	0.11	13.21	0.25	27.45	2.26	0.04	99.79	78.7
	core	54.54	0.57	1.44	0.20	12.93	0.34	27.77	2.27	0.08	100.15	79.3
opx-2	core	55.37	0.38	0.96	0.15	12.59	0.29	28.33	2.21	0.04	100.31	80.1
opx-3	core	54.91	0.44	1.61	0.35	11.74	0.25	28.70	2.17	0.05	100.23	81.3
opx-5	core	53.53	0.67	1.43	0.04	16.69	0.33	25.18	2.29	0.03	100.19	72.9
opx-6	core	55.12	0.43	1.36	0.39	11.19	0.23	29.04	2.15	0.06	99.98	82.2
opx-7	core	54.86	0.44	1.24	0.25	11.93	0.23	28.74	2.29	0.06	100.03	81.1
opx-8	core	54.37	0.55	1.45	0.32	14.34	0.30	26.74	2.00	0.02	100.09	76.9
opx-9	core	55.05	0.40	1.48	0.39	10.97	0.21	28.98	2.28	0.09	99.85	82.5
opx-10	core	55.20	0.54	1.37	0.41	10.96	0.21	29.44	2.15	0.06	100.35	82.7
opx-11	core	55.06	0.41	1.40	0.28	11.20	0.25	28.75	2.30	0.04	99.70	82.1

CAPTIONS

- Fig. 1 Illustration of structures below adjacent Kilauea and Mauna Loa volcanoes. The arrows indicate the paths of magma flow.
- Fig. 2 Olivine compositions for six dredged Mauna Kea submarine samples. Circles are core compositions and triangles are rim compositions. For each sample, the lower line of data points are for deformed grains and upper line is for undeformed grain. The boxes at the high Fo end are olivine compositions in equilibrium with whole rock compositions; those at the low Fo end are in equilibrium with glass compositions (Fe-Mg exchange $K_D = 0.3 \pm 0.03$ and ferrous iron = 85% of total iron).
- Fig. 3 Back-scattered electron images taken with a scanning electron microscope. A) An augite-plagioclase clot (x 40). Plagioclase is resorbed and augites show compositional contrast between cores and rims. B) A locally resorbed plagioclase with deep embayments (x 40). C) A rounded orthopyroxene enclosed by more magnesium orthopyroxene and augite rims (x 200). D) A rounded orthopyroxene in MK2-1 with plagioclase and glass inclusions (x 60). E) Anhedral orthopyroxene enclosed by fine-grain augites and olivines (x 40). F) Anhedral orthopyroxene with an embayed augite rim (x 60). G) A rounded orthopyroxene enclosed by fine-grain augites, and mantled by euhedral augite (x 120). H) An anhedral augite rimmed by orthopyroxene, and enclosed by fine-grained augites and olivines (x 170). The outermost layer contains fine-grain olivines.
- Fig. 4 Plagioclase compositions for four dredged Mauna Kea submarine samples. A horizontal line indicates the compositional variation in a grain. When the core and rim show compositional contrast under SEM, the compositional range for core is indicated by a thick solid line and that for rim is indicated by a thin solid line. The dotted lines indicate the compositional gap between core and rim. In some samples there are little compositional contrast between rims and cores; for these samples the

compositional ranges are indicated by thick solid lines. The box for each sample is the compositional range in equilibrium with glass calculated from the model of Grove et al. (1992) at 0.001-5 kb. The range for SU-22-64 is based on two glasses, while those for other samples are calculated from one glass composition.

Fig. 5 Augite compositions for five dredged Mauna Kea submarine samples. Symbols are as Fig. 3. The boxes are compositions in equilibrium with glass calculated with a Fe-Mg exchange $K_D=0.25\pm 0.2$ (Tormey et al., 1987; Grove et al., 1992) and ferrous iron=85% of total iron. * indicates augite rims enclosing orthopyroxene.

Fig. 6 Orthopyroxene compositions for five dredged Mauna Kea submarine samples. Symbols are as Fig. 3. $K_D=0.25\pm 0.2$ (Grove and Juster, 1989) and ferrous iron=85% of total iron.

Fig. 7 Representative core to rim compositional variations of plagioclase, orthopyroxene, and augite in SU-21-64. The inset in the plagioclase panel shows the zonation of an euhedral microphenocryst. For comparative purposes the vertical scale is the same in Figs. 7, 8, 9, 10, and 11.

Fig. 8 Representative core to rim compositional variations of plagioclase, orthopyroxene, and augite in MK2-1.

Fig. 9 Representative core to rim compositional variations of plagioclase and augite in SU-20-64. The inset in the plagioclase panel shows the zonation of an euhedral microphenocryst.

Fig. 10 Representative core to rim compositional variations of augite and orthopyroxene in MK1-8.

Fig. 11 Representative core to rim compositional variations of augite and orthopyroxene in SU-22-64. The variation shown for plagioclase is from rim to rim.

Fig. 12 Curves indicate Mg# in coexisting melt and solid. Each curve is calculated with a different Fe-Mg exchange K_D . The two boxes are compositions of the most iron-

rich augites in SU-20-64 and SU-21-64. The Mg# in their coexisting melt are estimated from $K_D=0.25\pm0.2$

Fig. 13 A closed system mass balance showing the amount of olivine precipitation required to generate various residual melts (lines labeled % MgO in residual melt) from parental magmas of various MgO contents indicated by the horizontal axis. A mean olivine composition of Fo_{86} is used for the calculation.

Fig. 14 Olivine proportions calculated by mixing between evolved melts (3~5% MgO) with no olivine and mafic melt (7~11% MgO) containing olivine. See text for the method of calculation. For each sample, different symbols indicate various evolved melt compositions. Each evolved melt was mixed with mafic melts with 7% MgO (the highest in each column), 9% MgO (the middle one in each column) and 11% MgO (the lowest in each column). The horizontal lines indicate olivine wt% in each sample. Olivine wt% was converted from vol% reported in table 1 of chapter 2 by assuming that the densities of olivine, plagioclase, pyroxene and groundmass are 3.3, 2.7, 3.2 and 2.68 g/cm³, respectively.

Fig. 15 An illustrative Ol-Di-Qtz pseudoternary (projected from the plagioclase corner of the Ol-Di-Qtz-Plag tetrahedron on to the Ol-Di-Qtz plane) modified from Stöpler (1980). When the pressure decreases, the multiple saturation point shifts towards the Qtz corner as indicated by the thick arrow. Point A represents a melt saturated with olivine, augite and orthopyroxene at a high pressure. As pressure decreases, melt with the composition of point A changes from 4-phase saturated (ol-plag-cpx-opx) to 3-phase saturated to saturation with only plagioclase and olivine.

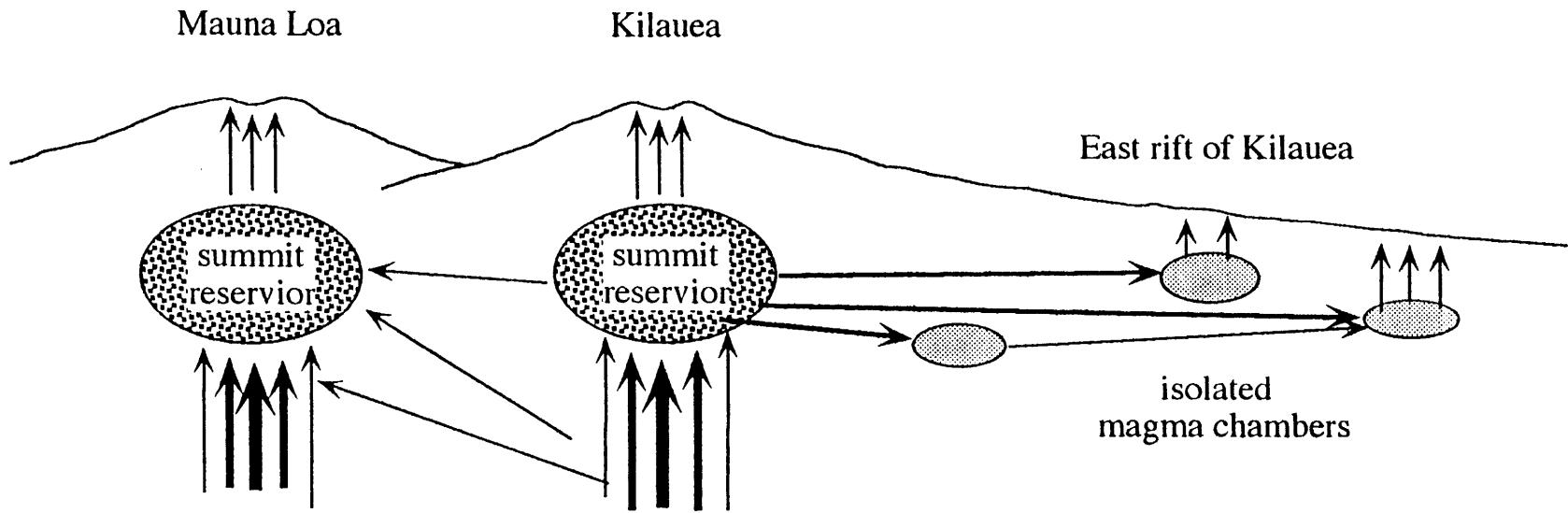


Fig. 1

Olivine [o = core, Δ = rim]

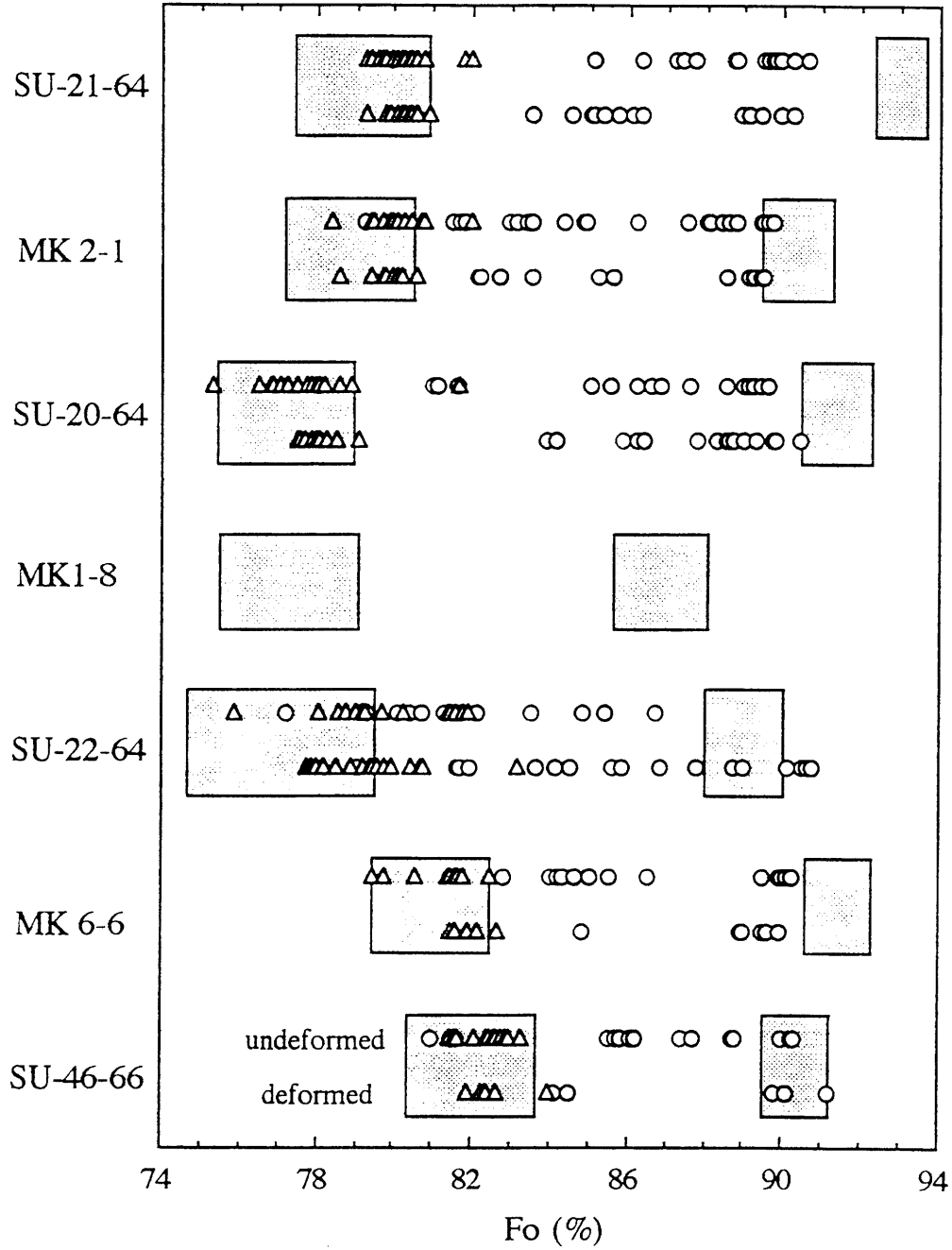


Fig. 2

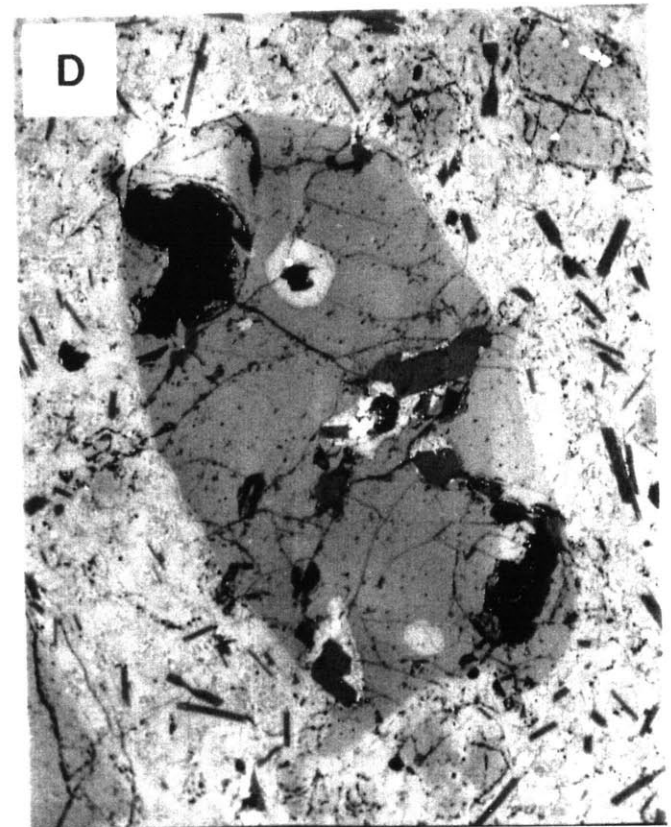
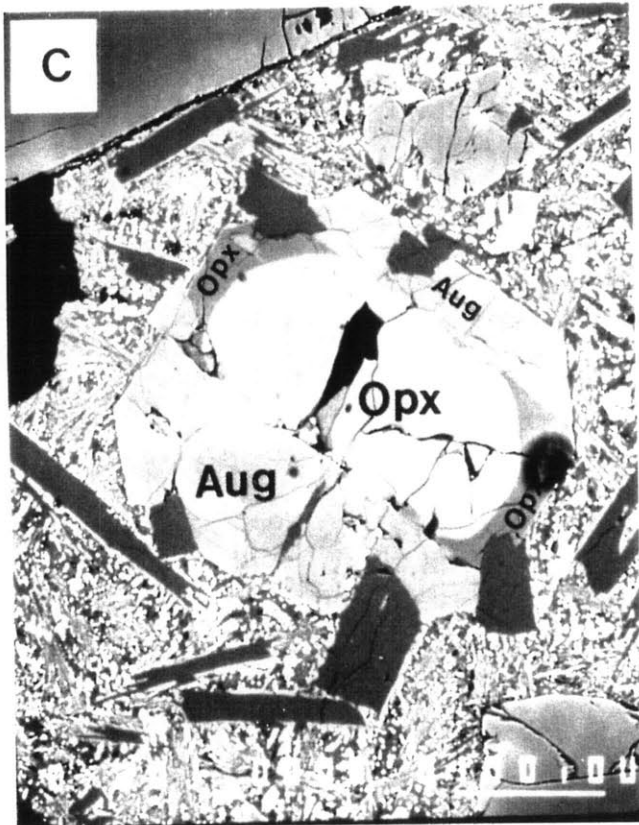
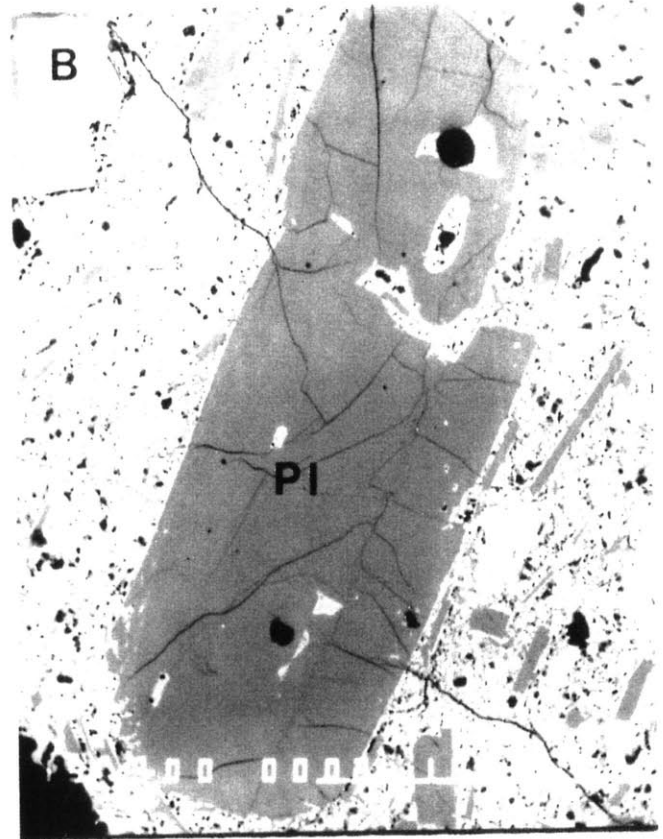
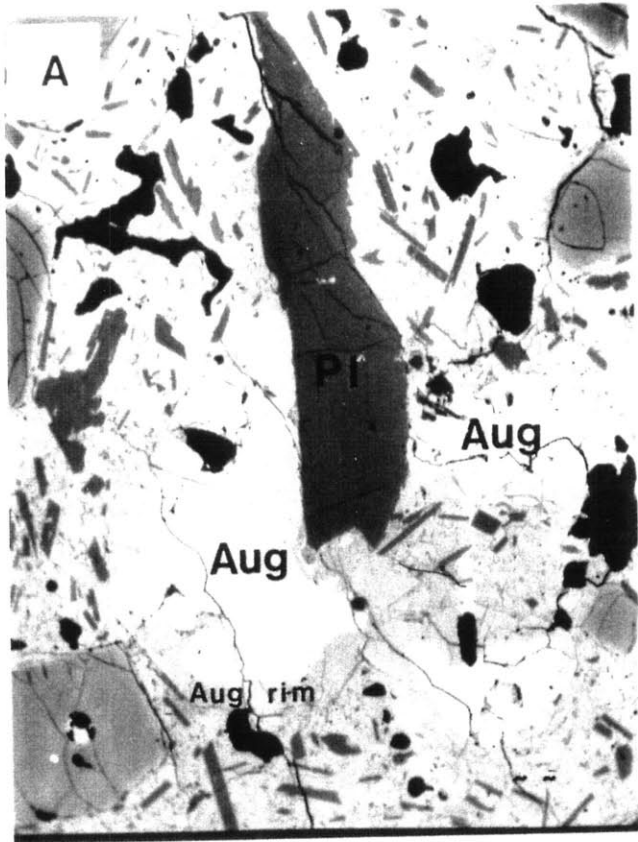


Fig. 3a

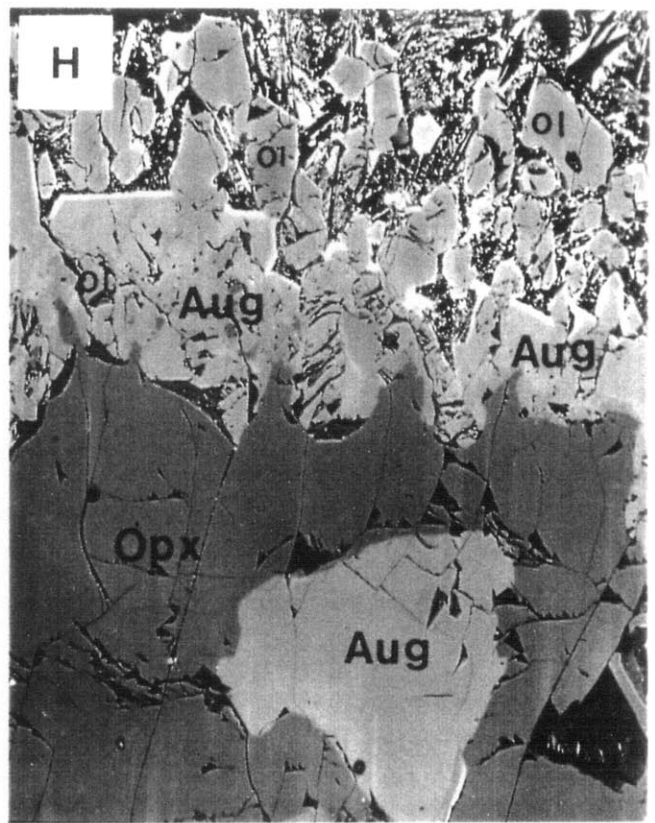
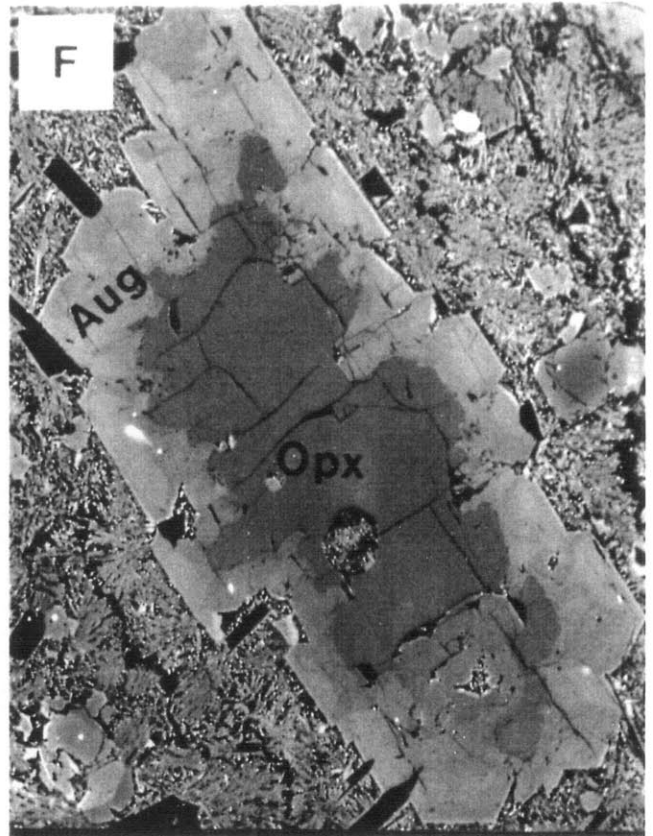
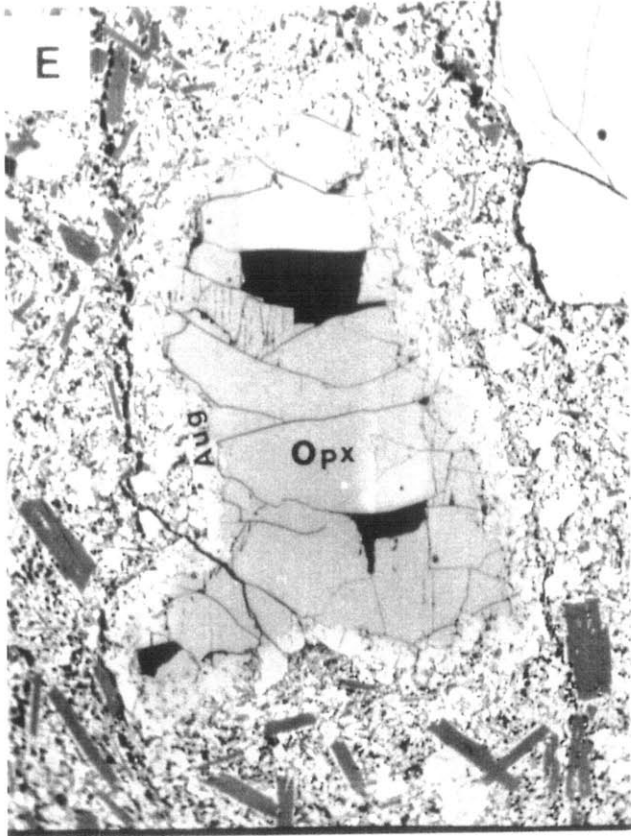


Fig. 3b

Plagioclase

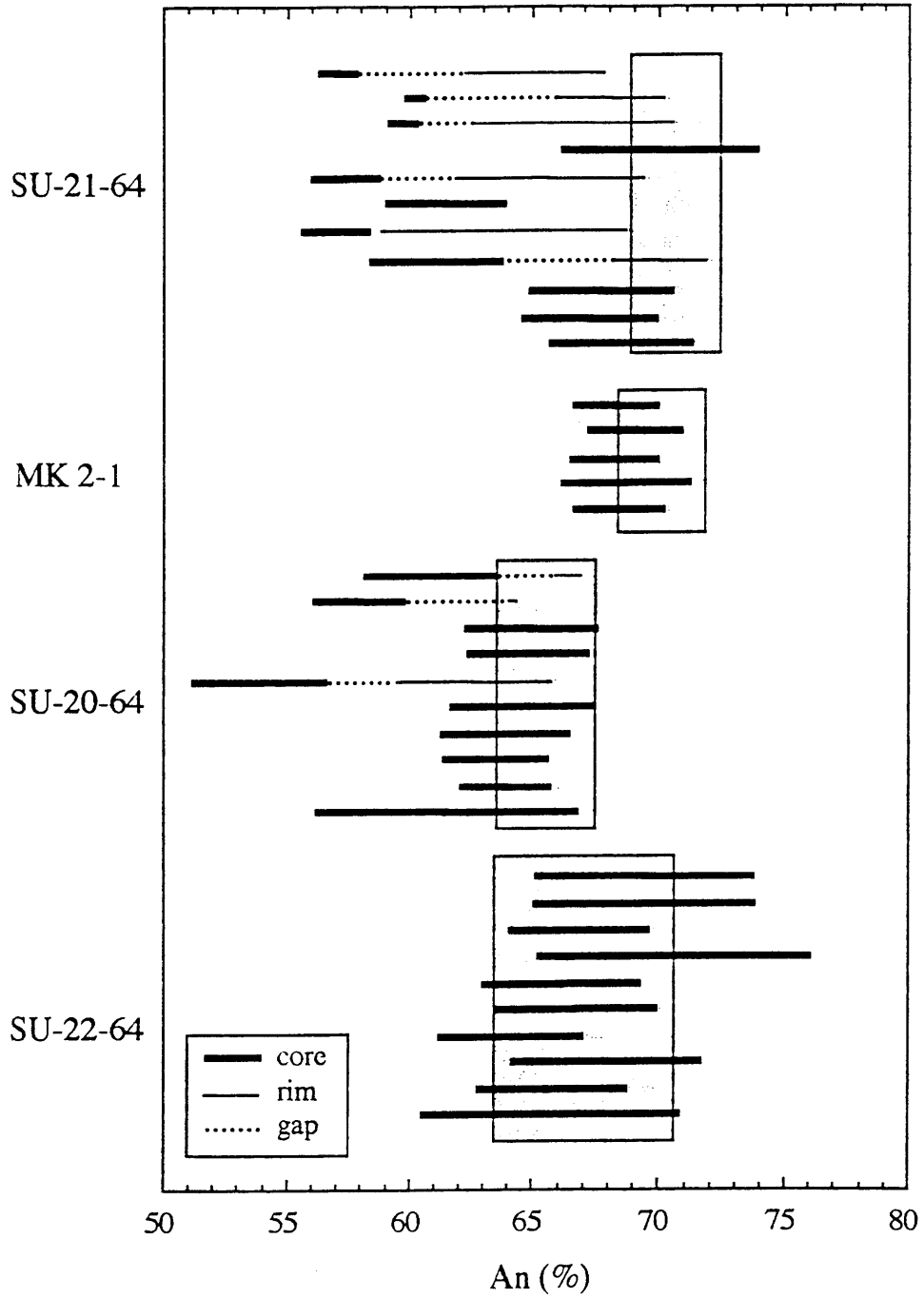


Fig. 4

Augite

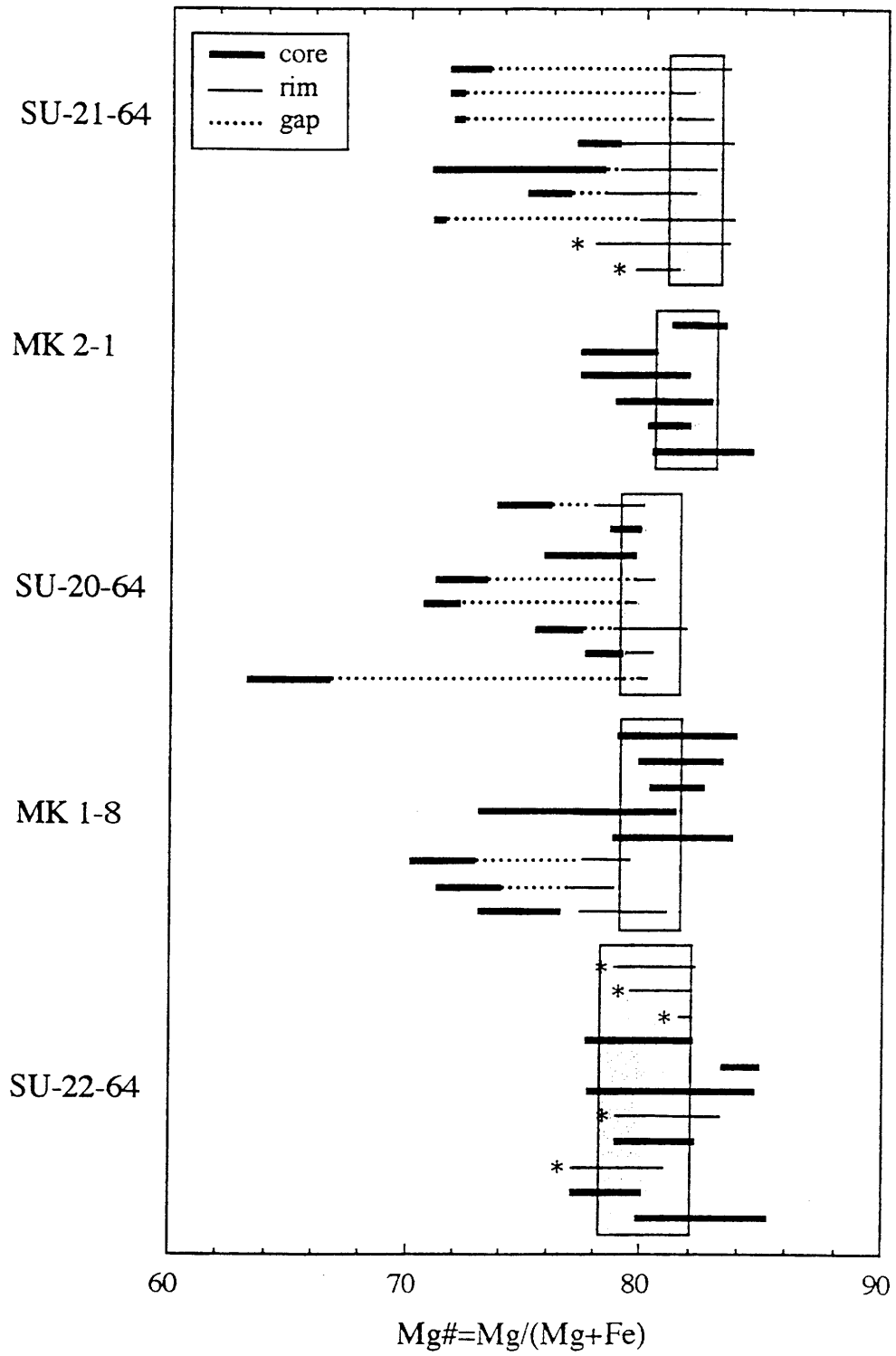


Fig. 5

Orthopyroxene

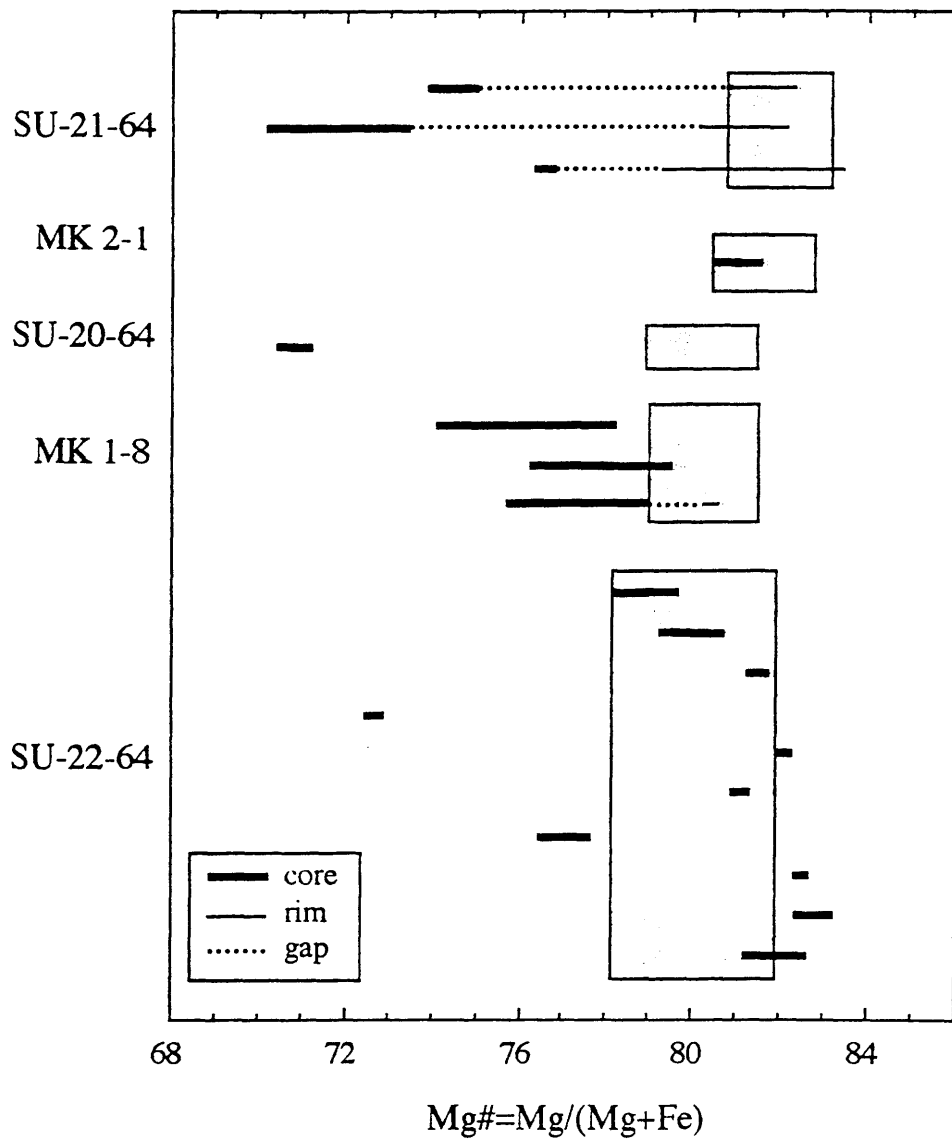
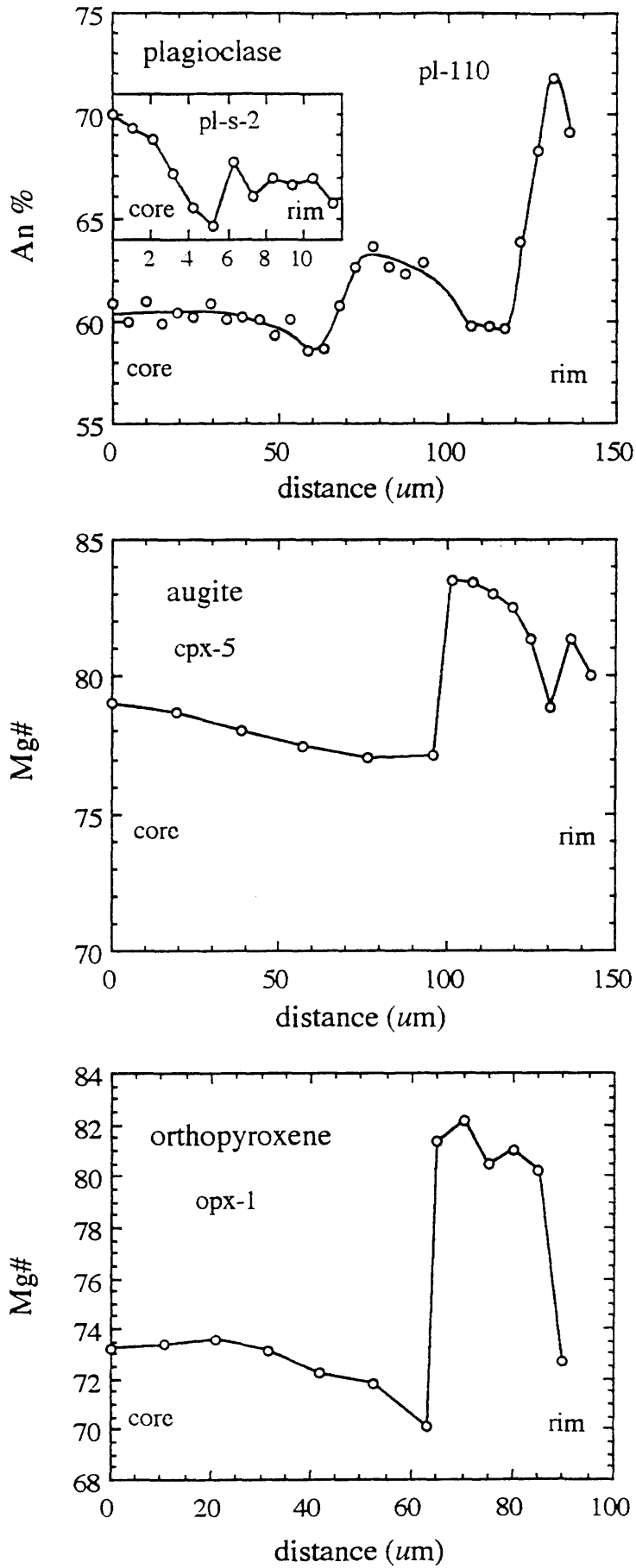


Fig. 6

SU-21-64



MK 2-1

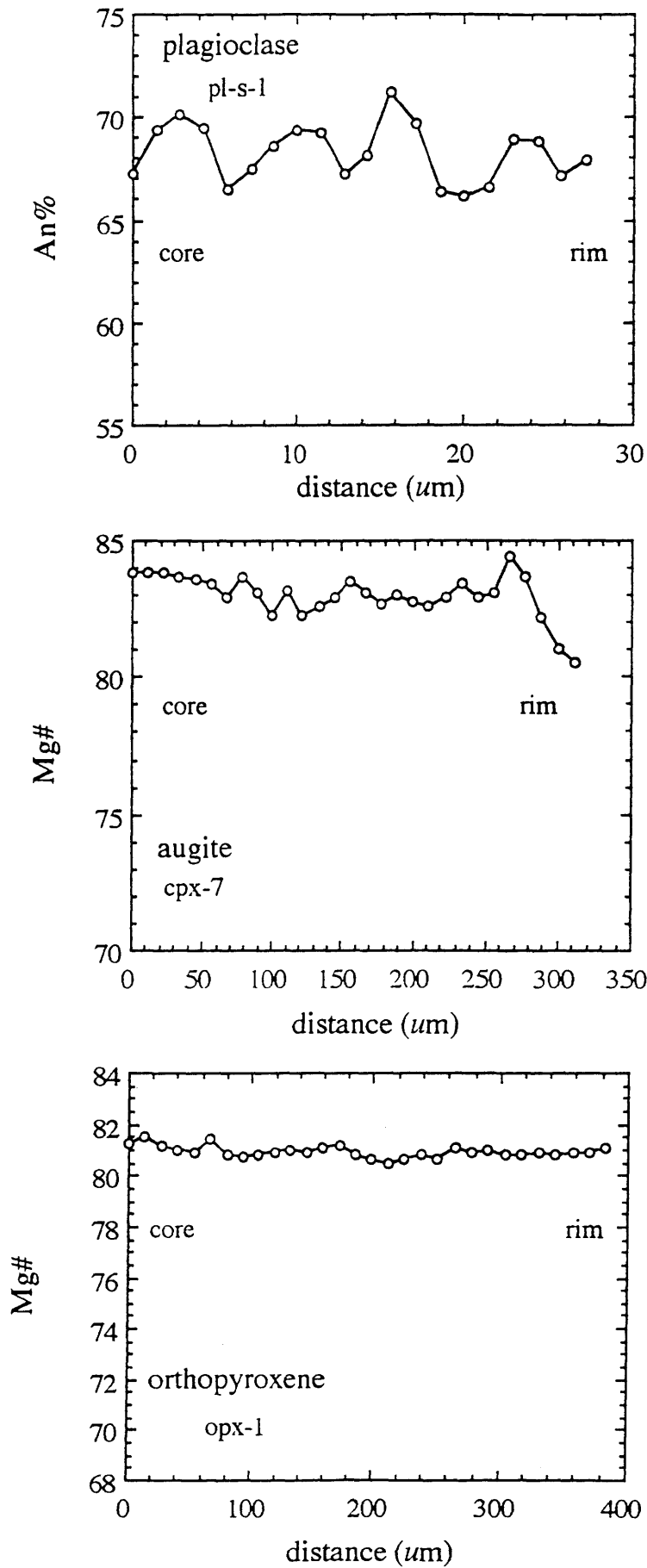


Fig. 8

SU-20-64

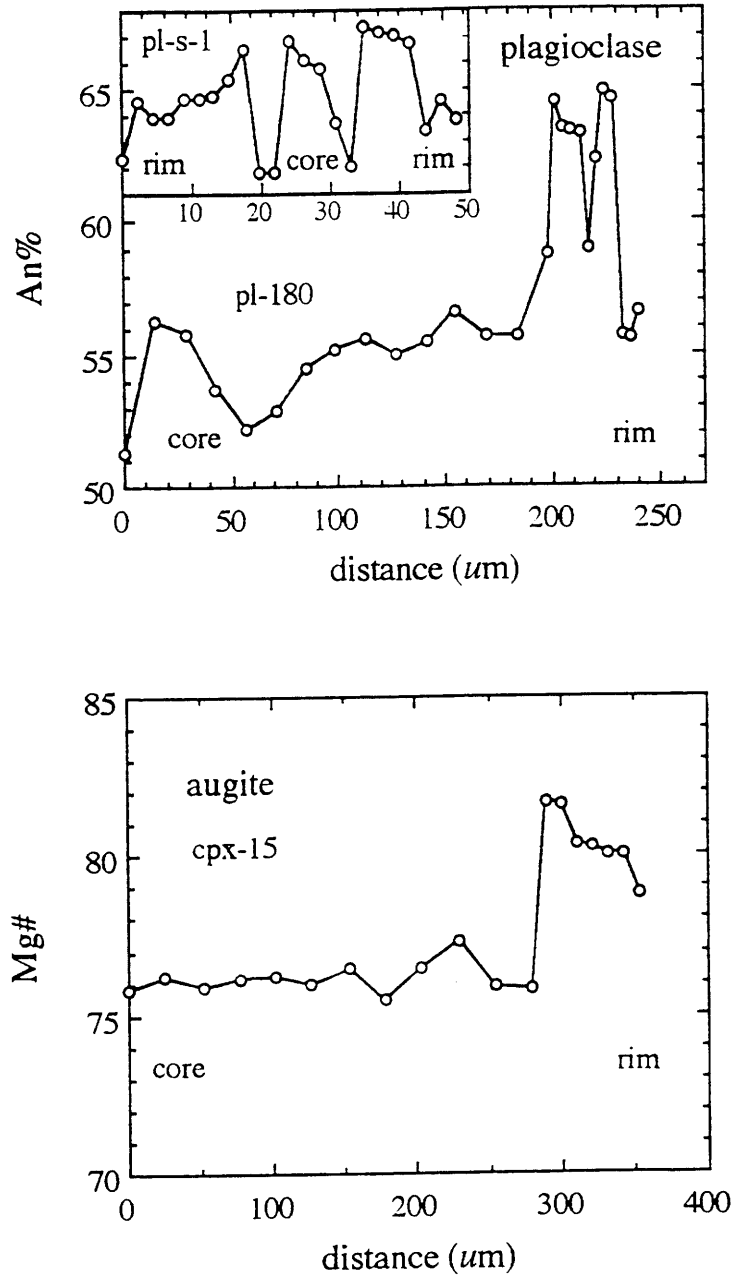


Fig. 9

MK 1-8

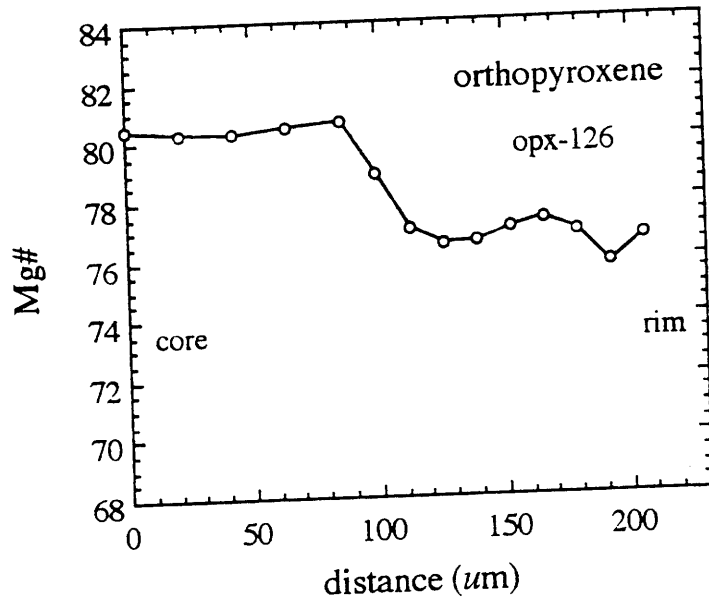
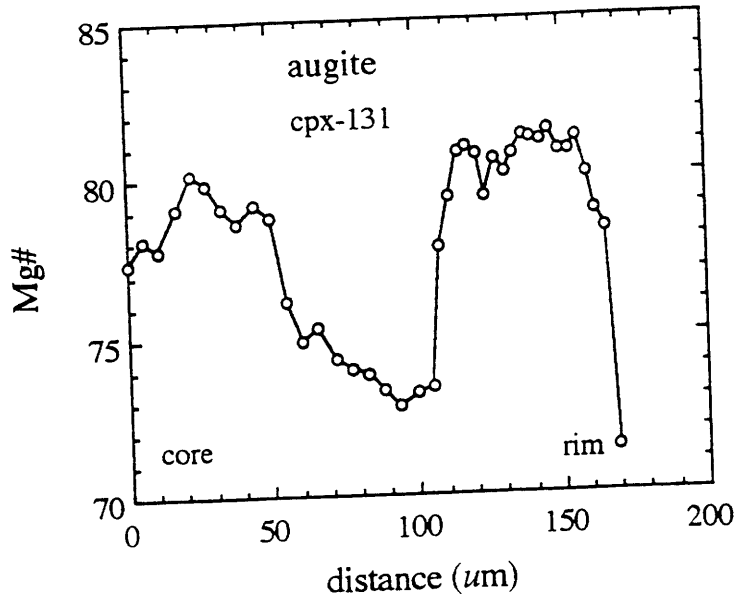


Fig. 10

SU-22-64

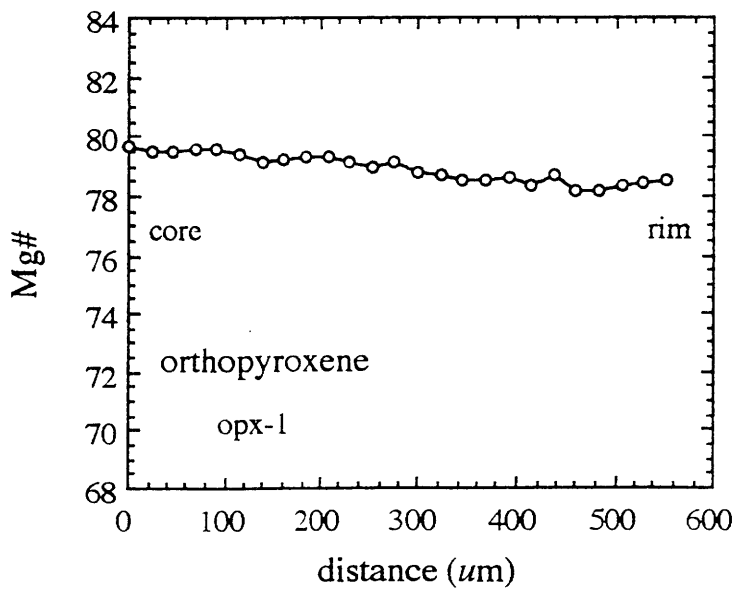
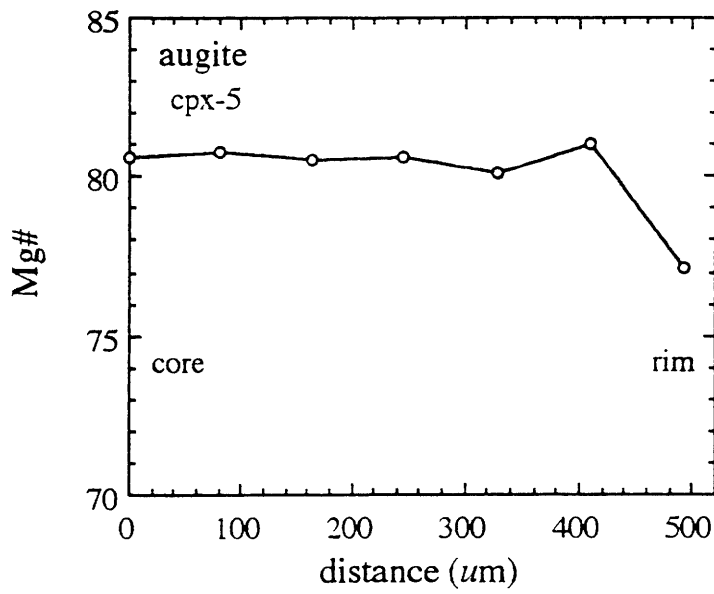
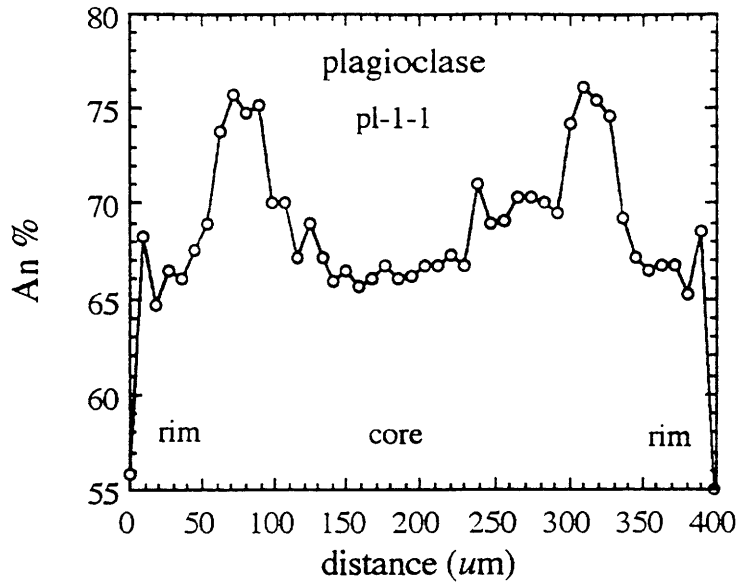


Fig. 11

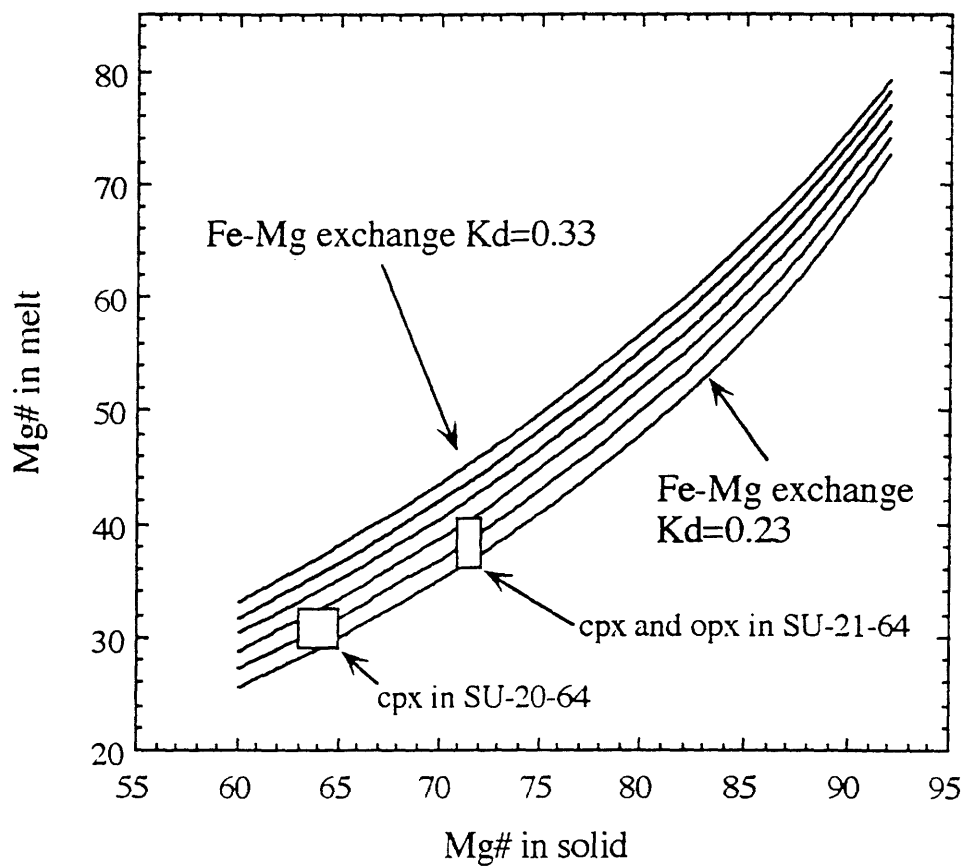


Fig. 12

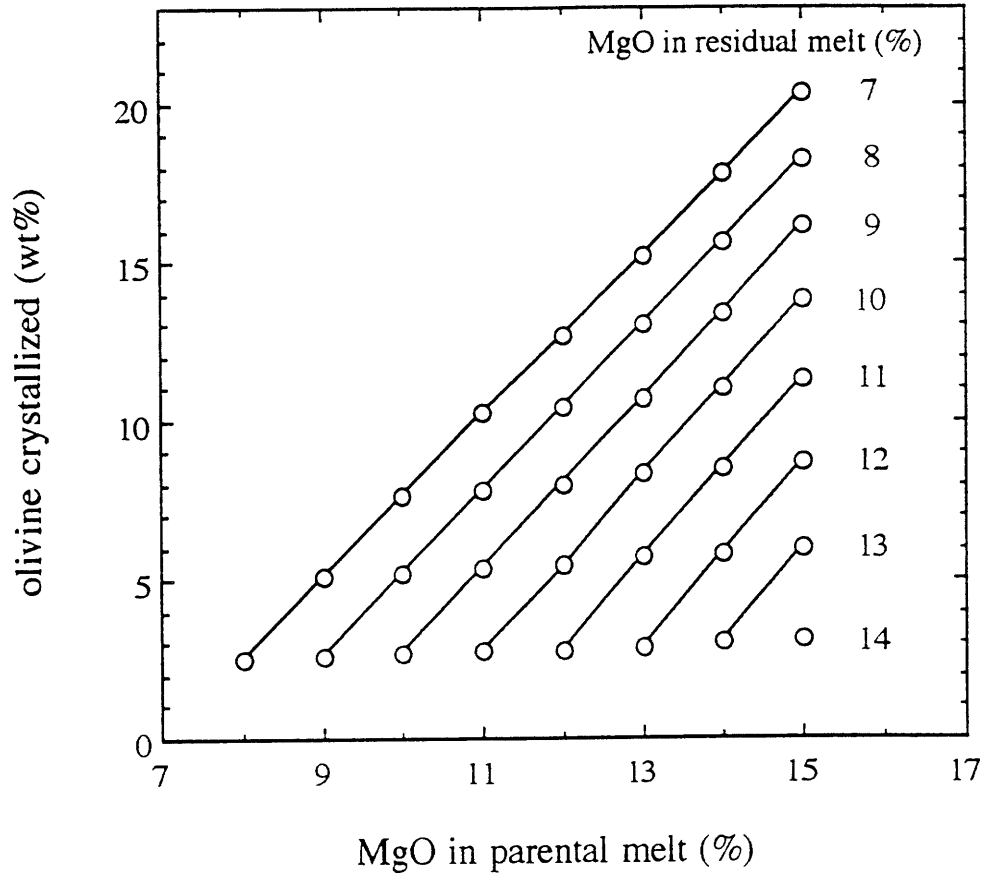


Fig. 13

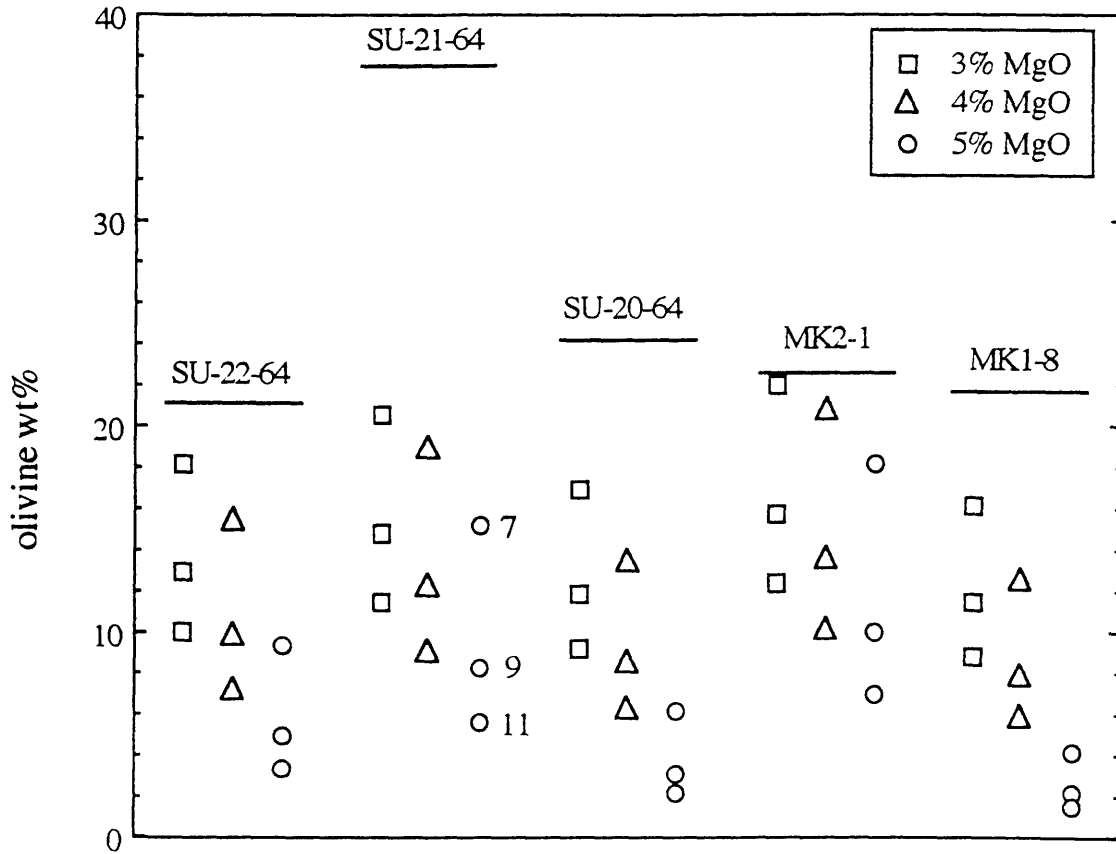


Fig. 14

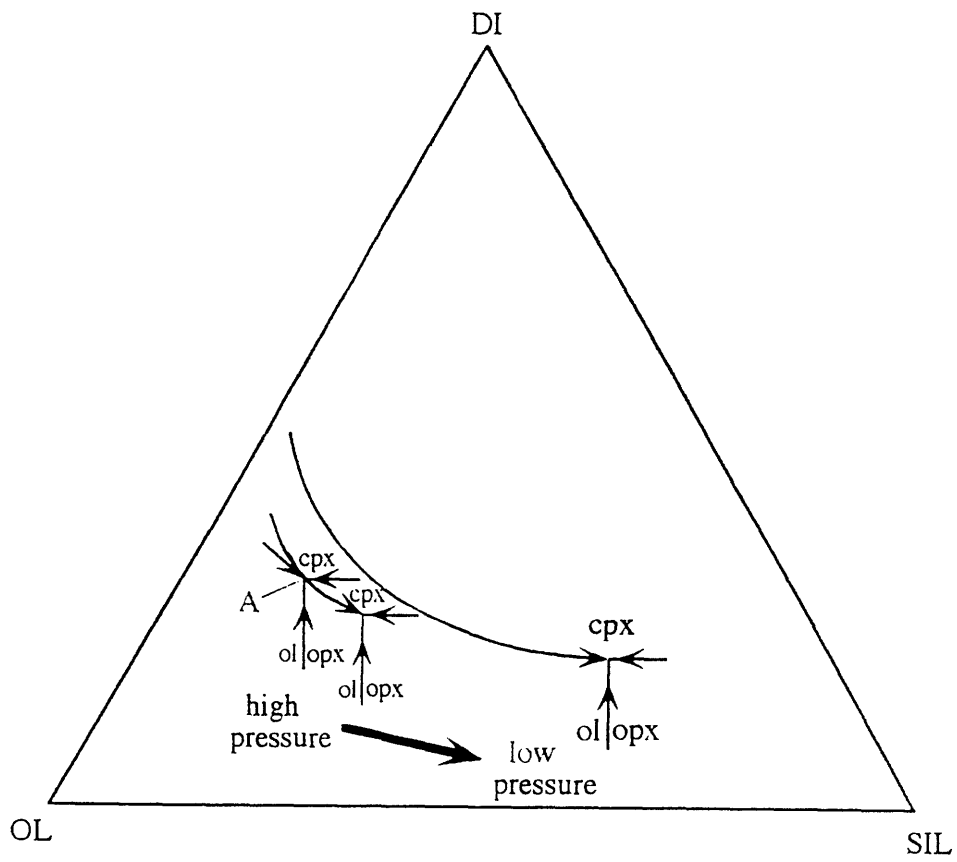


Fig. 15

CHAPTER FOUR

**Evolution of Mauna Kea volcano: Inferences from
lava compositions recovered in the Hawaii Scientific
Drilling Project**

ABSTRACT

The lower 776 m of core recovered during the initial phase of the Hawaii Scientific Drilling Project (HSDP) contains lavas erupted from Mauna Kea volcano. Tholeiitic and alkalic basalts, including an Fe-Ti rich flow, are intercalated in the upper 58 m of Mauna Kea lavas. Similar basaltic sections are subaerially exposed on the lower east flank of Mauna Kea. The Fe-Ti rich lavas reflect large amounts of clinopyroxene, plagioclase, and olivine fractionation within the crust and upper mantle, but the range from tholeiitic to alkalic compositions reflects variable extents of melting of a garnet-bearing source. Based on abundances of incompatible elements, the extent of melting for a basanitoid was a factor of 2 less than that for nearly coeval tholeiitic lavas. All flow units in the lower 718 m of the HSDP core are tholeiitic lavas. Their variability in major element compositions reflect variable accumulation of olivine. Incompatible element abundance ratios in these lavas reflect a complex temporal variation in extent of melting. Within the tholeiitic part of the core, lavas from 800 m to 950 m formed by the largest extent of melting, whereas tholeiitic lavas from the bottom of the core and from just below the tholeiitic to alkalic transition formed by lower degrees of melting. Inferred melt compositions at 16% MgO show that the ~200 to 400 ka Mauna Kea lavas from the HSDP core and the <250 ka subaerial exposures define an inverse correlation between SiO₂ and FeO contents. Based on experimental studies, this correlation is caused by differing pressures of melt segregation. Furthermore, abundances of Nb and SiO₂ are also inversely correlated in these calculated melts. In general, the younger lavas are relatively enriched in FeO and incompatible elements but are depleted in SiO₂. These trends are interpreted to reflect an overall trend of increasing pressure of melt segregation and decreasing extent of melting with decreasing eruption age. There are, however, geochemical variations which indicate short-term reversals in this long-term trend. Previously, the geochemical trends accompanying the transition from tholeiitic to alkalic volcanism at Hawaiian volcanoes have been interpreted as reflecting the effects of increasing distance from the plume axis. The long-term geochemical trends of

tholeiitic lavas in the HSDP core also reflect migration of Mauna Kea away from the Hawaiian plume.

INTRODUCTION

In order to understand how plume-related volcanism "works," it is imperative to determine how the geochemical characteristics of the lavas vary with time at an individual volcano. This is the major objective of the Hawaii Scientific Drilling Project (HSDP). It is well established that Hawaiian volcanoes evolve through a series of distinct stages with the voluminous shield stage forming more than 95% of each volcano (e.g., Macdonald et al., 1983; Clague and Dalrymple, 1987). As Hawaiian volcanoes evolve from the shield to postshield stage, eruption rates diminish, rift zones become less active, and eruption sites are more widely distributed. This transition is well exposed and consequently well-studied at large mature Hawaiian volcanoes such as Haleakala (Chen and Frey, 1985; Kurz et al., 1987; West and Leeman, 1987; Chen et al., 1990; Chen et al., 1991; Chen, 1993; West and Leeman, 1994), Kohala (Feigenson et al., 1983; Hofmann et al., 1987; Lanphere and Frey, 1987; Spengler and Garcia, 1988), and Mauna Kea (West et al., 1988; Frey et al., 1990; Frey et al., 1991; Kennedy et al., 1991; Yang et al., 1994; Wolfe et al., 1996). In these studies the temporal geochemical variations of the lavas have provided constraints on volcanic processes that are important as a Hawaiian volcano moves away from the hotspot.

Temporal geochemical variations during the extended period of shield-stage volcanism are less well known because continuous sections of shield-stage lavas containing a long temporal record are not subaerially exposed on the actively growing shields at Kilauea and Mauna Loa or at the older volcanoes where the shields are largely covered by postshield lavas. It is known, however, that there are important geochemical differences between shields (e.g., Tilling et al., 1987; Frey and Rhodes, 1993) and recent efforts have focused on documenting short- and long-term changes in the geochemistry of shield lavas from Kilauea (e.g., Hofmann et al., 1984; Tilling et al., 1987; Rhodes et al., 1989; Garcia et al., 1992; Pietruszka and Garcia,

1994; Chen et al., 1996) and Mauna Loa (e.g., Rhodes, 1988; Lipman et al., 1990; Kurz and Kammer, 1991; Garcia et al., 1995; Kurz et al., 1995; Rhodes and Hart, 1995)

A major objective of the HSDP is to determine and interpret temporal geochemical variations of lavas forming the shield of Mauna Kea volcano. Core from the first phase of HSDP recovered 280 m of Mauna Loa flows overlying 776 m of subaerially erupted Mauna Kea lavas ranging in age from ~200 to 400 ka (Sharp et al., 1996). Geochemical data show that the boundary between Mauna Loa and Mauna Kea flows is abrupt and clearly defined (Kurz et al., 1996; Lassiter et al., 1996; Rhodes, 1996). The objectives are (1) to compare the Mauna Kea lavas in the drill core with previously studied lavas exposed on the subaerial flanks of the volcano and with a small suite of submarine lavas dredged from the east rift zone at water depths of 1.6 to 3.3 km; and (2) to identify and interpret the compositional variations of Mauna Kea lavas in this drill core.

PREVIOUS STUDIES OF MAUNA KEA VOLCANO

At 4205 m above sea level, Mauna Kea is the tallest of the five shield volcanoes composing the island of Hawaii. The subaerially exposed portion of the volcano has been the focus of several petrologic and geochemical studies (Fodor and Vandermeyden, 1988; West et al., 1988; Frey et al., 1990; Frey et al., 1991; Kennedy et al., 1991; Wolfe et al., 1996). Postshield lavas erupted from widely scattered vents cover most of the subaerial surface of the volcano. The subaerially exposed Mauna Kea lavas have been divided into two stratigraphic units: a lower basaltic sequence, Hamakua Volcanics; and an upper hawaiite to mugearite sequence, Laupahoehoe Volcanics (Lanphere and Frey, 1987). Although a large and precise database for ages is not available, Hamakua lavas range in age from approximately 250 to 70 ka, and Laupahoehoe lavas range from approximately 65 to 4 ka (Wolfe et al., 1996)

The Laupahoehoe lavas are evolved alkalic lavas, hawaiites, and mugearites with <4.5% MgO (West et al., 1988; Wolfe et al., 1996). These lavas are nearly aphyric with only rare

olivine and plagioclase phenocrysts/xenocrysts, but some lavas contain xenoliths of dunite and gabbro (Fodor and Vandermeijden, 1988). There is a distinct compositional gap between the Laupahoehoe hawaiites and Hamakua basalts (Frey et al., 1990). The Laupahoehoe Volcanics, which contain no basaltic lavas, formed when magma supply rates were insufficient to maintain conduits for ascent of basaltic magma. That is, as Mauna Kea moved away from the long-term source of basaltic magma, the mantle plume, basaltic magma ponded at depth, perhaps at the mantle-oceanic crust boundary. As this basaltic magma cooled, it formed a dense clinopyroxene-rich mineral assemblage containing Fe-Ti oxides similar to some of the gabbroic xenoliths in Laupahoehoe lavas (Fodor and Vandermeijden, 1988; Kennedy et al., 1991). Segregation of this mineral assemblage created residual hawaiitic magmas which were sufficiently buoyant to erupt (Frey et al., 1990, Fig. 15)

Studies of Hamakua lavas have focused on stratigraphic sections from (1) the well-exposed and arid northwest flank, ~75 flows ranging in age from ~81 to 150 ka (Frey et al., 1990); (2) the south flank at elevations of 2750 to 3100 m, where Hamakua lavas directly underly Laupahoehoe lavas in Waikahalulu Gulch (Frey et al., 1990, Fig. 2); and (3) the windward, east flank where the oldest subaerially exposed Hamakua lavas outcrop in deep, 90 to 165 m, gulches formed by stream erosion (Frey et al., 1991).

The Waikahalulu Gulch high on the south flank is an important section because it includes Laupahoehoe lavas, 31 ± 9 ka, which directly overlie 12 evolved (5-6% MgO) alkalic Hamakua basalts. The lower five Hamakua lavas in this gulch are, however, tholeiitic basalts with 7-10% MgO. One of these lavas has a K/Ar age of 153 ± 38 ka (Wolfe et al., 1996). The near sea level sections on the east flank are dominantly intercalated alkalic and tholeiitic basalts, with some flows of ankaramite, picrite, and evolved Fe-Ti-rich alkalic lavas. An alkalic basalt (sample La-7) in one of these sections has a K/Ar age of 237 ± 31 ka (Wolfe et al., 1996). The intercalated tholeiitic and alkalic basalts in these sections have similar radiogenic isotopic ratios of Sr, Nd, and Pb (Kennedy et al., 1991). Frey et al. (1991) concluded that these tholeiitic and alkalic

basalts were formed from a garnet-bearing peridotite by different extents of melting. They also concluded that none of the MgO-rich picrites and ankaramites are representative of high MgO melts. Based on mineral and whole rock compositions and petrography, these lavas are best explained as complex mixtures of relatively evolved melts and accumulated olivine and clinopyroxene phenocrysts and xenocrysts. The evolved Fe-Ti-rich Hamakua lavas formed as residual melts after segregation of an olivine, clinopyroxene, and plagioclase-bearing assemblage (Frey et al., 1991), but they followed a very different liquid line of descent than Laupahoehoe lavas; most notably, Fe-Ti oxide was not an important fractionating phase during formation of the Hamakua Volcanics.

Submarine tholeiitic lavas dredged from the east rift of Mauna Kea have also been studied (Garcia et al., 1989; Frey et al., 1991; Yang et al., 1994). Because they erupted far from the volcano summit, these submarine lavas are presumed to be the oldest lavas recovered from the Mauna Kea shield. Based on their vesicularity, depth below sea level, and subsidence rates, Wolfe et al. (1996) estimated an eruption age of 400 ka for these submarine lavas. These lavas are MgO-rich, 11-20%, but like subaerially erupted picrites, they are not representative of crystallized MgO-rich melts. Their whole rock and mineral compositions reflect mixing of an evolved magma, <7% MgO, with a magma containing abundant olivine xenocrysts. The submarine sample, SU 22-64, dredged from the greatest depth and most distant from the summit is transitional in composition; that is, it has relatively lower SiO₂ content and higher abundances of incompatible elements, and it may have formed by a relatively lower extent of melting (Yang et al., 1994).

RESULTS

Major Elements Abundances of major elements were determined by X ray fluorescence (XRF) (Rhodes, 1996), and trace element abundances were determined by neutron activation and XRF [Table 1 and Rhodes (1996)]. Sample numbers in Table 1 indicate the core run and

depth in meters within this core run (see *Hawaii Scientific Drilling Project*, 1994). In general, only one sample from each core run was analyzed, and I identify samples by their core run number. The whole rock major and trace element data obtained for Mauna Loa lavas in the upper 280 m of the HSDP core are discussed by Rhodes (1996). In this paper I discuss the compositions of Mauna Kea lavas ranging from R158 at 281.3 m to R466 at 1052.4 m in the HSDP core. These lavas range from basaltic to picritic; no highly evolved lavas with <5.4% MgO are present. A total alkalis ($\text{Na}_2\text{O}+\text{K}_2\text{O}$) versus SiO_2 content plot shows the gradual transition from tholeiitic to alkalic basalt as shield building ends (Fig. 1). Note that I use this plot to define alkalic and tholeiitic basalts, but Wolfe et al. (1996) defined tholeiitic basalt as having normative quartz, transitional basalt as having normative olivine and hypersthene and alkalic basalt as having normative nepheline. In Fig. 1b, lavas from the HSDP core, except for R177 from flow unit 58, overlap with the fields defined by the Hamakua Volcanics and submarine lavas from the east rift, but none of the HSDP lavas are similar to the Laupahoehoe Volcanics.

Lavas from deeper than 342 m in the HSDP core, samples R180 to R466 (from flow units 59 to 227), lie well within the tholeiitic field forming an elongated field that overlaps with recent Kilauea lavas at 50 to 51% SiO_2 (Fig. 1a). Many of these tholeiitic Mauna Kea lavas are MgO-rich (12 to 28.2%), and they contain abundant olivine (Baker et al., 1996; Garcia, 1996). The trend of these high-MgO lavas to low SiO_2 contents is subparallel to the tholeiitic-alkalic dividing line (Fig. 1), and it is consistent with accumulation of olivine. The uppermost Mauna Kea lavas in the HSDP core, ranging from R158 in flow unit 45 at 281.3 m to R177 in flow unit 58 at 331.7 m, are compositionally diverse; 11 of the 12 samples from this part of the core plot close to or in the alkalic field (Fig. 1a). However, only one sample, R177, has more than 1% normative nepheline. The youngest Mauna Kea samples (R158, R159, and R160 from flow units 45 and 47 and spanning a range of 7.7 m) form a group of alkalic lavas close to the alkalic-tholeiitic boundary. The underlying three samples (R164, R166, and R167 in flow units

49, 51, and 52 from the next 18.7 m of core) have significantly higher $\text{Na}_2\text{O} + \text{K}_2\text{O}$, and they plot well within in the alkalic field. Below these alkalic lavas three samples (R168, R169, and R171 in flow units 53, 54, and 55 from 7.7 m of core) plot in the tholeiitic field, but in relation to the main trend they are offset to higher alkali contents (Fig. 1a). Below these marginally tholeiitic lavas are two thick units of aphyric alkalic lavas. The R174 samples from flow unit 57 have the lowest MgO contents, ~5.5%, found in the core, whereas sample R177 from flow unit 58 is a basanitoid with 8.2% MgO. The latter sample is in the basanite field on a total alkalis versus SiO_2 plot (Le. Bas et al., 1992), and it has 5.5% normative nepheline with $\text{FeO} = 0.85$ total iron, but it does not have modal nepheline. In summary, the transition from tholeiitic to alkalic volcanism in the HSDP core was gradual over a time span of at least 42 ka (Sharp et al., 1996) and includes ~50 m of core where basalts of varying alkalinity are intercalated (Fig. 2a).

Important aspects of the compositional variations among the Mauna Kea HSDP lavas are apparent in MgO variation plots (Fig. 3). Lavas from the lower parts of the core (429-1052 m) define an inverse SiO_2 -MgO trend (Fig. 3a). In contrast, at a given MgO content the nine alkalic lavas in the upper part of core are offset to lower SiO_2 and higher Fe_2O_3 (total iron); sample R177 has the lowest SiO_2 and highest Fe_2O_3 content (Figs. 3a and 3b). The three marginally tholeiitic lavas (R168, R169, and R171) intercalated with the alkalic lavas are also offset to lower SiO_2 contents (Fig. 3a). In addition, within the 100-m interval below the alkalic lavas, there are three high-MgO tholeiitic lavas (R189, R193, and R212) which are offset from the main trend of the tholeiitic lavas to lower SiO_2 and higher Fe_2O_3 (Figs. 3a and 3b).

Abundances of Al_2O_3 are inversely correlated with MgO, and the slope is also consistent with accumulation of olivine (Fo_{86}) [Fig. 3c and Baker et al. (1996)]. The negative Al_2O_3 -MgO trend is characteristic of Hawaiian lavas and opposite to the trends defined by mid-ocean ridge basalts which are controlled in part by plagioclase fractionation (e.g., Langmuir et al., 1992). In detail, however, several of the alkalic basalts are offset to slightly higher Al_2O_3 . The HSDP lavas with more than 7% MgO also show an inverse relationship between CaO and MgO

abundances (Fig. 3d). The five most evolved HSDP lavas are alkalic (R174-0.55, R174-9.65, R167, R166, and R164 with 5.4 to 6.3% MgO); in relation to the CaO-MgO trend of the higher MgO lavas, these alkalic lavas have lower CaO and correspondingly high $\text{Al}_2\text{O}_3/\text{CaO}$ of ~ 1.4 . The $\text{Al}_2\text{O}_3/\text{CaO}$ ratio ranges from 1.13 to 1.25 in all lavas from the lower 539 m of core and in 62 of the 73 Mauna Kea lavas analyzed (Fig. 2b). This range is similar to that of historical tholeiitic lavas with $>7\%$ MgO from Kilauea (1.08 to 1.27), but lower than historical tholeiitic lavas from Mauna Loa (1.27 to 1.34) (Frey and Rhodes, 1993; Feigenson and Patino, 1996; Hofmann and Jochum, 1996). The considerable variation of $\text{Al}_2\text{O}_3/\text{CaO}$ in the upper 232 m of Mauna Kea lavas reflects the five evolved lavas with $\text{Al}_2\text{O}_3/\text{CaO} \sim 1.4$, basanitoid R177 with $\text{Al}_2\text{O}_3/\text{CaO} = 1.47$, and five MgO-rich lavas, R171, R189, R197, R215, and R243 which have atypically low ratios of 1.02 to 1.10 (Fig. 2b).

Abundances of TiO_2 , Na_2O , and P_2O_5 are also inversely correlated with MgO (Figs. 3e, 3f, and 3g), but nine alkalic samples from the upper 50 m of Mauna Kea lavas are offset to higher abundances, with maximum TiO_2 content of 4.5% in sample R174 and Na_2O content of 3.24% in sample R177. These samples also have the highest P_2O_5 contents (Fig. 3g).

Incompatible Trace Elements Abundances of highly and moderately incompatible elements, such as Th, Ba, Nb, La, Sm, and Zr, are highly correlated in all Mauna Kea lavas (Fig. 4). These trends show that during the petrogenesis of Mauna Kea lavas the order of increasing incompatibility was heavy rare earth element (HREE)-Sm-Zr-light REE (LREE)-Nb-Ba-Th. Within the HSDP core the nine alkalic lavas in the upper 58 m of the Mauna Kea section have the highest abundances of incompatible elements; these abundances overlap the range of previously studied Hamakua alkalic lavas (Fig. 4).

Chondrite-normalized abundances of rare earth elements (REE) are typical of Hawaiian tholeiitic and alkalic lavas (Fig. 5). Light REE contents are quite variable, $(\text{La})_N = 25$ to 117 with $(\text{La}/\text{Ce})_N \geq 1$ in alkalic lavas and ~ 1 in tholeiitic lavas (N is chondrite-normalized).

Abundances of heavy REE, such as Yb, are also variable $(Yb)_N = 5.5$ to 18.1, but this variability is largely a result of olivine accumulation. Normalization of the 31 tholeiitic HSDP lavas with 7.4 to 16% MgO to MgO = 16% by olivine addition yields a mean Yb content of 1.6 ± 0.1 ppm (also see Feigenson and Patino, 1996; Hofmann and Jochum, 1996).

In the HSDP lavas, abundance ratios involving elements of similar incompatibility do not vary systematically with abundances of incompatible elements; e.g., Zr/Hf varies only from 38.7 to 44.4 and La/Nb from 0.80 to 0.91 with sample R371 = 0.765 (Figs. 6a and 6c). The high-precision Th data for HSDP lavas obtained by isotope dilution (Lassiter et al., 1996) yield a quite uniform Nb/Th ratio of 17.4 ± 1.4 (Fig. 6b), overlapping with the ratio 15.5 ± 1.7 previously reported for 20 Hamakua lavas (Kennedy et al., 1991). Like other Hawaiian shields, Mauna Kea lavas have a uniform Nb/Th ratio which differs from the bulk earth estimate of 8.6; this difference has been used to argue against a primitive mantle component in Hawaiian shield lavas (Hofmann, 1986; Frey et al., 1994; Hofmann and Jochum, 1996).

In contrast, abundance ratios involving elements of different incompatibility, such as La/Sm, La/Yb, and Zr/Nb, vary systematically with abundances of a highly incompatible element, such as Nb (Fig. 6). The nine alkalic lavas within the upper 50 m of the Mauna Kea section (281 to 332 m) have the highest La/Yb and lowest Zr/Nb (Fig. 7); these ratios overlap with those of the previously studied alkalic Hamakua lavas (Fig. 8). Although this part of the core is dominated by alkalic lavas with high La/Yb and low Zr/Nb, there is an abrupt transition in the 7.7-m interval containing the marginally tholeiitic samples R168, R169, and R171 which have lower La/Yb and higher Zr/Nb (Fig. 7); thus these ratios are highly correlated with alkalinity (Fig. 8). Slightly lower in the section at 416 m there is an anomalous sample, R208 from flow unit 75, which is tholeiitic in the $Na_2O + K_2O$ versus SiO_2 plot (Fig. 1), but unlike other tholeiites it has La/Yb, Zr/Nb (Fig. 7), and Sr/Y (Rhodes, 1996) which overlap with the overlying alkalic lavas. In relation to other tholeiitic lavas with a similar MgO content, it also has higher Na_2O , K_2O , TiO_2 , and P_2O_5 contents (Rhodes, 1996) and a crossing chondrite-

normalized REE pattern (Fig. 5). All other tholeiitic Mauna Kea lavas forming the lower 710 m of the HSDP core define a restricted La/Yb-Zr/Nb field which overlaps with the field for previously studied Hamakua tholeiitic lavas and the dredged submarine lavas from the east rift (Fig. 8). From ~420 to 800 m in the core, La/Yb and Zr/Nb do not vary systematically with depth, but samples from ~800 to 950 m define a minimum in La/Yb and a maximum in Zr/Nb (Fig. 7).

An important aspect of the La/Yb and Zr/Nb depth profiles is that the oldest six samples, R446 to R466 from flow units 211 through 227 and forming the lower 57 m of the core, have relatively high La/Yb and low Zr/Nb, and they define an inflection in the depth profiles that begins with sample R434 (flow unit 203) at 965 m (Fig. 7). This inflection is also clearly demonstrated by the REE data of Feigenson et al. (1996) and the more detailed sampling of Albarede (Albarede, 1996), who analyzed 17 samples from flow units 211 through 227. The data of Albarede (see expanded depth panel of Fig. 7a) indicate that this transition to higher La/Yb was episodic with flow units 211 to 218 of olivine and plagioclase-phyric basalt with La/Yb ~6 overlying flow units 219 to 227 of aphyric basalt with La/Yb ~7.

Fig. 9 shows how La/Yb has varied during growth of Mauna Kea from ≥ 400 ka to ~65 ka. The lowest La/Yb ratios are in some of the submarine lavas; however, submarine lava SU-22-64 which erupted distant from the summit (Yang et al., 1994) has a high value of 8.3. Within the tholeiitic part of the HSDP core; i.e., >241 ka, La/Yb varies from 4.9 to 7.0, with R208 at 326 ka having an anomalously high ratio of 8.9. Lavas erupted during the tholeiitic to alkalic transition, ~199 to 241 ka in the HSDP core and in Maulua Gulch, have large variations in La/Yb. Both tholeiitic and alkalic basalts from Waikahalulu gulch have relatively high La/Yb, but the highest values are characteristic of the overlying hawaiites, < 65 ka, forming the Laupahoehoe Volcanics.

DISCUSSION

Compositional effects of posteruptive alteration processes It is well established that posteruptive processes occurring in high rainfall Hawaiian environments result in preferential loss of K and Rb from subaerially erupted lavas (e.g., Frey et al., 1994). Obvious manifestations are $K_2O/P_2O_5 < 1$, compared to 1.4 to 2.0 in fresh shield lavas (e.g., Garcia et al., 1989), $K/Rb > 1000$, compared to ~ 500 in fresh shield lavas (e.g., Feigenson et al., 1983), and poor correlations of K and Rb abundances with abundances of relatively immobile incompatible elements, such as Nb (compare La-Nb and Rb-Nb panels in Fig. 4). The east flank of Mauna Kea volcano is a high rainfall region (350-800 cm/yr) and Frey et al. (1991) found that 35% of the Hamakua flows from the east flank have $K_2O/P_2O_5 < 1$. Ten of the HSDP samples also have $K_2O/P_2O_5 < 1$, and they have K/Rb ranging from 685 to 3280. Two of these, R331 and R333, are from ~ 700 m in the core, but the other eight are within the upper 170 m of Mauna Kea lavas (Fig. 2c). This result indicates that the uppermost lavas in the HSDP core were erupted in a wet subaerial environment and that they were exposed to surficial alteration processes for a longer time than most of the lower lavas. This inference based on K_2O/P_2O_5 is consistent with ages that indicate an average lava accumulation rate of ~ 7.8 mm/yr for the lower 641 m of Mauna Kea lavas and only ~ 0.9 mm/yr for the upper 135 m of Mauna Kea lavas in the HSDP core (Sharp et al., 1996). These accumulation rates are consistent with the most recent estimates for lava supply rate at Mauna Kea which indicate a maximum of 0.06 km³/yr for tholeiitic lavas forming the main shield with a precipitous decrease to 0.005 km³/yr for the Hamakua Volcanics, ~ 250 to 70 ka, and to 0.0004 km³/yr for the Laupahoehoe Volcanics, < 65 ka (Wolfe et al., 1996, Fig. 4).

Posteruptive alteration of Hawaiian tholeiites can also lower SiO_2 and increase total iron contents (e.g., Lipman et al., 1990; Frey et al., 1994). Compared to the general trend of HSDP tholeiitic lavas, three picrites, R189, R193, and R212, from the upper part of the tholeiitic section have anomalously low SiO_2 and high total iron contents (Figs. 3a and 3b). These vesicular picrites do not appear to be highly altered in thin section (Garcia, 1996), but they have

very low K_2O/P_2O_5 , < 0.7 ; thus it is likely that their anomalous SiO_2 and total iron contents resulted from post-eruptive alteration. Two of these samples, R189 and R212, also have atypically high Th/U (≥ 3.5 (Lassiter et al., 1996)); in fact, HSDP lavas define an inverse correlation between K_2O/P_2O_5 and Th/U. Loss of U during post-eruptive alteration of Mauna Kea lavas was previously recognized by Kennedy et al. (1991). Three picrites (R189, R197, R215) from this part of the core have anomalously low Al_2O_3/CaO (Fig. 2b). This is unlikely to be an alteration feature since Al_2O_3/CaO is typically increased during alteration (Lipman et al., 1990; Frey et al., 1994), and only one of these picrites (R189) has low K_2O/P_2O_5 . Anomalously low Al_2O_3/CaO can result from accumulation of clinopyroxene, but these samples contain less than 0.4 vol % clinopyroxene (Garcia, 1996).

Comparison of Tholeiitic to Alkalic Transition in HSDP Core and Subaerially Exposed Sections Prior to study of the HSDP core, stratigraphic sections of Mauna Kea lavas with a transition from tholeiitic to alkalic lavas were sampled in three east flank gulches (Laupahoehoe, Kaawalii, and Maulua) and in Waikahalulu gulch on the south slope. Intercalated tholeiitic and alkalic lavas in these sections and the HSDP core have similar isotopic ratios of Sr, Nd, and Pb (Kennedy et al., 1991; Lassiter et al., 1996). The time span for the alkalic to tholeiitic transition in the HSDP core is defined by an ^{40}Ar - ^{39}Ar age of 199 ± 9 ka for alkalic basalt R164, ~19 m below the Mauna Loa-Mauna Kea contact and 241 ± 5 ka for R177, the lowermost alkalic lava in the core (Sharp et al., 1996). This age range is consistent with the 237 ± 31 ka K-Ar age of an alkalic basalt from an east flank gulch (Wolfe et al., 1996). A tholeiitic lava exposed in Waikahalulu gulch high on the south flank of Mauna Kea has a younger K-Ar age of 153 ± 38 ka (Wolfe et al., 1996), but at the 95% confidence level this age overlaps with those reported for the east flank alkalic basalts. Thus the uppermost Mauna Kea lavas in the HSDP core and east flank gulches sample the same time frame of Mauna Kea evolution. This conclusion is strengthened by the occurrence of compositionally distinctive

high Fe-Ti basaltic lavas in the east flank gulches and in the HSDP core. Samples from core R174 (flow unit 57) are characterized by moderate MgO contents (5.5%) and high abundances of TiO₂ (4.5%), total iron (Fe₂O₃ ~15%), and P₂O₅ (0.57%) (Fig. 3). Such geochemical characteristics are typical of a distinctive group of Hamakua lavas, high Fe-Ti basalt, that occur in the upper portions of the Hamakua Volcanics; Wolfe et al. (1996) found 27 Hamakua lavas with TiO₂ > 4.05%, 4.5 to 6% MgO, and K₂O/P₂O₅ >1.6. Although they are geochemically similar, these lavas do not form a single liquid line of descent. For example, at similar MgO contents they range significantly in Al₂O₃/CaO (1.27 to 2.11).

The Fe-Ti rich samples in the HSDP core have relatively high Al₂O₃/CaO, ~1.4 (Fig. 2b), within the range found in Hamakua high Fe-Ti lavas. The R174 lavas are not as enriched in incompatible elements as some other high Fe-Ti lavas (Fig. 4), but all lavas in this group have a relative deficiency in Sr abundances (Fig. 5); consequently, plagioclase was an important fractionating phase during the petrogenesis of these lavas. Supporting evidence for this conclusion is the offset of R174 lavas to low Al₂O₃ (Fig. 3). However, neither the R174 lavas (Fig. 5) nor the other high Fe-Ti Mauna Kea lavas are depleted in Eu and relatively high oxygen fugacity has been inferred (Frey et al., 1991). Frey et al. (1991) and Wolfe et al. (1996) concluded that these Fe-Ti-rich Hamakua lavas formed when pockets of magma became isolated within the crust as magma supply rates decreased toward the end of shield building. As these magmas cooled, gabbroic cumulates segregated and created Fe-Ti-rich residual melts. Because the plagioclase/ clinopyroxene ratio in these cumulates varies with pressure, the Al₂O₃/CaO ratio of the residual melts reflects the pressure of crystallization. Using the equations of Yang et al. (1996) which relate pressure, temperature and melt composition for melts saturated with olivine, clinopyroxene and plagioclase, I estimate that many of the Hamakua high Fe-Ti lavas, including R174 samples, formed as residual melts within the upper crust at pressures ranging from 1 atm to ~0.4 GPa (Fig. 10). A few high Fe-Ti Hamakua lavas, with lower SiO₂ and higher Al₂O₃/CaO (>1.7), however, require crystal fractionation at higher pressures of 0.6 to

1.2 GPa (Fig. 10).

In contrast to the highly evolved high Fe-Ti lavas, which occur in most sections of Hamakua lavas, the basanitoid directly beneath the Fe-Ti-rich unit in the HSDP core (R177 from flow unit 58) has an unusual composition which has not been found in the subaerially exposed sequences. This aphyric lava has high abundances of incompatible elements (Fig. 5) and a moderate MgO content (8.21%) but anomalously low SiO₂ (43.7%) and CaO and high Fe₂O₃ (total iron) abundances (Fig. 3). An alkalic lava with low SiO₂ (40.6%) and CaO, high total iron, and a moderate MgO content (8.3%) also erupted from the Kanoa cone on the subaerial east flank, northwest of Hilo (Wolfe et al., 1996, Fig. 19); in relation to R177 it contains much more TiO₂ (6.1%) and P₂O₅ and has more normative nepheline (12.7%). Both lavas have K₂O/P₂O₅ >1.5, and there is no evidence that these unusual compositions result from alteration. No radiogenic isotope data are available for these highly alkalic lavas. Consequently, it is unknown whether they were derived from a distinctive source composition or if they formed by unusually low extents of melting. The compositional contrast between alkalic lava R177 at 331.6 m and the underlying tholeiitic lava R180 in flow unit 59 at 342 m [Table 1 of this paper and Rhodes (Rhodes, 1996)] shows the compositional diversity of nearly coeval magmas that erupted at Mauna Kea at ~240 ka.

Petrogenetic Inferences Resulting From Systematic Changes in Magma Composition as a Function of Depth in the HSDP Core

Role of crustal processes. The compositions of HSDP lavas were affected by mineral-melt segregation within the crust. The alkalic lavas with low MgO contents, especially the Fe-Ti-rich R174 samples, formed as residual melts after extensive crystal fractionation. Below 368 m in the core, MgO-rich picrites are abundant. The MgO content of Hawaiian primary magmas is a constraint on the melting processes involved in plume-related volcanism. Wright (Wright, 1984) proposed MgO contents of 20 to 22% for primary Hawaiian magmas. Also glasses

representing quenched melts containing ~15% MgO have been found on the submarine flanks of Kilauea (Clague et al., 1991). Melts with compositions similar to these glasses are saturated only with olivine and orthopyroxene at upper mantle pressures and volatile-free conditions (Eggins, 1992a; Wagner and Grove, 1992). This inference conflicts with evidence based on heavy REE abundances in Hawaiian shield lavas that garnet was a significant residual phase (e.g., Hofmann et al., 1984; Eggins, 1992b; Frey et al., 1994; Feigenson and Patino, 1996). A possible resolution of this paradox is that Hawaiian primary magmas contain more than 15% MgO (Eggins, 1992a; Garcia et al., 1995). Thus it is important to assess if any of the HSDP lavas with high-MgO contents are representative of high-MgO melts.

Yang et al. (Yang et al., 1994) used MgO-Ni abundance trends to show that dredged Mauna Kea shield lavas contain accumulated olivine; consequently, these lavas are not representative of high MgO melts. If Ni partition coefficients for olivine/melt from Hart and Davis (Hart and Davis, 1978) or Kinzler et al. (1990) are used, the same conclusion is valid for MgO-rich HSDP lavas; that is, the near-linear MgO-Ni trend from ~12 to 28% MgO can be explained by addition of Fo₈₆ olivine to lavas, such as R463, with ~12% MgO (Fig. 11). However, if a lower Ni partition coefficient is used (Morse et al., 1991), it is difficult to distinguish between olivine accumulation and fractionation (Fig. 11). Although there is ambiguity in interpreting the MgO-Ni trends, Baker et al. (1996) and Garcia (1996) conclude that primary magmas with 15-17% MgO are required to create the forsterite-rich olivines in HSDP lavas.

Mantle processes: Variable extents of melting Earlier I noted the systematic variations of La/Yb and Zr/Nb with depth in the HSDP core; in particular, the relative enrichment of the highly incompatible elements La and Nb in the uppermost alkalic Mauna Kea lavas and in tholeiitic lavas from the lowermost 57 m of core (Fig. 7). These incompatible element abundance ratios are not very sensitive to postmelting processes such as mineral accumulation and segregation; consequently, I infer that significant changes in primary magma composition

occurred during the ~200-kyr interval represented by the HSDP core. In order to evaluate variations in extent of melting and depth of melt segregation during this time period, it is necessary to infer primary magma compositions from the compositions of HSDP lavas. Whole rock compositions cannot be used directly because (1) the whole rocks may not be representative of melts and (2) none of the HSDP lavas are crystallized primary magmas (Baker et al., 1996; Garcia, 1996). In order to infer compositions of the primary magmas represented in the HSDP core, I focus on the 24 HSDP lavas which have <8% phenocrysts, $K_2O/P_2O_5 > 1.4$, and $\geq 7.4\%$ MgO; this subset includes 2 alkalic and 22 tholeiitic lavas. Based on these criteria and the absence of correlations between abundance ratios sensitive to fractionation of plagioclase and clinopyroxene, such as Al_2O_3/CaO , Sc/Y , and Sr/Nd , I assume that the compositions of these 24 lavas are representative of melts whose compositions were largely controlled by olivine fractionation. Primary magma compositions for these lavas were estimated by adjusting FeO contents to 85% of the total iron content and then adding equilibrium olivine in 1% increments to the measured lava compositions until the MgO content is 16%. This MgO content is typical of primary magmas inferred for other Hawaiian shields (e.g., Clague et al., 1991; Chen, 1993; Garcia et al., 1995). The following discussion is not sensitive to this choice of MgO content for primary magmas, but at 16% MgO these HSDP lavas are in equilibrium with olivine of $Fo = 90.3 \pm 0.4$ which is similar to the maximum Fo contents found in HSDP picritic lavas (Garcia et al., 1995; Baker et al., 1996).

The inferred primary magma compositions show systematic compositional variations with depth in the HSDP core. For example, incompatible elements and oxides, such as Nb, Zr, TiO_2 , P_2O_5 , and Na_2O , have higher abundances in the upper 50 m of the Mauna Kea core (Fig. 12). In addition, abundances of Nb, Zr, TiO_2 , and P_2O_5 reach minima at depths of 800 to 950 m and increase systematically from 950 m to the bottom of the core (Fig. 12). Abundances of these elements in the lowermost tholeiitic lavas, however, are lower than those of the alkalic lavas in the upper part of the Mauna Kea section. The maximum/minimum

abundance ratios for the inferred primary magmas are Nb = 2.5, La = 2.5, P₂O₅ = 2.2, Zr = 2.0, TiO₂ = 1.7 and Na₂O = 1.4. This ordering of elements corresponds to the order of increasing compatibility during partial melting of peridotite (e.g., Sun and McDonough, 1989).

I infer that the systematic variation in abundances of incompatible elements with depth corresponds to changes in extent of melting as a function of time. This inference is particularly plausible for the upper 343 m of Mauna Kea lavas which have very similar isotopic ratios of Sr, Nd, and Pb (Lassiter et al., 1996). Based on differences in abundances of Nb at 16% MgO, the extent of melting varied by a factor of 2.1, in the 343-m interval of Mauna Kea lavas from flow unit 45 to flow unit 120. The isotopic homogeneity of the tholeiitic to alkalic transition in the HSDP core (Lassiter et al., 1996) is also characteristic of the stratigraphic sections from the east flank gulches (Kennedy et al., 1991). At the same stage of volcano growth, intercalated tholeiitic and alkalic basalts with similar isotopic ratios also erupted at Haleakala (Chen et al., 1991) and Kohala (Hofmann et al., 1987; Lanphere and Frey, 1987). Apparently, at each of these volcanoes, both basalt types were derived from a common source by significantly different extents of melting, approximately a factor of 2 for Mauna Kea (this paper; Frey et al., 1991; Feigenson and Patino, 1996). The major conclusion is that as a Hawaiian volcano moves away from the mantle plume and magma production decreases, it is possible to extract and erupt magmas of similar age that were formed by very different extents of melting of a common source.

In the lowermost 433 m of the HSDP core, there are small but significant changes in isotopic ratios of Sr, Nd, and Pb (Lassiter et al., 1996); consequently, the source composition may also have been variable. These isotopic variations, however, are not strongly correlated with compositional changes in the inferred primary magmas. Therefore I assume that differences in incompatible element abundances and ratios at 16% MgO in the lower 433 m of core are also indicative of variations in extent of melting. With this assumption, five of the six analyzed tholeiites from ~800 m to 950 m in the core formed by relatively higher extents of

melting, a factor of 2.5 larger than basanitoid R177 from flow unit 58 at 332 m. A surprising result is that there is a trend to higher incompatible element contents, established by the five samples from units 218 to 227 at the bottom of the core (R452, R457, R463, R464, and R466 from 1009.5 to 1052.4 m); hence these lavas were formed by lower extents of melting. As this trend is apparent in measured La/Yb and Zr/Nb (Fig. 7) and in calculated abundances of incompatible elements at 16% MgO (Fig. 12), I am confident that these lavas reflect a significant change in the melting process.

In summary, a complex variation in extent of melting is recorded over the approximately 200-kyr interval represented by Mauna Kea lavas in the HSDP core. Basanitoid R177 at 332 m formed by the lowest extent of melting. From this level to ~800-950 m, the tholeiitic HSDP lavas record a slow increase in degree of melting culminating with a maximum recorded by lavas in the 800-950 m region. Below 950 m, there is a reversal in trend, and lavas within the lowermost 100 m define a trend of decreasing extent of melting with increasing depth. As a result, tholeiitic lavas at 400 and 1050 m formed by similar extents of melting.

Mantle processes: Constraints on residual mineralogy In contrast to the systematic variations in incompatible element abundances with depth in the core, abundances of Al_2O_3 and the $\text{Al}_2\text{O}_3/\text{CaO}$ ratio in the inferred primary magmas show no systematic trend with depth (Fig. 13). Except for basanitoid R177 which has >11% Al_2O_3 , the other 23 inferred primary compositions range in Al_2O_3 only from 10.4 to 10.7%. The $\text{Al}_2\text{O}_3/\text{CaO}$ ratio of these 23 samples ranges from 1.13 to 1.26. The uniformity of Al_2O_3 in lavas derived by variable extents of melting suggests control by an aluminous residual phase, such as garnet, during the melting process. Based on geophysical constraints, Hawaiian shield lavas segregate at depths where garnet is an important residual phase (Watson and McKenzie, 1991). This conclusion is consistent with the near constancy of Y and heavy REE abundances in Hawaiian shield lavas derived by variable extents of melting (e.g., Hofmann et al., 1984; Frey et al., 1994). Within the HSDP core, primary magmas below 400 m have a narrow range, ~1.5 to 1.6 ppm, in Yb

(sample R399 is an exception), but the alkalic and tholeiitic lavas from the uppermost Mauna Kea lavas have higher Yb contents of ~1.7 to 1.9 ppm Yb (Fig. 12). If these uppermost lavas were derived from a source with similar Yb content by lower extents of melting, as inferred from their Nb contents (Fig. 12), the bulk solid/melt partition coefficient for Yb was slightly less than unity. For a Yb garnet/melt partition coefficient of 5, this result requires less than 20% garnet in the residue.

Mantle processes: Constraints on depth of melt segregation The depth profiles for SiO₂ and FeO abundances in the inferred primary magma compositions differ from those for Al₂O₃, CaO, and incompatible elements. Compared to tholeiitic lavas in the core, the alkalic lavas were derived from primary magmas with relatively higher FeO and lower SiO₂ contents (Fig. 13). Abundances of these oxides in melts derived from spinel peridotite and probably garnet peridotite are sensitive to the pressure of melt segregation; as pressure increases, abundances of SiO₂ decrease and of FeO increase [e.g., see review by Langmuir et al. (1992), and Kinzler and Grove (1992), Hirose and Kushiro (1993), Takahashi et al. (1993), and Walter and Presnall (1994)]. Although abundances of SiO₂ and FeO are also dependent on extent of melting, from 2 to 3 GPa their abundances are not very sensitive to extent of melting (Hirose and Kushiro, 1993). Therefore I conclude that the combination of lower SiO₂ and higher FeO in the alkalic lavas reflects melt segregation at higher pressure. Within the tholeiitic part of the HSDP core, systematic variations in SiO₂ and FeO contents are more subdued. However, in the interval from 350 m to 950 m, the lowest SiO₂ (~48%) and highest FeO (>10.2%) contents are in uppermost tholeiitic lavas (Fig. 13). In addition, the six lowermost lavas in the core which define a trend of increasing abundances of incompatible elements (Fig. 12) also define a trend of decreasing SiO₂ content (Fig. 13). Thus HSDP lavas define a trend of decreasing extents of melting with increasing pressures of melt segregation.

Comparison of Inferred Primary Magmas Compositions for HSDP Core and Subaerially

Exposed Lavas Based on lava compositions and ages, the uppermost 50 m of Mauna Kea lavas in the HSDP core overlap with the lavas subaerially exposed low on the east flank of Mauna Kea. The lowermost lavas in the HSDP core may be comparable in age to the submarine lavas dredged from the east rift. Although these submarine lavas have not been dated, a gross estimate of 400 ka was made by Wolfe et al. (1996), who used a subsidence rate of 2.6 mm/yr and an inference based on vesicularity that some of the submarine lavas have subsided 1000 m (Moore and Peck, 1966). This age is similar to the 400 ± 26 ka reported for sample R423 from near the bottom of the HSDP core (Sharp et al., 1996). Thus the HSDP core contains an extended record of tholeiitic volcanism which fills the time gap between the east flank gulches and the dredged submarine lavas.

Following the process used for inferring primary magma compositions of HSDP lavas, I also calculated primary magma compositions for 11 tholeiitic and 18 alkalic lavas from subaerial exposures on Mauna Kea volcano and the most MgO-rich (6.9%) submarine glass [SU-46 of Yang et al. (1994)]. All of these lavas have <5% phenocrysts and are unaltered with $K_2O/P_2O_5 > 1.4$, but in order to have a suitable data base, I lowered the MgO limit to 6.8%. The inferred primary magma compositions for HSDP and subaerially exposed lavas show inverse correlations between SiO_2 versus FeO and SiO_2 versus Nb (Fig. 14). Inverse correlations between abundances of major oxides and SiO_2 content can result from the necessity for oxide abundances to sum to 100%. There is only a poor inverse correlation between Al_2O_3 and SiO_2 abundance, especially among the HSDP lavas (Fig. 14); thus I conclude that the inverse FeO- SiO_2 trend has petrogenetic significance. The relatively young alkalic lavas have the highest Nb and FeO contents and lowest SiO_2 contents. Following ideas presented earlier, I conclude that the compositions of Mauna Kea lavas, in general, show that pressures of melt segregation and extent of melting are inversely related. Compared to subaerially exposed lavas, the tholeiitic HSDP lavas and the submarine sample formed at lower pressures by larger extents of melting, with the highest extents of melting recorded by lavas in the 800-950 m interval of

the HSDP core and the submarine glass. Among the subaerially exposed lavas, the alkalic lavas reflect the lowest extent of melting and highest pressures of melt segregation.

In summary, Mauna Kea lavas show an overall trend for the pressure of melt segregation to increase and extent of melting to decrease as the volcano aged. Superimposed on this long-term trend there are short-term changes in extent of melting within the uppermost 50 m of Mauna Kea lavas and a reversal of the trend near the bottom of the HSDP core. Although no age is available, submarine sample SU22-64, which is transitional in composition (Yang et al., 1994) and has anomalously high La/Yb (Fig. 9), may also be an anomaly in the long-term trend.

In a comparison of alkalic and tholeiitic Hawaiian lavas representing different growth stages of several Hawaiian volcanoes, Langmuir et al. (1992, Fig. 65) also concluded that extent of melting is inversely related to pressure of melt segregation. A similar trend is also characteristic of lavas from the Galapagos (1992) and Main Lava Series from Skye, Scotland (Scarrow and Cox, 1995). At each of these localities the correlations between abundances of FeO, SiO₂, and incompatible elements, such as Nb, result largely from comparisons of alkalic and tholeiitic basalts. Among Mauna Kea lavas, however, much of the systematic variation in Fig. 14 is defined by tholeiitic lavas. Thus it is of interest to evaluate in more detail the temporal compositional variations of tholeiitic Mauna Kea lavas.

In the following discussion I use compositional data for all HSDP and subaerial and submarine Mauna Kea lavas that plot within the tholeiitic field (Fig. 1b). Previously, I used calculated primary magma compositions to infer temporal changes in the mantle melting processes. An alternative approach used by Frey and Rhodes (1993) is to compare suites of lavas on MgO variation diagrams. This alternative enables use of the entire data set and avoids assumptions inherent in estimating primary magma compositions. It is, however, viable only when the data define coherent MgO variation trends.

Abundances of Al₂O₃ and the moderately incompatible oxides, TiO₂ and P₂O₅, define

overlapping fields for the tholeiitic basalts from the HSDP core, the submarine east rift, and subaerially erupted lavas (Fig. 15). In contrast, Mauna Kea tholeiites from these locations are offset in a plot of MgO versus SiO₂; i.e., if lavas with 10 to 20% MgO are grouped as submarine, HSDP, and subaerially exposed suites, this is, in general, a sequence of decreasing SiO₂ content. Although there is scatter and overlap, this is also a sequence of increasing CaO and Fe₂O₃ (total iron).

What is the cause of these temporal variations in major element abundances? Two possibilities are differences in source composition or, as discussed earlier, differences in pressure of melt segregation. The former is likely to be accompanied by differences in radiogenic isotope ratios. Indeed, within the HSDP core the highest ⁸⁷Sr/⁸⁶Sr and lowest ¹⁴³Nd/¹⁴⁴Nd occur in the lower parts of the core, and some submarine lavas extend to even higher ⁸⁷Sr/⁸⁶Sr and lower ¹⁴³Nd/¹⁴⁴Nd (Yang et al., 1994; Lassiter et al., 1996). Nevertheless, there is no correlation between these isotopic ratios and SiO₂/FeO at a given MgO content. Moreover, Frey and Rhodes (1993) found no correlation between intershield differences in major element abundances and isotopic ratios of Sr, Nd, and Pb. Therefore I assume a uniform major element composition for the source of all Mauna Kea tholeiites. Following earlier discussion, the trends to lower SiO₂ and higher total iron contents from submarine east rift to HSDP core to subaerially exposed lavas can be interpreted as indicating increasing pressures of melt segregation. This is also a sequence of increasing mean La/Yb and decreasing mean Zr/Nb (Figs. 8 and 9) which is consistent with a decrease in extent of melting. If the submarine lavas are older than HSDP samples, the trend is for pressure of melt segregation to increase and extent of melting to decrease with decreasing age. This trend is the same as that inferred from the calculated primary magma compositions.

The increase in CaO content at a given MgO content from submarine east rift to HSDP to subaerially exposed lavas is not easily explained. If decreasing SiO₂ content reflects increasing pressure, it follows that CaO content increases with increasing pressure of melt segregation.

Existing experimental data for melting of spinel peridotite provide no supporting evidence for this inference (e.g., Kinzler and Grove, 1992; Hirose and Kushiro, 1993). Abundances of SiO₂ and CaO are also discriminants between some Hawaiian shields [see Frey et al., (1994), Fig. 11, Frey and Rhodes, (1993), Fig. 2]. Frey and Rhodes (1993) speculated that variable CaO contents indicate an important role for CO₂ during partial melting.

Implications For How the Hawaiian Plume "Works"

Studies of Hawaiian tholeiitic basalts show that (1) they retain information about the extent of melting and depths of melt segregation, and (2) these parameters vary systematically with time and location relative to the plume axis (e.g., Frey and Rhodes, 1993; Lassiter et al., 1996). For example, the intershield compositional differences between volcanoes formed along the spatial Loa (e.g., Mauna Loa and Hualalai) and Kea trends (e.g., Kilauea, Mauna Kea, and Kohala) are consistent with derivation of Loa lavas by higher extents of melting with melt segregation at lower pressures. In the context of a plume model a plausible interpretation is that the Loa volcanoes formed directly over the hot plume axis, whereas the Kea volcanoes form above the plume periphery from ascending mantle that is cooler and whose ascent is modified by plate motion.

The HSDP core shows the geochemical evolution of individual volcanoes, from ~10 to 100 ka for Mauna Loa and ~200 to 400 ka for Mauna Kea. By comparing the geochemical characteristics of Mauna Kea lavas in the HSDP core with results from subaerially exposed and submarine Mauna Kea lavas I infer the following trends as Mauna Kea moved away from the plume.

1. Among Mauna Kea lavas, the lowest ¹⁴³Nd/¹⁴⁴Nd are in some of the submarine lavas and the lowermost flows in the HSDP core (Yang et al., 1994; Lassiter et al., 1996). These lavas, ~400 ka, contain the largest proportion of an enriched (plume?) component.
2. As eruption age decreased from ~400 to 240 ka there was a general long-term trend for

tholeiitic magmas to segregate at higher pressure and form by lower extents of melting. This inverse trend between extent of melting and pressure of melt segregation is analogous to that which distinguishes Loa and Kea volcanoes. Although this trend has not been previously documented for the shield stage of Hawaiian volcanoes, a similar trend can be inferred for Haleakala, another Kea trend volcano. That is, at a given MgO content, submarine tholeiites from Haleakala have higher SiO₂ and CaO contents and lower total iron, TiO₂, and P₂O₅ contents than subaerial Haleakala tholeiites [see Chen et al., (1991), Fig. 4]. If these submarine Haleakala lavas are older than the subaerial lavas, there was also a trend for pressure of melt segregation to increase and extent of melting to decrease as the Haleakala shield-stage ended.

3. At ~330 ka, magma supply rate decreased precipitously (Sharp et al., 1996).
4. From ~240 to 200 ka, coeval tholeiitic and alkalic basalts with similar radiogenic isotopic ratios were erupted. Short-term variations in extent of melting are required.
5. From ~240 to 70 ka, shallow crustal level magma reservoirs crystallized, and some alkalic basaltic magmas ponded at various depths within the crust and upper mantle where they cooled, crystallized gabbroic cumulates, and formed residual Fe-Ti rich lavas.
6. Basaltic magmatism ceased at ~70 ka, and pockets of alkalic basalt stagnated near the crust-mantle boundary. With cooling, a clinopyroxene-rich assemblage containing Fe-Ti oxides crystallized and segregated, thereby creating low-density residual melts, the hawaiites of the Laupahoehoe Volcanics, which erupted from ~65 to 4 ka.

REFERENCES

- Albarede F. (1996) High-resolution geochemical stratigraphy of Mauna Kea flows from the former part of the Hawaii Scientific Drilling Project Core. *J. Geophys. Res.*, in press.
- Baker M. B., Alves S., and Stolper E. M. (1996) Petrography and petrology of the Hawaiian Scientific Drilling Project lavas: Inferences from olivine phenocryst abundances and compositions. *J. Geophys. Res.*, in press.
- Chen C.-Y. (1993) High-magnesian primary magmas from Haleakala Volcano, East Maui: Petrography, nickel, and major element constraints. *J. Volcanol. Geotherm. Res.* 55, 143-153.
- Chen C.-Y. and Frey F. A. (1985) Trace element and isotopic geochemistry of lavas from Haleakala volcano, East Maui, Hawaii: Implications for the origin of Hawaiian lavas. *J. Geophys. Res.* 90, 8743-8768.
- Chen C.-Y., Frey F. A., and Garcia M. O. (1990) Evolution of alkalic lavas at Haleakala Volcano, East Maui, Hawaii: Major, trace element and isotopic constraints. *Contrib. Mineral. Petrol.* 105, 197-218.
- Chen C.-Y., Frey F. A., Garcia M. O., Dalrymple G. B., and Hart S. R. (1991) The tholeiitic to alkalic basalt transition at Haleakala Volcano, East Maui, Hawaii: Petrogenetic interpretations based on major and trace element and isotope geochemistry. *Contrib. Mineral. Petrol.* 106, 183-200.
- Chen C.-Y., Frey F. A., Rhodes J. M., and Easton R. M. (1996) Temporal geochemical evolution of Kilauea volcano: Comparison of Hilina and Puna basalts. In *Earth Processes: Reading the Isotope Code*. Geophys. Monogr. Ser., Vol. 95, edited by A. Basu and S. R. Hart, pp. in press, AGU, Washington, D.C.
- Clague D. A. and Dalrymple G. B. (1987) The Hawaiian-Emperor volcanic chain. Part 1, Geologic evolution. *U.S. Geol. Surv. Prof. Pap.* 1350, 5-54.
- Clague D. A., Weber W. S., and Dixon J. E. (1991) Picritic glasses from Hawaii. *Nature* 353, 553-556.
- Eggs S. M. (1992a) Petrogenesis of Hawaiian tholeiites: 1, phase equilibria constraints. *Contrib. Mineral. Petrol.* 110, 387-397.
- Eggs S. M. (1992b) Petrogenesis of Hawaiian tholeiites: 2, Aspects of dynamic melt segregation. *Contrib. Mineral. Petrol.* 110, 398-410.
- Feigenson M. D., Hofmann A. W., and Spera F. J. (1983) Case studies on the origin of basalt. II. The transition from tholeiitic to alkalic volcanism on Kohala volcano, Hawaii. *Contrib. Mineral. Petrol.* 84, 390-405.

- Feigenson M. D. and Patino L. C. (1996) Rare earth element inverse modeling of Mauna Kea basalts from the Hawaiian Scientific Drilling Project: Importance of residual garnet during partial melting. *J. Geophys. Res.*, in press.
- Fodor R. V. and Vandermeiden H. J. (1988) Petrology of gabbroic xenoliths from Mauna Kea Volcano, Hawaii. *J. Geophys. Res.* 93, 4435-4452.
- Frey F. A., Garcia M. O., and Roden M. F. (1994) Geochemical characteristics of Koolau Volcano: Implications of intershield geochemical differences among Hawaiian volcanoes. *Geochim. Cosmochim. Acta.* 58, 1441-1462.
- Frey F. A., Garcia M. O., Wise W. S., Kennedy A., Gurriet P., and Albarede F. (1991) The evolution of Mauna Kea Volcano, Hawaii: Petrogenesis of tholeiitic and alkalic basalts. *J. Geophys. Res.* 96, 14,347-14,375.
- Frey F. A. and Rhodes J. M. (1993) Intershield geochemical differences among Hawaiian volcanoes: Implications for source compositions, melting process and magma ascent paths. *Phil. Trans. R. Soc. Lond. Ser. A*, 342, 121-136.
- Frey F. A., Wise W. S., Garcia M. O., West H., Kwon S.-T., and Kennedy A. (1990) Evolution of Mauna Kea Volcano, Hawaii: Petrologic and geochemical constraints on postshield volcanism. *J. Geophys. Res.* 95, 1271-1300.
- Garcia M. O. (1996) Petrography, olivine and glass chemistry of lavas from the Hawaii Scientific Drilling Project. *J. Geophys. Res.*, in press.
- Garcia M. O., Hulsebosch T. P., and Rhodes J. M. (1995) Olivine-rich submarine basalts from the southwest rift zone of Mauna Loa Volcano: Implications for magmatic processes and geochemical evolution. In *Mauna Loa Revealed: Structure, Composition, History, and Hazards*. Geophys. Monogr. Ser., Vol. 92, edited by J. M. Rhodes and J. P. Lockwood, pp. 219-239, AGU, Washington, D.C.
- Garcia M. O., Muenow D., and Aggrey K. E. (1989) Major element, volatile, and stable isotope geochemistry of Hawaiian submarine tholeiitic glasses. *J. Geophys. Res.* 94, 10,525-10,538.
- Garcia M. O., Rhodes J. M., Wolfe E. W., Ulrich G. E., and Ho R. A. (1992) Petrology of lavas from episodes 2-47 of the Puu Oo eruption of Kilauea volcano, Hawaii: Evaluation of magmatic processes. *Bull. Volcanol.* 55, 1-16.
- Geist D. J. (1992) An appraisal of melting processes and the Galapagos hotspot: Major and trace element evidence. *J. Volcanol. Geotherm. Res.* 52, 65-82.
- Hart S. R. and Davis K. E. (1978) Nickel partitioning between olivine and silicate melt. *Earth Planet. Sci. Lett.* 40, 203-219.

- Hirose K. and Kushiro I. (1993) Partial melting of dry peridotites at high pressures: Determination of compositions of melts segregated from peridotite using aggregates of diamond. *Earth Planet. Sci. Lett.* 114, 477-489.
- Hofmann A. W. (1986) Nb in Hawaiian magmas: Constraints on source composition and evolution. *Chem. Geol.* 57, 17-30.
- Hofmann A. W., Feigenson M. D., and Raczek I. (1984) Case studies on the origin of basalts III. Petrogenesis of the Mauna Ulu eruption, Kilauea, 1969-1971. *Contrib. Mineral. Petrol.* 88, 24-35.
- Hofmann A. W., Feigenson M. D., and Raczek I. (1987) Kohala revisited. *Contrib. Mineral. Petrol.* 95, 114-122.
- Hofmann A. W. and Jochum K. P. (1996) Source characteristics derived from very incompatible trace elements in Mauna Loa and Mauna Kea basalts (Hawaiian Scientific Drilling Project). *J. Geophys. Res.*, in press.
- Kennedy A. K., Kwon S.-T., Frey F. A., and West H. B. (1991) The isotopic composition of postshield lavas from Mauna Kea Volcano, Hawaii. *Earth Planet. Sci. Lett.* 103, 339-353.
- Kinzler R. J. and Grove T. L. (1992) Primary magmas of mid-ocean ridge basalts, 2, Applications. *J. Geophys. Res.* 97, 6907-6926.
- Kinzler R. J., Grove T. L., and Recca S. I. (1990) An experimental study on the effect of temperature and melt composition on the partitioning of nickel between olivine and silicate melt. *Geochim. Cosmochim. Acta.* 54, 1255-1265.
- Kurz M. D., Garcia M. O., Frey F. A., and O'Brien P. A. (1987) Temporal helium isotopic variations within Hawaiian volcanoes: Basalts from Mauna Loa and Haleakala. *Geochim. Cosmochim. Acta.* 51, 2905-2914.
- Kurz M. D. and Kammer D. P. (1991) Isotopic evolution of Mauna Loa volcano. *Earth Planet. Sci. Lett.* 103, 257-269.
- Kurz M. D., Kenna T. C., Kammer D. P., Rhodes J. M., and Garcia M. O. (1995) Isotopic evolution of Mauna Loa volcano: A view from the submarine southwest rift. In *Mauna Loa Revealed: Structure, Composition, History, and Hazards*,. Geophys. Monogr. Ser. , Vol. 92, edited by J. M. Rhodes and J. P. Lockwood, pp. 289-306, AGU, Washington, D.C.
- Kurz M. D., Kenna T. C., Lassiter J. C., and DePaolo D. J. (1996) Helium isotopic evolution of Mauna Kea volcano: First results from the 1 km drill core. *J. Geophys. Res.*, in press.
- Langmuir C. H., Klein E. M., and Plank T. (1992) Petrological systematic of mid-ocean ridge

- basalts: Constraints on melt generation beneath ocean ridges. In *Mantle Flow and Melt Generation at Mid-Ocean Ridges*. Geophys. Monogr. Ser., Vol. 71, edited by J. Phipps Morgan, D. K. Blackman, and J. M. Sinton, pp. 183-280, AGU, Washington, D.C.
- Lanphere M. A. and Frey F. A. (1987) Geochemical evolution of Kohala Volcano, Hawaii. *Contrib. Mineral. Petrol.* 95, 100-113.
- Lassiter J. C., DePaolo D. J., and Tatsumoto M. (1996) Isotopic evolution of Mauna Kea volcano: Results from the initial phase of the Hawaii Scientific Drilling Project. *J. Geophys. Res.*, in press.
- Le. Bas M. J., Le. Maitre R. W., and Woolley A. R. (1992) The construction of the total alkali-silica chemical classification of volcanic rocks. *Mineral. Petrol.* 46, 1022.
- Lipman P. W., Rhodes J. M., and Dalrymple G. B. (1990) The Ninole Basalt-Implications for the structure evolution of the Mauna Loa volcano, Hawaii. *Bull. Volcanol.* 53, 1-19.
- Macdonald G. A., Abbott A. T., and Peterson F. L. (1983) *Volcanoes in the Sea: The Geology of Hawaii*, edited, Univ. of Hawaii Press, Honolulu.
- Macdonald G. A. and Katsura T. (1964) Chemical compositions of Hawaiian lavas. *J. Petrol.* 5, 82-133.
- Moore J. G. and Peck D. L. (1966) Submarine lavas from the east rift zone of Mauna Kea, Hawaii (abstract). *Spec. Pap. Geol. Soc. Am.* 87, 218.
- Morse S. A., Rhodes J. M., and Nolan K. M. (1991) Redox effect on the partitioning of nickel in olivine. *Geochim. Cosmochim. Acta.* 55, 2373-2378.
- Pietruszka A. J. and Garcia M. (1994) The historical summit lavas of Kilauea volcano (1790-1982 A.D.): Geochemical variations in space and time. *EOS (Am. Geophys. Union Trans.)* 75 (44)(Fall Meet. Suppl.), 712.
- Rhodes J. M. (1988) Geochemistry of the 1984 Mauna Loa eruption: Implication for magma storage and supply. *J. Geophys. Res.* 93, 4453-4466.
- Rhodes J. M. (1996) The geochemical stratigraphy of lava flows sampled by the Hawaii Scientific Drilling Project. *J. Geophys. Res.*, in press.
- Episodic trace element and isotopic variations in historical Mauna Loa lavas: Implications for magma and plume dynamics. (1995), AGU, *Mauna Loa Revealed: Structure, Composition, History, and Hazards*,
- Rhodes J. M., Wenz K. P., Neal C. A., Sparks J. W., and Lockwood J. P. (1989) Geochemical evidence for invasion of Kilauea's plumbing system by Mauna Loa magma. *Nature* 337, 257-260.
- Scarrow J. H. and Cox K. G. (1995) Basalts generated by decompressive adiabatic melting of

- a mantle plume: A case study from the Isle of Skye, NW Scotland. *J. Petrol.* 36, 3-22.
- Sharp W. D., Turrin B. D., Renne P. R., and Lanphere M. A. (1996) The $^{40}\text{Ar}/^{39}\text{Ar}$ and K/Ar dating of lavas from the Hilo 1-km core hole, Hawaiian Scientific Drilling Project. *J. Geophys. Res.*, in press.
- Spengler S. R. and Garcia M. O. (1988) Geochemistry of the Hawi lavas, Kohala Volcano, Hawaii. *Contrib. Mineral. Petrol.* 99, 90-104.
- Sun S.-S. and McDonough W. F. (1989) Chemical and isotopic systematics of oceanic basalts: Implications for mantle composition and processes. In *Magmatism in the Ocean Basins*. 42, edited by A. D. Saunders and M. J. Norry, pp. 313-345, Geol. Soc. Spec. Pub., London.
- Takahashi E. T., Shimazaki Y., Tsuzaki H., Yoshida H., and Uto K. (1993) Melting study of a peridotite KLB-1 to 6.5 GPA and the origin of basaltic magmas. *Phil. Trans. R. Soc. Lond.* 342, 105-120.
- Tilling R. I., Wright T. L., and Millard H. T. (1987) Trace-element chemistry of Kilauea and Mauna Loa lava in space and time: A reconnaissance. *U.S. Geol. Surv. Prof. Pap.* 1350, 641-689.
- Wagner T. P. and Grove T. L. (1992) Primary magmas of the Hawaiian plume: Experimental evidence bearing on the plume paradox. *EOS (Am. Geophys. Union Trans.)* 73, Fall Meet. Suppl., 615.
- Walter M. J. and Presnall D. C. (1994) Melting behavior of simplified lherzolite in the system CaO-MgO-Al₂O₃-SiO₂-Na₂O from 7 to 35 kbar. *J. Petrol.* 35, 329-360.
- Watson S. and McKenzie D. (1991) Melt generation by plumes: A study of Hawaiian volcanism. *J. Petrol.* 32, 501-537.
- West H. B., Garcia M. O., Frey F. A., and Kennedy A. (1988) Nature and cause of compositional variation among the alkalic cap lavas of Mauna Kea Volcano, Hawaii. *Contrib. Mineral. Petrol.* 100, 383-397.
- West H. B. and Leeman W. P. (1987) Isotopic evolution of lavas from Haleakala Crater, Hawaii. *Earth Planet. Sci. Lett.* 84, 211-225.
- West H. B. and Leeman W. P. (1994) The open-system geochemical evolution of alkalic cap lavas from Haleakala crater, Hawaii, U.S.A. *Geochim. Cosmochim. Acta.* 58, 773-796.
- Wolfe E. W., Wise W. S., and Dalrymple G. B. (1996) Geology and petrology of Mauna Kea volcano, Hawaii: A study of postshield volcanism. *U.S. Geol. Surv. Prof. Pap.* 1557, in press.
- Wright T. L. (1984) Origin of Hawaiian tholeiite: A metasomatic model. *J. Geophys. Res.* 89,

3233-3252.

Yang H.-J., Frey F. A., Garcia M. O., and Clague D. A. (1994) Submarine lavas from Mauna Kea volcano, Hawaii: Implications for Hawaiian shield-stage processes. *J. Geophys. Res.* 99, 15,577-15,594.

Yang H.-J., Kinzler R. J., and Grove T. L. (1996) Experiments and models of anhydrous olivine-plagioclase-augite saturated melts from 0.001~10 kbar. *Contrib. Mineral. Petrol.*, in press.

Table 1. Trace Element Abundances in HSDP Lavas

	Mauna Loa Samples								Mauna Kea Samples							
	055-0.75	117-0.80	133-6.10	142-1.60	153-3.05	158-0.05	159-4.10	160-5.75	164-1.55	166-5.25	167-1.30	169-3.55	171-4.55	174-0.55	174-9.65	177-2.60
Depth, m	74.0	184.4	223.1	241.1	268.2	281.3	285.5	289.0	299.2	305.7	307.7	314.5	320.6	324.6	327.4	331.7
Flow unit	11	27	34	37	43	45	47	47	49	51	52	54	55	57	57	58
Sc	26.2	29.2	24.5	27.8	25.8	30.1	32.9	29.7±.2	29.6	29.5	29.1	31.4	30.8	30.8	30.9	25.5
Cr	670	260	864	620	856	783	635	911±3	127	141	143	175	1039	98	99	127
La	7.56	6.90	5.94	7.10	6.84	17.7	19.7	17.5±.1	19.0	21.4	21.2	16.3	10.8	27.3	28.0	23.7
Ce	20.2	19.6	16.3	18.7	17.7	42.4	45.9	41.1	46.4	49.6	50.9	41.0	26.5	67.4	67.6	59.3
Nd	13.1	13.1	11.0	13.2	13.0	26.1	28.3	25.9±.6	28.7	30.5	30.9	26.8	18.8	41.3	42.5	36.5
Sm	3.86	3.97	3.29	3.98	3.63	6.82	7.63	6.75±.08	7.15	7.77	7.47	6.94	4.96	10.4	10.35	9.00
Eu	1.44	1.50	1.23	1.46	1.39	2.32	2.60	2.31±.01	2.59	2.67	2.62	2.40	1.70	3.47	3.48	3.13
Tb	0.61	0.75	0.53	0.65	0.61	1.00	1.19	1.03±.08	1.02	1.14	1.11	1.07	0.83	1.61	1.56	1.31
Yb	1.62	1.90	1.47	1.75	1.52	2.10	2.19	1.98±.05	2.13	2.29	2.30	2.15	1.58	3.07	3.00	2.40
Lu	0.22	0.29	0.21	0.27	0.25	0.28	0.31	0.28±.01	0.31	0.32	0.33	0.31	0.25	0.40	0.42	0.33
Hf	2.68	2.78	2.27	2.81	2.65	4.83	5.45	4.85±.04	5.25	5.54	5.51	4.95	3.48	7.64	7.46	6.58
Th	0.27	0.46	0.16	0.47	-	0.91	1.33	1.24±.20	0.91	1.40	1.14	0.91	0.63	1.97	1.79	1.51

	Mauna Kea Samples															
	180-5.90	185-3.95	189-8.50	193-3.90	202-1.40	208-5.20	212-0.40	224-1.75	229-0.05	250-0.00	251-3.90	259-0.75	287-3.15	291-0.05	303-3.00	311-0.70
Depth, m	342.0	354.5	367.6	378.3	400.3	415.7	424.1	459.4	472.7	526.6	530.9	542.2	594.1	603.8	623.3	645.0
Flow unit	59	62	64	69	72	75	76	89	91	106	107	109	119	120	126	131
Sc	29.7	30.7	19.9±.3	22.7±.1	29.9	29.3±.1	22.6	29.6	27.4	26.7	29.4	23.0	31.3	30.3	22.5	29.6
Cr	440	313	1865±9	1380±20	209	552±3	1304	423	875	920	364	1540	333	688	1393	586
La	14.3	14.8	5.72±.13	8.45±.02	12.8	15.1±.1	7.76	12.9	10.7	11.0	13.6	7.55	13.4	10.3	8.22	9.55
Ce	36.6	36.9	14.8±.4	22.2±.8	33.8	37.9±.4	20.1	32.7	27.1	27.8	34.2	19.5	34.8	25.9	20.3	24.4
Nd	24.4	24.2	9.80±.42	14.5±.5	22.2	24.6±.2	13.7	21.1	18.0	17.9	21.4	13.0	23.3	17.5	14.9	17.2
Sm	6.50	6.45	2.69±.01	4.07±.09	6.03	6.35±.01	3.71	6.18	4.87	4.94	5.48	3.75	6.24	4.95	3.87	4.62
Eu	2.25	2.27	0.98±.01	1.46±.01	2.12	2.20±.03	1.32	2.20	1.78	1.74	2.00	1.36	2.22	1.78	1.40	1.69
Tb	1.05	1.13	0.41±.08	0.64±.01	1.00	1.00±.04	0.59	1.04	0.80	0.79	0.87	0.64	0.98	0.83	0.66	0.85
Yb	2.10	2.15	0.96±.02	1.37±.04	2.17	1.76±.10	1.38	1.99	1.69	1.59	1.94	1.29	2.14	1.72	1.31	1.93
Lu	0.29	0.30	0.14±.01	0.20±.01	0.29	0.27±.01	0.19	0.30	0.25	0.23	0.26	0.18	0.29	0.24	0.18	0.27
Hf	4.49	4.64	1.87±.02	2.88±.10	4.23	4.31±.18	2.69	4.37	3.70	3.69	3.91	2.57	4.80	3.58	2.75	3.37
Th	0.84	0.91	0.43	0.47±.04	0.79	0.88±.23	0.48	0.85	0.63	0.63	0.93	0.79	1.09	0.68	0.62	0.56

Table 1. (continued)

Mauna Kea Samples																
	315-3.35	319-1.30	322-3.50	327-2.80	340-5.15	347-6.35	350-2.45	356-1.45	365-0.05	371-0.30	374-5.90	379-3.80	382-4.35	385-5.55	399-4.30	401-4.90
Depth, m	658.2	669.4	677.6	689.8	720.3	738.7	747.4	759.7	781.2	797.4	798.6	821.4	829.2	835.6	869.1	875.4
Flow unit	132	137	138	141	147	152	153	155	159	164	165	167	169	170	176	177
Sc	25.1	24.7±.4	24.6	31.1	25.8	20.9±.3	30.7	30.3	21.8	23.7	22.0±.5	30.3	22.4	31.3	30.4	29.3
Cr	906	989±12	1030	338	867	1420±40	326	413	1450	1020	1460±40	565	1334	412	536	638
La	11.6	9.42±.09	8.27	12.4	11.1	7.23±.12	12.3	11.8	7.56	9.33	7.29±.11	9.03	7.85	10.0	11.9	9.52
Ce	29.6	24.2±1.1	20.9	31.1	28.4	18.2±.7	31.5	30.9	19.3	22.9	19.7±.4	23.5	19.9	26.0	30.2	24.4
Nd	19.3	16.2±0.2	14.2	21.3	18.9	12.0±.5	21.2	21.0	13.8	15.6	12.4±.2	16.6	13.0	17.3	21.3	17.9
Sm	5.30	4.43±.07	3.89	5.70	4.75	3.32±.06	5.71	5.62	3.58	4.13	3.46±.06	4.65	3.82	5.10	5.70	4.60
Eu	1.86	1.57±.02	1.44	2.04	1.71	1.20±.01	2.03	2.00	1.28	1.48	1.26±.02	1.66	1.38	1.84	2.00	1.71
Tb	0.82	0.71±.02	0.63	0.90	0.91	0.55±.01	0.99	0.93	0.64	0.73	0.55±.05	0.81	0.65	0.89	0.88	0.87
Yb	1.69	1.52±.05	1.60	1.92	1.67	1.15±.03	1.88	1.94	1.32	1.48	1.20±.02	1.83	1.35	1.90	2.12	1.77
Lu	0.26	0.22±.01	0.22	0.29	0.26	0.17±.01	0.27	0.27	0.16	0.21	0.17±.01	0.29	0.21	0.26	0.30	0.26
Hf	3.67	3.16±.05	2.83	4.21	3.39	2.41±.02	4.09	4.01	2.51	2.95	2.50±.02	3.34	2.77	3.55	3.88	3.38
Th	0.77	0.66±.04	0.62	0.91	0.62	0.51±.09	0.71	0.94	0.30	0.38	0.54±.07	0.61	0.64	0.56	0.66	0.66

Mauna Kea Samples

	424-9.30	428-2.70	434-7.90	442-2.10	446-2.40	452-3.90	457-4.30	463-6.00	464-7.10	466-5.00	Precision, %	KIL 1919
Depth, m	939.2	946.3	965.2	983.9	994.7	1009.5	1024.6	1043.7	1047.1	1052.4		
Flow unit	196	197	203	208	211	218	220	224	225	227		
Sc	29.1±.3	30.7	25.3	21.3	25.3	29.7	27.5	26.8±.1	27.2	26.9	1	30.9
Cr	479±3	393	838	1456	1005	364	690	720±2	752	664	1	249
La	9.33±.09	11.2	8.74	7.21	11.2	12.1	12.7	12.0±.04	11.8	12.8	1	15.2
Ce	24.5±.6	28.6	22.2	18.3	29.1	31.6	31.6	30.8±.9	30.6	32.8	3	38.0
Nd	16.7±.8	20.5	15.4	12.7	18.6	20.4	20.8	19.8±.2	19.3	21.5	3	23.8
Sm	4.54±.03	5.43	4.24	3.53	5.01	5.69	5.46	5.26±.04	5.25	5.60	1	5.90
Eu	1.67±.01	1.95	1.55	1.24	1.73	2.01	1.96	1.91±.02	1.87	1.98	1	2.06
Tb	0.82±.03	0.95	0.73	0.60	0.87	0.99	0.90	0.88±.01	0.91	0.78	6	0.88
Yb	1.75±.01	2.01	1.74	1.33	1.85	2.00	1.86	1.74±.01	1.79	1.86	2	1.94
Lu	0.26±.01	0.28	0.24	0.18	0.26	0.26	0.25	0.25±.01	0.25	0.26	3	0.27
Hf	3.42±.11	3.83	3.08	2.50	3.63	3.95	4.02	3.85±.01	3.82	4.05	2	4.32
Th	0.63±.01	0.70	0.44	0.68	1.01	0.84	0.78	0.85±.08	0.75	0.84	12	1.14

Trace element abundances are given in parts per million. These samples are aliquots of the powders analyzed for major and other trace elements by Rhodes [this issue]. Sample number indicates core run and depth in meters within each core. These abundances were determined by instrumental neutron activation at the Massachusetts Institute of Technology. Co and Ta data are not reported because samples were ground in WC. Data for the Mauna Loa lavas are discussed by Rhodes [this volume]. Precision (one sigma) of the data is indicated by replicate analyses of nine HSDP samples, and the average one-sigma precision is indicated in the column labeled "precision." Accuracy can be assessed from the data for KIL 1919. This sample is from the same flow as USGS standard Hawaiian basalt BHVO-1, and it was prepared by H. West and distributed as a standard rock for those analyzing the HSDP core. Except for Cr this sample has trace element abundances very similar to that of BHVO-1. The data are a mean of 21 NA analyses made during 1994. Based on a comparison of these data with nine analyses of BHVO-1 by isotope dilution made at the Max Planck Institut für Chemie, we have lowered our Ce abundances by 5.3%. To be consistent with this HSDP data, our previous NA data for Ce in Hawaiian lavas should be lowered by 5.3%.

FIGURE CAPTIONS

- Fig. 1 Abundances of $\text{Na}_2\text{O} + \text{K}_2\text{O}$ versus SiO_2 content (all in weight percent) with FeO as 0.85 of total iron. Alkalic-tholeiitic dividing line from Macdonald and Katsura (1964) and is given by $\text{Na}_2\text{O} + \text{K}_2\text{O} = 0.37 \text{ SiO}_2 - 14.43$. HSDP lavas with $\text{K}_2\text{O}/\text{P}_2\text{O}_5 < 1.6$ have lost K_2O during posteruptive alteration (see text); therefore the K_2O contents of these lavas were increased so that $\text{K}_2\text{O}/\text{P}_2\text{O}_5 = 1.6$, the average value for unaltered HSDP lavas. (a) HSDP lavas - alkalic lavas from the upper 58 m of core are labeled. At high SiO_2 , HSDP tholeiitic lavas overlap with recent Kilauea lavas (Garcia et al., 1992). In Fig. 1a and all subsequent figures, alkalic and tholeiitic HSDP lavas are indicated by solid and open triangles, respectively. (b) HSDP lavas compared to fields for subaerially exposed Mauna Kea lavas and lavas dredged from the submarine east rift. None of the HSDP lavas are similar to the Laupahoehoe Volcanics. Most HSDP lavas (R177 is an exception) overlap with the fields for Hamakua Volcanics. In this and subsequent figures, HSDP data are from this paper and Rhodes (1996) submarine lava data from Yang et al. (1994) Hamakua and Laupahoehoe data from West et al. (1988) and Frey et al. (1990, 1991).
- Fig. 2 (a) Alkalinity, (b) $\text{Al}_2\text{O}_3/\text{CaO}$ and (c) $\text{K}_2\text{O}/\text{P}_2\text{O}_5$ in Mauna Kea lavas versus depth in the HSDP core. Alkalinity is the vertical distance from the tholeiitic-alkalic dividing line in Fig. 1. Lavas with atypically low $\text{Al}_2\text{O}_3/\text{CaO}$ and $\text{K}_2\text{O}/\text{P}_2\text{O}_5$ are labeled.
- Fig. 3 Major oxide abundances versus MgO content in HSDP lavas (all in weight percent; Fe_2O_3 is total iron). Samples with distinctive features are labeled.
- Fig. 4 Abundances of incompatible trace elements versus Nb content in Mauna Kea lavas (all in parts per million). The highest abundances are in high Fe-Ti basalts which are relatively young Hamakua lavas. HSDP sample R174 belongs to this group. Samples offset to low Rb also have low $\text{K}_2\text{O}/\text{P}_2\text{O}_5$, and they have lost alkali metals during posteruptive alteration.

- Fig. 5 Abundances of incompatible elements in selected HSDP lavas normalized to primitive mantle (Sun and McDonough, 1989). R174 is an Fe-Ti rich basalt that is highly enriched incompatible elements and relatively depleted in Sr. R177 is the most alkalic HSDP lava analyzed. R185 (7.4% MgO) and R208 (10.0% MgO) are examples of the uppermost tholeiitic lavas, and they have crossing REE patterns. R401 is a tholeiitic lava (10.75% MgO) representative of lavas with low abundances of incompatible elements that occurs in the 800 to 950 m interval. R466 is the lowermost Mauna Kea lava; despite its high MgO content (11%) it has higher abundances of incompatible elements than overlying tholeiites with lower MgO contents. Stippled field for lavas below 340 m indicates range for 42 tholeiitic lavas.
- Fig. 6 Incompatible element abundance ratios in Mauna Kea lavas versus Nb content (parts per million). Error bar indicates two standard deviations. In Fig. 6b the Th data for HSDP lavas were determined by isotope dilution (Lassiter et al., 1996).
- Fig. 7 La/Yb and Zr/Nb versus depth in the HSDP core. Samples defining inflections are labeled. Stippled fields in Figs. 7a and 7b indicate regions with expanded depth scales in the top panels.
- Fig. 8 La/Yb versus Zr/Nb and alkalinity (see Fig. 2 caption) in Mauna Kea lavas. Hamakua tholeiitic lavas from Waikahalulu gulch and HSDP sample R208 have La/Yb and Zr/Nb which overlap with alkalic HSDP lavas, and they are offset to high La/Yb at alkalinity values of 0 to -1. The extremes in La/Yb and Zr/Nb are represented by some submarine lavas and the high Fe-Ti basalt.
- Fig. 9 La/Yb as a function of age during growth of Mauna Kea volcano. The vertical scale indicates the stratigraphic position of lavas within the HSDP core, Waikahalulu Gulch and Maulua Gulch with ages from Wolfe et al. (1996) and Sharp et al. (1996). Based on these ages, lavas in Waikahalulu Gulch are inferred to be younger than the uppermost HSDP lavas and lavas in Maulua Gulch are inferred to be

contemporaneous with the tholeiitic to alkalic transition in the HSDP core. The undated submarine lavas are inferred to be older than the lowermost HSDP lavas.

Fig. 10 $\text{Al}_2\text{O}_3/\text{CaO}$ and SiO_2 contents (in weight percent) in high Fe-Ti Hamakua lavas versus estimated pressures (Yang et al., 1996). HSDP lava R174 belongs to this group. Hamakua data are from Frey et al. (1991) and Wolfe et al. (1996) with sample numbers for two samples equilibrated at high pressure.

Fig. 11 Ni (in parts per million) versus MgO content (in weight percent) for HSDP, submarine, and subaerially exposed Mauna Kea lavas. The curves are for olivine fractionation and were calculated by adding 1% increments of olivine to the composition of lava R463, a MgO-rich lava with ~6% olivine (Garcia, 1996). Olivine Fe/Mg ratios are based on a K_D of 0.3 and Ni contents were determined following Hart and Davis (Hart and Davis, 1978), dashed line, or Kinzler et al. (1990), thin solid line; at 13% MgO the Ni partition coefficients are 8 and 7, respectively. The thick solid curve emanating from R463 shows the effects of a constant but lower Ni partition of 6 which is consistent with the results of Morse et al. (1991). The straight line is for addition of Fo_{86} olivine to R463.

Fig. 12 Abundances of incompatible elements (in parts per million) and oxides (in weight percent) in estimated primary magma compositions (16% MgO) for 24 HSDP lavas as a function of height in the HSDP core. Primary magma compositions were determined by adding equilibrium olivine in 1% increments until MgO contents were 16%. Solid symbols indicate alkalic lavas.

Fig. 13 Abundances of Al_2O_3 , SiO_2 , and FeO (in weight percent) and $\text{Al}_2\text{O}_3/\text{CaO}$ ratio in estimated primary magma compositions (16% MgO) for 24 HSDP lavas as a function of height in the HSDP core. See text and Fig. 12 caption for procedures used to calculate primary magma compositions. Solid symbols indicate alkalic lavas.

Fig. 14 Abundances of FeO, Nb, and Al_2O_3 versus SiO_2 content (all in weight percent except

for Nb in parts per million) in estimated primary magma compositions (16% MgO) for Mauna Kea lavas. See text and Fig. 12 caption for procedures used to calculate primary magma compositions.

Fig. 15 Abundances of oxides versus MgO content (all in weight percent) in tholeiites, picrites, and ankaramites from Mauna Kea volcano. Altered samples with $K_2O/P_2O_5 < 1$ are not plotted. On average, in the range of MgO = 10 to 20%, the lava groups, submarine-HSDP- subaerial, correspond to decreasing SiO_2 , higher Fe_2O_3 , (total iron) and higher CaO.

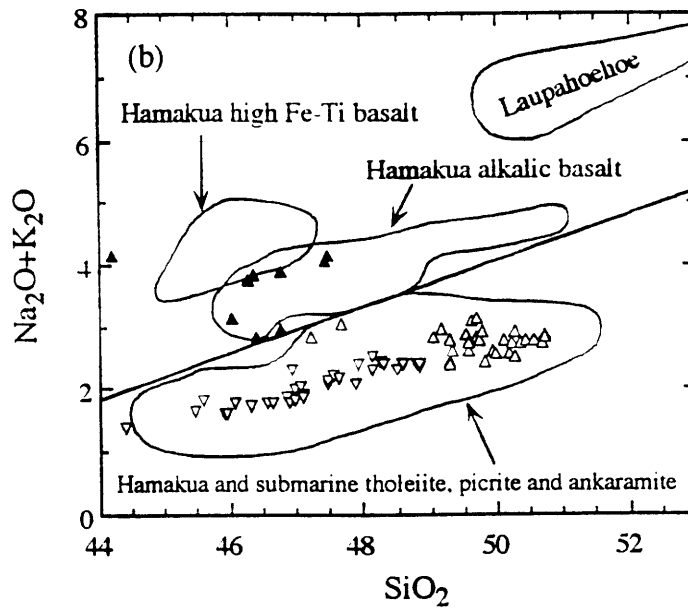
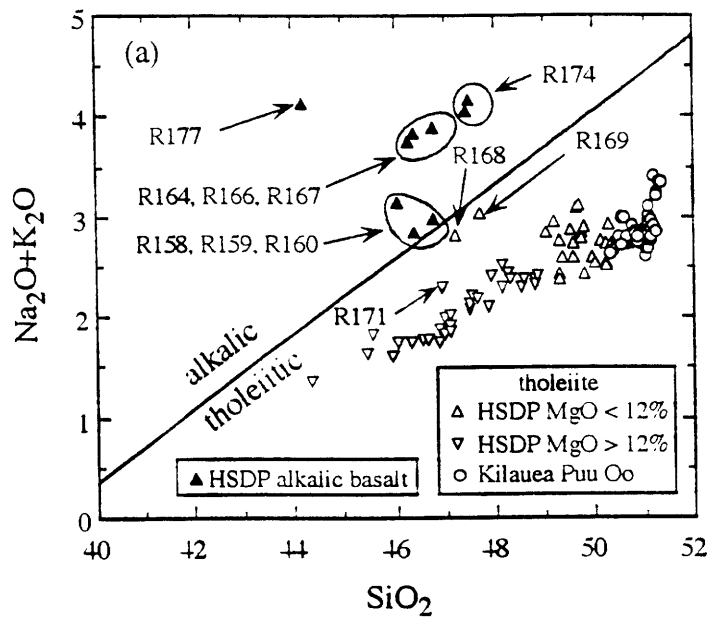


Fig. 1

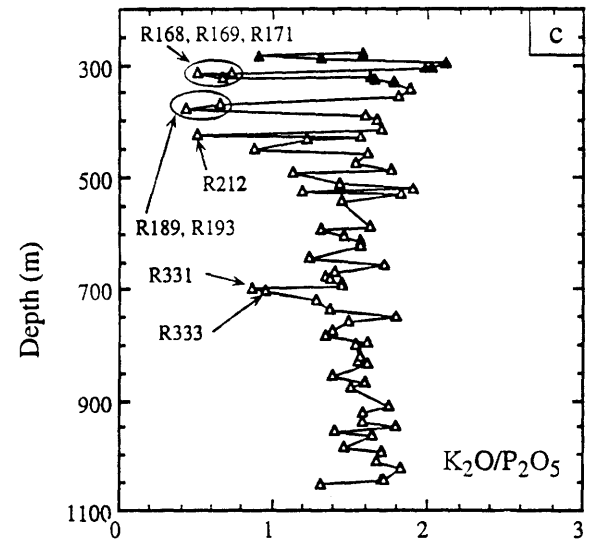
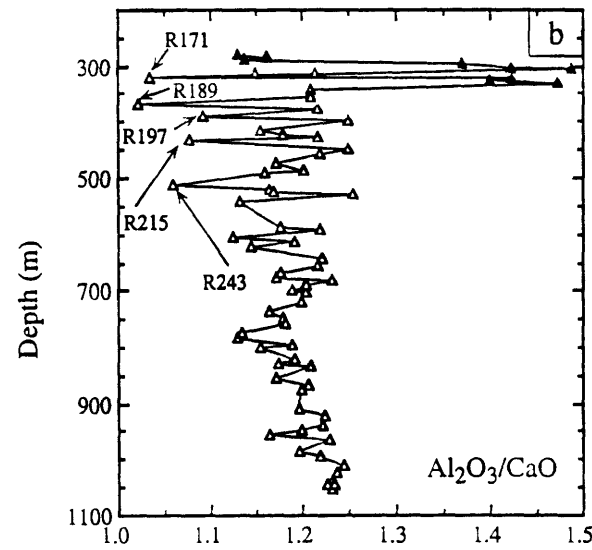
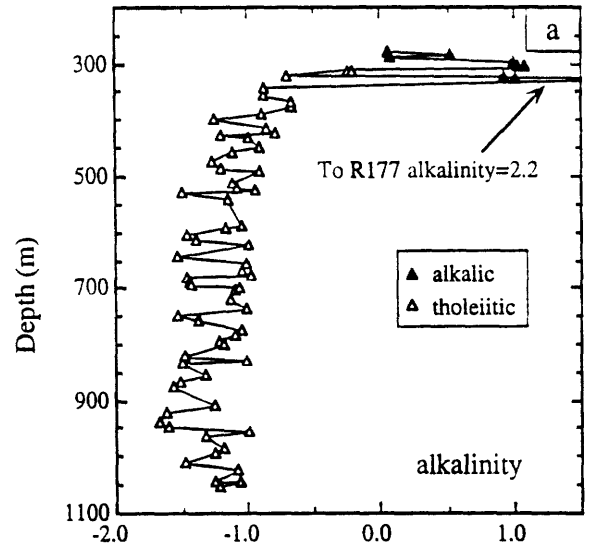


Fig. 2

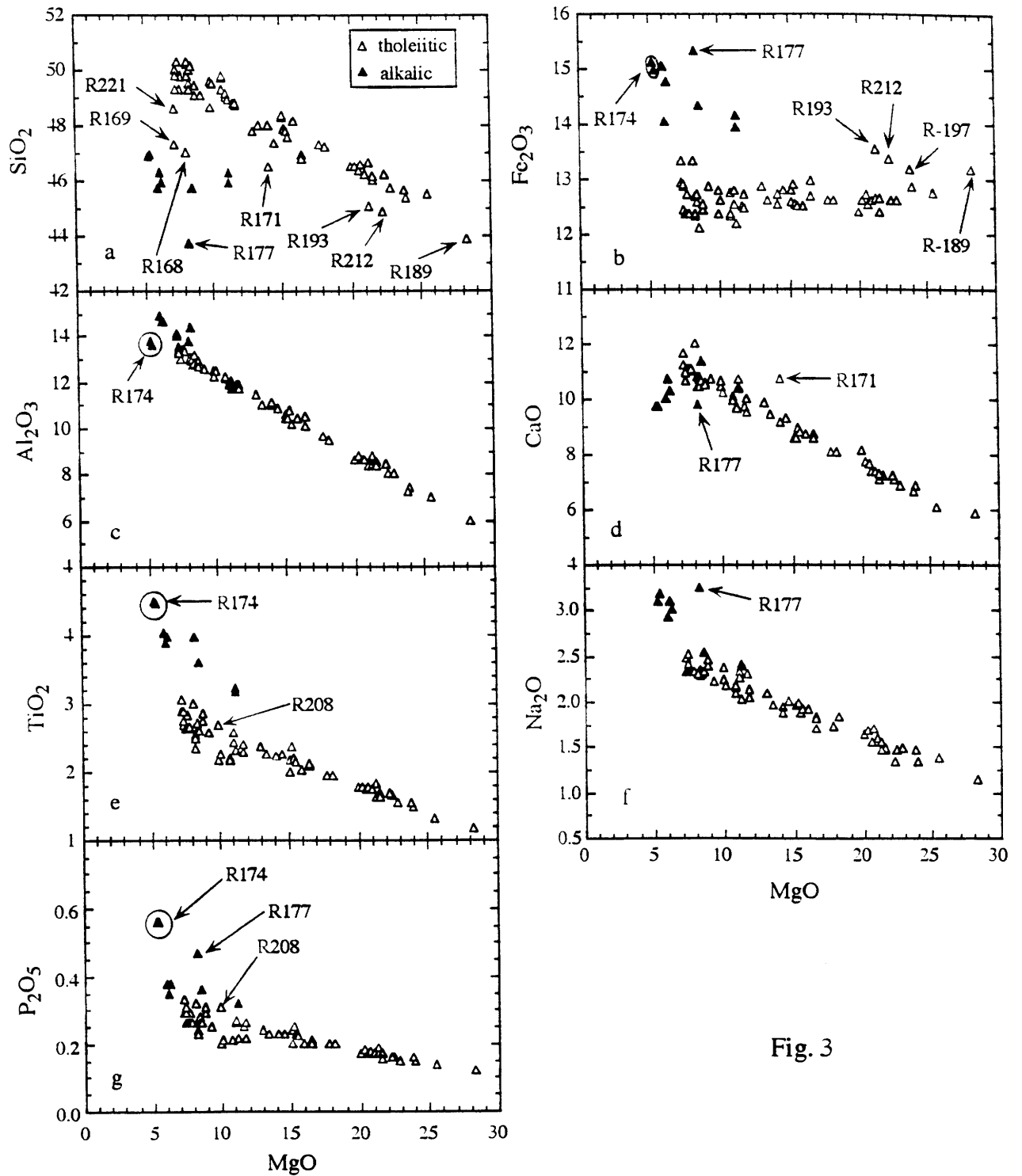


Fig. 3

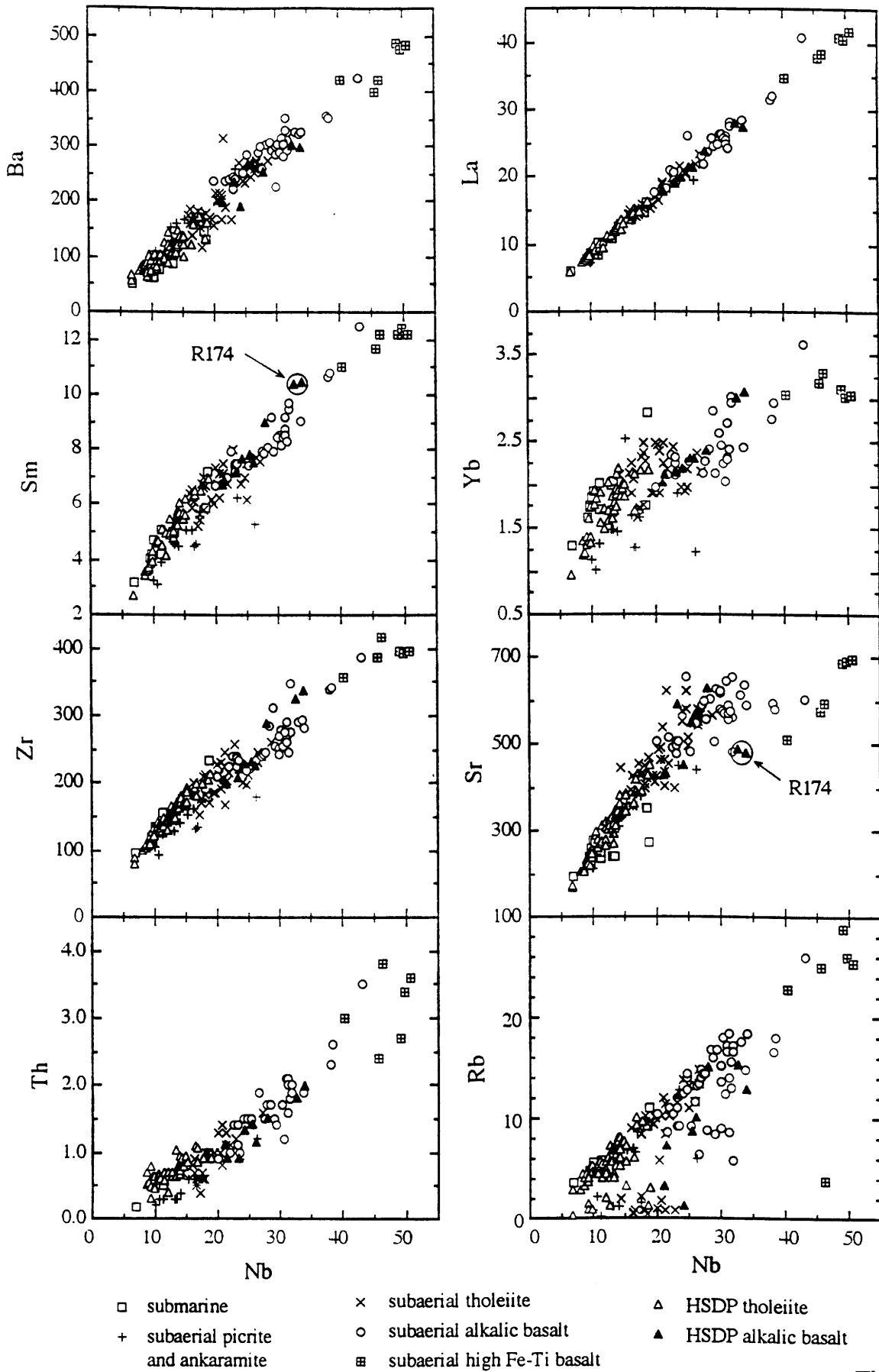


Fig. 4

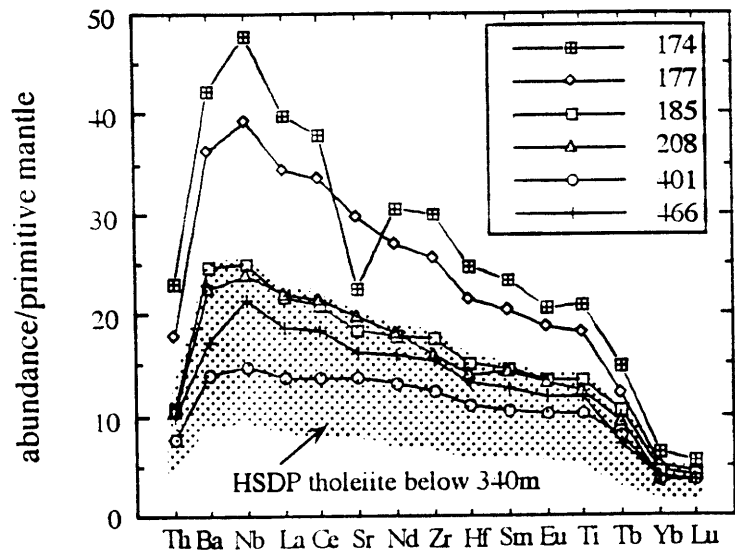


Fig. 5

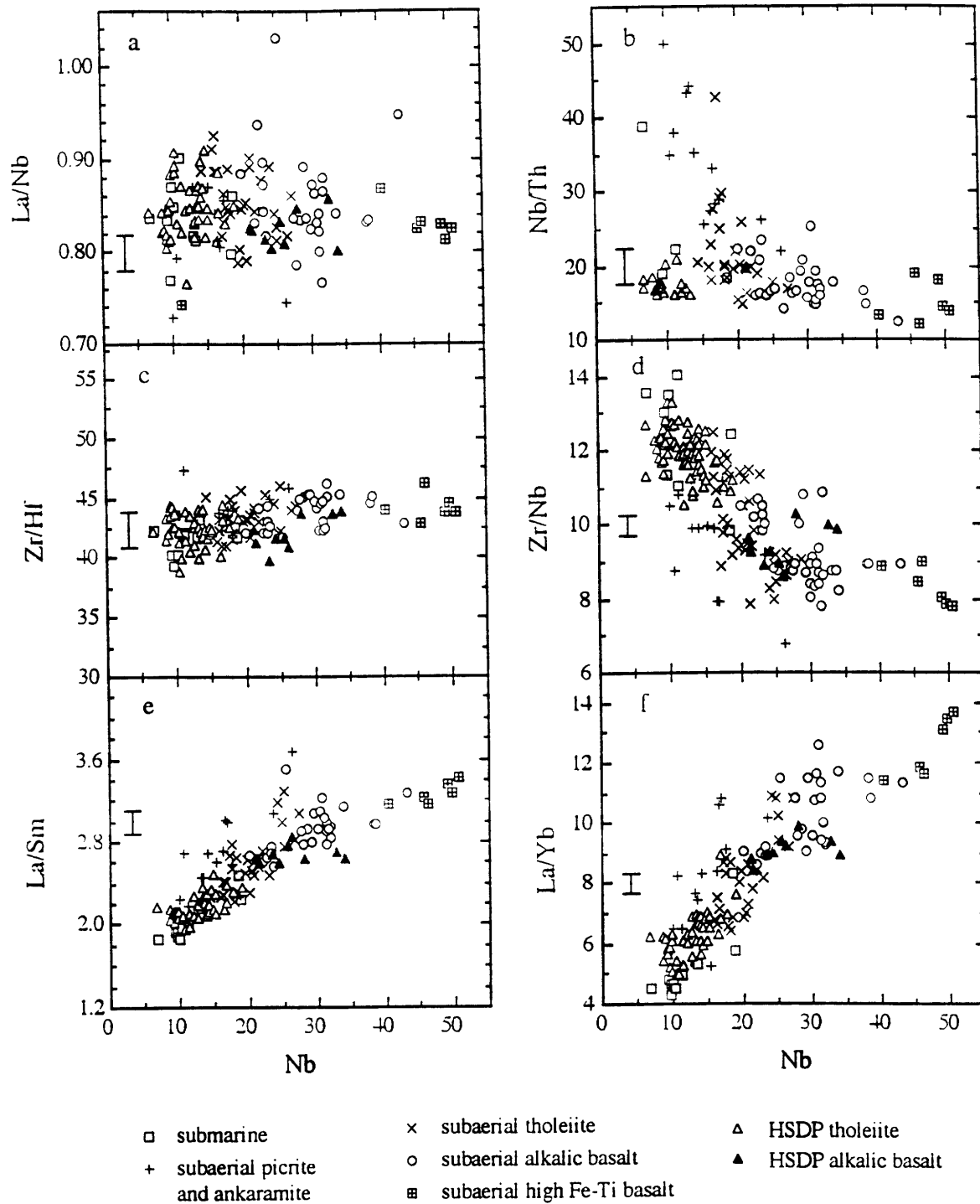


Fig. 6

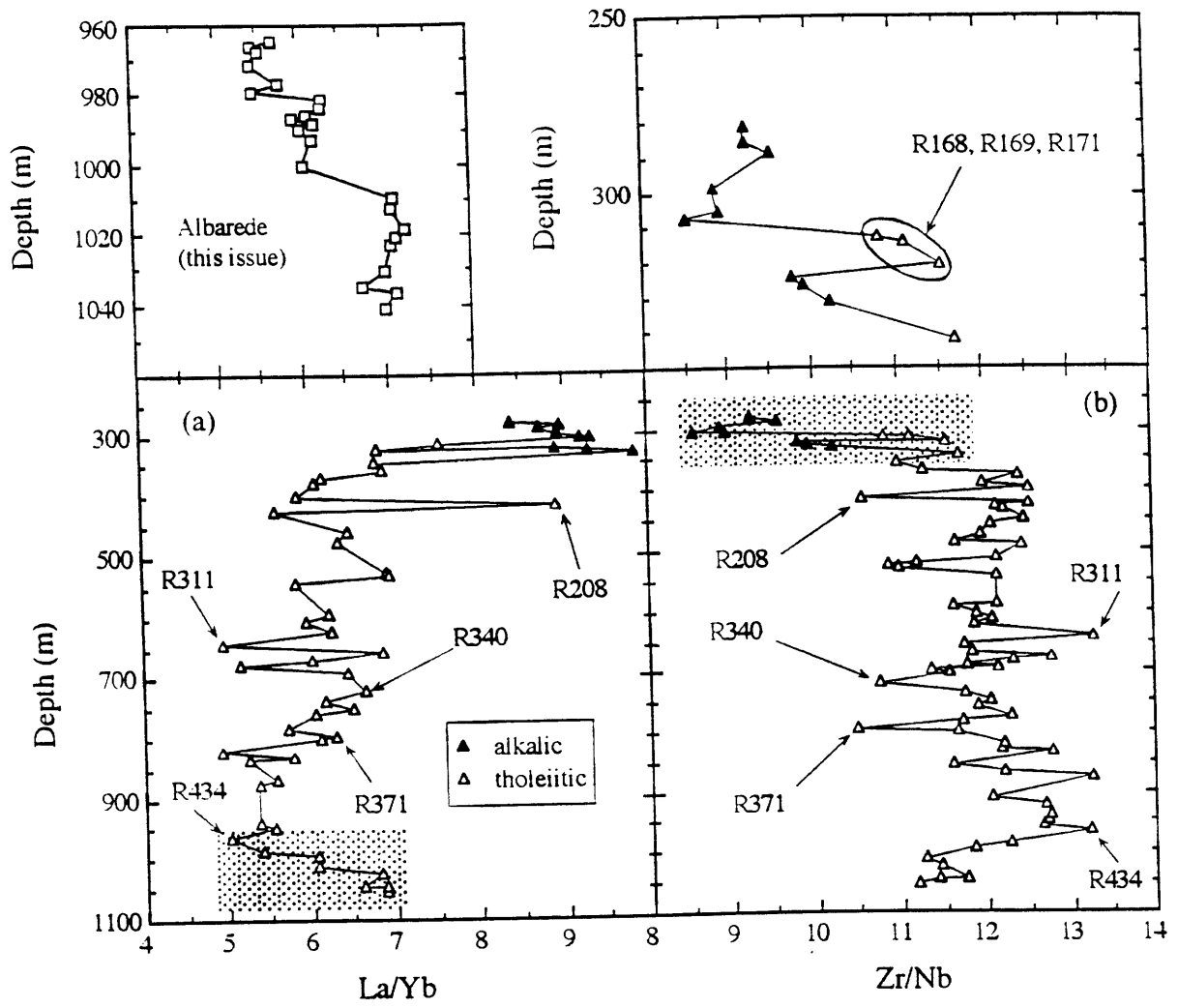


Fig. 7

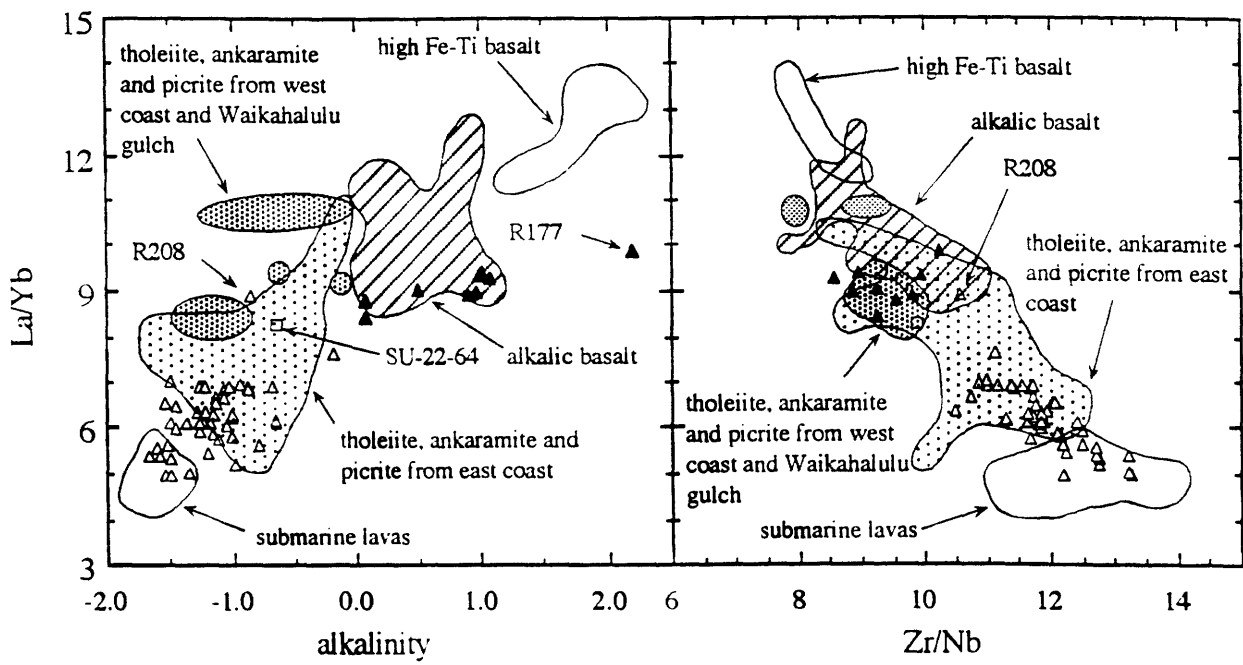


Fig. 8

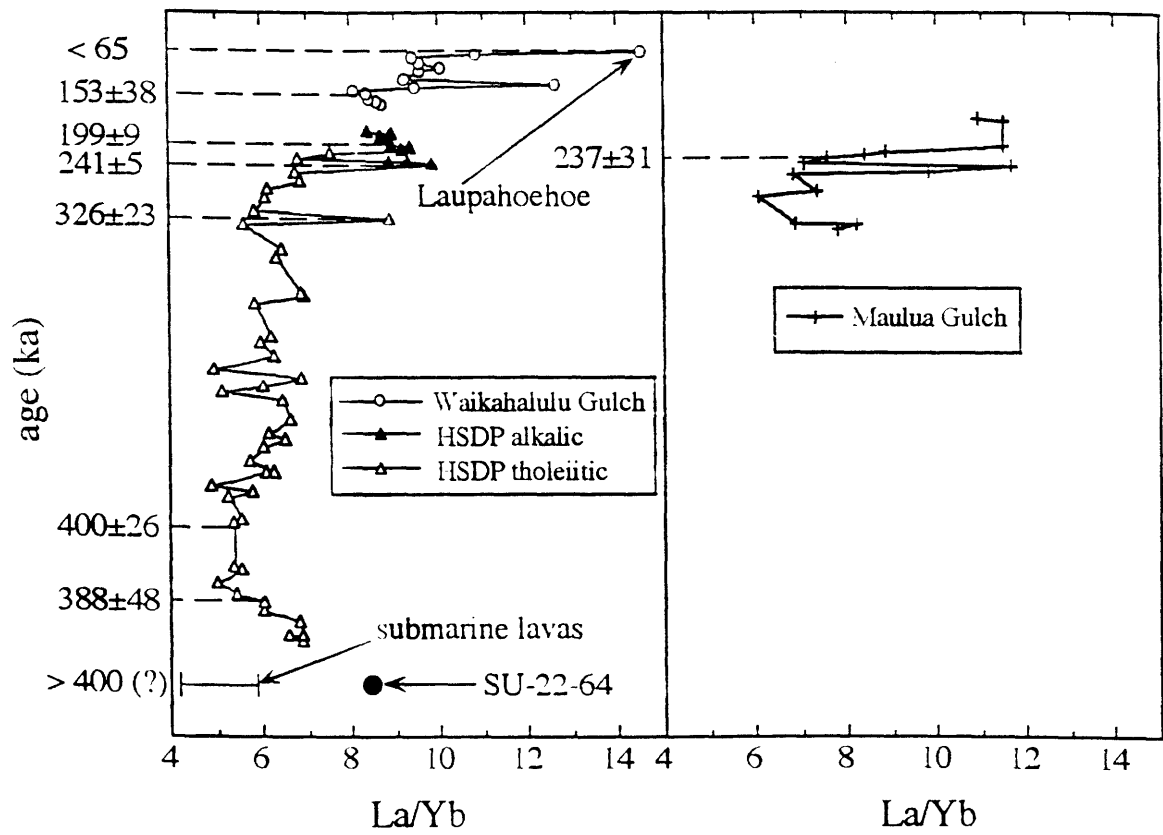


Fig. 9

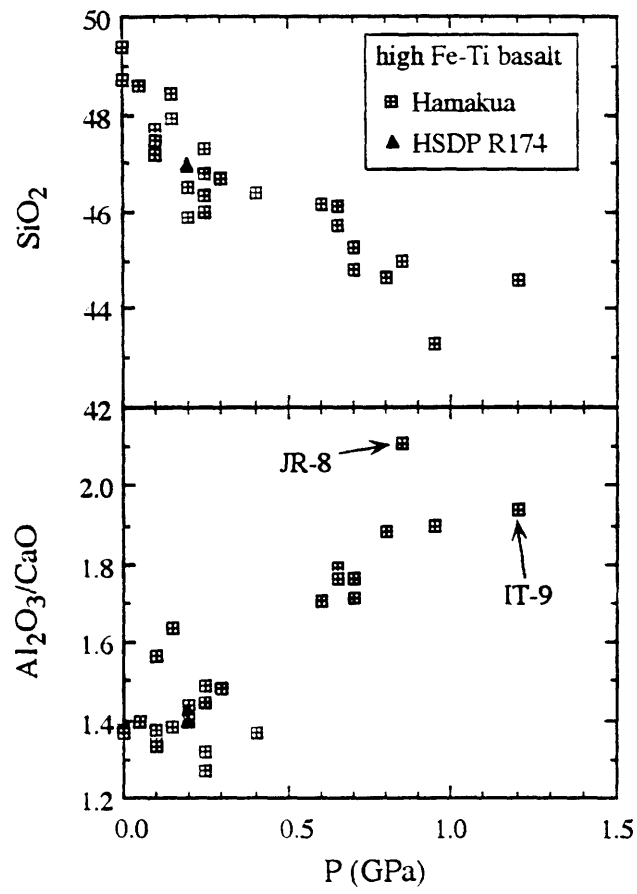


Fig. 10

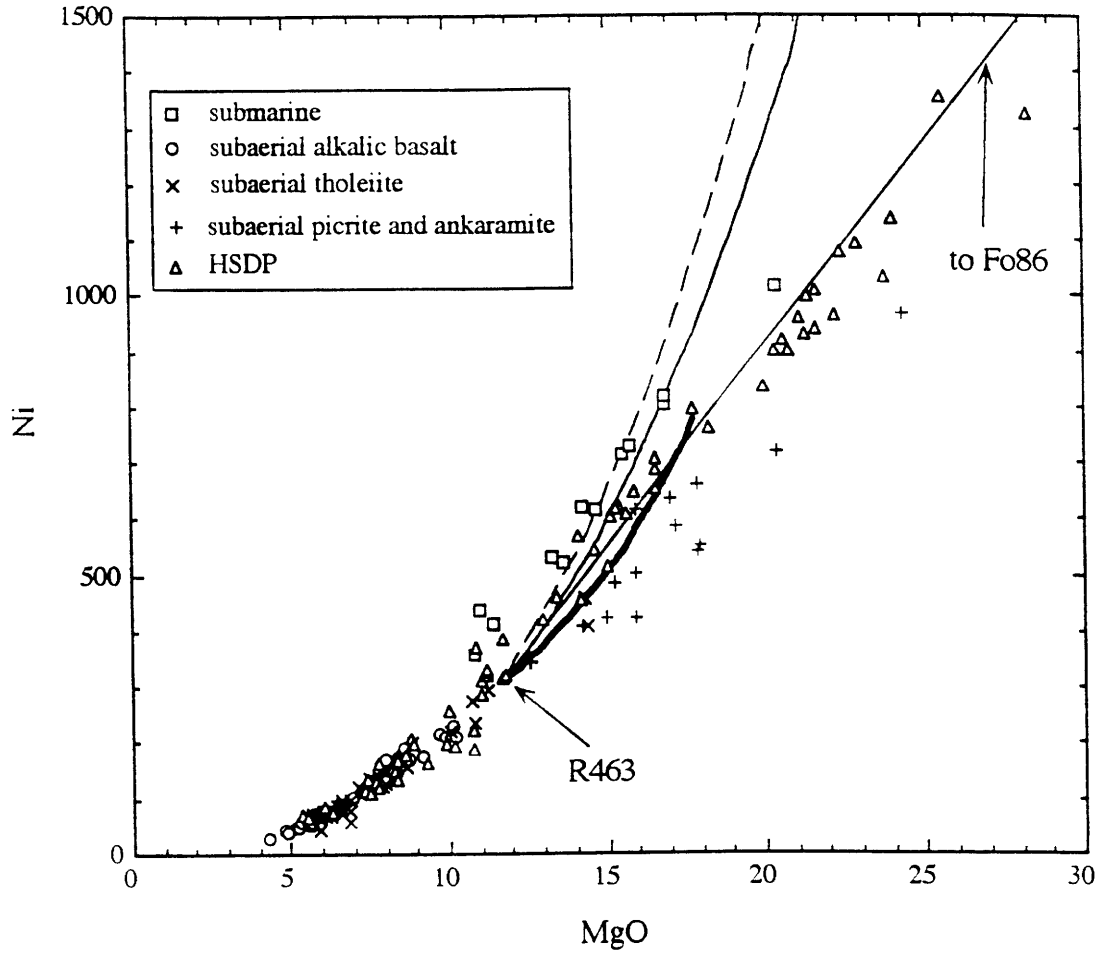


Fig. 11

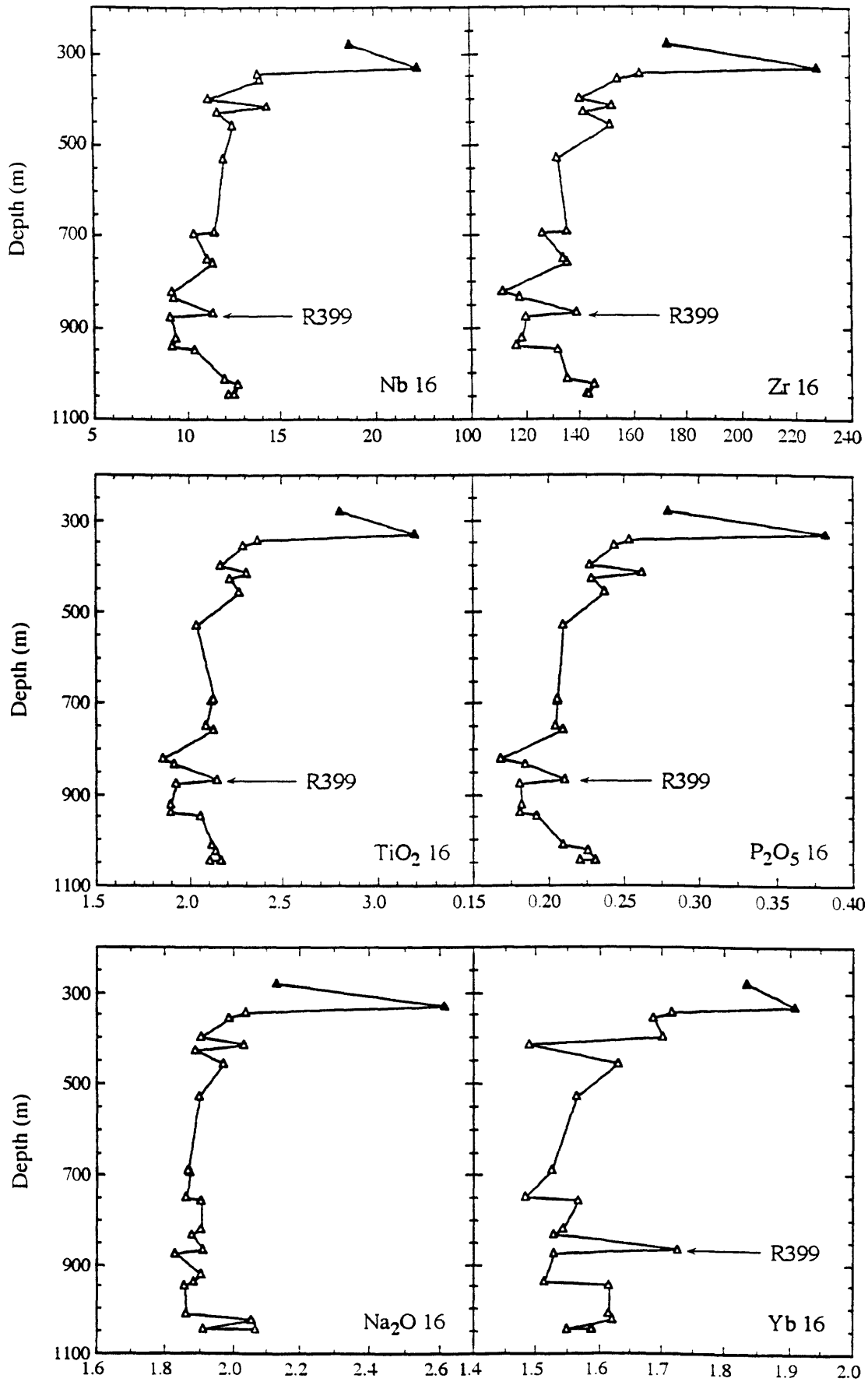


Fig. 12

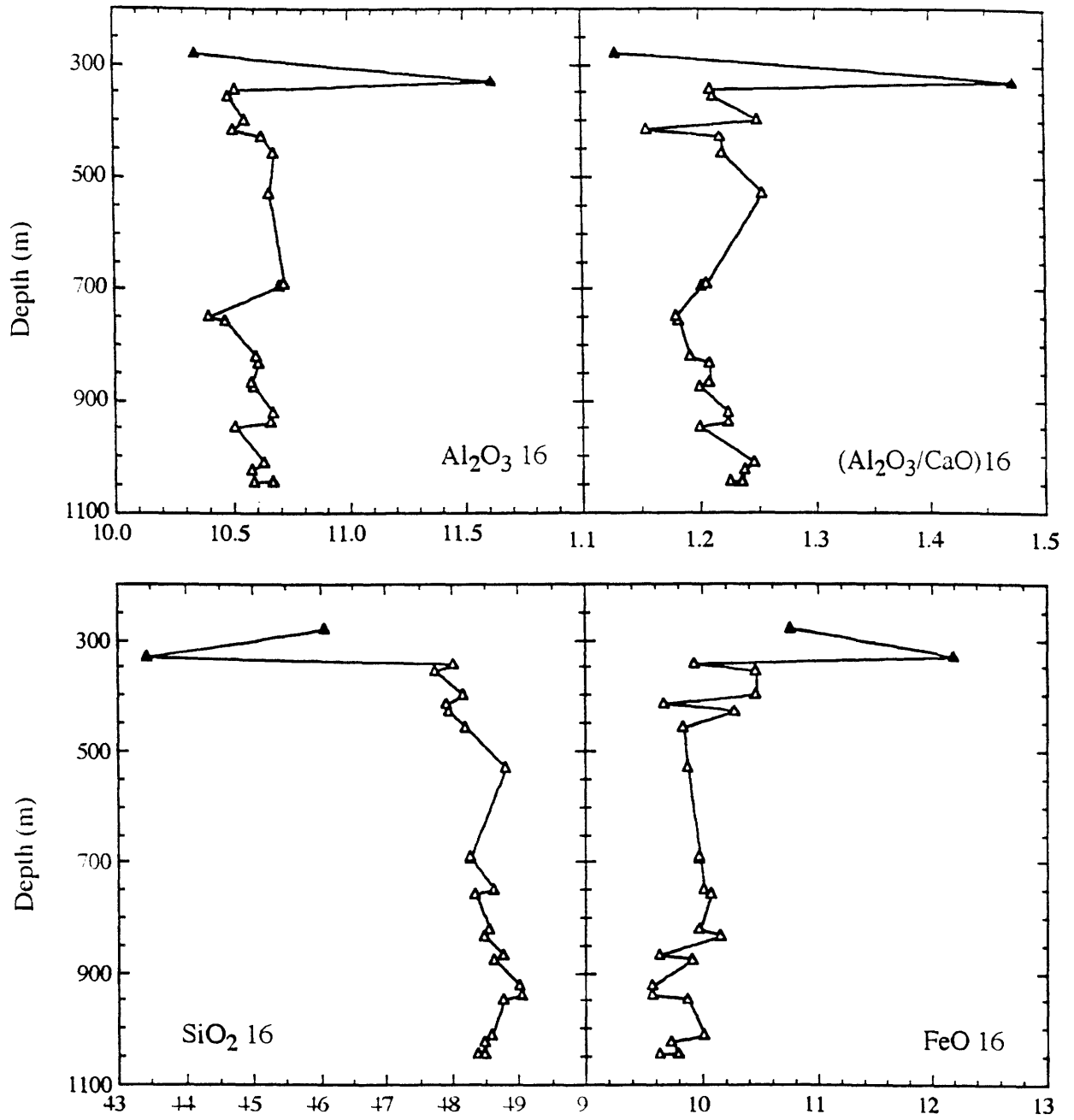


Fig. 13

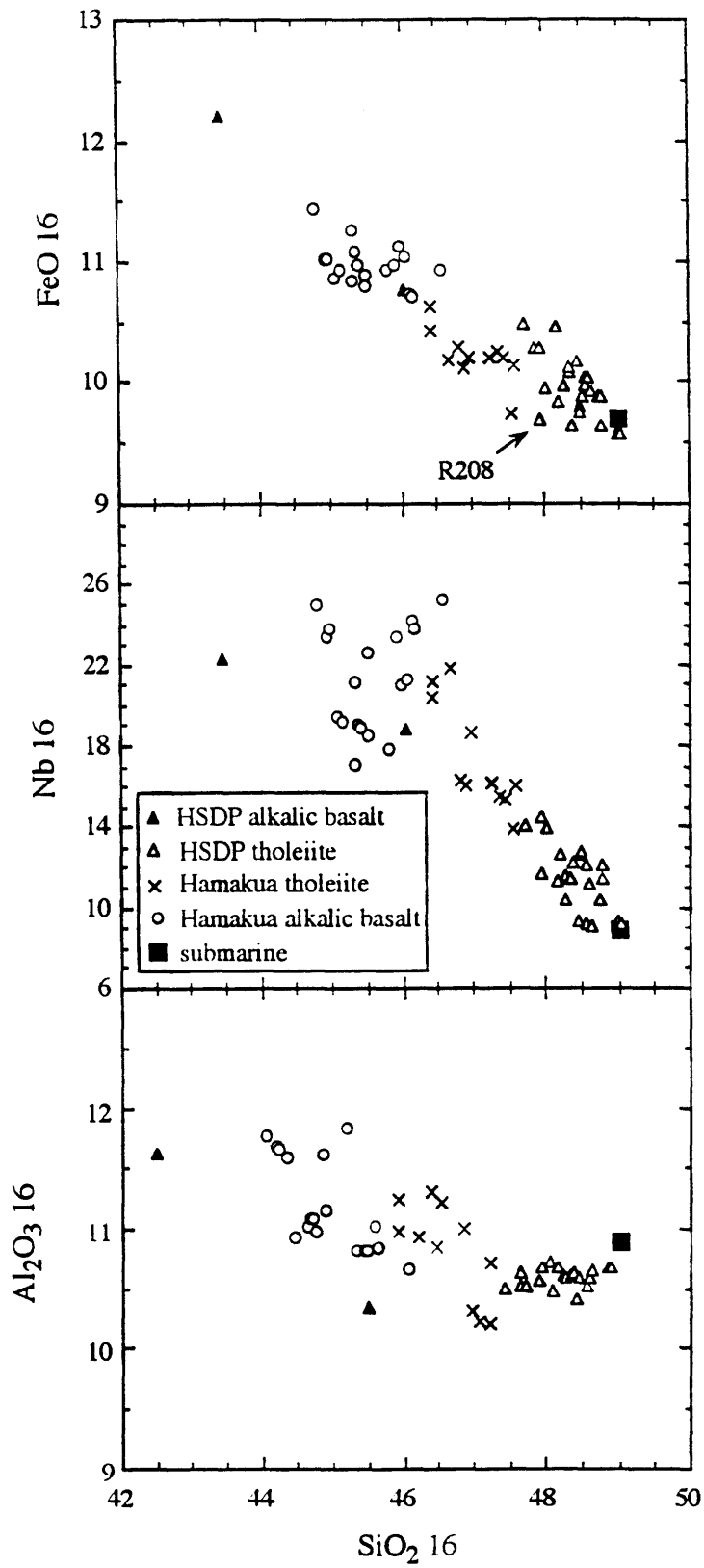


Fig. 14

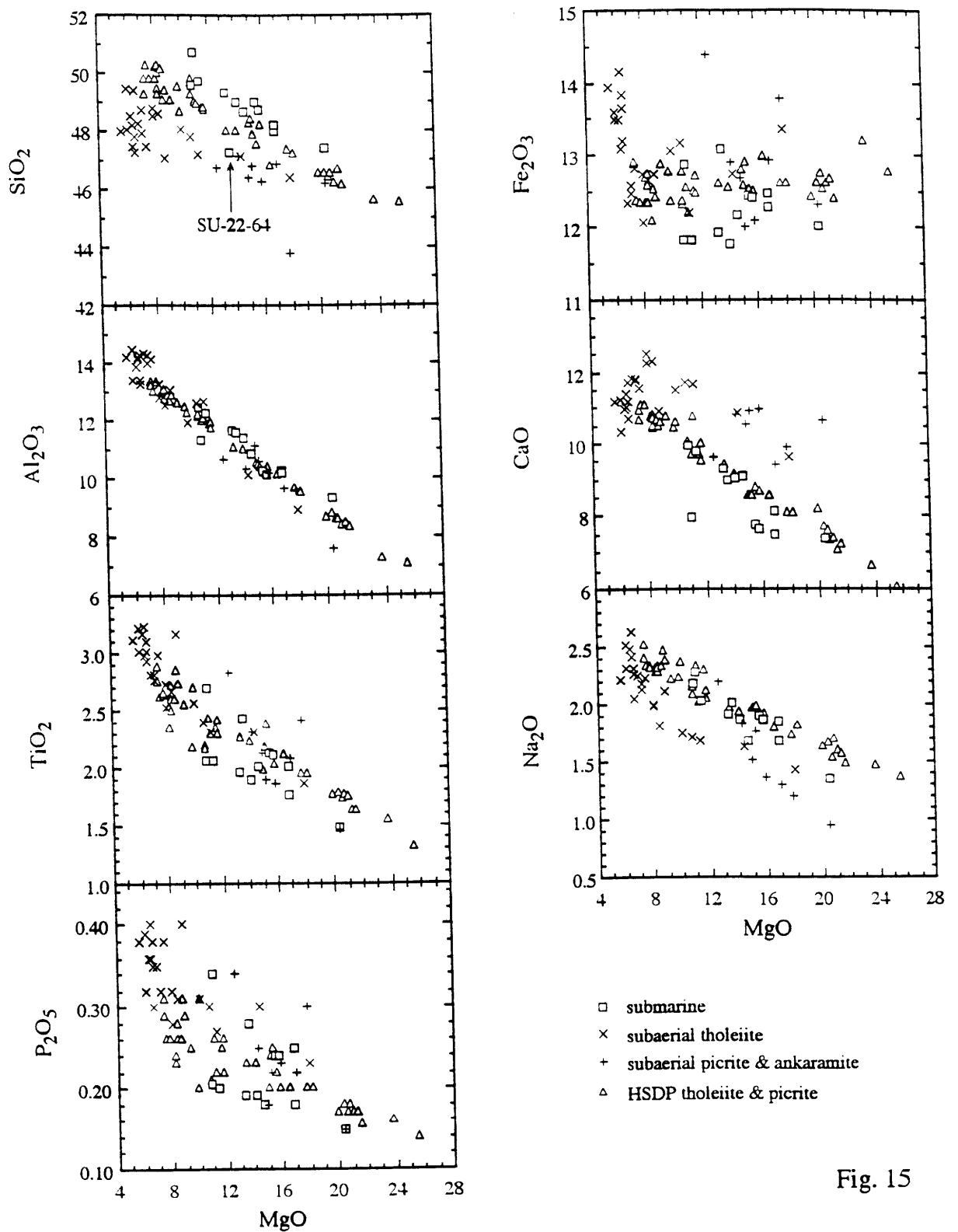


Fig. 15

CHAPTER FIVE

The geochemistry of Mt. Bureau basalts: implications for the plume composition and plume-MORB interaction

INTRODUCTION

The Kerguelen Archipelago in the southern Indian Ocean, on the Antarctic plate, is the third largest oceanic island group with an area of 6500 km². It was built on the northern part of the very large Kerguelen Plateau (Fig. 1a). The Kerguelen Plateau and its conjugate Broken Ridge form an igneous province that is interpreted to represent the initial voluminous volcanism (~115Ma) associated with arrival of the Kerguelen Plume below a recently formed Indian Ocean. As a result of the rapid northward movement of the Indian plate over the plume, a 5000 km long, ~80-38 Ma hotspot track formed the Ninetyeast Ridge. At ~38 Ma the newly formed Southeast Indian Ridge intersected the plume position, and as this spreading center moved northward the plume became isolated beneath the Antarctic plate. As a result, the plume resided beneath the northern part of the Kerguelen Plateau and constructed the ~38 to 0 Ma Kerguelen Archipelago. Thus, there is a very long term, ~115 Ma, record of volcanism attributed to the Kerguelen Plume and the Kerguelen Archipelago reflects the last 38 Ma of the volcanic activity (Weis et al., 1992) (Fig. 1b).

More than 80% of the archipelago is composed of nearly horizontal "flood basalt" lavas with no obvious vents and few dikes. Giret et al (1992) stated that these lavas define a regional dip of 5° to the east. As a result of extensive glacial erosion, the surficial lavas decrease in age from west to east. Locally, the dips of the lavas are affected by nearby intrusions. The abundance of the plutonic rocks, gabbro to syenite and granite, in the archipelago is unusual for an oceanic island, and these plutonic rocks have been studied in detail (e.g., Dosso et al., 1979; Giret and Lameyre, 1983; Weis and Giret, 1994). They range widely in age and size, but the oldest known rocks in the archipelago are gabbros, such as the Val Gabbro in the Southeast Province. The oldest K-Ar age, 39±3 Ma of the Val gabbro, (Giret and Lameyre, 1983) is slightly less than the youngest magnetic anomalies from the surrounding oceanic basement, that is anomaly 18 (~45 Ma) (Fig. 2 of **Munsch et al, 1994**). The exposed volcanic rocks on the Kerguelen Archipelago are younger, ranging from 26 to 0.2 Ma (Watkins et al., 1974; Giret

and Lameyre, 1983; Nougier et al., 1983). Many of the youngest lavas are in the Southeast Province where the flood basalt sequence is overlain by a 20-22 Ma lower Miocene Series ranging from alkaline basalt to trachyte, a 6.6-10.2 Ma upper Miocene Series ranging from basanite to phonolite and the very young Ross volcano, 4 to 0.2 Ma, which ranges from alkalic basalt to trachyte. These relatively young lavas have been studied in considerable detail (Watkins et al., 1974; Nougier et al., 1983; Weis et al., 1993).

In contrast, there have been only survey studies of the flood basalts which form the major portion of the archipelago. Watkins et al. (1974) analyzed major and some trace elements for sequences of lava flows on the Courbet peninsula and lavas from lower 150 meters of the Mt. Bureau section on the eastern Foch island (Fig. 1b). An important result was the K/Ar dating which indicated ages of 24.5 to 27.3 Ma for these flood basalts. White and Hofmann (1982) and White (unpublished) obtained Sr, Nd and Pb isotopic data for 4 of the Mt. Bureau lavas studied by Watkins et al (1974). These results show large isotopic variations within 100 meters of the section and three of the lavas have the lowest $^{87}\text{Sr}/^{86}\text{Sr}$ and highest $^{143}\text{Nd}/^{144}\text{Nd}$ found in archipelago lavas. Gautier et al. (1990) studied shield and younger lavas from different localities in the Kerguelen Archipelago (2 to 5 samples from each locality) and concluded that the rock types, age and Sr and Nd isotopic ratios of Kerguelen Archipelago lavas are correlated with the lowest $^{87}\text{Sr}/^{86}\text{Sr}$ ratios in ~26 Ma lavas from Mt. Bureau on Foch island (White and Hofmann, 1982) and the highest $^{87}\text{Sr}/^{86}\text{Sr}$ ratios in the relatively young highly alkaline lavas. The relatively high $^{87}\text{Sr}/^{86}\text{Sr}$ and low $^{143}\text{Nd}/^{144}\text{Nd}$ ratios in young alkalic lavas was confirmed by Weis et al. (1993) who studied lavas from the Southeast Province. Gautier et al. (1990) postulated a SEIR MORB - Kerguelen plume interaction model to explain the correlation of isotopic ratios with age (Fig. 1c). Storey et al. (1988) proposed a similar model but they also suggested that lavas with low $^{87}\text{Sr}/^{86}\text{Sr}$ ratios may contain a component derived from the Kerguelen Plateau lithosphere.

Because some of the plutonic rocks in the archipelago are similar to those occurring on

continents (Nougier and Lameyre, 1972; Nougier and Lameyre, 1973), initial discussions on the origin of the Kerguelen Archipelago focused on a continental versus oceanic origin (e.g. Watkins et al., 1974). However, the Sr, Nd and Pb isotopic ratios of these plutonic complexes are similar to those of the lavas which were derived from the Kerguelen Plume and none of these ratios have the extreme values typical of old continental crust; most recent studies have concluded that a continental origin is unlikely (e.g., Dosso et al., 1979; Weis and Giret, 1994). Recent Os isotopic data on some Kerguelen xenoliths, however, show continental affinities (Hassler and Shimizu, 1995). Also, lavas dredged from the east end of Broken Ridge (dredge 8) and recovered from drill Site 738 at the southern end of the Kerguelen Plateau (Fig. 1a) have Sr, Nd and Pb isotopic ratios and trace element ratios showing the effects of a continental component (Mahoney et al., 1995). Therefore, the role of the continental component in the source of archipelago must be reconsidered.

In this study, twenty-nine samples from the 630 meter Mt. Bureau section were analyzed for major and trace elements and Sr, Nd and Pb isotopes. Three samples from the lower, middle and upper part of the section were dated with the ^{39}Ar - ^{40}Ar method. The goals are to answer the following questions. How do the chemical and isotopic compositions vary with time? Over what time scale did these variations occur? How are the major and trace element abundances and isotopic ratios related? What is the relative importance of different source compositions such as asthenosphere, plateau lithosphere, continental lithosphere, and plume, and did the relative proportions of these components change systematically with time? Answers to these questions will bear on first order problems such as: what are the geochemical characteristics of the Kerguelen Plume and how have they changed with time? How did the proportions of source components change in plume-related volcanism as the plume location changed from a small newly opened, oceanic basin to a ridge-centered location to its present intraplate oceanic location.

SAMPLES

Mt. Bureau on Foch island (Fig. 1b), which is 630 meters high, was sampled in 1992 and 1993. Twenty-nine samples from the 1992 collection were analyzed for major and trace elements and Sr, Nd and Pb isotopic ratios (Fig. 1d). Three aphyric samples from the 1993 collection were selected for $^{39}\text{Ar}/^{40}\text{Ar}$ dating (Fig. 1d).

PETROGRAPHIC DESCRIPTION

General petrographic descriptions for each sample are listed in Table 1. Plagioclase, clinopyroxene, olivine and an opaque mineral are the main crystalline phases. The Mt. Bureau section forms two subsections defined by a change in petrography at 300 meters. In the upper subsection, plagioclase is the dominant phenocryst in phyrlic lavas. Microphenocrysts are clinopyroxene and olivine with clinopyroxene more abundant than olivine. Plagioclase ranges from euhedral to corroded to subhedral and forms aggregates. Clinopyroxenes are subhedral and often zoned. In contrast to lavas from the upper subsection, lavas from lower subsection contain phenocrysts of olivine and clinopyroxene in addition to plagioclase. Olivine interiors are fresh with iddingsite on edges. In some samples, olivine and clinopyroxene are more abundant than plagioclase. Seven of seventeen samples from the upper subsection and three of twelve samples, GM9254, GM9256 and GM9258, from the lower subsection are aphyric. Secondary minerals such as zeolite, chlorite and calcite are common in the whole section indicating that all samples have been affected by postmagmatic processes. GM9253 is an ankaramite dike containing clinopyroxene and olivine phenocrysts with clinopyroxene more abundant than olivine.

ANALYTICAL METHODS

For $^{39}\text{Ar}/^{40}\text{Ar}$ dating, three whole rocks were crushed and ground to 80~100 mesh then washed with distilled water in an ultrasonic bath. For each sample, 50~100mg were irradiated and analyzed in the CLAIR Lab at Massachusetts Institute of Technology (MIT) following the

method of (McDougall and Harrison,). Abundances of major elements and V, Cr, Ni, Zn, Ga, Rb, Sr, Y, Zr, Nb and Ba were determined by X-ray fluorescence (XRF) at the University of Massachusetts (U. Mass.) at Amherst following the method of Rhodes (1983). Abundances of trace elements, Sc, Co, Hf, Ta, Th and REE were determined by instrumental neutron activation analysis (INAA) at MIT following the method of Ila and Frey (1984). Precisions for major and trace elements were reported by Frey et al. (1990). All samples were acid leached following the method of Weis and Frey (1991) before being analyzed for Sr, Nd and Pb isotopic compositions and the abundances of U and Pb at the Belgian Centre for Geochronology. The analytical procedures and precisions were described in Weis et al. (1993).

RESULTS

$^{39}\text{Ar}/^{40}\text{Ar}$ dating Fleck et al. (1977) defined a plateau in an age-spectrum diagram as the part of a age vs. released ^{39}Ar diagram that contains contiguous gas fractions with > 50% of total ^{39}Ar released from the sample and no difference in age between any two fractions at the 95% level of confidence. In addition to this definition, increments with errors > 10 Ma are also excluded. Based on these constraints, the plateau ages are 26.7 ± 2.2 Ma for OB93-321, 26.4 ± 2.0 Ma for OB93-324B and 29.1 ± 1.6 Ma for OB93-336 (Fig. 2). These plateau ages agree with the isochron ages determined from $^{36}\text{Ar}/^{40}\text{Ar}$ - $^{39}\text{Ar}/^{40}\text{Ar}$ plots (Fig. 2). As the plateau ages have smaller errors than isochron ages, they are used for discussion. The large uncertainties of the isochron ages and the offset of initial $^{36}\text{Ar}/^{40}\text{Ar}$ ratios from the present day atmospheric ratio result from the large uncertainties in each increment as well as the narrow ranges of $^{36}\text{Ar}/^{40}\text{Ar}$ and $^{39}\text{Ar}/^{40}\text{Ar}$ ratios (Fig. 2). Watkins et al. (1974) reported K-Ar ages of 27.3 ± 0.5 to 26.4 ± 0.5 for three samples from the Mt. Bureau lower subsection. These ages are slightly lower than our data of 29.1 ± 1.6 for this lower subsection. Both data sets show a decrease in age toward the upper section. This result contrasts with K-Ar age inversions previously found in the stratigraphic sections at Anse de Duncan (Ile de l'Quest) and Mt.

Crozier; these inversions were explained by resetting due to intrusion of plutonic rocks (Giret and Lameyre, 1983). Apparently, Mt. Bureau lavas were not affected by this process.

Major elements If FeO is assumed to be 80% of total iron, all samples are hypersthene normative except an ankaramite dike, GM9253, which contains 0.32% normative nepheline. Normative nepheline increases with the increasing proportion of ferrous iron. If ferrous iron is 90% of total iron, one additional sample from the lower subsection, GM9257, become nepheline normative (0.82% normative nepheline) and the normative nepheline in GM9253 increases to 1.16%. Other lavas with MgO > 6% contain normative hypersthene and olivine. In a silica-total alkali diagram, most Mt. Bureau samples plot in the tholeiitic field close to tholeiitic-alkalic boundary for Hawaiian lavas; i.e., they have transitional character. Mt. Bureau lavas overlap with basalts from Loranchet peninsula and central plateau (Fig. 3b). In addition to GM9253, three samples, GM9250, GM9252 and GM9257, from the lower subsection, plot in the alkalic field (Fig. 3a). The effects of alteration on normative composition and the silica-alkali diagram will be discussed later.

Abundances of MgO do not vary systematically with stratigraphic height (Fig. 4). Samples from the upper subsection have MgO ranging from 5.12 to 3.37% while those from the lower subsection span a wider range from 13.35 to 4.47%, with nine of twelve samples varying from 13.35 to 5.69% (Table 2 and Fig. 4).

In MgO variation diagrams, samples with MgO > 6% are more scattered than those with MgO < 6% (Fig. 5a), and they have distinct trace element abundance ratios and Sr, Nd and Pb isotopic ratios. Based on these differences, the lavas are divided into three groups (the detailed geochemical characteristics of these groups will be described later; in terms of major element contents, lavas with < 6% MgO form group A whereas group B and C lavas have > 6% MgO). In contrast to lavas with MgO > 6% (group B and C), lavas with MgO < 6% (group A), including all lavas from the upper subsection, show systematic MgO variation trends except in the MgO-total iron plot. Abundances of CaO and Al₂O₃ are positively correlated with MgO

content while abundances of SiO₂, Na₂O, K₂O and Al₂O₃/CaO are inversely correlated with MgO content (Figs 5a and 5b). In detail, the five most evolved (lowest MgO) samples have Al₂O₃ contents that deviate to higher values from the general trend (Fig. 5a). These lavas also define an inflection at ~4% MgO in the MgO-TiO₂ inverse correlation (Fig. 5a). Abundances of P₂O₅ and MgO are inversely correlated except for the two most evolved samples which are offset to lower P₂O₅ (Fig. 5a).

Trace elements - first series transition metals All samples define positive correlations of Ni and Cr with MgO (Fig. 6). As in MgO-major element plots, lavas with MgO < 6% (group A) define the most coherent MgO-Sc and MgO-V variations. In these lavas, MgO and Sc are positively correlated (Fig. 6). As in the MgO-TiO₂ plot, V and MgO are negatively correlated but the five most evolved lavas define an inflection to lower V contents (Fig. 6).

incompatible elements Abundances of immobile incompatible elements such as Th, high field strength elements (HFSE) and rare earth elements (REE) are highly correlated in all Mt. Bureau lavas (Fig. 7). Ba forms a good correlation with La except for the two samples GM 9255 and GM9251 with the highest MgO contents which are enriched in Ba (Fig. 7). These two samples have abundant zeolite (Table 1). Sr contents in high MgO samples (group B and C) are positively correlated with La, except for the high Sr in GM9257. This sample is relatively altered. Its high Sr content may result from alteration. However, GM9257 also has a slightly high Al₂O₃/CaO ratio (Fig. 5b) relative to other group B and C samples indicating it may contain cumulative plagioclase. For the low MgO samples (group A), Sr contents are nearly constant ranging from 321 to 382 ppm over a two-fold increase in La (Fig. 7). In a spider diagram, group A samples show strong depletions of Sr relative to Ce and Nd (Fig. 8a). Relative to other samples, the alkalic ankaramite dike, GM9253, is enriched in Sr and the highly incompatible elements, Ba and Nb (but not in Th); it is depleted in the less incompatible elements, Zr, Hf, Sm and Yb (Fig. 7). All samples with MgO < 6% (group A) have smooth light rare earth elements (LREE) enriched chondrite-normalized patterns, but samples with MgO

> 6% (group B and C) have positive Eu anomalies (Fig. 8b); the presence of these small but consistent Eu anomalies have been confirmed by duplicate INAA analyses. Sample GM9246 has a crossing REE pattern and sample GM9248 is enriched in Lu relative to Yb (Fig. 8b).

The effects of zeolitilisation on chemical compositions As noted earlier, all Mt. Bureau lavas contain zeolites (Table 1) which formed during hydrothermal alteration (Giret et al., 1992). The effects of zeolitilisation on the compositions of lavas depend on the phases formed and the extent of alteration. Wood et al. (1976) concluded that zeolitilisation in the Icelandic lavas decreased their MgO and SiO₂ contents but had no effects on other major elements such as Ca, Mn, Na, P and Fe. For Kerguelen Archipelago lavas, Giret et al (1992) defined a vertical zoneography in which five zeolite zones were identified based on the P-T stability fields for different zeolites. For example, the uppermost zone contains phillipsite and chabzite which were stable at 40-80 °C while the lowest zone contains laumontite and chlorite which were formed at 170-240 °C. This zoneography is comparable to that of Icelandic basalts (Walker, 1960). The zeolite in group A samples is phillipsite which occurs only at the top of the zoneography (Giret et al., 1992).

Did zeolite formation result in compositional changes of Mt. Bureau lavas? As Mg is not a major constitute in zeolite, zeolitilisation tends to decrease the MgO contents in lavas; for example, zeolitilisation in Icelandic basalts causes decreases in MgO contents (Wood et al., 1976). The well defined MgO-immobile element trends (i.e. MgO-P₂O₅ and MgO-Sc) in group A samples suggest that their MgO contents were not modified by zeolitilisation. Therefore, zeolitilisation apparently did not have significant effects on major elements, except for K₂O. Giret et al. (1992) also concluded that zeolitilisation in Kerguelen Archipelago did not change the Na, Si and Ca contents in the host lavas.

In contrast, abundances of four elements, Rb, K, U and Pb are poorly correlated with La, an immobile element during alteration (Fig. 9). Because it is well established that these four elements are mobile during postmagmatic alteration (Wood et al., 1976; Kennedy et al., 1991;

Roden et al., 1994), deviations from the general trends in figure 9 are interpreted in terms of loss or gain of these elements. Based on the La-Rb plot, eight samples GM9259, GM9258, GM9256, GM9245, GM9243, GM9241, GM9238 and GM9237 have lost Rb (Fig. 9). Relative loss of Rb is not strongly correlated with a deficiency in K₂O. Among these eight samples only GM9243 and GM9241 have distinctly higher K/La ratios. Sample GM9244 is relatively low in K₂O but not in Rb. In the 19 samples analyzed for U and the 20 samples analyzed for Pb, GM9254 and GM9243 have lost U and Pb and GM9255 is enriched in U and Pb relative to La (Fig. 9). Sample GM9255 also has the highest Ba/Nb ratio of ~16. Except for sample GM9255 and GM9251 which have Ba/La higher than the chondritic value, Ba and La are highly correlated in Mt. Bureau lavas. Some zeolites are rich in Ba (Table 4 of Wood et al., 1976) and samples GM9255 and GM9251 contain more abundant zeolite than other samples. Unlike GM9255, sample GM9246 is only enriched in Pb but not in U, Rb and K₂O (Fig. 9). In summary, based on the La-X plots, it is suggested that twelve samples have been significantly modified in abundances of mobile elements. Hereafter, these twelve samples are referred to as altered samples.

Obviously, mobility of K₂O is important in classifying lavas as tholeiitic, alkalic or transitional. The loss of K₂O decreases normative orthoclase and diopside and increases other normative minerals. If K₂O contents are adjusted to a K/La ratio of 395 which is typical of the unaltered lavas, the normative quartz in the most altered sample, GM9243, decreases from 2.24 to 0.05% and normative orthoclase increases from 3.79 to 7.75%. In a silica-alkali diagram, the loss of K₂O moves a sample toward tholeiitic field (Fig. 3a). Using corrected K₂O contents, GM9241, GM9243 and GM9238 plot near the alkalic-tholeiitic boundary (Fig. 3a).

Sr, Nd, and Pb isotopes Mt. Bureau lavas define an inverse ⁸⁷Sr/⁸⁶Sr-¹⁴³Nd/¹⁴⁴Nd correlation with higher ⁸⁷Sr/⁸⁶Sr and lower ¹⁴³Nd/¹⁴⁴Nd than SEIR MORBs (Fig. 10). Apparently, the acid leaching procedures were successful in removing the alteration phases with high ⁸⁷Sr/⁸⁶Sr that are typically present in zeolitized OIB (Wood et al., 1976). ⁸⁷Sr/⁸⁶Sr and

$^{143}\text{Nd}/^{144}\text{Nd}$ ratios in samples from the upper subsection (composed of group A lavas) vary in narrow ranges: from 0.705037 to 0.705288 and from 0.512551 to 0.512631, respectively (Fig. 4). These ranges overlap with those of the lower Miocene lavas from Southeast Province of the Kerguelen Archipelago (Fig. 10) (Weis et al., 1993). Samples from the lower subsection range widely in $^{87}\text{Sr}/^{86}\text{Sr}$ ratio, from 0.703965 to 0.705511, and in $^{143}\text{Nd}/^{144}\text{Nd}$ ratio, from 0.512577 to 0.512887 (Fig. 4). These ranges encompass the entire variation in previously studied Kerguelen Archipelago lavas (Fig. 10b) (Watkins et al., 1974; White and Hofmann, 1982; Storey et al., 1988; Gautier et al., 1990; Weis et al., 1993). Three group A samples from the bottom of the section, GM9259, GM9258 and GM9256, have the highest $^{87}\text{Sr}/^{86}\text{Sr}$ ratios and they overlap with the youngest (upper Miocene) samples from Southeast Province (Fig. 10b) which were suggested to be the representative of the Kerguelen Plume (Weis et al., 1993). There are no systematic variations in $^{87}\text{Sr}/^{86}\text{Sr}$ and $^{143}\text{Nd}/^{144}\text{Nd}$ ratios with stratigraphic height (Fig. 4). Although a MgO- $^{87}\text{Sr}/^{86}\text{Sr}$ correlation is not well defined, samples with > 6% MgO (group B and C) have the lowest $^{87}\text{Sr}/^{86}\text{Sr}$ ratios (Fig. 11). Using a $^{39}\text{Ar}/^{40}\text{Ar}$ age of 29 Ma and the measured Rb/Sr ratios results in minimum age corrections for $^{87}\text{Sr}/^{86}\text{Sr}$ because many samples have lost Rb through alteration (Fig. 9). Age corrections for $^{87}\text{Sr}/^{86}\text{Sr}$ for the highest Rb/Sr sample are about 0.011%, which is smaller than the variation in the upper subsection (0.036%) (Fig. 10b). Age corrections for $^{143}\text{Nd}/^{144}\text{Nd}$ are 0.005~0.006%, also much less than the variation in upper section (0.016%).

In Pb isotope space, all Mt. Bureau samples plot above the Northern Hemisphere Reference Line (NHRL) (Fig. 12); i.e. they have Dupal anomaly characteristics (Dupre and Allegre, 1983; Hart, 1984). The ranges for $^{206}\text{Pb}/^{204}\text{Pb}$, $^{207}\text{Pb}/^{204}\text{Pb}$ and $^{208}\text{Pb}/^{204}\text{Pb}$ ratios are 18.127~18.482, 15.478~15.590 and 38.45~38.98, respectively (Fig. 12). Thirteen of the twenty samples have $^{206}\text{Pb}/^{204}\text{Pb}$ ratios within a narrow range, 18.127~18.297, similar to those of the youngest lavas (6.6~10.2 Ma upper Miocene) from Southeast Province (Fig. 12); thus compared to the 20-22 Ma lower Miocene lavas from the Southeast Province, most of the

26~29 Ma Mt. Bureau lavas have lower $^{206}\text{Pb}/^{204}\text{Pb}$ ratios. Therefore, there is no systematic temporal variation in $^{206}\text{Pb}/^{204}\text{Pb}$ ratio. Unlike $^{87}\text{Sr}/^{86}\text{Sr}$ ratios, the $^{206}\text{Pb}/^{204}\text{Pb}$ ratios of high and low MgO lavas are indistinguishable and there is no correlation between $^{206}\text{Pb}/^{204}\text{Pb}$ and $^{87}\text{Sr}/^{86}\text{Sr}$ (Fig. 13). However, high MgO samples (group B and C) tend to have lower $^{208}\text{Pb}/^{204}\text{Pb}$ and $^{87}\text{Sr}/^{86}\text{Sr}$ ratios (Fig. 11). Although, there is no correlation between $^{206}\text{Pb}/^{204}\text{Pb}$ and $^{207}\text{Pb}/^{204}\text{Pb}$ ratios, there is a positive correlation between $^{206}\text{Pb}/^{204}\text{Pb}$ and $^{208}\text{Pb}/^{204}\text{Pb}$ for samples with MgO < 6% (group A), except for GM9256. Reliable age corrections for Pb isotopes are difficult as both U and Pb in some samples have been modified by alteration (Fig. 9). The $^{238}\text{U}/^{204}\text{Pb}$ ratios range from 10 to 27 in 19 samples and the $^{232}\text{Th}/^{204}\text{Pb}$ ratios vary from 5 to 486 in 20 samples (Table 3). The average $^{238}\text{U}/^{204}\text{Pb}$ and $^{232}\text{Th}/^{204}\text{Pb}$ ratios in samples whose U and Pb have not been affected by alteration are 15.1 ± 1.4 and 89.7 ± 16.0 , respectively. By assuming alteration is a recent event, these ratios were used for age correcting $^{206}\text{Pb}/^{204}\text{Pb}$ and $^{208}\text{Pb}/^{204}\text{Pb}$ ratios in samples whose U and Pb contents have been modified. Age corrections are 0.37% for $^{206}\text{Pb}/^{204}\text{Pb}$ and 0.33% for $^{208}\text{Pb}/^{204}\text{Pb}$, less than the measured variations in $^{206}\text{Pb}/^{204}\text{Pb}$ (1.6%) and $^{208}\text{Pb}/^{204}\text{Pb}$ (1.4%). The age correction for $^{207}\text{Pb}/^{204}\text{Pb}$ ratio is insignificant due to the low abundance of ^{235}U .

Grouping of samples Lavas with MgO greater and less than 6% have distinct $^{87}\text{Sr}/^{86}\text{Sr}$ and $^{143}\text{Nd}/^{144}\text{Nd}$ ratios (Fig. 11). Group A lavas have < 6% MgO and are characterized by high $^{87}\text{Sr}/^{86}\text{Sr}$ and $^{208}\text{Pb}/^{204}\text{Pb}$ and low $^{143}\text{Nd}/^{144}\text{Nd}$ ratios (Fig. 11). They also have distinct La/Nb, Ba/Nb, Th/La, Sr/Nd, and La/Yb ratios (Figs 14a and 14b). Lavas with MgO < 6% are referred as group A samples. Also, their La/Nb, Ba/Nb, Th/La, Nb/Th and Nb/Ta ratios overlap with the chondritic values whereas Hf/Sm and Zr/Hf ratios are higher than chondritic values (Figs. 14a and 14b).

Four samples with MgO ranging from 6.18 to 8.71 %, GM9248, GM9250, GM9252, and GM9257, have similar $^{87}\text{Sr}/^{86}\text{Sr}$ (Fig. 10a), La/Nb and Ba/Nb ratios (Fig. 14a), although

their $^{143}\text{Nd}/^{144}\text{Nd}$ and $^{206}\text{Pb}/^{204}\text{Pb}$ ratios are more variable (Figs. 10a and 12). They plot in or close to the alkalic field in a silica-total alkali diagram (Fig. 3a). These four samples are referred as group B samples. Group B samples have higher La/Nb, Ba/Nb, Sr/Nd, Zr/Hf, and Zr/Nb and lower Th/La and La/Yb ratios than group A samples while their Nb/Ta and Hf/Sm overlap with group A samples (Figs. 14a and 14b). These Kerguelen Archipelago lavas have the lowest $^{87}\text{Sr}/^{86}\text{Sr}$ and highest $^{143}\text{Nd}/^{144}\text{Nd}$ and they are similar to three Mt. Bureau lavas studied by White and Hofmann (1982).

Group C includes three samples, GM9246, GM9251 and GM9255, which have the highest MgO and the lowest abundances of incompatible trace elements, but $^{87}\text{Sr}/^{86}\text{Sr}$ and $^{143}\text{Nd}/^{144}\text{Nd}$ ratios are between those of group A and B samples. Their abundance ratios of incompatible elements are more scattered than group A and B. At a given $^{206}\text{Pb}/^{204}\text{Pb}$, group B and C have lower $^{208}\text{Pb}/^{204}\text{Pb}$ ratios than those of group A samples (Fig. 12). Group B and C samples are from the lower subsection of Mt. Bureau while group A samples appear throughout the section. All Mt. Bureau lavas have Nb/U and Ce/Pb ratios similar to those in ocean island basalts (Hofmann et al., 1986) except the altered samples, GM9257 and the ankaramite dike (Fig. 14b). The ankaramite dike, GM9253, has the highest abundances of highly incompatible elements and highest La/Yb and lowest Zr/Nb ratios (Fig. 14b).

DISCUSSION

General geochemical variations in group A samples

The role of crystal fractionation All group A samples have < 6% MgO, and they are much more evolved than primary magmas derived from peridotite. Thus, it is likely that these lavas were strongly affected by crustal processes. It is evident from their isotopic variability (Fig. 4) that group A samples did not evolve from the same parental magma. Nevertheless, major element versus MgO variation plots and the broad inverse correlations between abundances of immobile incompatible elements and MgO indicate that crystal fractionation was

an important process.

In group A samples, the positive Al_2O_3 -MgO and Sr/Nd-MgO correlations (Figs. 5a and 14a) and the Sr negative anomalies in the spider diagram (Fig. 8a) are consistent with plagioclase fractionation. All group A samples have similar Sr contents but La contents vary from 21 to 40 ppm (Fig. 7) indicating that the partition coefficient of Sr (D_{Sr}) between the fractionation assemblage and residual liquid was about unity. Qualitatively, this requires a major proportion (~40-50%) of plagioclase in the fractionating assemblage. The five most evolved lavas deviate to higher Al_2O_3 from the MgO- Al_2O_3 trend (Fig. 5a) implying that plagioclase was less important in the fractionating assemblage for these samples. However, some of these samples have slightly lower Sr contents than other group A samples (Fig. 7). This can be explained by higher D_{Sr} for the albitic plagioclase at low temperatures (Blundy and Wood, 1991).

The negative MgO- SiO_2 (Fig. 5a) and positive MgO-Ni (Fig. 6) correlations are consistent with segregation of olivine. The inverse correlation of MgO- $\text{Al}_2\text{O}_3/\text{CaO}$ (Fig. 5b) and positive trends of MgO-Ca (Fig. 5a) and MgO-Sc (Fig. 6) require segregation of clinopyroxene. The decrease of Sc with increasing La in group A samples (Fig. 7) indicates that D_{Sc} between fractionating phases and residual liquid was greater than unity. Qualitatively, this result requires that clinopyroxene was also a major (~50%) fractionating component.

As opaque minerals occur in all group A lavas, it is inferred that they also fractionated and controlled abundances of TiO_2 and V in the lavas. Relative to the general negative MgO- TiO_2 and MgO-V correlations, the five most evolved samples have lower TiO_2 and V contents (Figs. 5a and 6) indicating the bulk D_{Ti} and D_{V} were greater than unity during the formation of these five samples. This requires > 7% of ilmenite (~50% of TiO_2), or > 15% of titanomagnetite (~23% of TiO_2 ; Frey et al., 1991). These five samples have more abundant opaque minerals than other samples. In the MgO- P_2O_5 plot, the two most evolved samples, GM9242 and GM9240 which contain most abundant apatite, deviate from the correlation trend

to lower P_2O_5 values (Figs. 5a and 15f). Their offset from the general trend results from fractionation of apatite because D_P between silicate melt and apatite increases as temperature decreases (Watson, 1979). These two samples also have highest Hf/Sm ratios among Mt. Bureau samples (Fig. 14b) reflecting the high D_{Sm} between apatite and melt (Watson and Green, 1981).

The compatibilities of elements during crystal fractionation can be inferred by using element-element plots (Hanson, 1989). In this type of plot, a correlation trend intercepts the axis of the more compatible element. Figures 7 and 16 are some examples of these plots. For example, in La versus Na_2O , Sr and Sc plots, Na_2O increases, Sr remains constant and Sc decreases with the increase of La (Figs. 7 and 16). This gives the compatibility order of $Na < Sr < Sc$. By using this technique, the order of compatibility during evolution of group A samples is suggested as $Th < La < Ce < Nb < Ta \sim Zr < Hf < Nd < Ba < Sm < Ti \sim Eu < Tb < Yb \sim Y < Lu < Na < Sr < Sc$. The mobile elements, K, Rb, U and Pb are not considered as they were affected by alteration. This order of compatibility differs from that for mantle melting in that Ba, and Sr are more compatible than LREE, reflecting the role of plagioclase fractionation. Also, Nb and Ta are more compatible than La as indicated by the negative correlation between MgO and La/Nb (Fig. 14a). Because Nb is less compatible than La in clinopyroxene (Hart and Dunn, 1993; Hauri et al., 1994a), and it is unlikely that Nb would preferentially partition into plagioclase and olivine given the differences in ionic charge and radius between Nb and Ca, Na, Mg and Fe, the most likely phase for controlling the abundance of Nb is an Fe-Ti oxide. An important role for fractionation of Fe-Ti oxide is also evident in the five most evolved lavas which are offset from the general trend to lower TiO_2 and V contents (Fig. 5a and 15c). The compatibility of Ti in the five most evolved samples is between Na and Sr, thereby reflecting the control of Fe-Ti oxide. In summary, the differences between the order of compatibility for mantle melting and that inferred from group A samples show that the compositional variations in group A lavas were controlled by post-melting crystal fractionation.

Since the compositional variations indicate that group A lavas with MgO contents ranging from 4.23 to 5.12 % are saturated with olivine, plagioclase, augite and oxide minerals, it is of interest to evaluate if the models developed from experimental data predict saturation of these phases. The method of Langmuir et al. (1992) predicts that all the group A samples are saturated with plagioclase only, whereas the method presented in chapter one predicts that all group A lavas, except GM9259, are saturated with olivine, plagioclase and augite at 0.001-2 kb. Therefore, the latter method is more consistent with inferences from the compositional trends of group A lavas. Neither approach provides constraints on the saturation of oxide minerals, hence these approaches cannot reliably predict the liquid line of descent (LLD) for group A lavas.

Parental magmas for group A lavas A possible parental magma for group A lavas is the most MgO-rich group A sample, GM9259 (5.69% MgO), which is from the bottom of the Mt. Bureau section. It contains olivine, plagioclase and clinopyroxene phenocrysts. This sample has the lowest total iron and highest CaO contents among all Mt. Bureau lavas; thus it is an end-member composition. Although group A samples form coherent trends in most MgO variation diagrams, there is a compositional gap between GM9259 and the other group A samples (Fig. 5a). Relative to other group A samples, GM9259 has lower total iron, higher CaO, Al₂O₃ contents (Fig. 5a) and a higher Sr/Nd ratio (Fig. 14a). Based on the LLD calculation in chapter 1 and that of Langmuir et al. (1992), plagioclase is the only liquidus phase of GM9259 at pressures ranging from 0.001 to 5 kb. The liquid line of descent (LLD) calculated for this sample cannot explain most of the group A samples in MgO-variation diagrams (Fig. 5a). Consequently, GM9259 is not related to other group A samples by crystal fractionation.

An alternative interpretation is that sample GM9259 represents a mixture of group A melt and crystals. High Al₂O₃, CaO, and Sr/Nd and low total iron are consistent with addition of plagioclase and clinopyroxene. This inference is supported by abundant corroded

plagioclase and clinopyroxene in this sample. If the elements such as LREE and Nb are perfectly incompatible, about 40% crystal addition to GM9258, an aphyric sample overlying GM9259, can explain the abundances of these elements in GM9259. The low $\text{Al}_2\text{O}_3/\text{CaO}$ ratio in GM9259 indicates that cumulate mineral assemblage has $\text{Al}_2\text{O}_3/\text{CaO}$ ratio less than the melt (Fig. 5b). Assuming plagioclase with An_{70} and clinopyroxene with 20% CaO and 3% Al_2O_3 , a plagioclase/clinopyroxene ratio of 3/2 in the cumulate mineral assemblage is required to account for the $\text{Al}_2\text{O}_3/\text{CaO}$ ratio in GM9259. The inferred plagioclase/clinopyroxene ratio is not very sensitive to variations in mineral compositions. This ratio is higher than that estimated from the LLD calculation for other group A samples ($\sim 4/5$). The relatively high abundance of plagioclase explains why plagioclase is the calculated liquidus phase for this composition. Samples GM9259 and GM9258 have similar Sr and Sc contents. If the cumulate crystals are in equilibrium with the aphyric lava, GM9258, the bulk solid/melt partition coefficients are unity for Sr and Sc. If Sr and Sc are perfectly incompatible in clinopyroxene and plagioclase, respectively, this results in a plagioclase/melt partition coefficient of 1.7 for Sr and a clinopyroxene/ melt partition coefficient of 2.5 for Sc. These values are consistent with D_{Sr} and D_{Sc} for these phases (Blundy and Wood, 1991; Gallahan and Nielsen, 1992).

Since GM9259, the most MgO-rich group A sample, is not a suitable parental magma for other group A lavas, I calculated the LLDs for GM9233 and GM9243, which have the highest MgO contents of the group A samples (except for GM9259). They have similar MgO contents but different SiO_2 contents implying that group A lavas were not derived from a common parent. Because a reliable model for predicting fractionation involving Fe-Ti oxide is not yet developed, I use the chapter one method which models fractionation of olivine, plagioclase and augite. Their calculated LLDs provide close fits to the group A lavas that define a negative MgO- TiO_2 trend (Figs. 5a and 15). This result is consistent with the inference from the MgO- TiO_2 trend that significant fractionation of Fe-Ti oxide did not occur until the magmas evolved to < 4% MgO and 3.8% TiO_2 .

The scatter in the general MgO-SiO₂ correlation defined by group A samples:

Evidence for control by partial melting

Although there is a general negative correlation between SiO₂ and MgO (Fig. 5a), in detail there is complexity to this trend. Five group A samples, GM9243, GM9241, GM9238, GM9232 and GM9231 have lower SiO₂ contents relative to samples with similar MgO contents (Fig. 15). Therefore, successful modeling of the MgO-SiO₂ trends of group A lavas requires different parental magmas; GM9243 for the low SiO₂ group and GM9233 for the high SiO₂ group (Fig. 5a). It is known that SiO₂ contents can be modified during zeolitisation (Wood et al., 1976). However, as discussed earlier, the coherent trends in most MgO variation diagrams indicate that the major element trends of Mt. Bureau lavas were not significantly affected by zeolitisation. At low pressures, SiO₂ contents are sensitive to the petrogenetic role of the low SiO₂ phases such as olivine and Fe-Ti oxides. However, the relatively high abundances of incompatible elements such as P₂O₅ and La in low SiO₂ samples (Fig. 15) are inconsistent with addition of Fe-Ti oxides. The general positive MgO-CaO and MgO-Al₂O₃ correlations preclude the interpretation of different extents of olivine fractionation. At a given MgO content, low SiO₂ contents can also result from fractionation at high pressure (Langmuir et al., 1992, Fig. C5). However, at a given MgO content high pressure fractionation will also result in a lower CaO content than low pressure fractionation due to the early segregation of augite. Because there is no difference in CaO contents between the low SiO₂ samples and high SiO₂ samples at a given MgO content (Fig. 5a), it is inferred that low SiO₂ contents are not results of high pressure fractionation.

An alternative hypothesis is that despite their evolved compositions the low SiO₂/MgO ratios in some group A lavas reflect the effects of the melting process. The five low SiO₂ samples also have higher total iron and generally high incompatible element contents than other group A samples with similar MgO contents (sample GM9229 is an exception) (Figs. 15b, f, g, h). Three of these five samples, GM9243, GM9241, and GM9238, plot in the alkalic field of a silica-total alkali diagram, after removing the effects of alteration by adjusting the K₂O contents

to an unaltered K/La ratio of 395 (Fig. 3a). The other two low SiO₂ samples, GM9232 and GM9231, also plot closer to the alkalic-tholeiitic boundary than most of the group A lavas (Fig. 3a). Although the low and high SiO₂ groups overlap in abundances of incompatible elements, the distinction between groups is reinforced by the four samples, GM9258, GM9256, GM9254 and GM9233, with low abundances of incompatible elements (Figs. 15f, g, h) and relatively high SiO₂ contents (Fig. 15a). These samples also have low La/Yb ratios (Fig. 14b). Low SiO₂ contents, high abundances of total iron and incompatible elements are characteristics of melts segregated at high pressures and formed by relatively smaller extents of melting. This interpretation has been applied to explain the compositional variations in MORB and Hawaiian basalts (Langmuir et al., 1992; Yang et al., 1996). If this hypothesis is valid for group A samples, at intermittent levels within the upper subsection, above 300 m, the evolved lavas reflect derivation from primary melts that formed at relatively high pressures and low extents of melting. In contrast, the three group A samples at or near the bottom of the section with relatively high ⁸⁷Sr/⁸⁶Sr ratios (Fig. 4) were derived from primary melts that formed at relatively low pressures and high extents of melting.

Compositional variations with stratigraphic height in the upper subsection All samples from the upper subsection belong to group A (Fig. 4). The lower part of the upper subsection is characterized by the intercalation of lavas with variable MgO contents. The two lowest lavas from 300 to 320 meters containing 4.23% MgO are overlain by the most MgO-rich lava in the upper subsection, GM9243 (5.12% MgO), followed by an apatite saturated lava, GM9242 with low MgO content (3.53%). Above GM9242 is another relatively high MgO lava, GM9241 with 4.99% MgO followed by the most evolved lava in Mt. Bureau section, GM9240 (3.37% MgO). Modeling the compositions of melts saturated with oxide minerals and apatite is difficult because of insufficient experimental data. However, the high abundances of incompatible elements such as P₂O₅ and La in the most evolved lavas (GM9240 and GM9242) can be explained by deriving from primary melts that formed at relatively high pressures with

low extents of melting, for example, from the adjacent flows GM9243 or GM9241 (Figs. 15f and 15h). By assuming that Th, Zr and Hf are perfectly incompatible during fractionation, the highly evolved samples, GM9240 and GM9242, can be related to GM9243 and GM9241 by ~40% crystal segregation. Overlying GM9240 are three lavas with higher MgO contents (4.67-4.85%), then there are three lavas that define a trend of continuously increasing abundances of incompatible elements (i.e., La in Fig. 4) and decreasing MgO and TiO₂ contents. They may represent a time of very low magma supply to a magma reservoir. These highly fractionated lavas are followed by GM9233, with higher MgO content (4.95%). Its low abundances of incompatible elements (Fig. 15f, g, h), low La/Yb (Fig. 14b), and relatively high SiO₂ content (Fig. 15a) are characteristics of lavas from the bottom of the lower subsection, GM9259, GM9258 and GM9256 (Figs 4 and 15). However, GM9233 has lower ⁸⁷Sr/⁸⁶Sr and ²⁰⁸Pb/²⁰⁴Pb ratios than these group A lavas from the lower subsection (Fig. 11). Above GM9233 are two lavas with relatively low SiO₂ and high total iron contents, GM9232 and GM9231. They have compositional characteristics similar to those of some lavas from the bottom of the upper subsection that are inferred to be derived from primary magmas formed at relatively high pressures and low extents of melting. The uppermost lava, GM9229 is characterized by higher abundances of trace elements than lavas with similar MgO contents (Figs. 4 and 15). Among group A lavas, it has a relatively high iron content and the highest TiO₂ and V contents (Figs. 6 and 15); thus it defines the composition whereby further fractionation results in a more important role for Fe-Ti oxide fractionation.

In summary, the diverse compositions result from different extents of crystal fractionation from primary magmas that formed over a range in pressure and by variable extents of melting. A possible scenario is that lavas forming the upper subsection were erupted from distinct isolated magma chambers. The continuous compositional variations in lavas from 400-480 meters (samples GM9237, GM9236, GM9235, and GM9234) indicate that these lavas were derived from a common parent, possibly from a common magma chamber, by increasing

extent of fractionation. Although there are isotopic differences between group A lavas from upper and lower subsections, many lavas from the upper section were derived from parental magmas that formed by relatively lower extents of melting.

The Sr, Nd and Pb isotopic compositions of group A lavas: implications for plume isotopic compositions

The isotopic composition of the Kerguelen Plume has been a issue of debate. Weis et al. (1993) suggested that the upper Miocene lavas from the Southeast Province erupted when the Kerguelen Island was distant from the SEIR; therefore, these lavas were not affected by a MORB component, and they are the best indicator of the Kerguelen Plume composition. Class et al. (1993; 1996) argued that the Sr, Nd and Pb isotopic ratios in lavas forming the Ninetyeast Ridge can be used to define an “evolving plume”. Frey and Weis (1995; 1996) proposed that the Kerguelen Plume is isotopically heterogeneous, but that one plume end-member is defined by the high $^{87}\text{Sr}/^{86}\text{Sr}$ - low $^{143}\text{Nd}/^{144}\text{Nd}$ of the Kerguelen array (Fig. 10). Comparing Mt. Bureau lavas with other Kerguelen Archipelago lavas of different ages may provide insight into the isotopic evolution of the Kerguelen Plume.

Mt. Bureau group A lavas have $^{87}\text{Sr}/^{86}\text{Sr}$ and $^{143}\text{Nd}/^{144}\text{Nd}$ ratios similar to those of the lower Miocene lavas (22Ma) from the Southeast Province except for three samples from the bottom of the section which have lower $^{143}\text{Nd}/^{144}\text{Nd}$ and higher $^{87}\text{Sr}/^{86}\text{Sr}$ which overlap with those of the upper Miocene lavas (9Ma) in the Southeast Province (Fig. 10). This is inconsistent with the temporal variation suggested by Gautier et al. (1990) which requires the highest $^{87}\text{Sr}/^{86}\text{Sr}$ ratios in the youngest lavas. Furthermore, $^{206}\text{Pb}/^{204}\text{Pb}$ and $^{208}\text{Pb}/^{204}\text{Pb}$ in the upper Miocene lavas are lower than those of older lower Miocene lavas (Fig. 12). This is contradictory to an “evolving plume” which requires increases in $^{206}\text{Pb}/^{204}\text{Pb}$ and $^{208}\text{Pb}/^{204}\text{Pb}$ in younger lavas. The absence of systematic temporal variations in Sr and Pb isotopic ratios indicates that the data are not consistent with temporal evolution of a homogeneous plume; they may reflect a heterogeneous plume or mixing of components from different sources. In the following discussions of the petrogenesis of group B and C lavas, group A lavas will be

considered as representative of the Kerguelen Plume component.

The origin of the isotopic diversity of the Mt. Bureau lavas

Kerguelen Plume-SEIR MORB interaction Lavas from group B and C are isotopically distinct from group A and adjacent flows in the lower subsection have significantly different isotopic ratios. What is the cause of this diversity? As the Kerguelen Archipelago evolved from a ridge-centered location at ~40 Ma to its present day intraplate position, the ~29 Ma Mt. Bureau lavas erupted near the Southeast Indian Ridge (SEIR) (Fig. 1c). Therefore, a possible model to explain the isotopic variations is mixing of plume and depleted asthenosphere (Storey et al., 1988; Gautier et al., 1990). Did mixing occur in the source region or after partial melting? These two processes are illustrated in a $(^{143}\text{Nd}/^{144}\text{Nd})_i - (\text{La}/\text{Nd})_n$ plot (Fig. 17). Because partial melting does not change isotopic ratios but changes La/Nd ratio which is not significantly affected by crystal fractionation, melts derived from a source by various extents of melting form a horizontal line in Fig. 17. Mixing between two melts, for example a Mt. Bureau group A sample, GM9254, and a SEIR N-MORB, 6-25, are shown as thin lines. Mixing between two sources and partial melting of a mixed source are depicted as thick lines. Clearly, the $^{143}\text{Nd}/^{144}\text{Nd}$ and La/Nd ratios of group B and C lavas can be explained by mixing of ~40-60% of ~3% melts from MORB source and ~60-40% group A lavas or by variable extents of melting of a mixed source containing ~40-60% plume source and ~60-40% SEIR source.

To determine more precisely the mixing end-members for group B and C samples, I examine Kerguelen Plume-SEIR MORB mixing in a $^{206}\text{Pb}/^{204}\text{Pb} - ^{208}\text{Pb}/^{204}\text{Pb}$ plot (Fig. 18), because mixing between two end-member defines a straight line in a Pb isotope plot and the two end-members can be inferred from the extremes of the linear trend formed by the data set. The $^{206}\text{Pb}/^{204}\text{Pb} - ^{207}\text{Pb}/^{204}\text{Pb}$ plot is not useful because of the large overlap between SEIR MORB and Mt. Bureau samples (Fig. 18). With the inferred end-members, I calculated mixing curves in a $^{87}\text{Sr}/^{86}\text{Sr}$ and $^{143}\text{Nd}/^{144}\text{Nd}$ plot. The final step is to distinguish between melt mixing and source mixing by modeling the abundance ratios of rare earth elements.

Dosso (1988) identified four end-members for SEIR MORB based on studies of dredged samples from the SEIR. They are “normal ridge”, so called N-MORB including two end-members, SEIR1 ($^{143}\text{Nd}/^{144}\text{Nd} = 0.51305$; $^{206}\text{Pb}/^{204}\text{Pb} < 17.4$; $^{208}\text{Pb}/^{204}\text{Pb} < 37.4$) and SEIR2 ($^{143}\text{Nd}/^{144}\text{Nd} = 0.51305$; $^{206}\text{Pb}/^{204}\text{Pb} = 18.1$; $^{208}\text{Pb}/^{204}\text{Pb} = 38.1$), a St. Paul-type ($^{143}\text{Nd}/^{144}\text{Nd} < 0.5128$, $^{87}\text{Sr}/^{86}\text{Sr} > 0.7041$; $^{206}\text{Pb}/^{204}\text{Pb} > 19.0$; $^{208}\text{Pb}/^{204}\text{Pb} > 39.3$) and a Kerguelen related end-member. For the purpose of this discussion, only the first three are considered because the last component is probably derived from the Kerguelen Plume.

Pb isotopes must be interpreted with caution because Pb was a mobile element during zeolitisation (Fig. 9). The two group C samples, GM9255 and GM9246, had gained Pb during alteration. Their Pb isotopic compositions may be modified; therefore, they will not be considered. In the $^{206}\text{Pb}/^{204}\text{Pb}$ - $^{208}\text{Pb}/^{204}\text{Pb}$ plot, two unaltered low $^{87}\text{Sr}/^{86}\text{Sr}$ Mt. Bureau samples, GM9257 and GM9251, are consistent with mixing between group A archipelago samples and the SEIR N-MORB (Fig. 18). They are best explained by mixing a group A sample, GM9254, with the SEIR2 component suggested by Dosso et al. (1988). Sample GM9254 is a suitable group A sample for this model because it is intercalated within group B and C lavas, and it is aphyric. Three other group B samples, GM9252, GM9250 and GM9248, can be explained by mixing between GM9254 and the SEIR samples recovered from dredges 4 and 5 (Dosso et al., 1988) which were interpreted as mixtures of the SEIR2 and St. Paul components (Fig. 18). Therefore, this model provides plausible interpretations for the Pb isotopic ratios of group B and C samples.

Although Sr and Nd isotopes were used to support this model in previous studies (Storey et al., 1988; Gautier et al., 1990), no modeling calculations were made. The curvature of a mixing curve in the $^{87}\text{Sr}/^{86}\text{Sr}$ - $^{143}\text{Nd}/^{144}\text{Nd}$ plot is determined by Sr/Nd ratios in the two mixing end-members. Because the compatibilities of Sr and Nd are similar during melting in garnet and spinel fields, Sr/Nd ratios in melts derived from large extents of melting, such as tholeiitic basalts, do not differ from those in their source. However, Sr/Nd ratios in magmas

decrease when plagioclase fractionation occurs; therefore, a complexity is introduced by plagioclase fractionation and accumulation. Group B and C samples have high Sr/Nd ratios (~20, see Fig. 14) and positive Eu anomalies (Fig. 9) showing that cumulative plagioclase may control their Sr contents (GM9252, GM9250 and GM9246 have ~20% of plagioclase phenocryst). To qualitatively evaluate if the plume-SEIR MORB interaction model can explain the Sr and Nd isotopes, mixing curves are calculated in the $^{87}\text{Sr}/^{86}\text{Sr}$ - $^{143}\text{Nd}/^{144}\text{Nd}$ plot, and the effects of plagioclase addition are considered

Most of the SEIR N-MORB and samples from dredges 4 and 5 have Sr/Nd ratios (~13) slightly less than the chondritic value of 15.8. This is consistent with the depleted characteristics of the MORB source and may also indicate that plagioclase was not an important fractionating phase. Based on the method in chapter one and that of Langmuir et al. (1992), these samples are saturated with only olivine, but they are close to the multiple saturation surface of olivine and plagioclase. The SEIR sample from dredge 10-14 which has high Sr/Nd (26.4) and $\text{Al}_2\text{O}_3/\text{CaO}$ (1.47) reflecting plagioclase accumulation is an exception (Dosso et al., 1988). Therefore, the Sr/Nd ratios in these SEIR samples may be similar to their sources. For the modeling purposes, I used Sr/Nd ratios varying from the observed low values of ~13 to the chondritic ratio of 15.6 for SEIR N-MORB. On the other hand, all Mt. Bureau group A lavas have fractionated plagioclase and their Sr/Nd ratios (~6 to 12) are lower than their sources. Based on a choice of different Sr/Nd ratios, four mixing models between SEIR MORB and a group A sample, GM9254, are indicated in the $^{87}\text{Sr}/^{86}\text{Sr}$ - $^{143}\text{Nd}/^{144}\text{Nd}$ plot (Fig. 19). They use (1) measured Sr/Nd ratios in SEIR MORB and GM9254, (2) measured Sr/Nd ratios in SEIR MORB and the chondritic Sr/Nd ratio for the plume component, (3) the chondritic Sr/Nd ratio for SEIR MORB and the measured Sr/Nd ratio in GM9254, and (4) the chondritic Sr/Nd ratio for SEIR MORB and plume component. The Sr/Nd ratios of the mixing components in these models are listed in Table 4. All four models can be considered as melt mixing and models 2 and 4 are valid for source mixing. Because the measured Sr/Nd ratios in SEIR

MORB are close to the chondritic value, results from model 3 are similar to model 1 and those from model 4 are similar to model 2.

In the $^{87}\text{Sr}/^{86}\text{Sr}$ - $^{143}\text{Nd}/^{144}\text{Nd}$ plot, group B and C samples plot close to the field defined by model 1 (Fig. 19). Addition of plagioclase with high $^{87}\text{Sr}/^{86}\text{Sr}$ ratios, for example, plagioclase in equilibrium with high $^{87}\text{Sr}/^{86}\text{Sr}$ Mt. Bureau lavas could explain the small discrepancies. In model 2, the chondritic Sr/Nd ratio is used for the plume component and this model can explain all group B and C samples in $^{87}\text{Sr}/^{86}\text{Sr}$ - $^{143}\text{Nd}/^{144}\text{Nd}$ space (Fig. 19). Notice that GM9252 and GM9250 plot within plume-SEIR E-MORB mixing region (Fig. 19). This result is required by the Pb isotopic plot (Fig. 18). Although, model 2 provides a satisfactory explanation for the isotopic ratios of group B and C samples, both end-members have Sr/Nd ratios lower than group B and C samples (~19); therefore, the mixtures have Sr/Nd ratios lower than measured ratios in the lavas. Addition of plagioclase can account for this discrepancy, but in this case, the plagioclase must have $^{87}\text{Sr}/^{86}\text{Sr}$ ratios similar to those in the mixtures in order to avoid shifting the positions of these samples in the $^{87}\text{Sr}/^{86}\text{Sr}$ - $^{143}\text{Nd}/^{144}\text{Nd}$ plot. To be consistent with Pb isotope data, GM9248 requires addition of plagioclase with lower $^{87}\text{Sr}/^{86}\text{Sr}$ ratios (Fig. 19).

Source mixing or melt mixing? Although Pb, Sr and Nd isotopes of group B and C samples can be explained by MORB-plume interaction, these parameters are unable to distinguish source mixing from melt mixing. For example, models 2 and model 4 can be applied for melt mixing as well as source mixing, because the Sr/Nd ratios in the melts are assumed to equal those in the source. To resolve this problem, I modeled the abundances of REE for melt mixing and source mixing, then, compared the modeled abundance ratios or the REE chondrite normalized pattern to group B and C samples. The proportions of SEIR MORB and plume components in mixing models were estimated from the $^{87}\text{Sr}/^{86}\text{Sr}$ - $^{143}\text{Nd}/^{144}\text{Nd}$ diagram.

The primary melts for SEIR MORB and Mt. Bureau sample GM9254 were calculated

by incrementally adding 1 wt% of equilibrium crystals to the observed lava compositions. The fractionation sequence was assumed to be olivine followed by olivine and plagioclase. For SEIR N-MORB, sample 6-25 was chosen because its Sr, Nd and Pb isotopic compositions are close to the suggested SEIR 2 component (Dosso et al., 1988). Two primary melts were estimated. The first was calculated by adding only olivine to 6-25 until MgO=20%. This composition is in equilibrium with Fo₉₃ and serves as a primary melt derived from a depleted source with a Sr/Nd ratio of 12.8. The second was calculated by adding olivine and plagioclase to 6-25 to reach the chondritic Sr/Nd ratio then adding olivine until 13% MgO. This composition is in equilibrium with Fo₉₁ and serves as a primary melt derived from a less depleted source. Clinopyroxene is not added, because sample 6-25 was only saturated with olivine and plagioclase based on the method in chapter one. The primary melt for another SEIR sample, 4-43 which contains the St. Paul component, was also calculated, because mixing between this sample and GM9254 can explain the isotopic data of some group B samples. This sample has a Sr/Nd ratio 14.8 close to the chondritic value (15.6). Therefore, only olivine were added until the melt is in equilibrium with Fo₉₁. Two primary melts were calculated for GM 9254. As discussed earlier, GM 9254 is saturated with clinopyroxene, plagioclase and olivine at low pressure. These minerals were added to the composition of GM9254. Due to insufficient constraint on the proportion of Fe-Ti oxide, it was ignored in this calculation. Two primary melts were obtained by adding olivine-plagioclase-clinopyroxene to 6 or 7 % MgO, and then adding olivine and plagioclase to reach the chondritic Sr/Nd ratio, and then adding olivine until the melt is in equilibrium with Fo₉₁. These two primary melts have similar REE abundances. The second was used for the mixing models. The abundances of major elements and La, Nd, Sm, Eu, Tb, Y and Sr of these primary melts are listed in Table 5 along with the mineral proportions.

Four samples, GM9257, GM9251, GM9252 and GM9248, whose mixing end-members can be inferred from their Pb, Sr and Nd isotopes were modeled by mixing between

melts derived from plume and MORB sources. Table 6 lists the mixing end-members for each sample. Model 1 involves mixing of observed lava compositions; that is samples GM9257 and GM9251 were modeled by mixing between the observed plume derived melt, GM9254, and three SEIR N-MORBs, 9-8, 7-2 and 6-25 from Dosso et al. (1988), and samples GM9252 and GM9248 were modeled in a same way but with different N-MORB, samples 5-1, 4-63 and 4-43, which contain the St. Paul component. Model 2 is similar to model 1, except the primary melt estimated from GM9254 was used rather than the observed compositions for plume component. Model 3 assumes mixing between the observed GM9254 composition and the primary melts estimated for SEIR MORB. Two primary melts inferred from a SEIR N-MORB, 6-25, were considered for modeling GM9257 and GM9251. The primary melt estimated from 4-43 was used for modeling samples GM9252 and GM9248. Model 4 calculates mixing between primary melts derived from plume and MORB sources. The calculated La/Nd and Nd/Sm ratios were compared to the measured values. These four models have similar results. Most of the calculated La/Nd and Nd/Sm ratios are 10% lower than the measured values for samples GM9257, GM9252, GM9251 and GM9248 (Fig. 20). Because the offsets (> 10%) are larger than the uncertainties from measurements (~3-4%), it is suggested that group B and C samples are not satisfactorily explained by mixing of group A melts and various SEIR MORB..

Source mixing is more difficult to model because the source compositions are unknown. However, source compositions can be calculated from primary melt compositions with assumptions for melting models, partition coefficients and extents of melting. In this section, the abundances of REE, Y and Sr in two samples, GM9257 and GM9251 were modeled by melting from mixed sources containing SEIR and plume components. First, I calculated the compositions of the sources; then, I compare the melt compositions derived by different extents of melting to the compositions of GM9257 and GM9251. Abundances of La, Nd, Sm, Eu, Tb, Y and Sr in the SEIR N-MORB source were calculated from two primary melts estimated for sample 6-25 by assuming non-modal batch melting and 5%, 10% and 15% of melting (Table

7). The Sm, Eu, Tb and Y contents in the source calculated with $F=20\%$ are higher than those in primitive mantle (Table 7) and inconsistent with the depleted characteristics of MORB. Thus, it is inferred that the maximum extent of melting for SEIR MORB is less than 20%. The primitive mantle source (Sun and McDonough, 1989) was used for the plume to evaluate if the Kerguelen plume contains enriched material.

The sources of samples GM9257 and GM9251 are assumed to be mixtures of MORB and plume sources, the proportions of these two sources were estimated from the mixing curves in a $^{87}\text{Sr}/^{86}\text{Sr}$ - $^{143}\text{Nd}/^{144}\text{Nd}$ plot (Fig. 19). Table 8 lists the possible sources for GM9257 and GM9251 calculated from mixing a plume source (primitive mantle) with six possible SEIR N-MORB sources (Table 7). The least depleted and most depleted sources are used for further non-modal melting calculations in garnet and spinel fields. Comparing the observed lava compositions to compositions derived from melting calculations is improper because postmelting processes such as fractionation and crystal accumulation have modified the primary melt composition. However, these postmelting processes do not significantly change the shape of a chondrite-normalized REE pattern. The REE patterns calculated from melting with residual garnet (Fig. 21a) provide better fits to the observed compositions than those calculated from melting in the spinel stability field (Fig. 21b). The calculations with residual garnet in sources show that abundances of REE in a 3% melt from the least depleted source and a 1% melt from the most depleted source are too high for primary melts of GM9257 which has fractionated to 7.37% MgO (Fig. 21a). The 5% melt from the least depleted source can evolve to GM9257 by ~40% fractionation. However, this 5% melt has lower La/Nd and higher Tb/Y ratios than GM9257 (Fig. 21a). The same result is obtained for modeling GM9251 as melts derived from a mixed source (Fig. 21c). Sample GM9251 has 12.96% MgO, and it may be close to a primary melt composition. The REE abundances in GM9251 are comparable to the 5% melt from the least depleted source and 3% melt from the most depleted source (Fig. 21c). The relatively low Y contents in the modeled melts (Figs 21a, c) are sensitive to the garnet

proportion used for the residue. The relatively low La/Nd ratios in modeled melts implies that these lavas were derived from a source with higher La/Nd ratio. This indicates that the plume source is enriched in LREE relative to primitive source. Finally, it is emphasized that these calculations are illustrative and not unique, but they show that low $^{87}\text{Sr}/^{86}\text{Sr}$ samples can be modeled by partial melting of mixed sources containing different proportions of plume and SEIR MORB sources.

Kerguelen Plume-Kerguelen Plateau interaction An alternative for the low $^{87}\text{Sr}/^{86}\text{Sr}$ group B and C samples is that they result from plume-derived melts contaminated by lithosphere-derived melts (Storey et al., 1988). The Kerguelen Plateau was drilled at the southern end (ODP Leg 119, Site 738) and central portion (ODP Leg 120, Sites 747, 748, 749, and 750; Fig. 1a). In addition, basement samples were obtained by dredging in the central part (Bassias et al., 1987) and the northeast margin of the plateau (Broken Ridge) (Mahoney et al., 1995). Site 738 recovered basaltic basement samples with highest $^{87}\text{Sr}/^{86}\text{Sr}$ and lowest $^{143}\text{Nd}/^{144}\text{Nd}$ ratios (Mahoney et al., 1995). They also have low $^{206}\text{Pb}/^{204}\text{Pb}$ and high $^{208}\text{Pb}/^{204}\text{Pb}$ at a given $^{206}\text{Pb}/^{204}\text{Pb}$, corresponding to high long term integrated ratios of Pb/U and Th/Pb. Their high La/Nb, La/Ta, Th/Nb and Th/Ta ratios reflect depletions of Nb and Ta relative to other incompatible elements (Mahoney et al., 1995). Similar but less extreme geochemical characteristics were found in basaltic basement from the east end of Broken Ridge (Mahoney et al., 1995). These are characteristics of a continental component. The central part of the Kerguelen Plateau is isotopically heterogeneous (Table 9). Samples from Sites 747 and 748 have $^{87}\text{Sr}/^{86}\text{Sr}$ and $^{143}\text{Nd}/^{144}\text{Nd}$ ratios similar to the Mt. Bureau group A lavas while those from site 750 are intermediate between group A and B samples (Fig. 10). Samples from Site 749 are isotopically heterogeneous, lavas with the lowest $^{87}\text{Sr}/^{86}\text{Sr}$ ratios and highest $^{143}\text{Nd}/^{144}\text{Nd}$ ratios overlap with the field for SEIR MORB (Fig. 10). Site 749 samples may represent a lithospheric component for explaining the Sr and Nd isotopic ratios of group B and C samples. Mixing between Mt. Bureau group A samples and site 749 samples is evaluated in

Pb isotope space. In the $^{206}\text{Pb}/^{204}\text{Pb}$ - $^{208}\text{Pb}/^{204}\text{Pb}$ plot, three group B samples with high $^{206}\text{Pb}/^{204}\text{Pb}$ ratios, GM9252, GM9250, and GM9248, lie outside the field defined by mixing between Mt. Bureau group A lavas and samples from sites 749 (Fig. 18). In the same plot, another group B sample, GM9257 and a group C sample, GM9251 overlap with site 749 samples thereby requiring large proportions of a Site 749 component in a mixing model. However, in the $^{207}\text{Pb}/^{204}\text{Pb}$ - $^{208}\text{Pb}/^{204}\text{Pb}$ plot, these two samples plot away from Site 749 samples close to the group A lavas with low $^{207}\text{Pb}/^{204}\text{Pb}$ ratios (Fig. 18). This inconsistency implies that these two samples cannot be explained by mixing between plume and a depleted Kerguelen Plateau component. Consequently, interaction between Kerguelen Plume and Kerguelen Plateau is an unlikely explanation for group B and C samples.

Isotopic variations in the Mt. Bureau section: implications for plume-MORB interaction Two important results from the Mt. Bureau study are: (1) high $^{87}\text{Sr}/^{86}\text{Sr}$ (group A) and low $^{87}\text{Sr}/^{86}\text{Sr}$ (group B and C) lavas are intercalated (Fig. 4), in other words, there are no systematic correlations between stratigraphic height and Sr, Nd and Pb isotopic ratios, and (2) there is an abrupt change from intercalation of group A, B and C lavas to only group A lavas (Fig. 4). The absence of systematic isotopic variation with time is inconsistent with the proposed systematic decrease in the proportion of MORB component in lavas forming the Kerguelen Archipelago as the archipelago evolved from a ridge-center position to an intraplate position (Fig. 1c, Gautier et al., 1990). Systematic variations of isotopic ratios with time require that mixing was vigorous so that homogeneity was attained in a short time interval. However, the isotopic variations in the Mt. Bureau lower subsection indicate that lavas were derived from diverse sources in a short time interval, probably < 1 Ma based on ^{39}Ar - ^{40}Ar dating. Calculations for modeling the REE patterns and La/Nd and Nd/Sm ratios of the low $^{87}\text{Sr}/^{86}\text{Sr}$ Mt. Bureau lavas favor incorporation of MORB source into the plume source regime. Nevertheless, in what tectonic setting did mixing occur? Is the near-ridge setting a requirement for the mixing as suggested by Gautier et al. (1990) or did the Kerguelen Plume entrain MORB

asthenosphere in an intraplate setting? Although entraining asthenosphere material into a plume has been suggested (e.g. Hart et al., 1992; Hauri et al., 1994b), the absence of MORB signatures (i.e. low $^{87}\text{Sr}/^{86}\text{Sr}$) in young Kerguelen lavas (< 22 Ma) which erupted in an intraplate position indicates that this process was not important in controlling the isotopic variations in young Kerguelen archipelago lavas. On the other hand, lavas with MORB signatures erupted when the Kerguelen Archipelago was closer to the ridge implying that the Kerguelen Plume incorporated MORB source, perhaps similar to present Iceland Plume. If the breakup of the northern part of the Kerguelen Plateau and Broken Ridge by spreading of the SEIR occurred at ~35 Ma (Royer and Stanwell, 1989) and the spreading rate was 2.7 cm/yr (half rate) (Cande and Mutter, 1982), at 29 Ma, the Kerguelen Archipelago was ~160 km from the Southeast Indian Ocean Ridge. Whether a separation of 160 km resulted in an overlap between upwelling regimes of the Kerguelen Plume and SEIR source requires estimates of the widths of both upwelling regimes. For the Kerguelen Plume, it is assumed that the plume derived melts ascended almost vertically; therefore, the area of the Kerguelen Archipelago roughly corresponds to the horizontal cross section of the plume. This gives ~50 km for the radius of the Kerguelen Plume (Fig. 22). For SEIR MORB, a passive upwelling model requires that the upwelling rate is of the order of the spreading rate, making the boundary of the melting regime close to 45° (Morgan, 1987). This result suggests that melting regime has a width about twice the depth to the solidus (Fig. 22). I assume that melting started at ~75 km (25 kb) based on the U-Th disequilibrium studies which show evidence of residual garnet (Gill and Condomines, 1992; Rubin and Macdougall, 1992; LaTourrette et al., 1993). Based on these estimates, it is inferred that there was no overlap between the upwelling regime of the Kerguelen Plume and SEIR source when Mt. Bureau lavas erupted (29 Ma), because the distance between the archipelago and SEIR ridge at 29 Ma (160 km) was greater than the sum of the widths of the upwelling regimes of the Kerguelen Plume and SEIR source (125 km). In this case, a plausible explanation for the low $^{87}\text{Sr}/^{86}\text{Sr}$ Mt. Bureau lavas is that the MORB

component was incorporated into the Kerguelen Plume when it was closer to the ridge, i.e. prior to 29 Ma (Fig. 22a). After incorporating the MORB component, the plume was heterogeneous; if mixing was not vigorous, some parts of the plume might not be affected by the MORB source whereas other parts of the plume might contain a large proportion of MORB source. As the ridge moved away from plume, this heterogeneous plume source kept ascending and generated the observed intercalation of high $^{87}\text{Sr}/^{86}\text{Sr}$ and low $^{87}\text{Sr}/^{86}\text{Sr}$ lavas (Fig. 22b). Melts derived from melting of subsequent upwelling plume source did not contain significant amounts of MORB component (Fig. 22c). This interpretation suggests that the lower Mt. Bureau subsection represents the last episode of melting of a mixed source containing plume and MORB source.

Comparisons of $^{87}\text{Sr}/^{86}\text{Sr}$ ratios in volcanic and plutonic rocks: constraints on the time scale of heterogeneity

The inference that a MORB component was incorporated into the Kerguelen Plume when it was in a near ridge setting is supported by the isotopic data of ~6-40 Ma plutonic rocks (Weis and Giret, 1994). The ~40 Ma microgabbro in the Anse du Jardin on the Loranchet Peninsula, one of the oldest rocks in the Kerguelen Archipelago, is the only pluton with initial $^{87}\text{Sr}/^{86}\text{Sr}$ ratios comparable to the low $^{87}\text{Sr}/^{86}\text{Sr}$ Mt. Bureau lavas (Fig. 23). Other ~40 Ma plutons such as the Val Gabbro on the Jeanne Peninsula and the Monts Mamelles on the Courbet Peninsula have initial $^{87}\text{Sr}/^{86}\text{Sr}$ ratios similar to the high initial $^{87}\text{Sr}/^{86}\text{Sr}$ Mt. Bureau lavas (Fig. 23). This implies that the Kerguelen Plume was heterogeneous from ~40 to ~29 Ma. Because none of the 40 Ma plutons have initial $^{87}\text{Sr}/^{86}\text{Sr}$ lower than the 29 Ma Mt. Bureau lavas (Fig. 23), it is inferred that the proportion of the MORB component in the Kerguelen Plume was not related to the distance to the ridge center. The plutons younger than 27 Ma have initial $^{87}\text{Sr}/^{86}\text{Sr}$ ratios similar to Mt. Bureau group A lavas (Fig. 23). This is consistent with the inference that ~29 Ma may represent the last time when a MORB-source component contributed to the volcanism from the Kerguelen Plume. The initial $^{87}\text{Sr}/^{86}\text{Sr}$ ratios of basalts and plutons younger than ~27 Ma range from 0.705 to 0.706 (Fig.

23) indicating that this extent of heterogeneity persisted for ~27 Ma; this may represent the heterogeneity in the "pure" Kerguelen Plume.

CONCLUSIONS

In summary, the 26-29 Ma Mt. Bureau lavas represent a transition when the Kerguelen Plume evolved from a near ridge setting to an intraplate position. Intercalation of lavas with diverse isotopic compositions in the lower subsection is due to source heterogeneity resulting from incorporation of MORB source into the Kerguelen Plume when the Kerguelen Plume was located near the SEIR. Lavas in the lower subsection represent the last time when the MORB source was important. Lavas from the upper subsection have relatively homogeneous isotopic compositions. The slight differences in isotopic compositions between group A lavas from the upper subsection and the bottom of lower subsection may reflect intrinsic heterogeneity of the Kerguelen Plume or the result of homogenizing the Kerguelen Plume source and the incorporated MORB source.

Group A lavas contain large proportions of Kerguelen Plume component. Their chemical compositions were largely controlled by crystal fractionation. The scatter in the major element variation trends are attributed to the diversity of parental magma compositions. As indicated by the SiO₂ and trace element contents and La/Yb ratios, lavas segregated at higher pressures were derived by smaller extents of melting. The REE patterns indicate that group B and C lavas from the lower subsection can be modeled by partial melting of mixed sources containing different proportions of plume and MORB components.

It is inferred that the Kerguelen Plateau lithosphere does not play a significant role in generating group B and C lavas, if this lithosphere beneath the Kerguelen Archipelago has Pb isotopic compositions similar to those drilled from the center and southern parts of the Kerguelen Plateau. However, this inference needs to be confirmed by detailed studies on the lithosphere beneath the Kerguelen Archipelago such as the ongoing studies of lower crust and

upper mantle xenoliths by Hassler and Shimizu (1996) and Mattielli (Mattielli et al., 1996). Such studies will also provide insights into magma-lithosphere interaction that might occur during the ascent of plume generated melts.

REFERENCES

- Bassias Y., Davies H., Leclaire L., and Weis D. (1987) Basaltic basement and sedimentary rocks from the southern sector of the Kerguelen-Heard Plateau: new data and their Meso-Cenozoic paleogeographic and geodynamic implication. *Bull. Mus. Natl. Hist. Nat. C*, 9:, 367-403.
- Blundy J. D. and Wood B. J. (1991) Crystal-chemical control on the partitioning of Sr and Ba between plagioclase feldspar, silicate melts, and hydrothermal solution. *Geochim. Cosmochim. Acta*. 55, 193-209.
- Cande S. C. and Mutter J. C. (1982) A revised identification of the oldest sea-floor spreading anomalies between Australia and Antarctica. *Earth Planet. Sci. Lett.* 58, 151-160.
- Class C., Goldstein S. L., and Galer S. J. G. (1996) Discussion of "Temporal evolution of the Kerguelen plume: geochemical evidence from ~38 to 82 Ma lavas forming the Ninetyeast Ridge" by F.A. Frey and D. Weis. *Contrib. Mineral. Petrol.* in press.
- Class C., Goldstein S. L., Galer S. J. G., and Weis D. (1993) Young formation of a mantle plume source. *Nature* 362, 715-721.
- Dosso L., Bougault H., Beuzart P., Calvez J.-Y., and Joron J.-L. (1988) The geochemical structure of the South-East Indian Ridge. *Earth Planet. Sci. Lett.* 88, 47-59.
- Dosso L., Vidal P., Cantagrel J. M., Lameyre J., Marot A., and Zimine S. (1979) "Kerguelen: continental fragment of oceanic island?": petrology and isotopic geochemistry evidence. *Earth Planet. Sci. Lett.* 43, 46-60.
- Dupre B. and Allegre C. J. (1983) Pb-Sr isotope variation in Indian Ocean basalts and mixing phenomena. *Nature* 303, 143-146.
- Fleck R. J., Sutter J. F., and Elliot D. H. (1977) Interpretation of discordant $^{40}\text{Ar}/^{39}\text{Ar}$ spectra of Mesozoic tholeiites from Antarctica. *Geochim. Cosmochim. Acta*. 41, 15-32.
- Frey F. A., Jones W. B., Davis H., and Weis D. (1991) Geochemical and Petrological Data for Basalts from Sites 756, 757, and 758: Implications for the Origin and Evolution of Ninetyeast Ridge. *Proc. ODP, Sci. Results* 121, 611-659.
- Frey F. A. and Weis D. (1995) Temporal evolution of the Kerguelen plume: geochemical evidence from ~38 to 82 lavas forming the Ninetyeast Ridge. *Contrib. Mineral. Petrol.* 121, 12-28.
- Frey F. A. and Weis D. (1996) Reply to the Class et al. discussion of "Temporal evolution of the Kerguelen plume: geochemical evidence from ~38 to 82 Ma lavas forming the Ninetyeast Ridge" by F.A. Frey and D. Weis. *Contrib. Mineral. Petrol.* in press.
- Frey F. A., Wise W. S., Garcia M. O., West H., Kwon S.-T., and Kennedy A. (1990)

- Evolution of Mauna Kea Volcano, Hawaii: Petrologic and geochemical constraints on postshield volcanism. *J. Geophys. Res.* 95, 1271-1300.
- Gallahan W. E. and Nielsen R. L. (1992) The Partitioning of Sc, Y, and the rare earth elements between high-Ca pyroxene and natural mafic to intermediate lavas at 1 atmosphere. *Geochim. Cosmochim. Acta.* 56, 2387-2404.
- Gautier I., Weis D., Mennessier J.-P., Vidal P., Giret A., and Loubet M. (1990) Petrology and geochemistry of the Kerguelen Archipelago basalts (South Indian Ocean): evolution of mantle sources from ridge to intraplate position. *Earth Planet. Sci. Lett.* 100, 59-76.
- Gill J. and Condomines M. (1992) Short-lived radioactivity and magma genesis. *Science* 257, 1368-1376.
- Giret A. and Lameyre L., (1983) A study of Kerguelen plutonism: Petrology, geochronology and geological implications., Cambridge University Press, Cambridge.
- Giret A., Verdier O., and Nativel P., (1992) The zeolitisation of Kerguelen Islands, Southern Indian Ocean., Terra Scientific Publishing Company, Tokyo.
- Hamelin B., Dupre B., and Allegre C. J. (1986) Pb-Sr-Nd isotopic data of Indian Ocean ridges: new evidence of large-scale mapping of mantle heterogeneities. *Earth Planet. Sci. Lett.* 76, 288-298.
- Hanson G. N., (1989) An approach to trace element modeling using a simple igneous system as an example., Mineralogical Society of America, .
- Hart S. R. (1984) A large-scale isotope anomaly in the Southern Hemisphere mantle. *Nature* 309, 753-757.
- Hart S. R. and Dunn T. (1993) Experimental cpx/melt partitioning of 24 trace elements. *Contrib. Mineral. Petrol.* 113, 1-8.
- Hart S. R., Hauri E. H., Oschmann L. A., and Whitehead J. A. (1992) Mantle plumes and entrainment: The isotopic evidence. *Science* 256, 517-520.
- Hassler D. R. and Shimizu N. (1995) Old peridotite xenoliths from the Kerguelen islands. *EOS (Am. Geophys. Union Trans.)* 76, 693.
- Hassler D. R. and Shimizu N. (1996) The osmium isotopic composition of peridotite xenoliths from the northeastern Kerguelen Islands. *Goldschmister conference abstract* 1, 237.
- Hauri E. H., Wagner T. P., and Grove T. L. (1994a) Experimental and natural partitioning of Th, U, Pb and other trace elements between garnet, clinopyroxene and basaltic melts. *Chem. Geol.* 117, 149-166.
- Hauri E. H., Whitehead J. A., and Hart S. H. (1994b) Fluid dynamic and geochemical aspects of entrainment in mantle plume. *J. Geophys. Res.* 99, 24,275-24,300.

- Hofmann A. W., Feigenson M. D., and Raczek I. (1984) Case studies on the origin of basalts III. Petrogenesis of the Mauna Ulu eruption, Kilauea, 1969-1971. *Contrib. Mineral. Petrol.* 88, 24-35.
- Hofmann A. W., Jochum K. P., Seufert M., and White W. M. (1986) Nb and Pb in oceanic basalts: new constraints on mantle evolution. *Earth Planet. Sci. Lett.* 79, 33-45.
- Ila P. and Frey F. A. (1984) Utilization of neutron activation analysis in the study of geological materials. *Atomkernenerg. Kerntect.* 44, 710-716.
- Kennedy A. K., Kwon S.-T., Frey F. A., and West H. B. (1991) The isotopic composition of postshield lavas from Mauna Kea Volcano, Hawaii. *Earth Planet. Sci. Lett.* 103, 339-353.
- Langmuir C. H., Klein E. M., and Plank T. (1992) Petrological systematic of mid-ocean ridge basalts: Constraints on melt generation beneath ocean ridges. In *Mantle Flow and Melt Generation at Mid-Ocean Ridges*. Geophys. Monogr. Ser., Vol. 71, edited by J. Phipps Morgan, D. K. Blackman, and J. M. Sinton, pp. 183-280, AGU, Washington, D.C.
- LaTourrette T. Z., Kennedy A. K., and Wasserburg G. J. (1993) Thorium-uranium fractionation by garnet: evidence for a deep source and rapid rise of ocean basalts. *Science* 261, 739-742.
- Macdonald G. A. and Katsura T. (1964) Chemical compositions of Hawaiian lavas. *J. Petrol.* 5, 82-133.
- Mahoney J. J., Jones W. B., Frey F. A., Salters V. J., Pyle D. G., and Davies H. L. (1995) Geochemical characteristics of lavas from Broken Ridge, the Naturaliste Plateau and southernmost Kerguelen Plateau: Cretaceous plateau volcanism in the southeast Indian Ocean. *Chem. Geol.* 120, 315-345.
- Mattielli N., Weis D., Gregoire M., Mennessier J. P., Cottin J. Y., and Giret A. (1996) Kerguelen basic and ultrabasic xenoliths: evidence for long-lived Kerguelen hotspot activity. *Lithos*, in press.
- McDougall I. and Harrison T. M., *Geochronology and Thermochronology by the $^{40}\text{Ar}/^{39}\text{Ar}$ Method.*, Oxford, Oxford.
- Michard A., Mintigny R., and Schlich R. (1986) Geochemistry of the mantle beneath the Rodriguez Triple Junction and the South-East Indian Ridge. *Earth Planet. Sci. Lett.* 78, 104-114.
- Morgan P. J. (1987) Melt migration beneath mid-ocean spreading centers. *Geophys. Res. Lett.* 14, 1238-1241.
- Nougier J. and Lameyre J. (1973) Les nordmarkites des îles Kerguelen (T.A.A.F.) dans leur

- cadre structural-problem de leur origin et de celle de certaines roches plutoniques alcalines en domaines oceaniques. *Bull. Soc. Geol. Fr* (7) XV, 306-311.
- Nougier J. and Lemeyre J. (1972) The problem of the origin of the plutonic rocks of the Kerguelen Islands, southern Indian Ocean. *EOS (Am. Geophys. Union Trans.)* 53, 547.
- Nougier J., Pawlowski D., and Cantagrel J. M., (1983) Chrono-spatial evolution of the volcanic activity in southeastern Kerguelen (T.A.A.F.), Cambridge University Press, Cambridge.
- Rhodes J. M. (1983) Homogeneity of lavas flows; chemical data for historic Mauna Loa eruption. *Proceedings of Lunar Planetary Science conference 13 th part 2, Journal of Geophysical Research, supplement* 88, A869-A879.
- Roden M. F., Trull T., Hart S. R., and Frey F. A. (1994) New He, Sr, Nd and Pb isotopic constraints on the constitution of the Hawaiian plume: Results from Koolau Volcano, Oahu, Hawaii. *Geochim. Cosmochim. Acta.* 58, 1431-1440.
- Royer J.-Y. and Stanwell D. T. (1989) Evolution of the Eastern Indian Ocean since the Late Cretaceous: Constraints from geosat altimetry. *J. Geophys. Res.* 90(B10), 13755-13782.
- Rubin K. H. and Macdougall J. D. (1992) Th-Sr isotopic relationships in MORB. *Earth Planet. Sci. Lett.* 114, 149-157.
- Salters V. J., Storey M., Sevigny J. H., and Whitechurch H. (1992) Trace element and isotopic characteristics of Kerguelen-Heard Plateau basalts. *Proc. ODP, Sci. Results* 120, 55-62.
- Storey M., Saunders A. D., Tarney J., Leat P., Thirlwall M. F., Thompson R. N., Menzies M. A., and Marriner G. F. (1988) Geochemical evidence for plume-mantle interactions beneath Kerguelen and Heard Islands, Indian Ocean. *Nature* 336, 371-374.
- Sun S.-S. and McDonough W. F. (1989) Chemical and isotopic systematics of oceanic basalts: Implications for mantle composition and processes. In *Magmatism in the Ocean Basins*. 42, edited by A. D. Saunders and M. J. Norry, pp. 313-345, Geol. Soc. Spec. Pub., London.
- Walker G. P. L. (1960) Zeolite zones and dike distribution in relation to the structure of the basalts of Eastern Iceland. *J. Geol.* 68, 515-528.
- Watkins N. D., Gunn B. M., Nougier J., and Baksi A. K. (1974) Kerguelen: Continental Fragment or Oceanic Island? *Geol. Soc. Am. Bull.* 85, 201-212.
- Watson E. B. (1979) Apatite saturation in basic to intermediate magmas. *Geophys. Res. Lett.*

6(12), 937-940.

- Watson E. B. and Green T. H. (1981) Apatite/liquid partition coefficients for the rare earth elements and strontium. *Earth Planet. Sci. Lett.* 56, 405-421.
- Weis D., Bassias Y., Gautier I., and Mennessier J.-P. (1989) Dupal anomaly in existence 115 Ma ago: Evidence from isotopic study of the Kerguelen Plateau (South Indian Ocean). *Geochim. Cosmochim. Acta.* 53, 2125-2131.
- Weis D. and Frey F. A. (1991) Isotope geochemistry of Ninetyeast Ridge basalts: Sr, Nd, and Pb evidence for the involvement of the Kerguelen hot spot. *Ocean Drill Proc. Sci. Results* 121, 591-610.
- Weis D., Frey F. A., Leyrit H., and Gautier I. (1993) Kerguelen Archipelago revisited: geochemical and isotopic study of the Southeast Province lavas. *Earth Planet. Sci. Lett.* 118, 101-119.
- Weis D. and Giret A. (1994) Kerguelen plutonic complexes: Sr, Nd, Pb isotopic study and inferences about their sources, age, and geodynamic setting. *Mem. Soc. Geol. France* 166, 47-59.
- Weis D., White W. M., Frey F. A., Duncan R. A., Fisk M. R., Dehn J., Ludden J., Saunders A., and Storey M., (1992) The influence of mantle plumes in generation of Indian oceanic crust., AGU, Washington, D.C.
- White W. M. and Hofmann A. W. (1982) Sr and Nd isotope geochemistry of oceanic basalts and mantle evolution. *Nature* 296, 821-825.
- Wood D. A., Gibson I. L., and Thompson R. N. (1976) Elemental mobility during zeolite facies metamorphism of the Tertiary basalts of eastern Iceland. *Contrib. Mineral. Petrol.* 55, 241-254.
- Yang H.-J., Frey F. A., Rhodes J. M., and Garcia M. O. (1996) Evolution of Mauna Kea volcano: Implications from lava compositions recovered in the Hawaii Scientific Drilling Project. *J. Geophys. Res.*, in press.

Table 1. Petrographic description of Mt. Bureau lavas

Samples	Height (m)	Rock Type	General petrographic description
GM9229	620	aphyric basalt	Matrix contains fine-grain plag, cpx, opaques and pocket of zeolite.
GM9230	610	ol-cpx-plag basalt	Plag are euhedral to anhedral, sometimes zoned or broken to pieces. Also form aggregates with cpx phenocryst. Also contain opaques.
GM9231	580	plag basalt	With pocket of zeolite. Plag phenocrysts are euhedral, zoned or aggregate as groups. Matrix contains fine-grain plag, cpx and opaques.
GM9232	530	(ol)-plag basalt	Textures are similar to GM9231.
GM9233	510	(ol)-plag basalt	Textures are similar to GM9231. Plag also form aggregates with cpx and zeolite.
GM9234	480	aphyric basalt	Matrix are plag, cpx, ol, opaques and zeolite. Abundant opaque.
GM9235	460	aphyric basalt	Matrix are plag, cpx, opaques and zeolite. Abundant opaque.
GM9236	460	aphyric basalt	As GM9235.
GM9237	440	aphyric basalt	As GM9235
GM9238	410	ol-plag basalt	Plag are euhedral to subhedral, also form aggregates. Matrix as GM9234.
GM9239	400	ol-cpx-plag basalt	Microphenocrysts are plag, cpx and ol. Matrix as GM9234.
GM9240	360	aphyric basalt	Rare plag phenocrysts or fragments. Abundant opaque and apatite. Matrix as GM9235
GM9241	350	ol-cpx-plag basalt	Phenocrysts are ol, plag, and pseudomorphose zeolite.
GM9242	340	aphyric basalt	As GM9240
GM9243	330	ol-cpx-plag basalt	As GM9241
GM9244	320	cpx-plag basalt	Plag and cpx phenocrysts are subhedral. Matrix as GM9235.
GM9245	300	cpx-plag basalt	As GM9244
GM9246	280	plag-ol-cpx basalt	Phenocrysts are aggregates of cpx and plag lath. Ol phenocrysts are fresh with iddingsite on edge. Secondary minerals include zeolite and chlorite.
GM9248	250	pl-cpx-ol basalt	Textures are similar to GM9246.
GM9250	180	cpx-ol-plag basalt	Plag phenocrysts are subhedral and form aggregates. Ol phenocrysts are fresh with iddingsite on edge. Corroded cpx phenocrysts associate with plag. Matrix as GM9234.
GM9251	150	plag-cpx-ol basalt	Some plag phenocrysts are altered. Abundant zeolite. Ol as GM9250.
GM9252	145	ol-plag basalt	Plag phenocrysts are corroded and form aggregates. Ol as GM9250. Chlorite in matrix.
GM9253	130	ankaramite dike	Cpx > Ol. Matrix are plag, cpx and opaques. Secondary minerals are zeolite and calcite.
GM9254	130	aphyric basalt	Matrix as GM9235.
GM9255	130	pl-cpx-ol basalt	as GM9251. Secondary minerals are zeolite and chlorite.
GM9256	80	subaphyric basalt	Rare phenocryst of corroded plag. Matrix as GM9235.
GM9257	75	ol-cpx basalt	abundant cpx and ol phenocrysts. Also contain zeolite.
GM9258	60	aphyric basalt	Rare plag phenocrysts. Matrix as GM9235.
GM9259	40	ol-plag basalt	Abundant plag and cpx phenocrysts are subhedral and zoned. Matrix as GM9235. Secondary minerals are zeolite and calcite.

Table 1 Abundances of major and trace elements and Sr, Nd and Pb isotopic ratios

	GM 9255	GM 9251	GM 9246	GM 9253	GM 9248	GM 9257	GM 9250
height (m)	130	150	280	130	250	75	180
group	C	C	C	dike	B	B	B
SiO ₂	45.92	46.40	46.36	44.72	47.09	46.21	47.97
TiO ₂	1.55	1.60	1.87	3.40	1.44	2.45	2.38
Al ₂ O ₃	13.89	13.84	14.91	13.73	16.49	16.35	15.81
Fe ₂ O ₃	12.58	12.62	14.17	13.55	11.98	13.62	13.21
MnO	0.18	0.18	0.21	0.19	0.18	0.19	0.20
MgO	13.35	12.96	10.18	9.32	8.71	7.37	6.48
CaO	9.57	9.59	9.43	10.94	10.73	9.67	9.81
Na ₂ O	1.91	2.10	2.24	1.65	2.50	2.99	3.07
K ₂ O	0.54	0.54	0.17	1.85	0.43	0.69	0.64
P ₂ O ₅	0.18	0.19	0.14	0.60	0.20	0.37	0.28
Total	99.66	100.00	99.66	99.94	99.74	99.89	99.84
Rb	11.4	10.5	1.4	35.2	5.8	17.3	10.5
Sr	274	271	226	557	252	518	375
Ba	158	141	53	683	98	160	156
Sc	26.5	26.1±0.3	29.3±0.1	27.9	29.5±0.1	25.1	29.5
V	165	176	211	250	174	199	278
Cr	693	655±11	290±3	217	271±1	80	92
Co	66.6	64.0±0.3	61.0±1.1	52.6	51.4±0.3	52.2	45.9
Ni	380	376	241	120	170	86	80
Zn	86	97	103	118	75	87	92
Ga	16.0	17.2	18.5	20.3	17.0	18.0	21.4
Y	16.1	16.8	21.5	23.1	20.7	26.8	27.4
Zr	94	107	93	230	117	196	184
Nb	9.3	10.3	7.9	49.9	8.3	13.4	13.7
Hf	2.23	2.32±0.01	2.22±0.01	5.07	2.52±0.08	4.12	3.98
Ta	0.66	0.58±0.07	0.42±0.05	2.86	0.57±0.06	0.81	0.74
Th	0.57	0.89±0.09	0.19±0.13	4.0	0.65±0.23	0.87	1.21
U	0.45	0.17	0.03	0.31	0.08	0.15	0.26
Pb	1.90	0.4	3.8	0.95	0.27	0.84	1.02
La	9.2	9.49±0.16	5.85±0.02	37.4	8.80±0.07	15.1	15.2
Ce	20.8	20.8±1.7	14.8±1.9	70.9	21.2±1.1	35.9	33.1
Nd	12.5	13.5±0.64	10.8±0.01	33.1	12.9±0.92	21.4	19.7
Sm	3.08	3.22±0.16	3.19±0.25	7.65	3.33±0.14	5.34	4.97
Eu	1.13	1.21±0.05	1.26±0.04	2.4	1.24±0.02	1.96	1.78
Tb	0.51	0.58±0.03	0.68±0.01	0.84	0.63±0.01	0.87	0.75
Yb	1.33	1.43±0.01	1.92±0.01	1.94	1.88±0.16	2.38	2.28
Lu	0.20	0.22±0.01	0.32±0.01	0.24	0.31±0.02	0.33	0.33
⁸⁷ Sr/ ⁸⁶ Sr	0.704394	0.704411	0.704587	0.704840	0.703965	0.704017	0.704070
¹⁴³ Nd/ ¹⁴⁴ Nd	0.512801	0.512770	0.512775	0.512659	0.512879	0.512887	0.512809
²⁰⁶ Pb/ ²⁰⁴ Pb	18.270	18.229	18.257	18.397	18.419	18.222	18.467
²⁰⁷ Pb/ ²⁰⁴ Pb	15.536	15.478	15.491	15.590	15.500	15.509	15.539
²⁰⁸ Pb/ ²⁰⁴ Pb	38.68	38.52	38.49	38.93	38.55	38.45	38.78

Table 1 Continued

	GM 9252	GM 9259	GM 9243	GM 9241	GM 9233	GM 9254	GM 9238
height (m)	145	40	330	350	510	130	410
group	B	A	A	A	A	A	A
SiO ₂	48.08	49.97	49.10	50.05	51.05	51.31	49.93
TiO ₂	2.38	2.31	3.49	3.37	3.44	3.17	3.66
Al ₂ O ₃	15.76	15.46	14.28	13.70	13.53	13.53	13.63
Fe ₂ O ₃	13.30	11.71	14.10	14.04	13.84	13.99	14.53
MnO	0.21	0.16	0.19	0.20	0.17	0.20	0.19
MgO	6.18	5.69	5.12	4.99	4.95	4.88	4.85
CaO	9.87	11.48	9.91	9.48	8.74	8.46	8.75
Na ₂ O	3.11	2.47	2.72	2.88	2.64	2.96	2.97
K ₂ O	0.66	0.55	0.63	0.77	1.11	1.05	1.02
P ₂ O ₅	0.29	0.26	0.44	0.43	0.39	0.38	0.44
Total	99.82	100.07	99.99	99.91	99.84	99.93	99.98
Rb	11.2	3.8	6.4	15.2	19.7	16.7	12.3
Sr	374	339	382	372	351	331	347
Ba	161	164	246	257	222	230	280
Sc	29.4±0.1	27.8±0.1	28.8	28.2	30.5	28.6±0.07	27.8
V	272	226	296	283	285	299	287
Cr	90±1	155±1	81	82	56	21±1	48
Co	46.5±0.1	40.7±0.3	42.2	42.5	43.3	40.3±0.3	43.0
Ni	74	82	55	66	55	37	37
Zn	97	107	136	133	131	136	125
Ga	21.8	20.7	22.9	24.2	23.3	22.6	23.6
Y	27.7	23.0	33.0	32.6	28.8	31.6	33.5
Zr	184	156	263	257	242	241	264
Nb	13.5	16.6	31.6	30.5	23.5	24.1	30.7
Hf	4.10±0.02	3.62±0.04	6.32	5.98	5.78	5.57±0.08	6.25
Ta	0.88±0.02	0.92±0.01	1.76	1.81	1.54	1.45±0.02	1.87
Th	1.39±0.19	1.70±0.04	3.28	2.91	1.99	2.63±0.15	3.29
U	0.34	0.12	0.14		0.36	0.13	
Pb	1.13	0.70	0.87		1.80	0.37	
La	15.7±0.3	15.1±0.2	27.6	28.1	21.0	22.9±0.2	28.1
Ce	37.1±1.6	35.0±1.9	64.5	64.0	53.3	51.6±1.0	66.8
Nd	23.0±1.6	20.1±1.1	36.1	36.5	32.1	31.3±3.8	36.3
Sm	5.30±0.12	5.03±0.07	7.86	7.61	7.01	7.17±0.13	7.67
Eu	1.86±0.03	1.73±0.05	2.53	2.49	2.39	2.38±0.03	2.60
Tb	0.94±0.06	0.81±0.04	1.21	1.19	1.03	1.14±0.04	1.21
Yb	2.42±0.07	1.76±0.08	2.68	2.55	2.27	2.62±0.01	2.63
Lu	0.36±0.01	0.26±0.01	0.39	0.36	0.32	0.39±0.01	0.38
⁸⁷ Sr/ ⁸⁶ Sr	0.704095	0.705511	0.705037		0.705191	0.705282	
¹⁴³ Nd/ ¹⁴⁴ Nd	0.512787	0.512577	0.512596		0.512631	0.512598	
²⁰⁶ Pb/ ²⁰⁴ Pb	18.482	18.226	18.353		18.131	18.372	
²⁰⁷ Pb/ ²⁰⁴ Pb	15.556	15.536	15.542		15.510	15.541	
²⁰⁸ Pb/ ²⁰⁴ Pb	38.83	38.94	38.95		38.66	38.98	

Table 1 Continued

	GM 9230	GM 9237	GM 9239	GM 9232	GM 9256	GM 9258	GM 9229
height (m)	610	440	400	530	80	60	620
group	A	A	A	A	A	A	A
SiO ₂	50.92	50.59	50.91	50.07	51.41	51.08	51.18
TiO ₂	3.31	3.63	3.61	3.67	3.20	3.29	3.91
Al ₂ O ₃	13.46	13.31	13.39	13.00	13.18	13.26	12.87
Fe ₂ O ₃	13.60	14.56	14.13	15.25	14.51	15.08	14.40
MnO	0.21	0.22	0.19	0.20	0.24	0.20	0.19
MgO	4.84	4.70	4.67	4.64	4.64	4.47	4.43
CaO	9.24	8.44	8.63	8.26	8.30	8.29	8.12
Na ₂ O	2.74	2.96	2.90	2.92	2.97	2.94	2.77
K ₂ O	1.07	1.06	1.23	1.23	0.83	0.88	1.45
P ₂ O ₅	0.40	0.46	0.44	0.49	0.39	0.39	0.53
Total	99.78	99.93	100.10	99.71	99.66	99.87	99.84
Rb	23.5	15.8	25.6	25.5	8.0	8.0	28.9
Sr	373	355	335	333	343	339	345
Ba	279	285	274	267	255	251	315
Sc	28.1	27.2±0.2	27.1±0.4	27.7±0.3	27.3±0.2	28.1	28.0
V	293	299	281	311	277	284	322
Cr	36	30±1	48±1	33±1	11±1	14	68
Co	43.3	39.2±0.1	41.3±0.6	42.7±0.3	44.5±0.1	42.4	36.8
Ni	47	38	34	36	28	40	52
Zn	124		122	147	132	136	141
Ga	23.2	24.3	24.0	23.3	24.0	24.3	25.1
Y	33.0	34.8	34.3	37.0	33.0	34.4	37.8
Zr	257	277	259	284	235	240	317
Nb	25.5	30.3	29.9	30.9	25.6	25.1	32.3
Hf	6.05	6.20±0.11	6.17±0.15	6.64±0.12	5.56±0.07	5.82	7.30
Ta	1.45	1.82±0.08	1.77±0.02	1.83±0.03	1.57±0.06	1.55	1.93
Th	2.67	3.26±0.08	3.50±0.25	3.09±0.02	3.12±0.01	2.94	3.10
U					0.41	0.37	0.61
Pb	2.2				1.75	1.60	2.60
La	26.2	28.7±0.1	27.8±0.4	28.0±1.1	24.6±0.6	25.9	31.3
Ce	62.0	65.8±1.6	64.3±0.1	69.2±0.5	57.6±1.1	58.6	76.4
Nd	36.0	37.9±3.8	34.0±3.0	38.5±3.1	32.9±3.4	35.4	43.3
Sm	7.89	8.24±0.11	7.60±0.21	8.51±0.01	7.16±0.28	7.65	8.92
Eu	2.43	2.66±0.036	2.54±0.03	2.75±0.03	2.43±0.01	2.59	2.83
Tb	1.25	1.29±0.04	1.14±0.03	1.22±0.08	1.11±0.03	1.22	1.34
Yb	2.69	2.89±0.07	2.85±0.23	2.88±0.03	2.63±0.31	2.92	2.96
Lu	0.39	0.43±0.01	0.39±0.01	0.43±0.01	0.39±0.01	0.40	0.41
⁸⁷ Sr/ ⁸⁶ Sr	0.705288				0.705416	0.705446	0.705276
¹⁴³ Nd/ ¹⁴⁴ Nd	0.512577				0.512539	0.512593	0.512618
²⁰⁶ Pb/ ²⁰⁴ Pb	18.127				18.338	18.283	18.129
²⁰⁷ Pb/ ²⁰⁴ Pb	15.521				15.546	15.536	15.537
²⁰⁸ Pb/ ²⁰⁴ Pb	38.77				38.49	38.97	38.80

Table 1 Continued

	GM 9231	GM 9244	GM 9245	GM 9236	GM 9235	GM 9234	GM 9242
height (m)	580	320	300	460	460	480	340
group	A	A	A	A	A	A	A
SiO ₂	50.22	51.58	51.12	51.66	51.67	51.95	53.12
TiO ₂	3.62	3.81	3.78	3.50	3.52	3.34	3.24
Al ₂ O ₃	13.15	13.59	12.89	13.09	13.17	13.01	13.33
Fe ₂ O ₃	15.09	13.31	14.54	14.36	14.36	14.58	13.82
MnO	0.22	0.19	0.22	0.22	0.21	0.22	0.21
MgO	4.40	4.27	4.26	4.08	3.96	3.65	3.53
CaO	8.47	8.51	8.09	7.47	7.41	7.57	6.82
Na ₂ O	2.89	3.10	2.93	3.14	3.09	3.15	3.20
K ₂ O	1.25	1.04	1.32	1.48	1.51	1.40	1.85
P ₂ O ₅	0.49	0.53	0.53	0.69	0.69	0.72	0.60
Total	99.78	99.92	99.67	99.68	99.59	99.58	99.70
Rb	27.8	27.1	22.8	25.7	36.8	36.2	46.0
Sr	340	371	360	347	347	335	321
Ba	269	301	305	310	303	325	361
Sc	27.9	26.3	26.6	25.8	26.0	25.1	24.0
V	304	296	320	257	255	214	244
Cr	41	73	42	10	10	5	2
Co	44.4	35.3	38.3	35.4	34.7	34.4	46.7
Ni	38	56	44	33	26	22	26
Zn	148	131	144	148	147	154	153
Ga	22.4	24.6	24.0	22.9	24.2	25.7	24.6
Y	37.9	38.2	39.2	40.9	39.5	45.1	41.8
Zr	284	320	330	312	313	353	461
Nb	31.2	34.0	34.4	34.1	34.9	37.5	39.8
Hf	6.61	7.40	7.52	7.22	7.13	8.05	10.1
Ta	1.83	2.16	1.95	2.01	2.12	2.19	2.29
Th	2.7	3.45	3.29	3.99	4.13	4.39	5.60
U	0.55		0.56			0.83	
Pb	2.30		2.40			3.10	
La	28.6	32.4	33.2	34.1	33.5	37.8	40.4
Ce	65.7	75.2	78.5	83.3	79.5	87.2	96.6
Nd	36.7	40.1	40.0	43.7	44.8	47.5	49.3
Sm	8.72	9.78	8.99	9.77	9.78	10.70	10.6
Eu	2.73	2.90	2.94	3.15	3.10	3.23	3.24
Tb	1.29	1.46	1.50	1.25	1.44	1.59	1.61
Yb	3.09	3.22	3.19	3.14	3.20	3.80	3.39
Lu	0.42	0.46	0.47	0.42	0.45	0.53	0.48
⁸⁷ Sr/ ⁸⁶ Sr	0.705167		0.705203			0.705114	
¹⁴³ Nd/ ¹⁴⁴ Nd	0.512627		0.512619			0.512603	
²⁰⁶ Pb/ ²⁰⁴ Pb	18.248		18.205			18.279	
²⁰⁷ Pb/ ²⁰⁴ Pb	15.512		15.527			15.513	
²⁰⁸ Pb/ ²⁰⁴ Pb	38.79		38.81			38.83	

Table 1 continued

	GM 9240
height (m)	360
group	A
SiO ₂	52.46
TiO ₂	3.37
Al ₂ O ₃	13.14
Fe ₂ O ₃	14.49
MnO	0.24
MgO	3.37
CaO	7.13
Na ₂ O	3.13
K ₂ O	1.79
P ₂ O ₅	0.57
Total	99.70
Rb	49.2
Sr	322
Ba	342
Sc	24.8
V	263
Cr	6
Co	34.9
Ni	33
Zn	159
Ga	25.4
Y	44.0
Zr	413
Nb	38.5
Hf	9.39
Ta	2.01
Th	4.80
U	0.91
Pb	2.60
La	38.2
Ce	90.7
Nd	46.2
Sm	10.1
Eu	3.18
Tb	1.50
Yb	3.56
Lu	0.51
⁸⁷ Sr/ ⁸⁶ Sr	0.705227
¹⁴³ Nd/ ¹⁴⁴ Nd	0.512613
²⁰⁶ Pb/ ²⁰⁴ Pb	18.297
²⁰⁷ Pb/ ²⁰⁴ Pb	15.510
²⁰⁸ Pb/ ²⁰⁴ Pb	38.86

Table 3 Age corrections for Pb isotopes

sample	U (ppm)	Pb (ppm)	Th (ppm)	$(^{206}\text{Pb}/^{204}\text{Pb})_m$	$(^{208}\text{Pb}/^{204}\text{Pb})_m$	$(^{238}\text{U}/^{204}\text{Pb})_m$	$(^{238}\text{U}/^{204}\text{Pb})_{ac}$	$(^{232}\text{Th}/^{204}\text{Pb})_m$	$(^{232}\text{Th}/^{204}\text{Pb})_{ac}$	$(^{206}\text{Pb}/^{204}\text{Pb})_i$	$(^{208}\text{Pb}/^{204}\text{Pb})_i$
GM9259	0.12	0.70	1.73	18.226	38.94	10.9	10.9	163	163	18.177	38.81
GM9258	0.37	1.60	2.94	18.283	38.97	14.7	14.8	121	121	18.217	38.80
GM9257	0.15	0.84	0.87	18.222	38.45	11.3	11.3	68	68	18.171	38.35
GM9256	0.41	1.75	3.12	18.338	38.49	14.9	14.9	117	117	18.271	38.32
GM9255	0.45	1.90	0.57	18.270	38.68	15.0	15.0	20	90	18.202	38.55
GM9254	0.13	0.37	2.73	18.372	38.98	22.4	15.1	487	90	18.304	38.85
GM9253	0.31	0.95	4.00	18.397	38.93	20.8	15.1	278	90	18.329	38.80
GM9252	0.34	1.13	1.25	18.482	38.83	19.2	19.2	73	73	18.395	38.73
GM9251	0.17	0.40	0.82	18.229	38.52	26.9	15.1	134	90	18.161	38.39
266 GM9250	0.26	1.02	1.21	18.467	38.78	16.3	16.3	78	78	18.394	38.67
GM9248	0.08	0.27	0.48	18.419	38.55	18.8	18.8	117	117	18.334	38.38
GM9246	0.03	3.80	0.28	18.257	38.49	0.5	15.1	5	90	18.189	38.36
GM9245	0.56	2.40	3.29	18.205	38.81	14.8	14.8	90	90	18.138	38.68
GM9243	0.14	0.87	3.28	18.353	38.95	10.3	15.1	249	90	18.285	38.82
GM9240	0.91	2.60	4.80	18.297	38.86	22.3	15.1	121	90	18.229	38.73
GM9234	0.83	3.10	4.39	18.279	38.83	17.0	17.0	93	93	18.202	38.70
GM9233	0.36	1.80	1.99	18.131	38.66	12.7	12.7	72	72	18.074	38.56
GM9231	0.55	2.30	3.02	18.248	38.79	15.2	15.2	86	86	18.181	38.67
GM9230		2.20	2.67	18.127	38.77		15.1	80	80	18.059	38.66
GM9229	0.61	2.60	3.10	18.129	38.80	14.9	14.9	78	78	18.062	38.69

Subscript m indicates measured values. Subscript ac indicates ratios for age corrections. Subscript i indicate ratios age corrected to 29Ma.

Table 4 Sr/Nd ratios of mixing components for group B and C samples

	SEIR component	Plume component
Model 1	observed Sr/Nd	observed Sr/Nd
Model 2	observed Sr/Nd	chondritic Sr/Nd
Model 3	chondritic Sr/Nd	observed Sr/Nd
Model 4	chondritic Sr/Nd	chondritic Sr/Nd

Table 5 The compositions of primary melts calculated from SEIR samples, 6-25 and 4-43 (Dosso et al.,1988), and Mt. Bureau sample GM9254.

	SiO ₂	TiO ₂	Al ₂ O ₃	Fe ₂ O ₃	FeO	MnO	MgO	CaO	Na ₂ O	K ₂ O	P ₂ O ₅
sample 6-25	50.38	1.45	14.98	1.59	8.15	0.18	7.99	11.86	2.53	0.15	0.12
primary melt I	47.67	1.03	10.68	1.14	8.51	0.11	19.95	8.45	1.80	0.11	0.08
primary melt II	48.87	1.07	14.82	1.18	7.65	0.13	12.90	10.54	2.21	0.11	0.09
sample 4-43	50.61	1.08	15.83	1.45	7.41	0.17	8.72	12.31	2.12	0.19	0.11
primary melt	48.61	0.85	12.67	1.46	7.68	0.13	16.97	9.80	1.68	0.15	0.09
sample GM9254	51.31	3.17	13.63	2.10	10.70	0.20	4.88	8.46	2.96	1.05	0.38
primary melt I	48.44	1.69	12.10	1.47	9.26	0.10	16.12	7.86	2.04	0.54	0.20
primary melt II	48.98	1.70	12.06	1.39	8.75	0.10	15.18	8.95	2.00	0.52	0.19

	La	Sr	Nd	Sm	Eu	Tb	Y	Sr/Nd
sample 6-25	3.3	115	8.99	3.09	1.20	0.76	33.6	12.8
primary melt I	2.4	82	6.39	2.20	0.85	0.54	23.9	12.8
primary melt II	2.5	105	6.75	2.31	0.90	0.57	24.9	15.6
sample 4-43	4.4	114	7.70	2.48	0.93	0.57	26.3	14.8
primary melt	3.5	91	6.11	1.97	0.74	0.45	20.9	14.8
sample GM9254	22.9	331	31.30	7.17	2.38	1.14	31.6	10.6
primary melt I	12.7	271	17.22	3.99	1.33	0.64	17.6	15.7
primary melt II	12.3	265	16.90	3.98	1.34	0.65	17.7	15.7
D for plag/melt	0.19	1.5	0.11	0.08	0.07	0.047	0.017	

Ferrous iron equals 85% of total iron. Primary melts are calculated by incrementally adding 1 wt% of equilibrium crystals as described in text. Olivine compositions are calculated with Fe-Mg exchange coefficient of 0.3. Plagioclase compositions are calculated from the model of Grove et al., (1992). Augite compositions are calculated from the equations in chapter one. The olivine:plagioclase proportion is 3:7. The olivine:plagioclase:augite proportion is 8:42:50. The plagioclase/melt partition coefficients at 1200 C are from Drake and Weill (1975). Augite/melt partition coefficients are from Hofmann (1984). Trace element are assumed to be perfectly incompatible in olivine.

Table 6 End-member for group B and C samples in melt mixing models

		target	end-member	
			SEIR component	Plume component
Model 1	GM 9257		observed 9-8	observed GM9254
			observed 7-2	observed GM9254
			observed 6-25	observed GM9254
	GM 9251		observed 9-8	observed GM9254
			observed 7-2	observed GM9254
			observed 6-25	observed GM9254
	GM 9252		observed 5-1	observed GM9254
			observed 4-63	observed GM9254
			observed 4-43	observed GM9254
	GM 9248		observed 5-1	observed GM9254
			observed 4-63	observed GM9254
			observed 4-43	observed GM9254
Model 2	GM 9257		observed 9-8	primary melt of GM9254
			observed 7-2	primary melt of GM9254
			observed 6-25	primary melt of GM9254
	GM 9251		observed 9-8	primary melt of GM9254
			observed 7-2	primary melt of GM9254
			observed 6-25	primary melt of GM9254
	GM 9252		observed 5-1	primary melt of GM9254
			observed 4-63	primary melt of GM9254
			observed 4-43	primary melt of GM9254
	GM 9248		observed 5-1	primary melt of GM9254
			observed 4-63	primary melt of GM9254
			observed 4-43	primary melt of GM9254
Model 3	GM 9257		primary melt I of 6-25	observed GM9254
			primary melt II of 6-25	observed GM9254
	GM 9251		primary melt I of 6-25	observed GM9254
			primary melt II of 6-25	observed GM9254
	GM 9252		primary melt of 4-43	observed GM9254
	GM 9248		primary melt of 4-43	observed GM9254
Model 4	GM 9257		primary melt I of 6-25	primary melt of GM9254
			primary melt II of 6-25	primary melt of GM9254
	GM 9251		primary melt I of 6-25	primary melt of GM9254
			primary melt II of 6-25	primary melt of GM9254
	GM 9252		primary melt of 4-43	primary melt of GM9254
	GM 9248		primary melt of 4-43	primary melt of GM9254

Table 7a Source compositions calculated from primary melt I of 6-25 (Table 5) using non-modal batch melting

	La	Sr	Nd	Sm	Eu	Tb	Y	Sr/Nd
primary melt I	2.35	82.0	6.39	2.2	0.85	0.54	23.9	12.8
source (5% melting)	0.123	4.6	0.376	0.143	0.058	0.039	1.85	12.1
source (10% melting)	0.238	8.4	0.667	0.235	0.092	0.060	2.80	12.6
source (15% melting)	0.352	12.3	0.960	0.331	0.128	0.082	3.69	12.8
source (20% melting)	0.469	16.4	1.280	0.441	0.171	0.109	4.85	12.8
primitive mantle	0.687	21.1	1.354	0.444	0.168	0.108	4.55	15.6

The ol:opx:cpx:sp proportion in the source is 60:25:5:10. The ol:opx:cpx:sp proportion entering melt is 1:1:4:4. Partition coefficients are from Hofmann (1984). Composition of primitive mantle are from Sun and McDonough (1989).

Table 7b Source compositions calculated from primary melt II of 6-25 (Table 5) using non-modal batch melting

	La	Sr	Nd	Sm	Eu	Tb	Y	Sr/Nd
primary melt II	2.51	105	6.75	2.31	0.9	0.57	24.9	15.6
source (5% melting)	0.137	6.5	0.468	0.195	0.082	0.057	2.48	13.8
source (10% melting)	0.260	11.5	0.776	0.292	0.118	0.079	3.47	14.8
source (15% melting)	0.383	16.5	1.083	0.389	0.154	0.101	4.46	15.2
source (20% melting)	0.506	21.4	1.391	0.485	0.190	0.123	5.45	15.4
primitive mantle	0.687	21.1	1.354	0.444	0.168	0.108	4.55	15.6

The ol:opx:cpx:sp proportion in the source is 6:2:1:1. Other parameters are the same as Table 6a.

Table 8a Compositions of possible mixed sources for GM9257

depleted source (DS)	% of DS	La	Sr	Nd	Sm	Eu	Tb	Y
primary melt II (5% melting)	90	0.247	9.4	0.645	0.245	0.099	0.067	2.89
primary melt II (10% melting)	80	0.388	14.4	0.949	0.338	0.133	0.088	3.79
primary melt II (15% melting)	70	0.505	18.3	1.191	0.411	0.160	0.104	4.50
primary melt I (5% melting)	95	0.208	7.0	0.523	0.188	0.075	0.050	2.26
primary melt I (10% melting)	85	0.350	11.6	0.839	0.287	0.111	0.072	3.23
primary melt I (15% melting)	75	0.469	15.3	1.098	0.370	0.142	0.091	3.99

Table 8b Compositions of possible sources for GM9251

depleted source (DS)	% of DS	La	Sr	Nd	Sm	Eu	Tb	Y
primary melt II (5% melting)	75	0.330	11.6	0.780	0.282	0.112	0.074	3.20
primary melt II (10% melting)	60	0.473	16.3	1.065	0.368	0.143	0.094	4.01
primary melt II (15% melting)	55	0.550	19.0	1.232	0.419	0.162	0.105	4.51
primary melt I (5% melting)	80	0.292	9.5	0.669	0.233	0.091	0.060	2.66
primary melt I (10% melting)	60	0.418	13.5	0.942	0.319	0.122	0.079	3.50
primary melt I (15% melting)	50	0.520	16.7	1.157	0.387	0.148	0.095	4.12

Depleted source (DS) is the source calculated from primary melt I and II of 6-25 (Table 6). Primitive mantle composition is used for plume source. The proportions of depleted and plume sources in GM9257 and GM9251 are derived from $^{87}\text{Sr}/^{86}\text{Sr}$ - $^{143}\text{Nd}/^{144}\text{Nd}$ mixing curves. Only the most and least depleted sources used for melting calculation.

Table 9 Sr, Nd, and Pb isotopic ratios from Leg 120

Hole	Core, section	Interval (cm)	$^{87}\text{Sr}/^{86}\text{Sr}$	$^{143}\text{Nd}/^{144}\text{Nd}$	$^{206}\text{Pb}/^{204}\text{Pb}$	$^{207}\text{Pb}/^{204}\text{Pb}$	$^{208}\text{Pb}/^{204}\text{Pb}$
747C	12R-2	122-124	0.705660	0.512445	17.417	15.463	37.937
747C	12R-4	30-36	0.705438	0.512470	17.381	15.428	37.804
747C	12R-4	45-46	0.705508	0.512435	17.466	15.461	37.977
747C	16R-2	81-84	0.705866	0.512410	17.608	15.508	38.072
747C	16R-2	85-87	0.705895	0.512452	18.275	15.643	38.459
748C	76R-7	65-67	0.705162		18.284	15.621	38.421
748C	76R-6	106-110	0.705157	0.512491	18.305	15.613	38.495
749C	12R-4	144-148	0.704268	0.512751	17.980	15.587	38.204
749C	15R-2	35-37	0.704237	0.512763	18.200	15.625	38.435
749C	15R-5	127-130	0.704306	0.512764	17.978	15.587	38.213
749C	16R-7	107-109	0.703506	0.512914	18.031	15.579	38.222
749C	16R-7	75-77	0.703531	0.512898	18.065	15.574	38.028
750B	15R-5	126-130	0.704972		17.617	15.472	37.909
750B	16R-3	134-136	0.705012	0.512902	18.112	15.585	38.405
750B	16R-6	58-63	0.705130	0.512917			
750B	17R-3	26-30	0.705300	0.512808	17.565	15.510	38.071

Nd data are normalized to BCR-1=0.51262. Pb data are normalized to NBS981.

FIGURE CAPTIONS

- Fig. 1 a) Map of the Indian Ocean. The numbers on the Kerguelen Plateau, Ninetyeast Ridge, Broken Ridge and Naturaliste Plateau indicate the drill and dredge sites.
b) Map of Kerguelen Archipelago.
c) An evolution model for the Kerguelen Archipelago (Gautier et al., 1990). Tholeiitic lavas erupted at ~45 Ma when the spreading of the Southeast Indian Ridge (SEIR) separated the Kerguelen Plateau and Broken Ridge at ~40 Ma. Lavas with transitional characteristics erupted at ~29-26 Ma when the Kerguelen Archipelago was near the SEIR. Alkalic lavas erupted when the archipelago evolved to an intraplate setting.
d) Mt. Bureau stratigraphic section. Black regions indicate lava flows sampled in 1992 and 1993. Arrows indicate samples studied by Watkins et al. (1974). Their stratigraphic positions are inferred from figure 7 of Watkins et al (1974). Also indicated are three samples from 1993 collection used for $^{39}\text{Ar}/^{40}\text{Ar}$ dating.
- Fig. 2 Plateau and isochron ages of three Mt. Bureau samples from 1993 collection. Both ages are calculated with the program in MIT CLAIR Lab.
- Fig. 3 a) SiO_2 vs. $\text{Na}_2\text{O}+\text{K}_2\text{O}$. All in wt%. Ferrous iron equals 0.85% of total iron. The tholeiitic-alkalic dividing line is from Macdonald and Katsura (1964). Solid lines connect data for altered samples and adjusted compositions whose K_2O contents are corrected so that K/La ratio=395. The adjusted compositions are normalized to original total.
b) Comparison of Mt. Bureau lavas with other Kerguelen Archipelago lavas in SiO_2 - $\text{Na}_2\text{O}+\text{K}_2\text{O}$ space. Data sources are Weis et al. (1993), Gautier et al., (1990) and Storey et al., (1988).
- Fig. 4 MgO, La, $^{87}\text{Sr}/^{86}\text{Sr}$ and $^{206}\text{Pb}/^{204}\text{Pb}$ variations with stratigraphic height.
- Fig. 5 a) MgO vs. major elements (all in wt%). The thin line in each panel is the liquid line

of descent calculated from GM9259 with the method in chapter one. The thick lines in each panel are the liquid line of descent calculated from sample GM9243 and GM9233. See text for grouping samples.

b) MgO vs. Al₂O₃/CaO

Fig. 6 MgO (%) vs. Sc, V, Ni and Cr (ppm)

Fig. 7 La vs. Ba, Th, Nb, Zr, Sm, Yb, Sr and Sc.

Fig. 8 a) Incompatible element abundances of representative group A, B and C samples normalized to primary mantle estimates (Sun and McDonough, 1989).

b) Chondrite normalized REE patterns of Mt. Bureau lavas. Chondritic values are from Sun and McDonough (1989). In the upper panel the stippled area indicated group A includes all group A samples except for GM9259; only some representative group A samples are shown. In the lower panel, all group B and C samples are plotted.

Fig. 9 La vs. the mobile elements, K₂O, Rb, U and Pb. All in ppm, except for K₂O which is in wt%. Altered samples are labeled. In La-K₂O panel, the solid line indicates K/La=395.

Fig. 10 a) ⁸⁷Sr/⁸⁶Sr-¹⁴³Nd/¹⁴⁴Nd of Mt. Bureau samples.

b) Initial ⁸⁷Sr/⁸⁶Sr-¹⁴³Nd/¹⁴⁴Nd. Mt. Bureau data are corrected to 29Ma. Upper and lower Miocene lavas are from Weis et al., (1993) and corrected to 9 and 22 Ma, respectively. Kerguelen Plateau data are from Salters et al., (1992) and corrected to 110Ma. Also shown are fields of measured values of lavas from site 749 and those corrected to 29Ma. SEIR field is defined by data from Dosso et al., (1988), Michard et al., (1986) and Hamelin et al., (1986)

Fig. 11 MgO (%) vs. ⁸⁷Sr/⁸⁶Sr, ¹⁴³Nd/¹⁴⁴Nd, ²⁰⁶Pb/²⁰⁴Pb and ²⁰⁸Pb/²⁰⁴Pb ratios.

Fig. 12 ²⁰⁶Pb/²⁰⁴Pb vs. ²⁰⁷Pb/²⁰⁴Pb and ²⁰⁸Pb/²⁰⁴Pb for Mt. Bureau samples. Data for

the upper and lower Miocene lavas are from Weis et al., (1993). NHRL is the north hemisphere reference line defined by Hart (1984). A solid line connects measured and age corrected data for a representative sample.

- Fig. 13 $^{87}\text{Sr}/^{86}\text{Sr}$ vs. $^{206}\text{Pb}/^{204}\text{Pb}$. Data sources are the same as Fig. 12. The mixing curve is defined by site 738 and dredges 4 and 5 on SEIR (Dosso et al., 1988)
- Fig. 14 a) MgO (%) vs. La/Nb, Ba/Nb, Nb/Th, Nb/Ta, Th/La and Sr/Nd. Arrows indicate chondritic values.
b) MgO vs. Nb/U, Ce/Pb, Zr/Hf, Hf/Sm, La/Yb and Zr/Nb. The bracket in MgO vs. Nb/U and Ce/Pb plots indicate typical ratios for the ocean island basalts (Hofmann et al., 1986)
- Fig. 15 MgO variation diagrams for Mt. Bureau group A lavas. In panels b, c, g and h, sample GM9259 is out of scale. The solid circles are samples with relatively low SiO₂ contents.
- Fig. 16 Element vs. element plots for evaluating the relative compatibility of elements. The correlation trends intercept the more compatible elements. In each panel, R is a correlation coefficient. In Zr-Ta panel, the most evolved two samples are not included for the regression, because their Ta contents were affected by apatite fractionation. A least square regression was not carried out for the La-Na₂O plot. However, there is a general increase of Na₂O with the increase of La.
- Fig. 17 Source mixing and melt mixing in a $(^{143}\text{Nd}/^{144}\text{Nd})_i$ vs. $(\text{La}/\text{Nd})_n$ (normalized to the primitive mantle value of Sun and McDonough (1989)) plot. The La and Nd contents in the Kerguelen Plume source is assumed to be of primitive mantle. The $(^{143}\text{Nd}/^{144}\text{Nd})_i$ ratio of Mt. Bureau group A sample, GM9254, is used for the Kerguelen Plume. The source of SEIR MORB was calculated from dredged sample 6-25 (Dosso et al., 1988) assuming 15% of non-modal melting. The horizontal lines indicate the paths of non-modal partial melting. The thin lines between two

horizontal lines indicate mixing between two melts and the thick line connecting two sources indicates source mixing.

Fig. 18 Initial $^{206}\text{Pb}/^{204}\text{Pb}$ vs. initial $^{207}\text{Pb}/^{204}\text{Pb}$ and $^{208}\text{Pb}/^{204}\text{Pb}$ ratios. Data sources for the SEIR and Kerguelen Plateau are the same as in Fig. 10. Data for dredged Plateau samples are from Weis et al., (1989). Data for Kerguelen Plateau Site 738 and Broken Ridge dredge 8 are from Mahoney et al., (1995). The Kerguelen Plateau data are not age corrected because there are no measurements of Pb and U concentrations. The SEIR1, SEIR2, and St. Paul components are from Dosso et al. (1988)

Fig. 19 The $^{87}\text{Sr}/^{86}\text{Sr}$ vs. $^{143}\text{Nd}/^{144}\text{Nd}$ plot for SEIR MORB and the Kerguelen Plume mixing. Data source for SEIR MORB are the same as Fig. 10. A Mt. Bureau group A sample, GM9254, is used for the Kerguelen Plume component. See text for different models.

Fig. 20 The La/Nd and Nd/Sm ratios calculated from mixing melts derived from plume and MORB sources. The vertical axis indicates the relative difference between the calculated values and measured values. The dash lines separate results for each sample. The mixing end-members for each mixing calculation are listed in Table 6 in an order corresponding to the order of left to right in each panel.

Fig. 21 a) Comparison between REE patterns of GM9257 and those calculated from non-modal melting with residual garnet in the source. See text for the derivation of source and melt compositions. Upper and lower panels use the inferred least and most depleted sources, respectively. In each model the source is a mixture of plume and MORB sources. The mineral proportions in plume source is ol:opx:cpx:sp:gt = 50:20:15:9:6 and that in MORB source is 60:20:10:6:4. The relative proportions of these two sources in the mixed source are determined from a $^{87}\text{Sr}/^{86}\text{Sr}$ - $^{143}\text{Nd}/^{144}\text{Nd}$ plot. The mineral proportion in the source for each

model is indicated in each panel. The mineral proportion entering the melt is ol:opx:cpx:sp:gt = 1:1:3:2:3. The partition coefficients are from Hofmann et al. (1984).

- b) Comparison between REE patterns calculated from non-modal melting in spinel stability field and that of GM9257. The source for each model is a mixture of plume and MORB sources. The mineral proportion in the plume source is ol:opx:cpx:sp = 50:20:15:15 and that in the MORB source is 6:2:1:1. The mineral proportion in the source is indicated in each panel. The mineral proportion entering the melt is ol:opx:cpx:sp = 1:1:4:4. Other parameters are the same as a).
- c) Comparison between REE patterns of GM9251 and those calculated from non-modal melting with residual garnet in the source. Parameters are the same as those in a), except for the source composition and mineral proportion. The differences result from the different proportions of plume and MORB sources in the mixed source.

Fig. 22 The relationship between the upwelling regimes of MORB source and the Kerguelen Plume as the Kerguelen Archipelago evolved from a near ridge setting to an intraplate setting. See text for the method of estimating widths of the upwelling regimes of MORB source and Kerguelen Plume. a) From 35 to 29 Ma. The field with dark dots indicates the MORB source that was incorporated into the plume when there was an overlap area between the upwelling regimes of MORB source and the Kerguelen Plume. Also shown are the flow lines of the SEIR MORB and Kerguelen Plume source. b) At ~29 Ma, there was no overlap between the upwelling regimes of MORB source and the Kerguelen Plume. The MORB source (field with dark dots) that was incorporated when the SEIR ridge was closer to the Kerguelen Plume kept ascending and generated the observed Mt. Bureau lavas with low $^{87}\text{Sr}/^{86}\text{Sr}$ ratios. c) The MORB source in the Kerguelen Plume was "used up".

No lavas with $^{87}\text{Sr}/^{86}\text{Sr}$ ratios erupted after 29 Ma.

Fig. 23 Age vs. initial $^{87}\text{Sr}/^{86}\text{Sr}$ ratio for plutonic and volcanic rocks from the Kerguelen Archipelago. The data for plutonic rocks are from Weis et al. (1994). The upper and lower Miocene data are from Weis et al. (1993). The Mt. Ross data are the unpublished data of Weis.

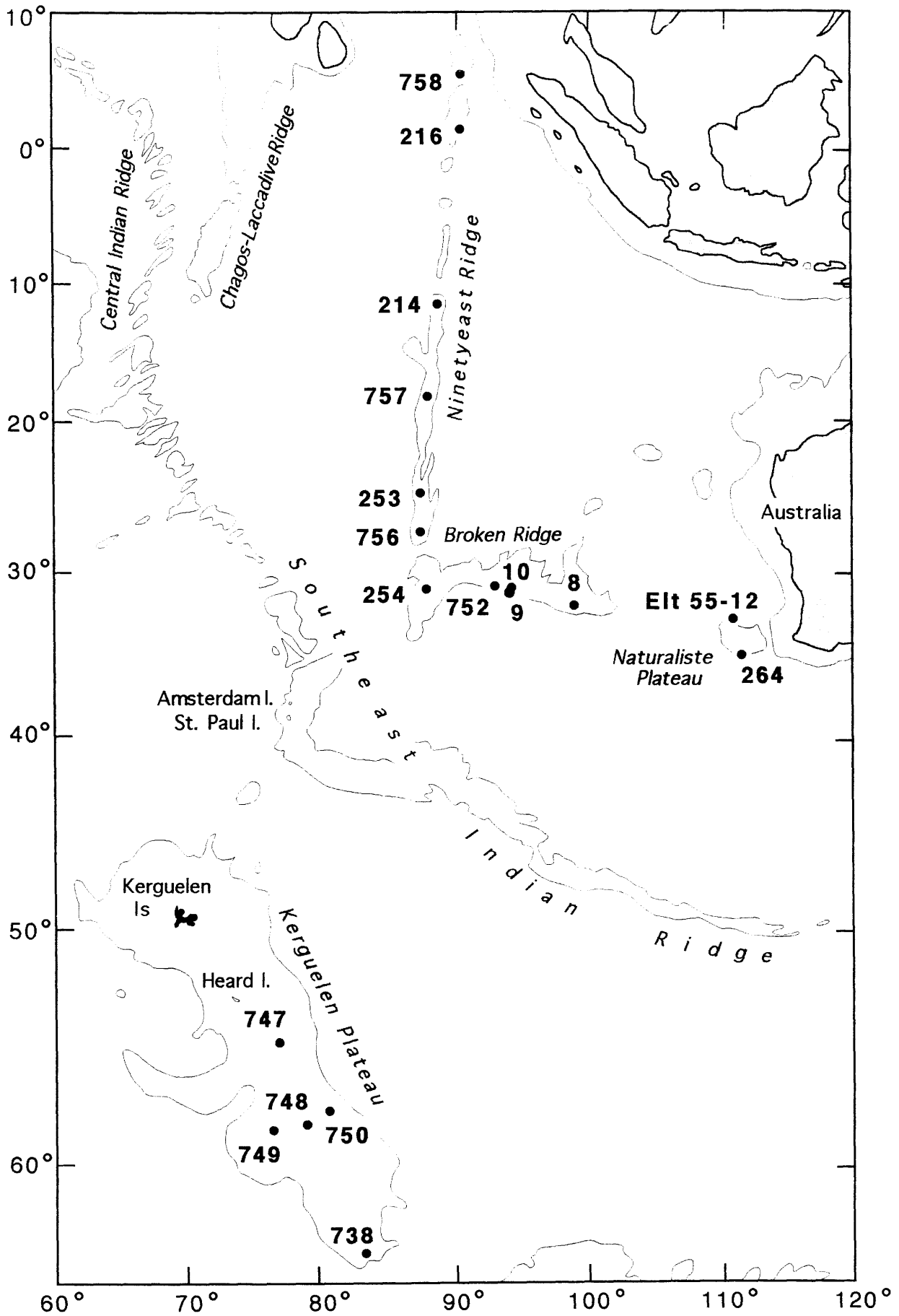


Fig. 1a

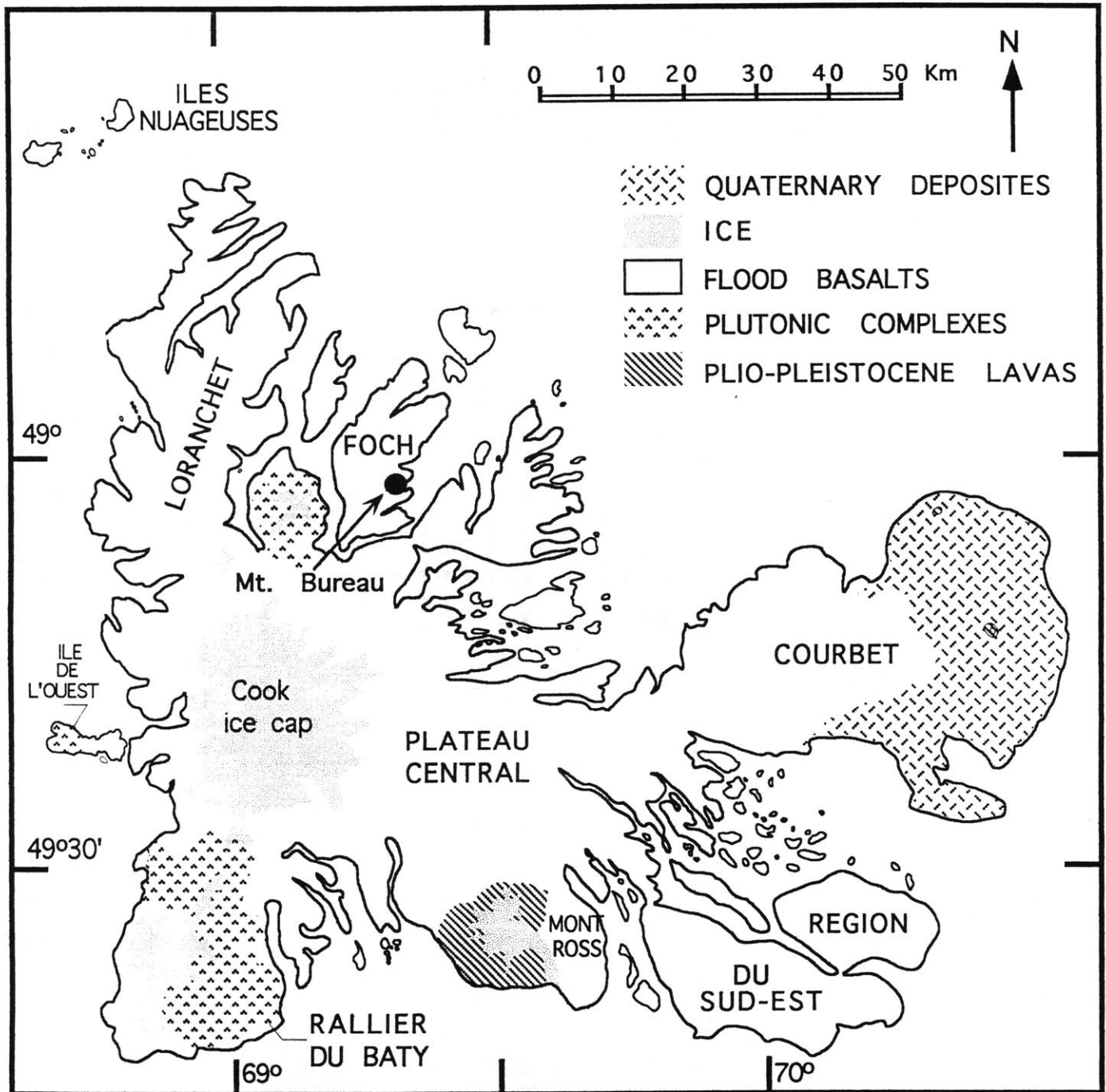
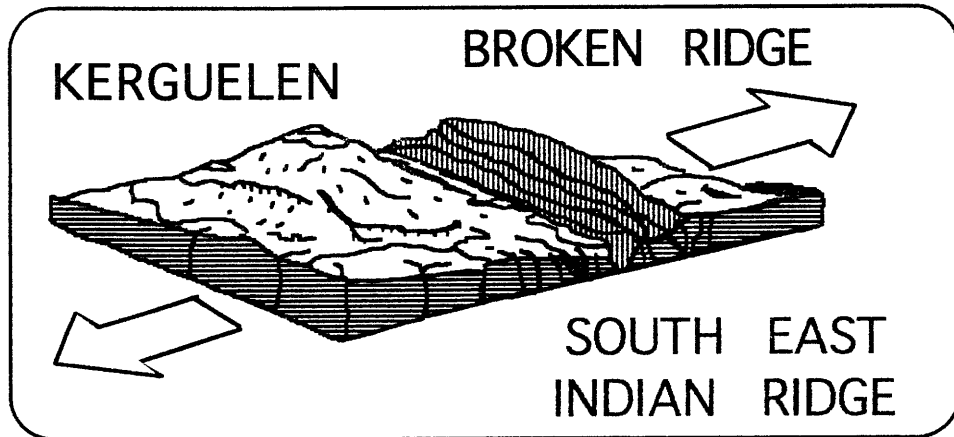


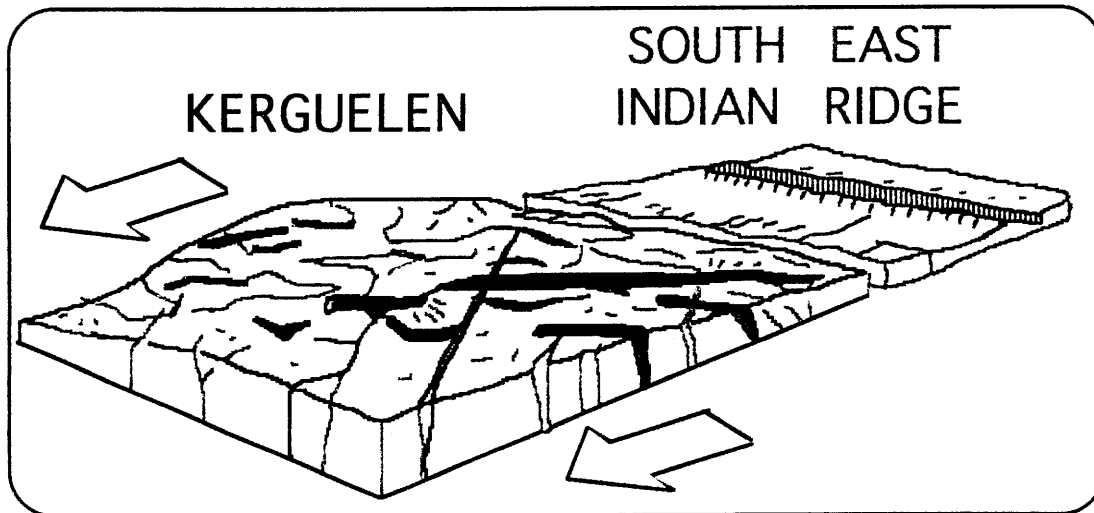
Fig. 1b

THE FORMATION AND THE EVOLUTION OF THE KERGUELEN ISLANDS



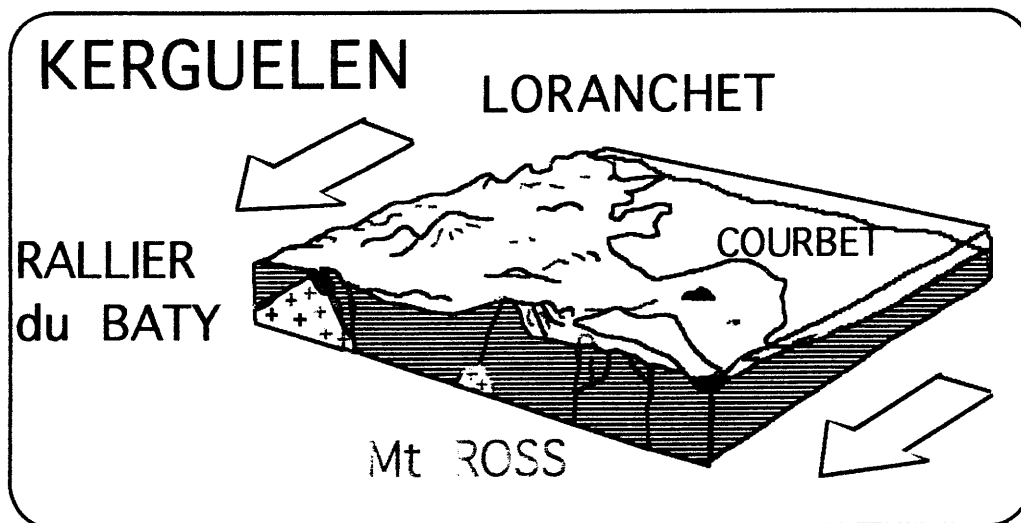
45 Ma

THOLEIITIC
STAGE



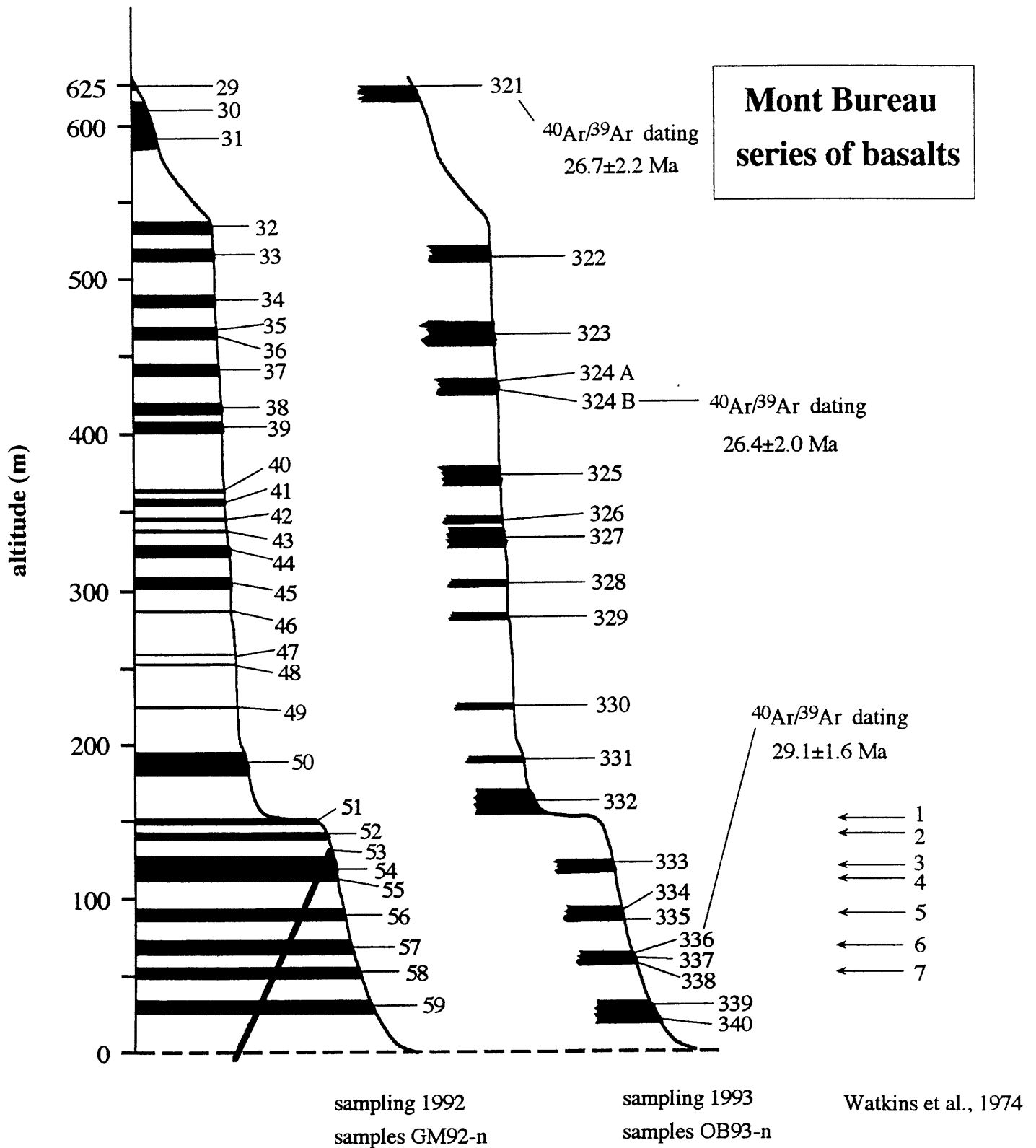
29 Ma
to
26 Ma

TRANSITION
STAGE



22 Ma
to
Present

ALKALINE
STAGE



(The white levels are those without outcrop or very weathered.)

Fig. 1d

OB93-336

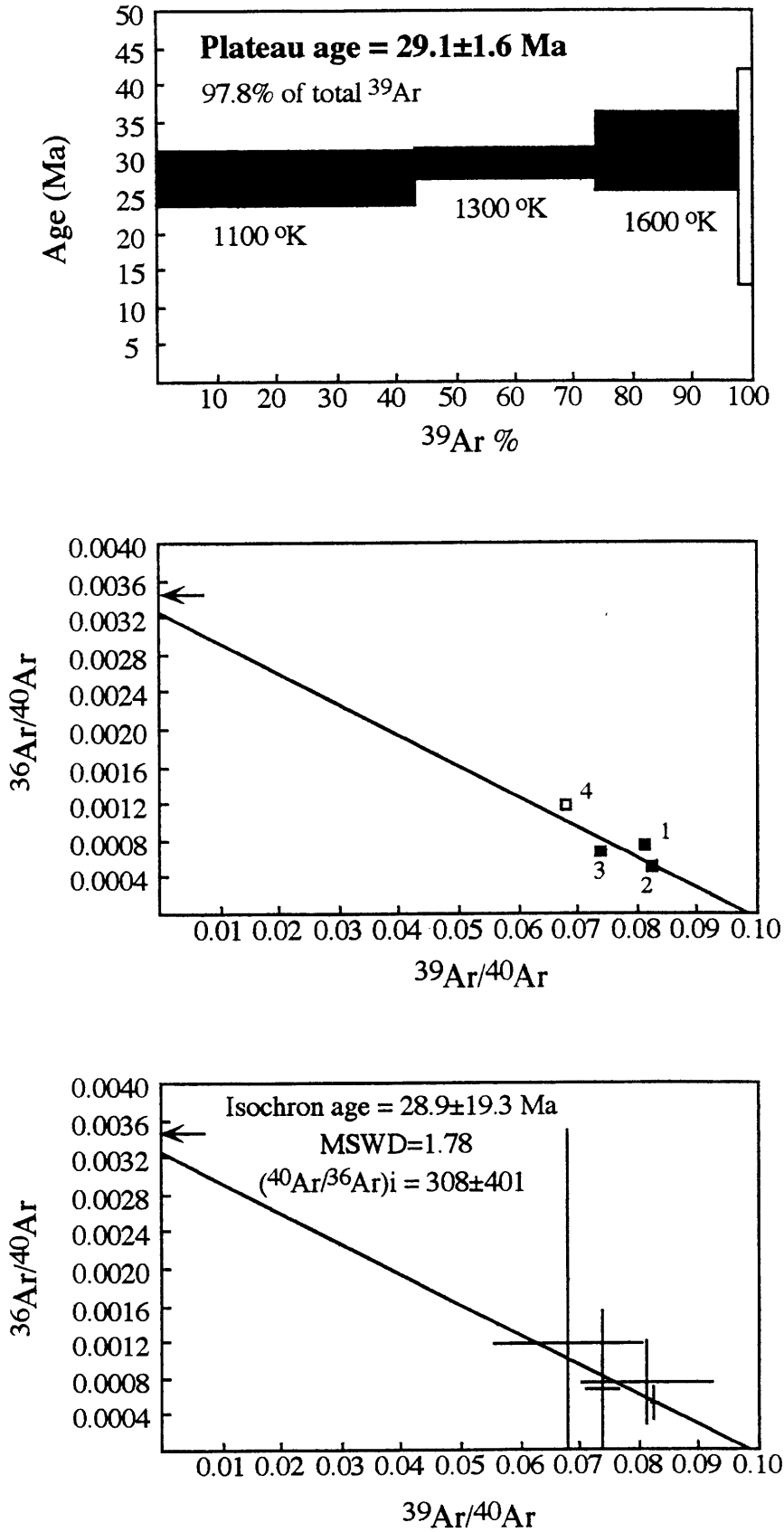


Fig. 2a

OB93-324B

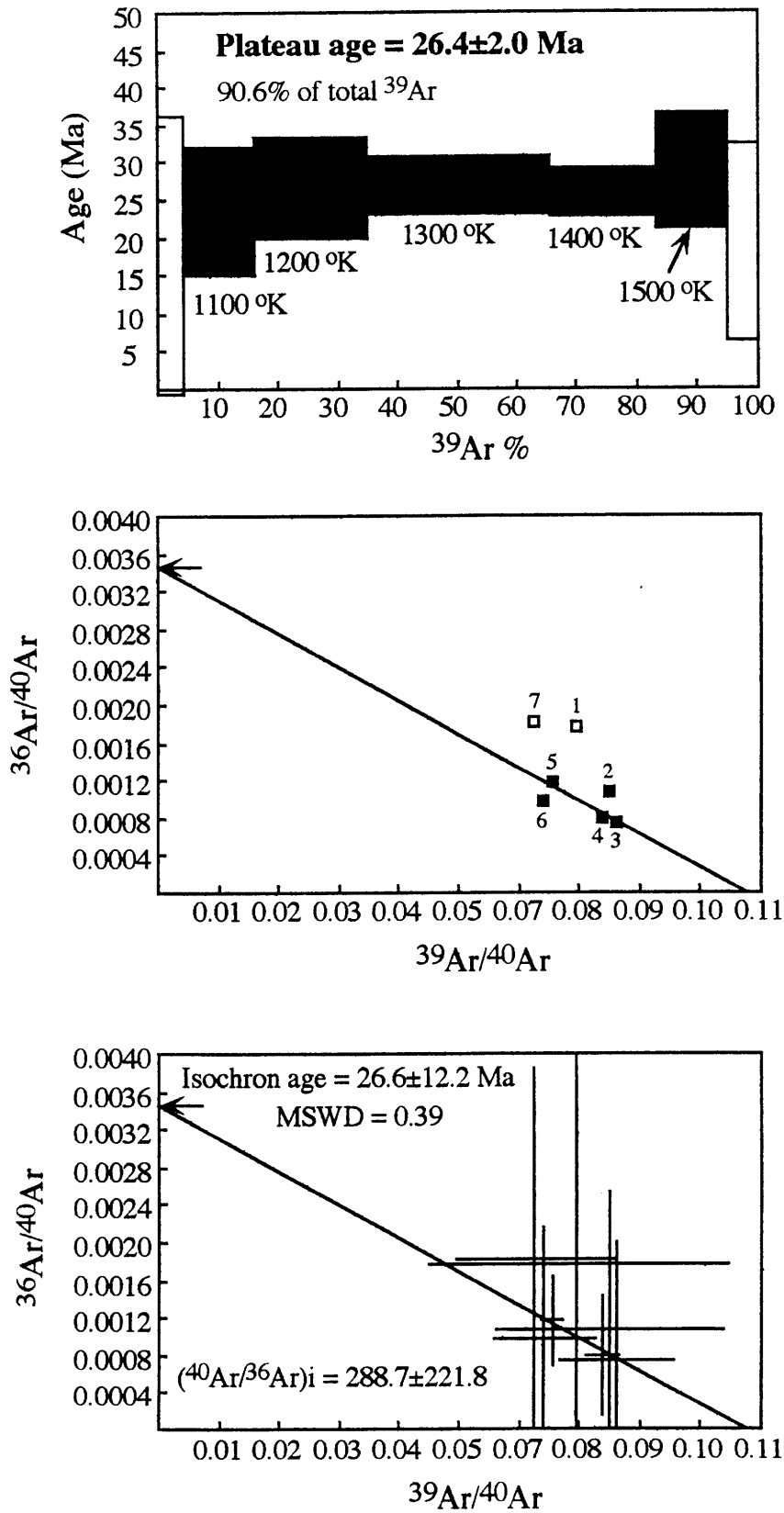


Fig. 2b

OB93-321

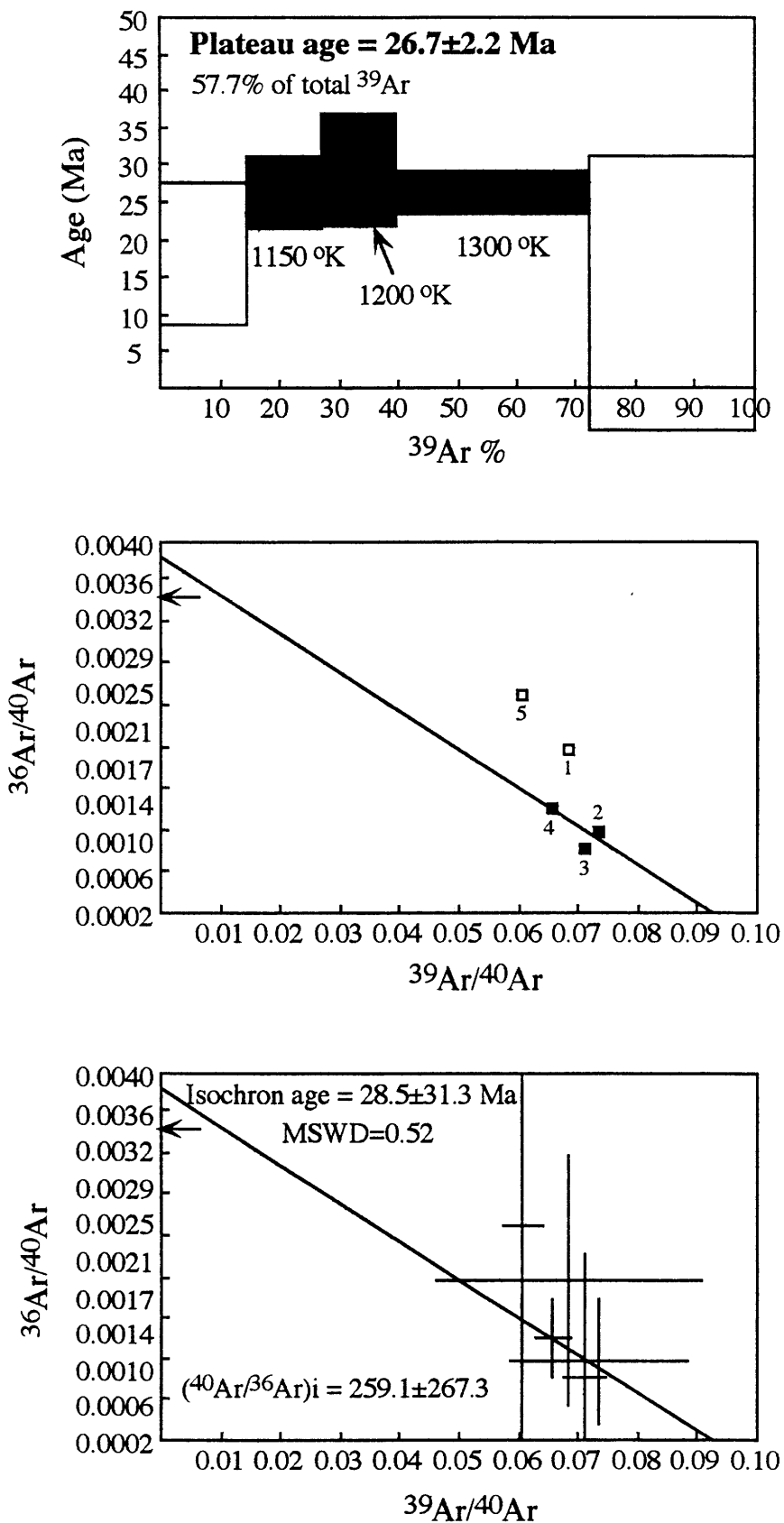


Fig. 2c

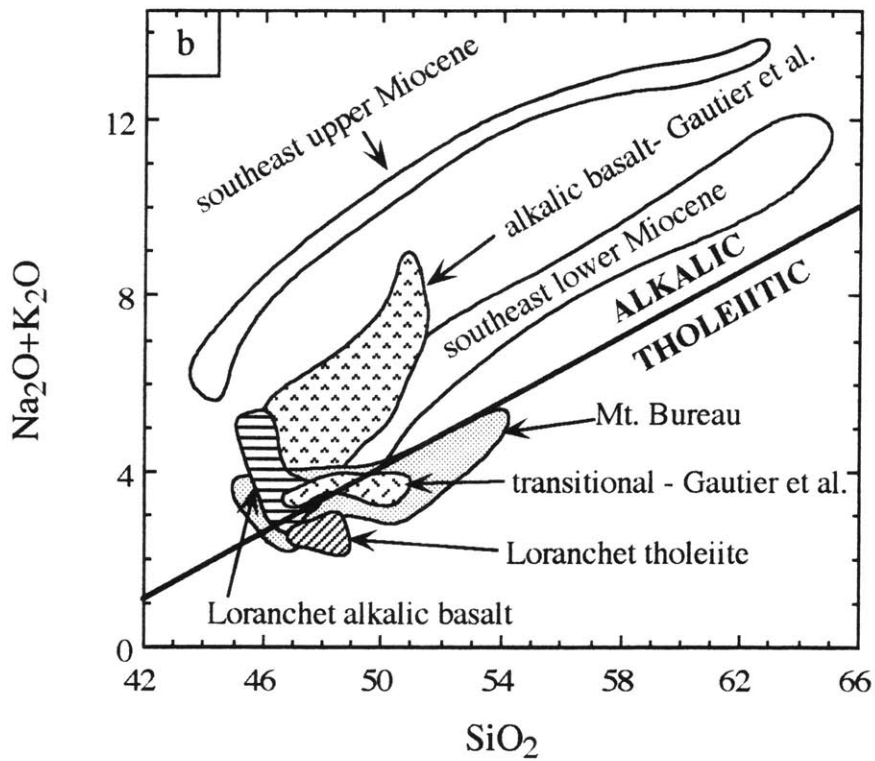
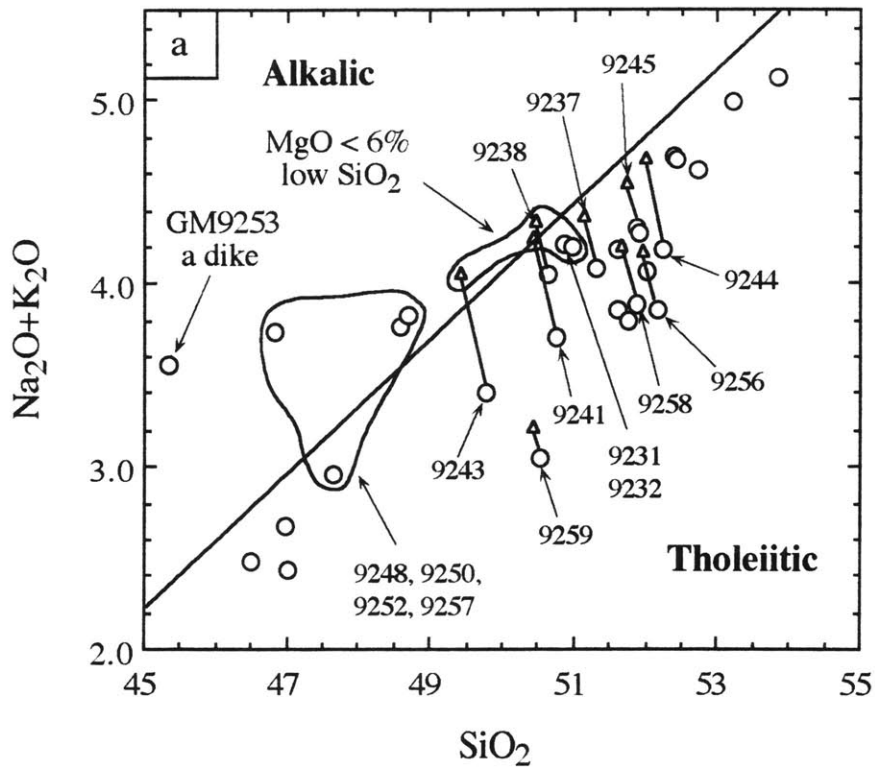


Fig. 3

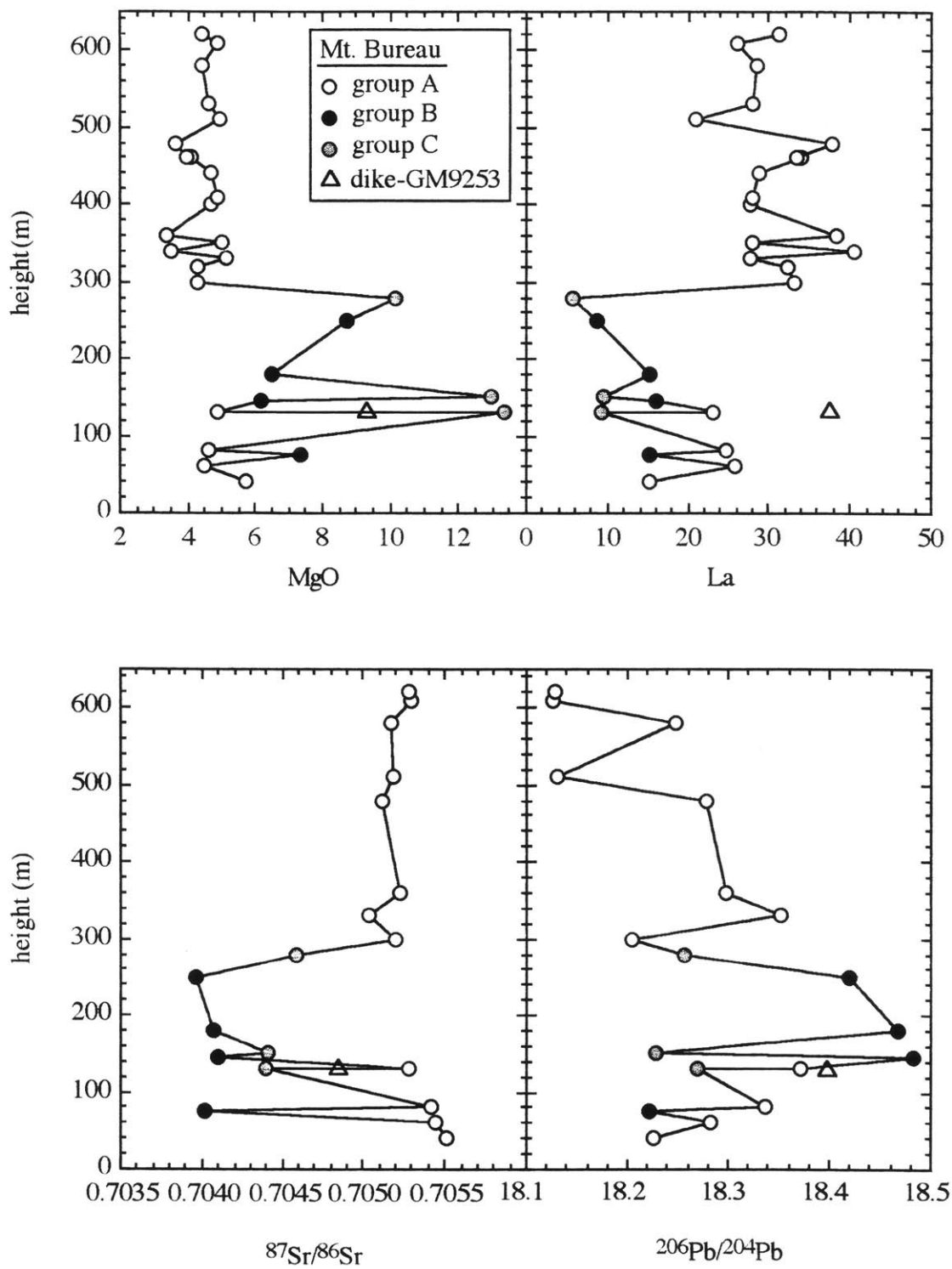


Fig. 4

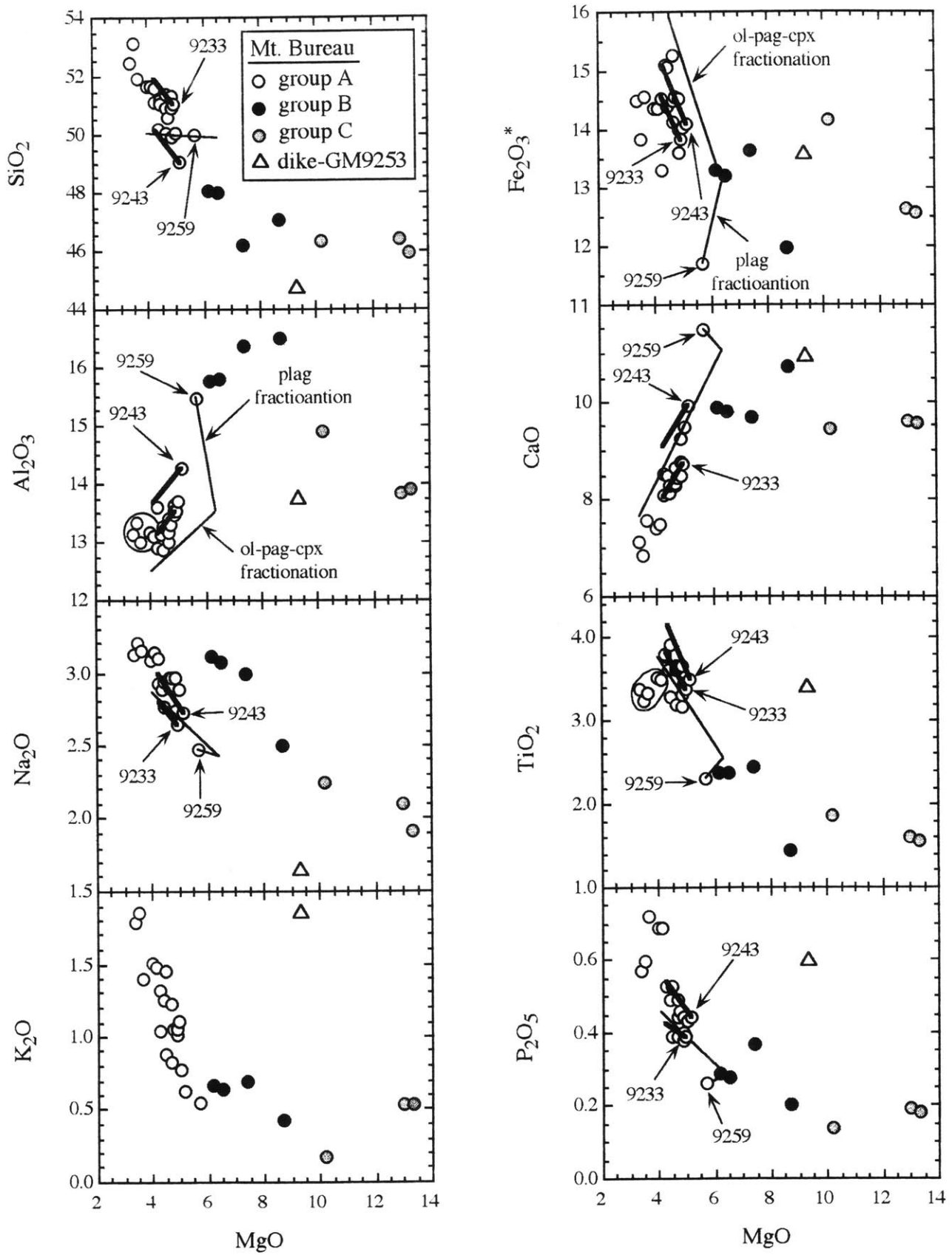


Fig. 5a

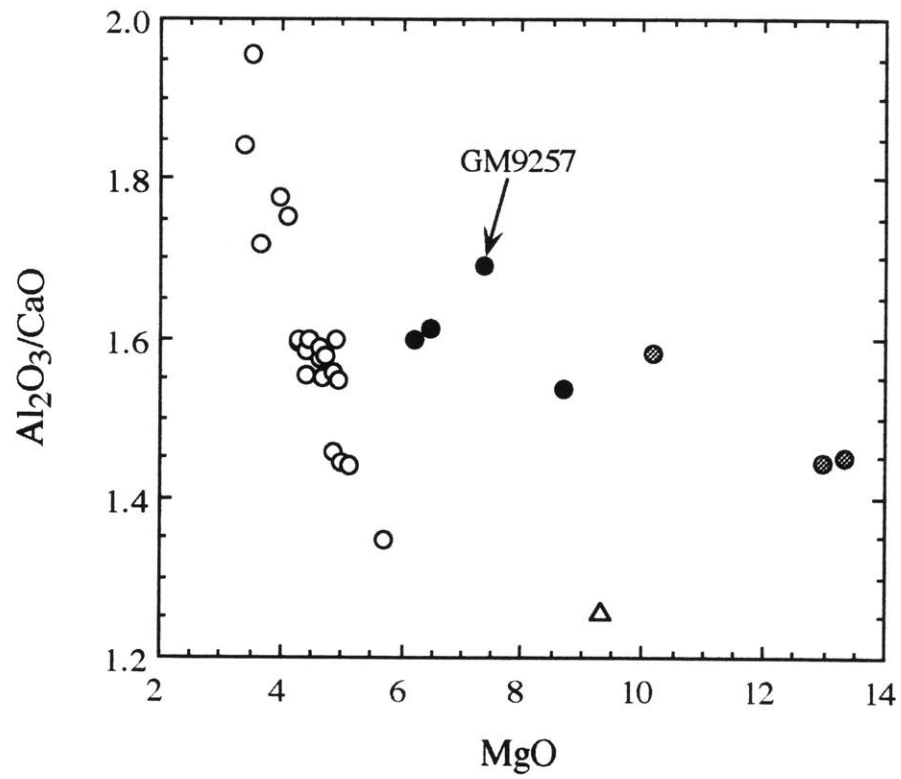


Fig. 5b

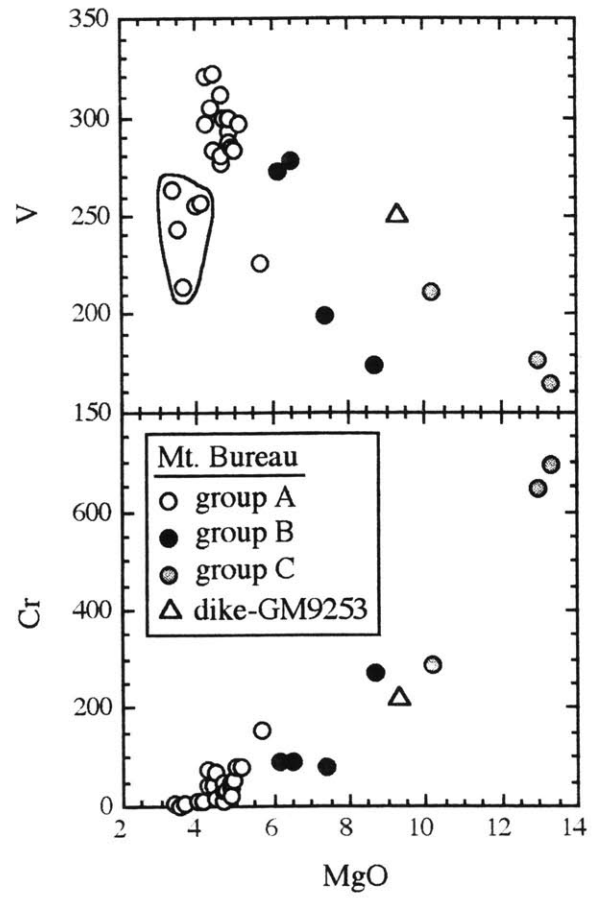
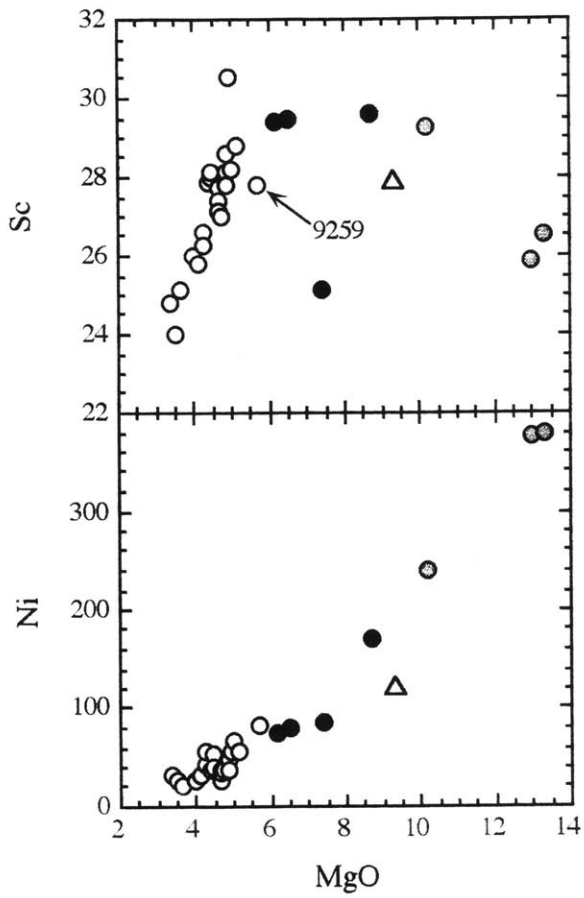


Fig. 6

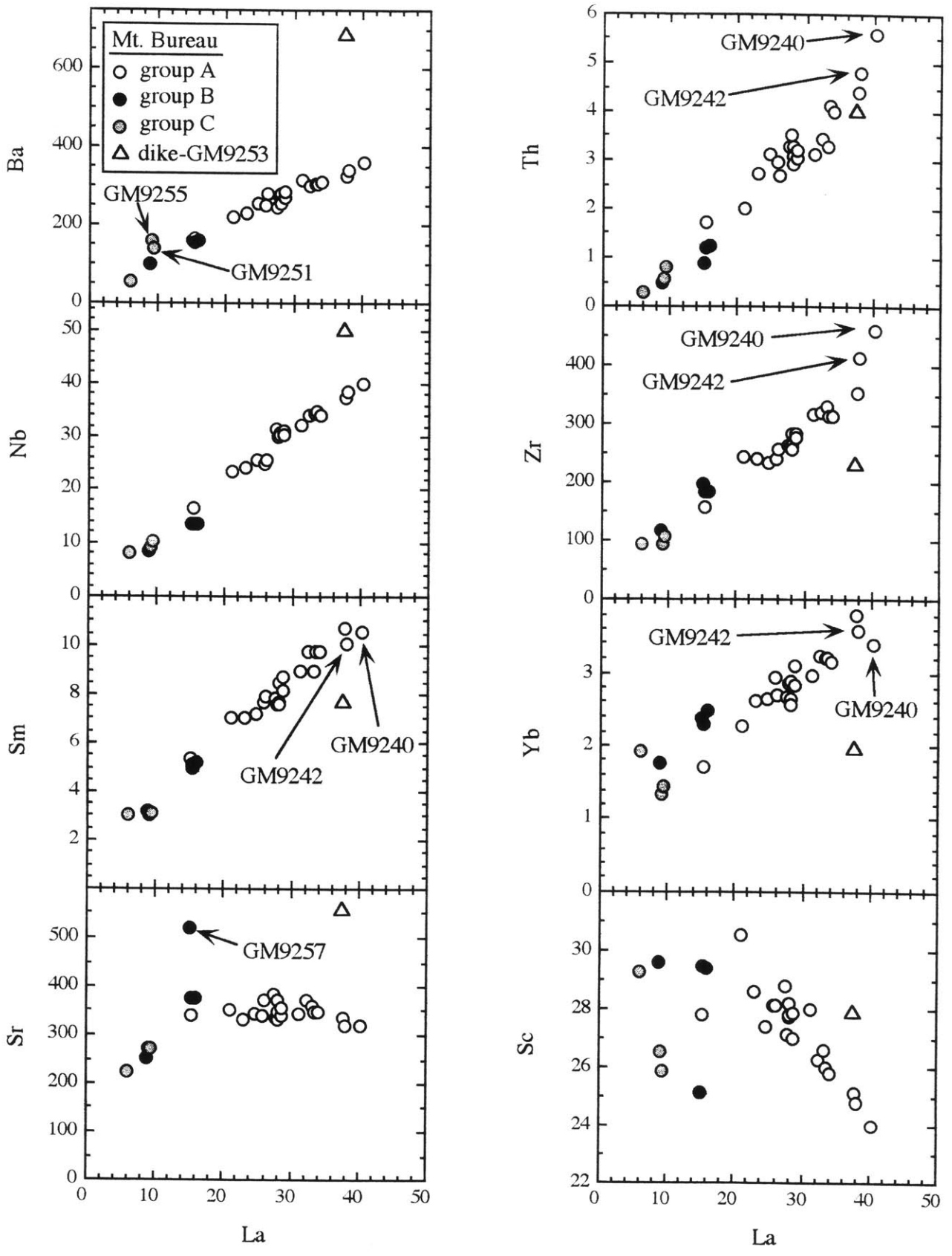


Fig. 7

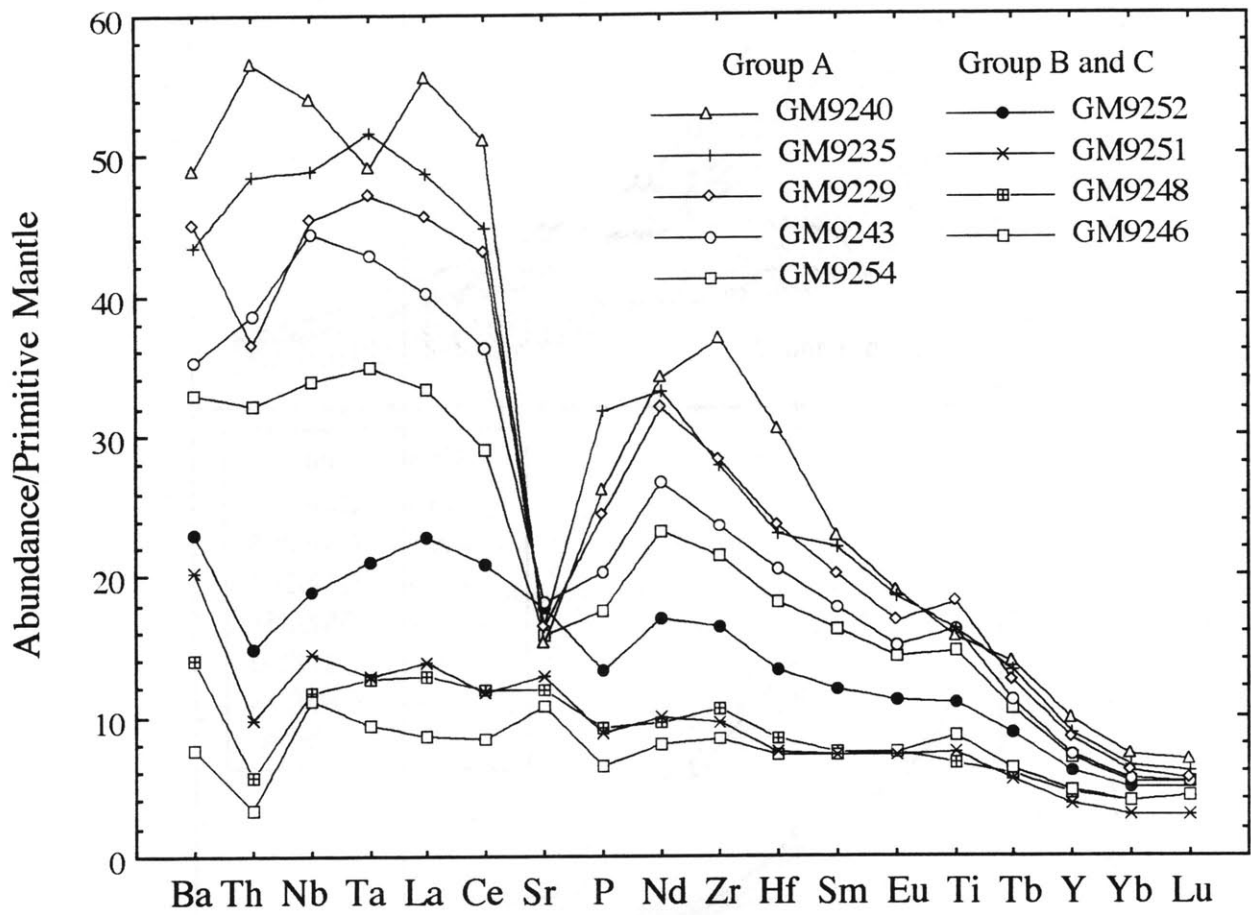
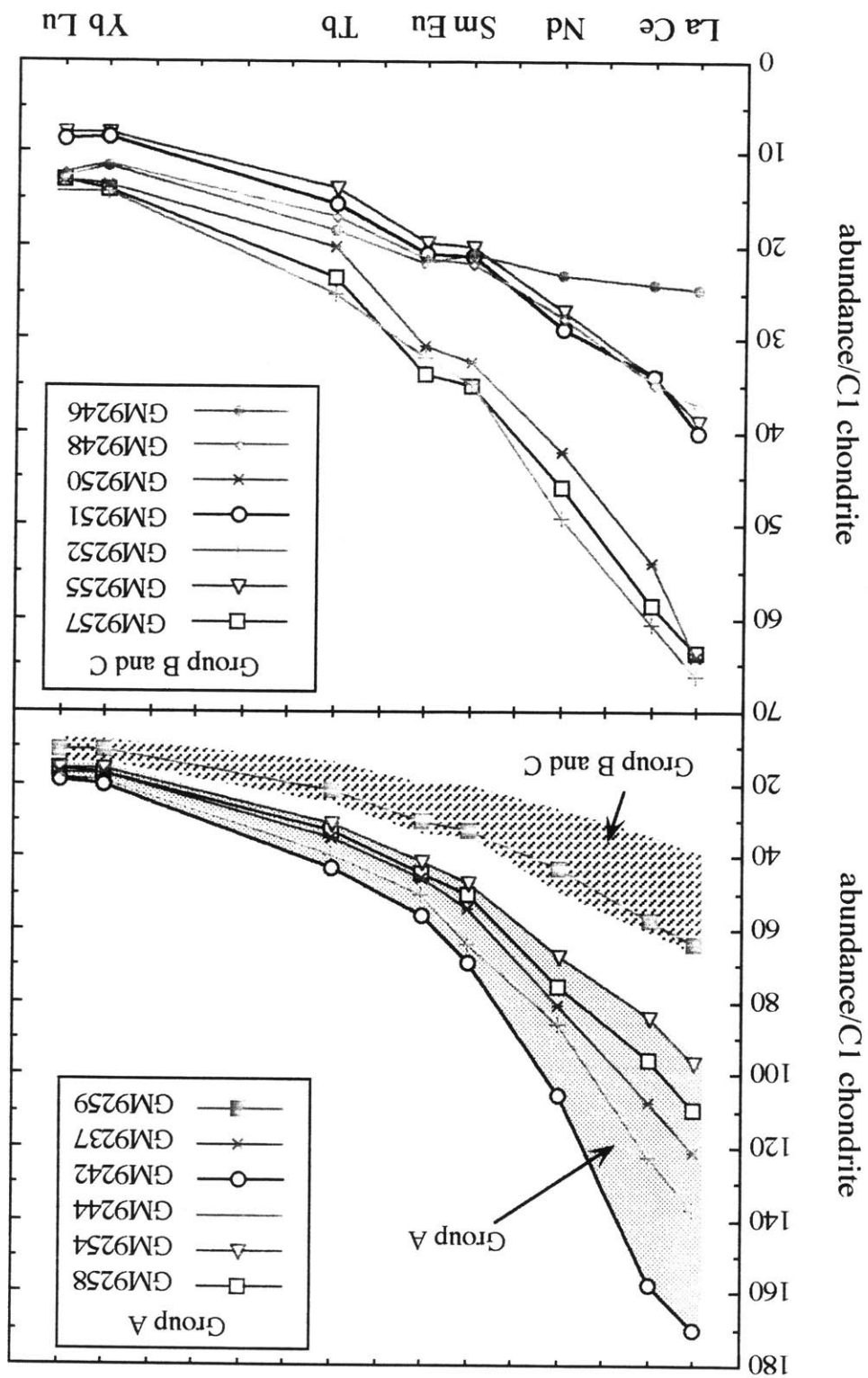


Fig. 8a

Fig. 8b



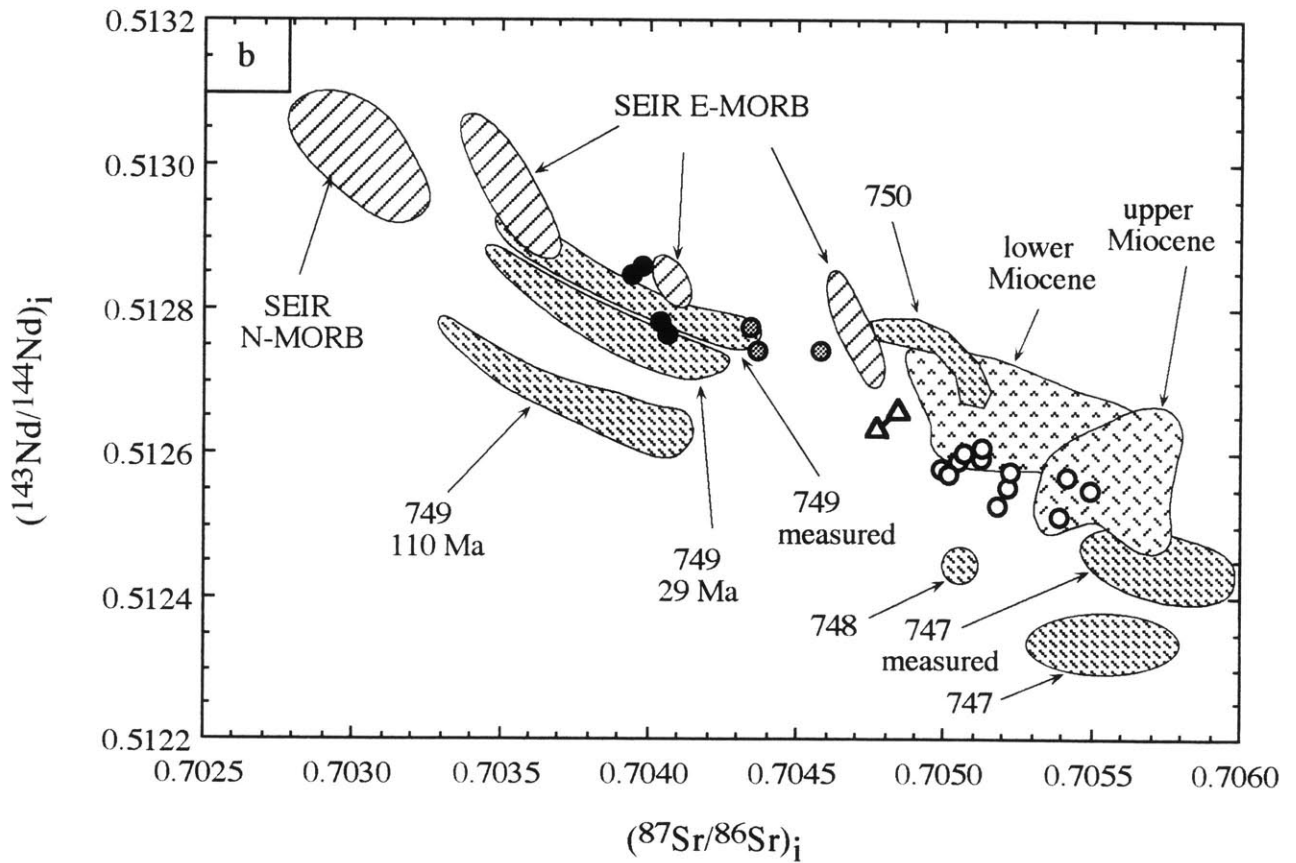
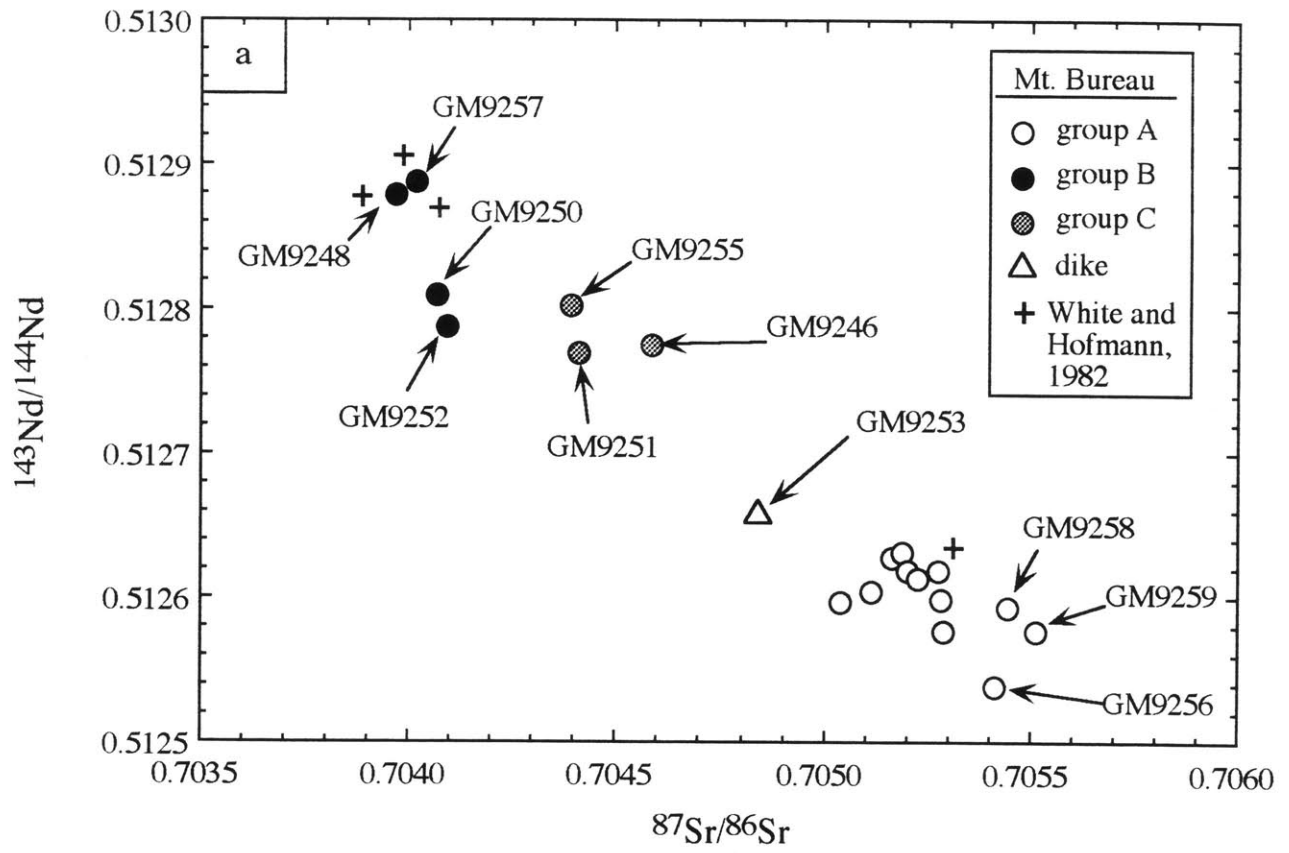


Fig. 10

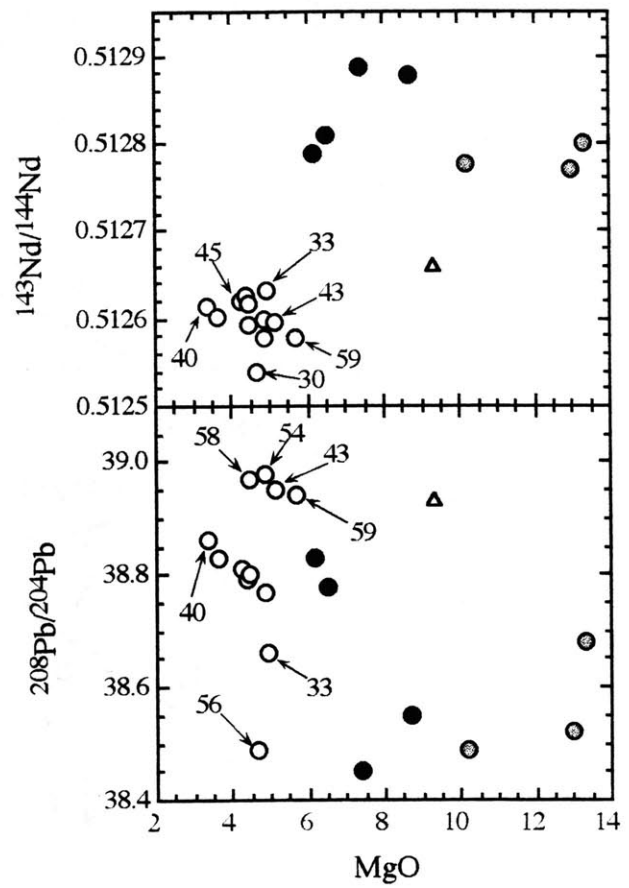
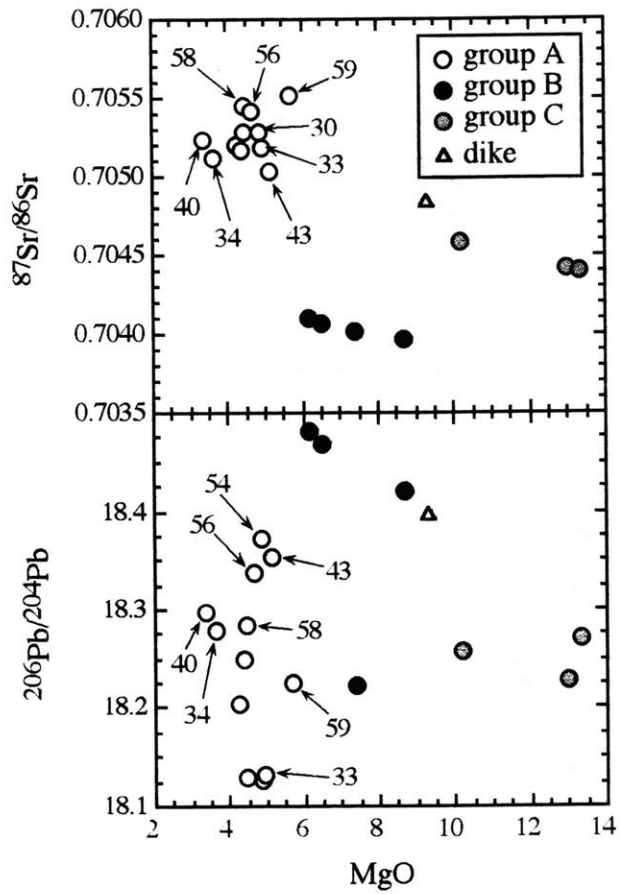


Fig. 11

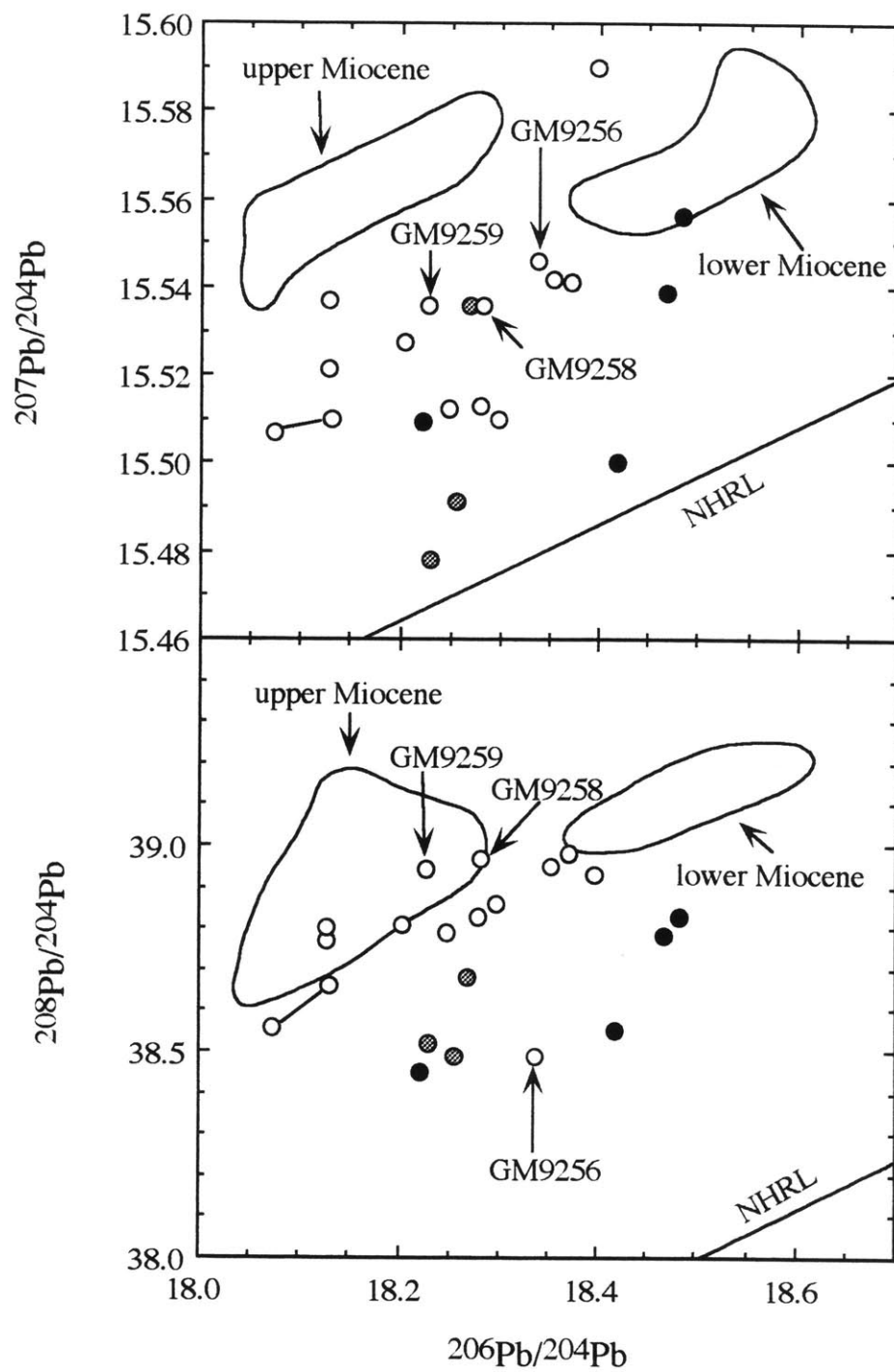


Fig. 12

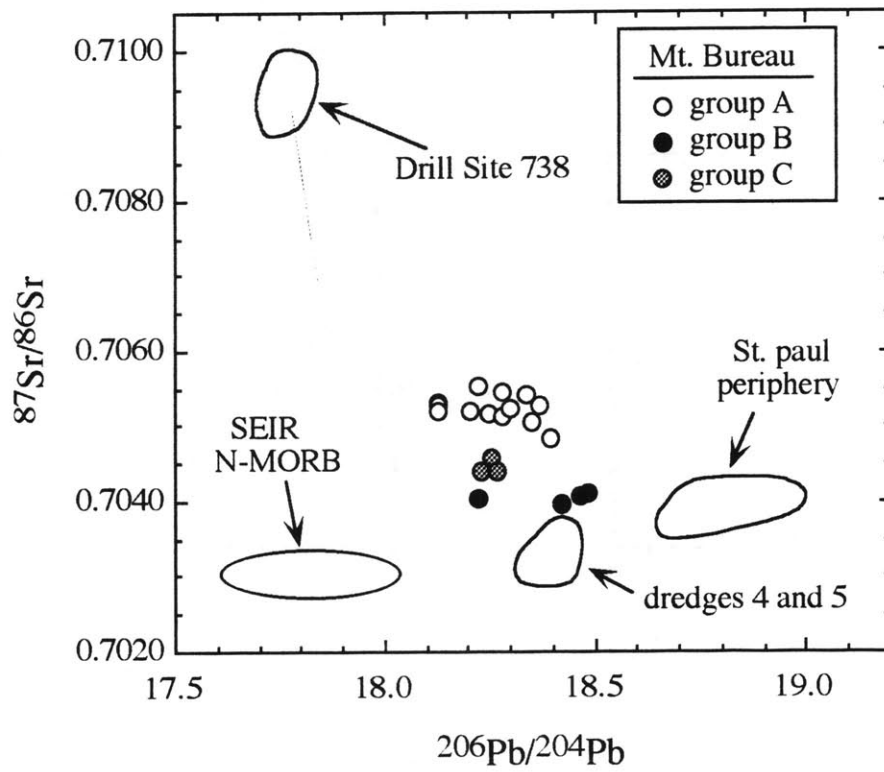


Fig. 13

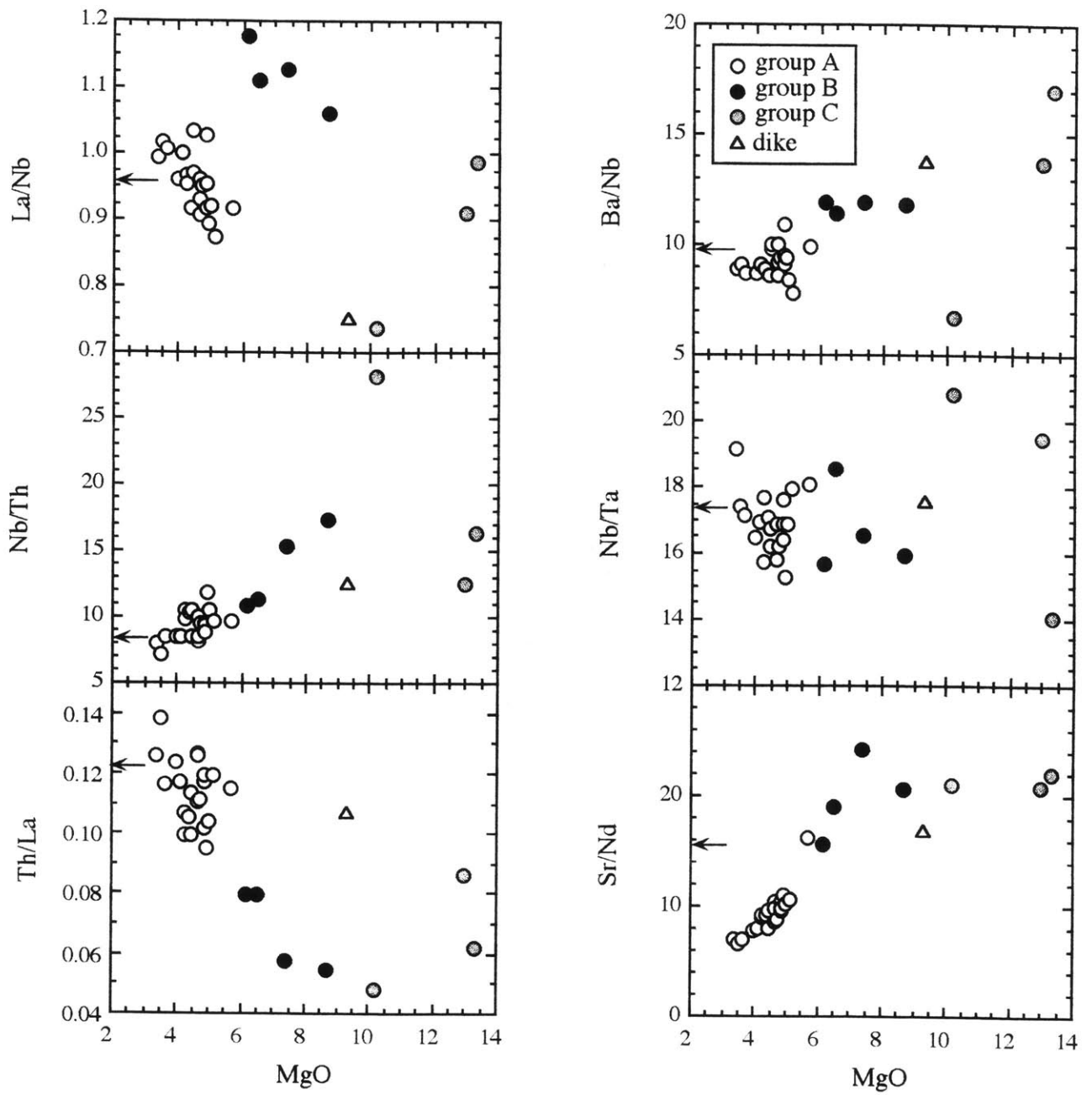


Fig. 14a

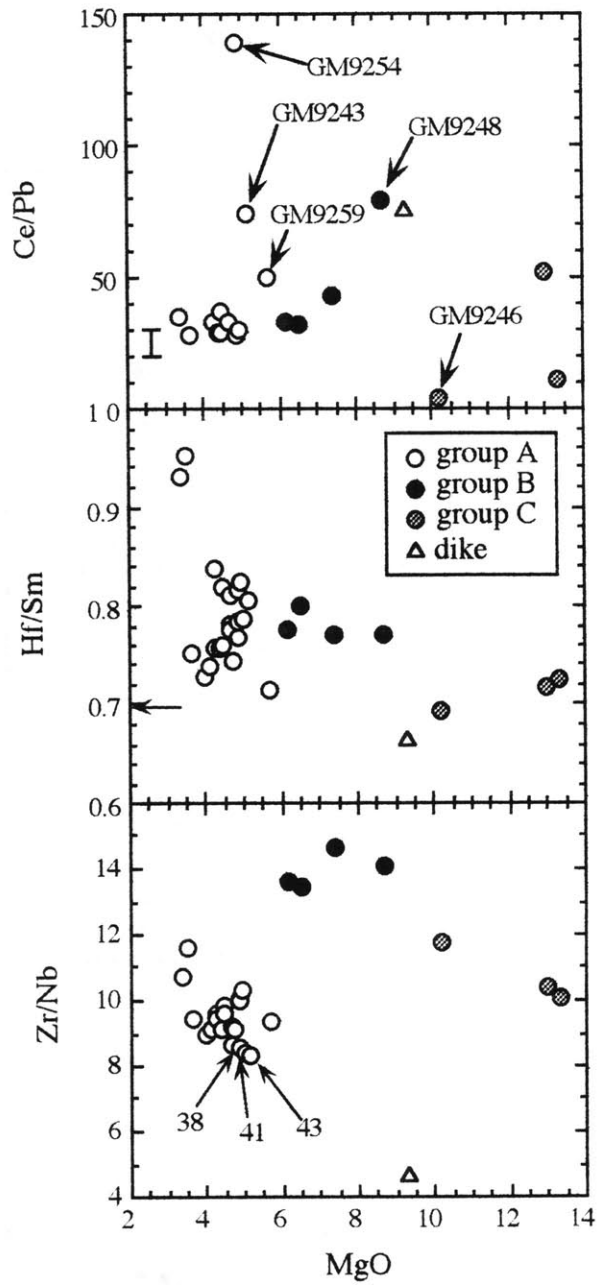
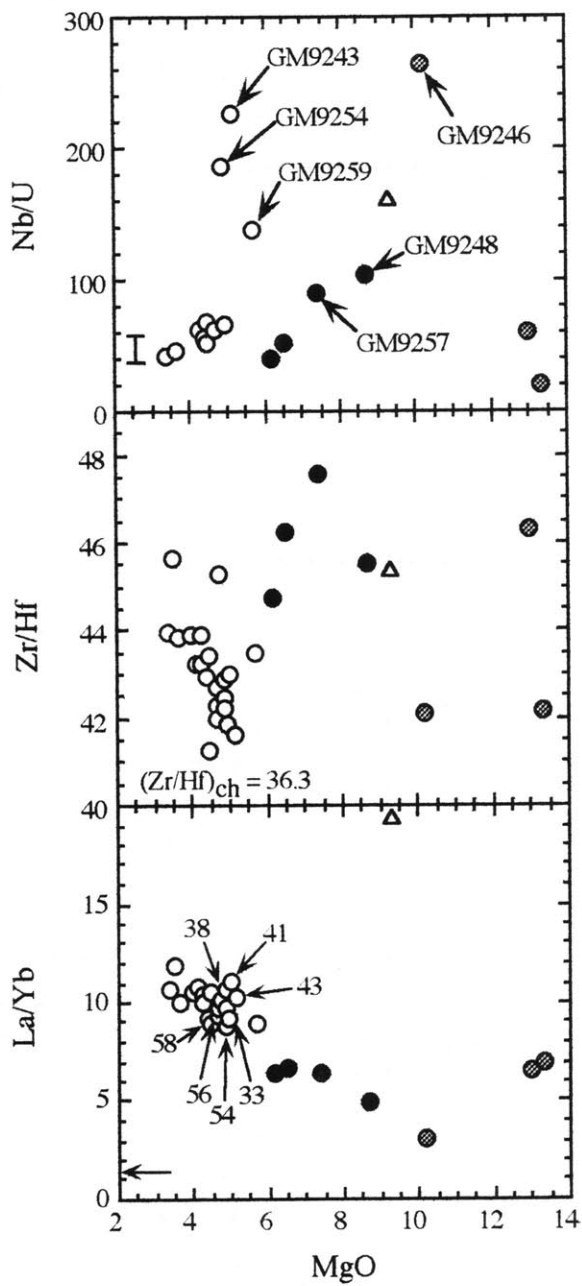


Fig. 14b

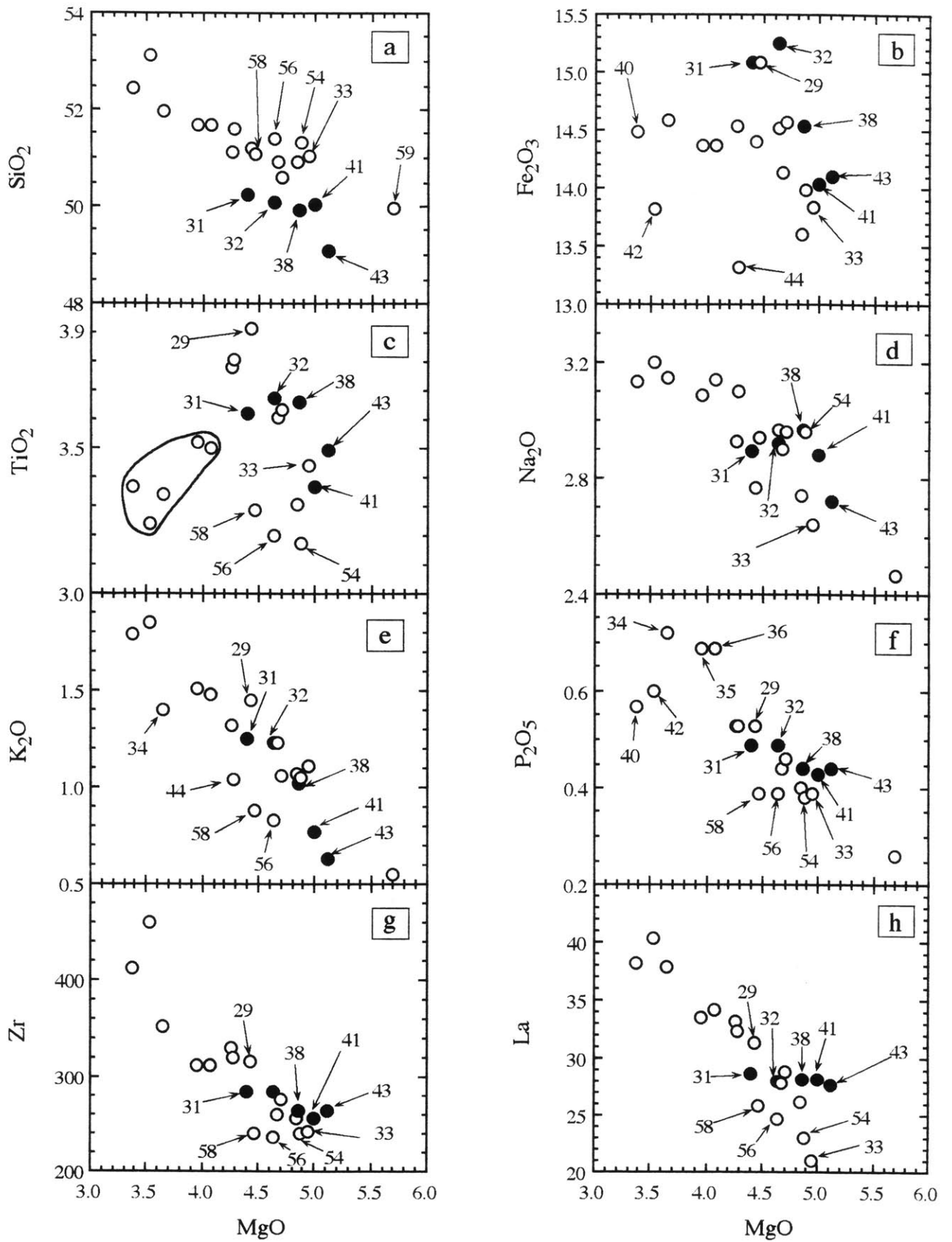
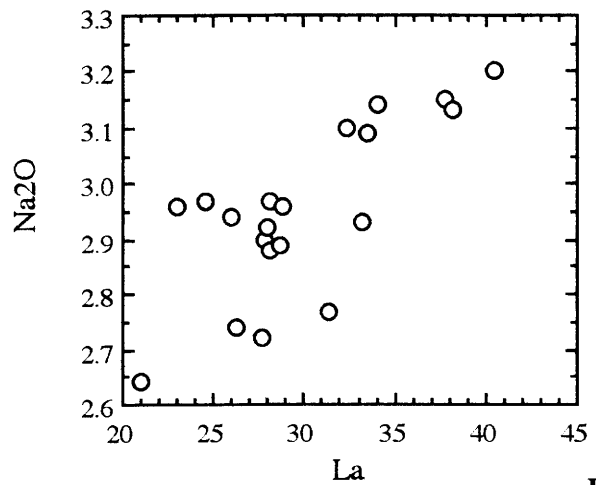
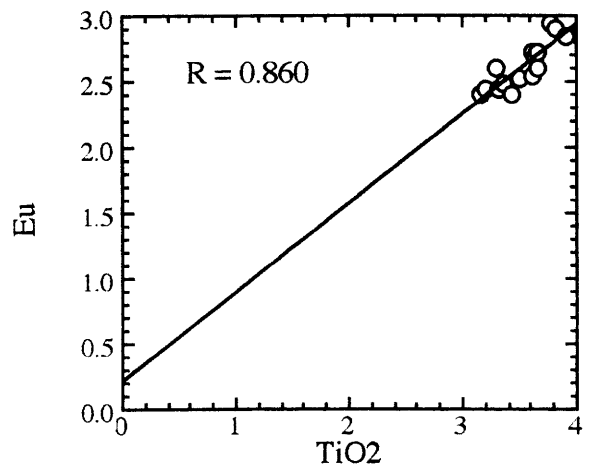
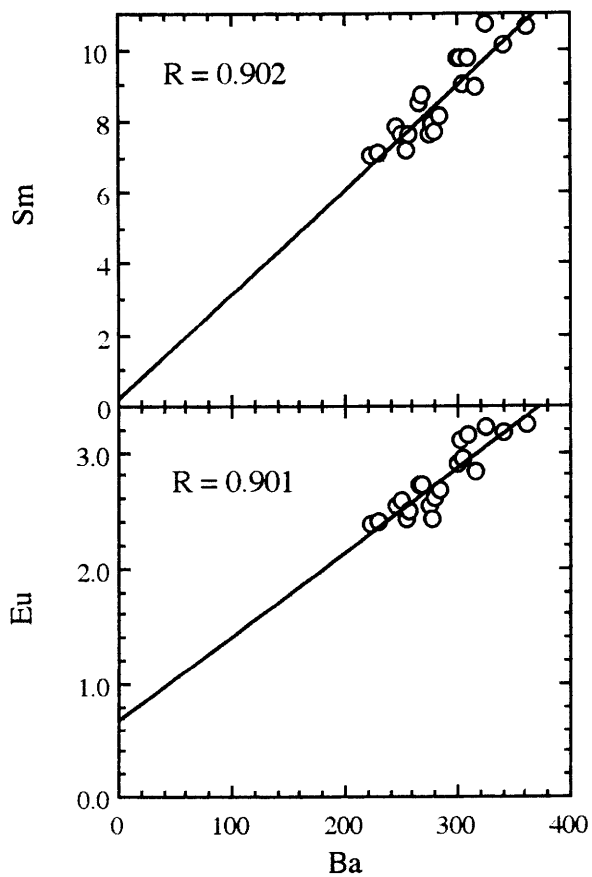
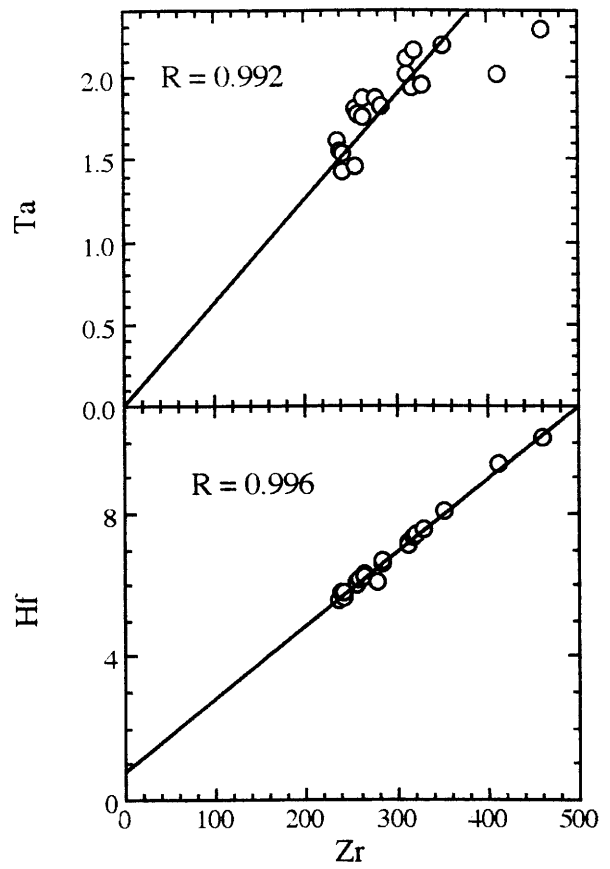
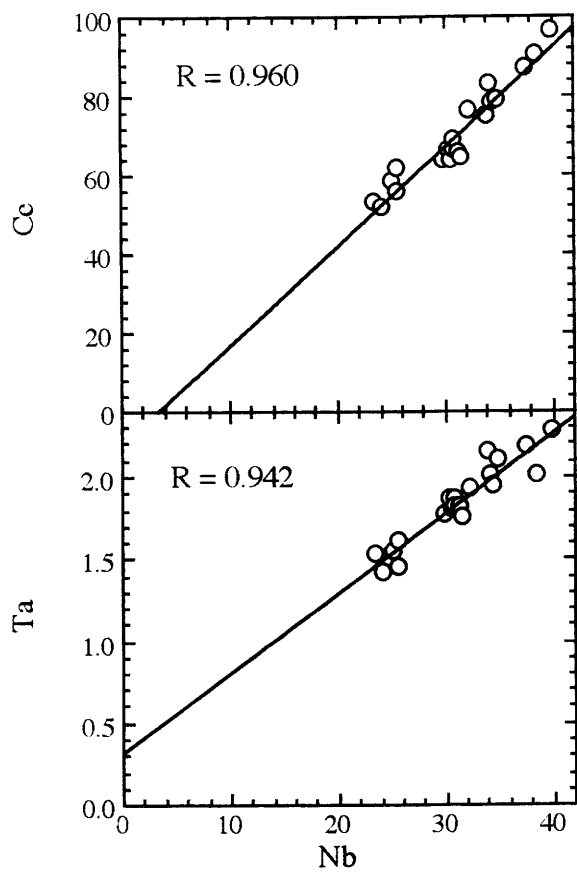


Fig. 15



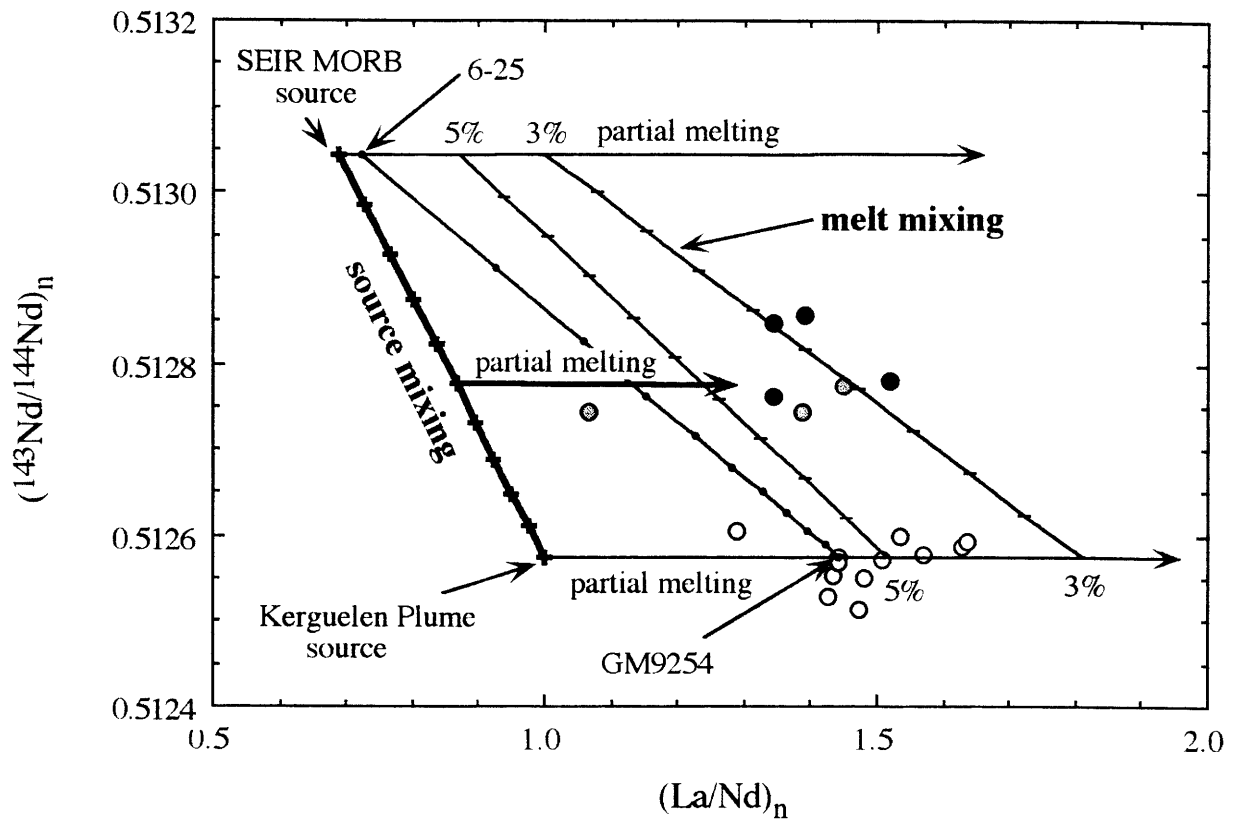


Fig. 17

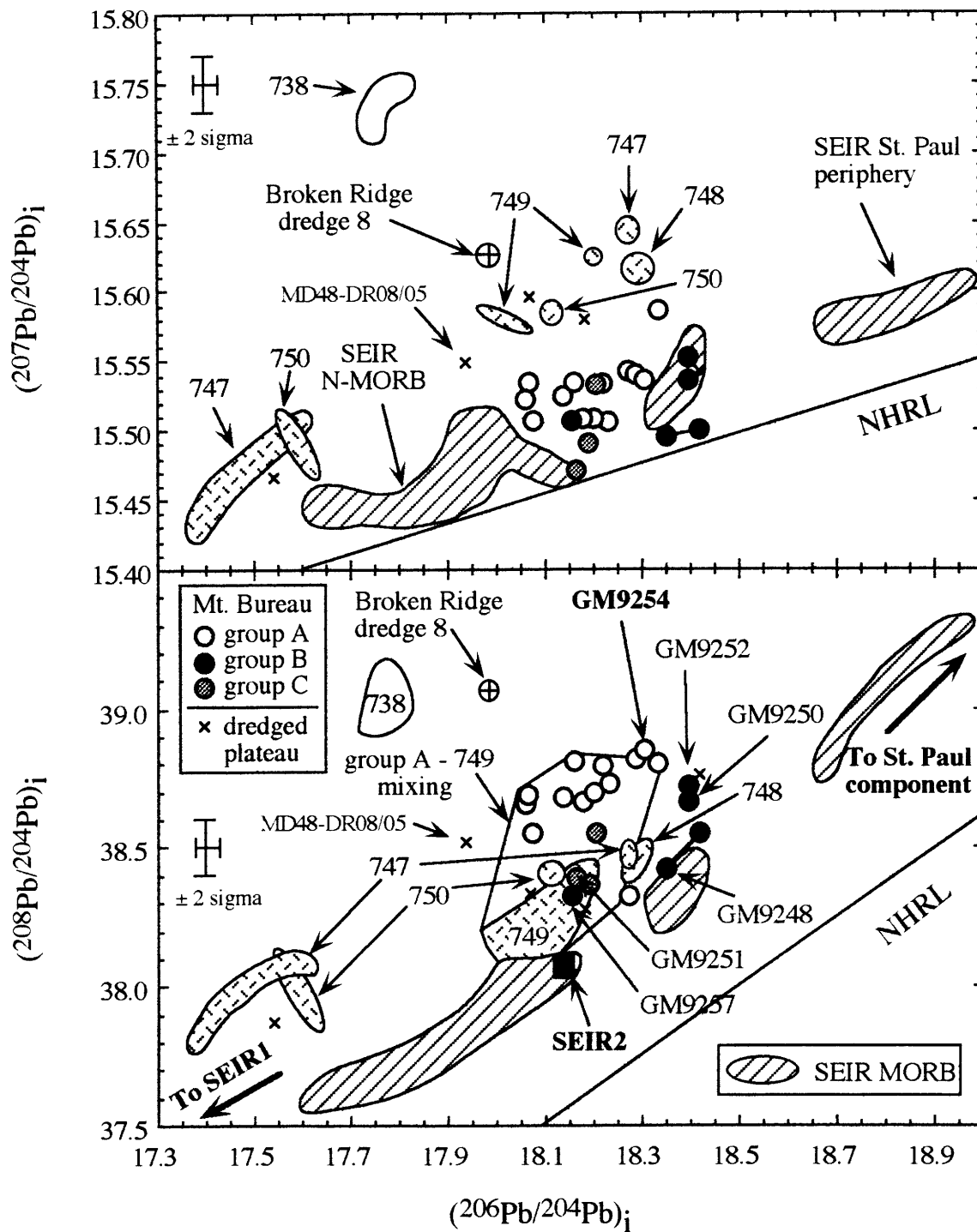


Fig. 18

SEIR MORB - Kerguelen Plume mixing

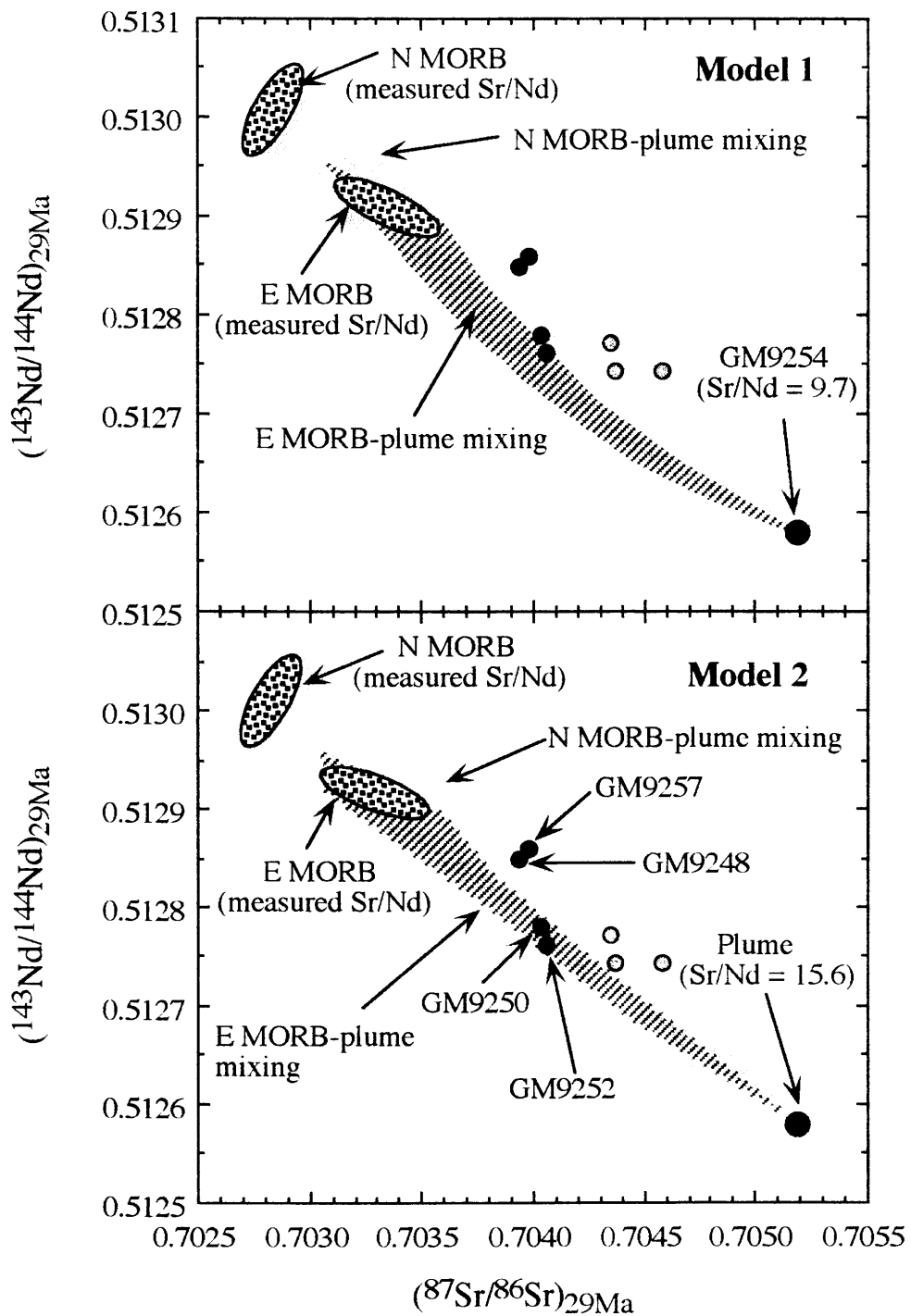


Fig. 19

SEIR-Kerguelen plume melt mixing

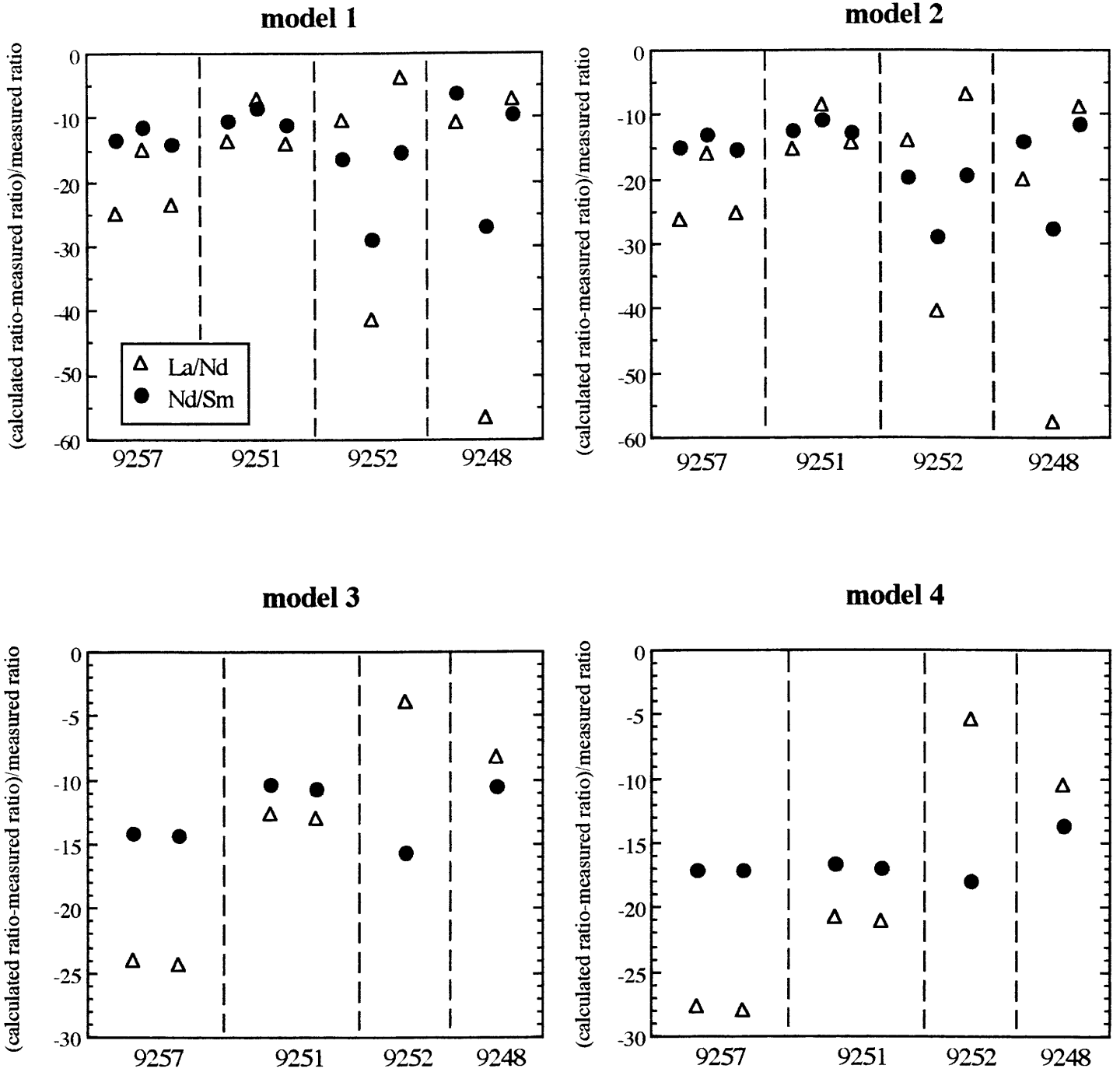


Fig. 20

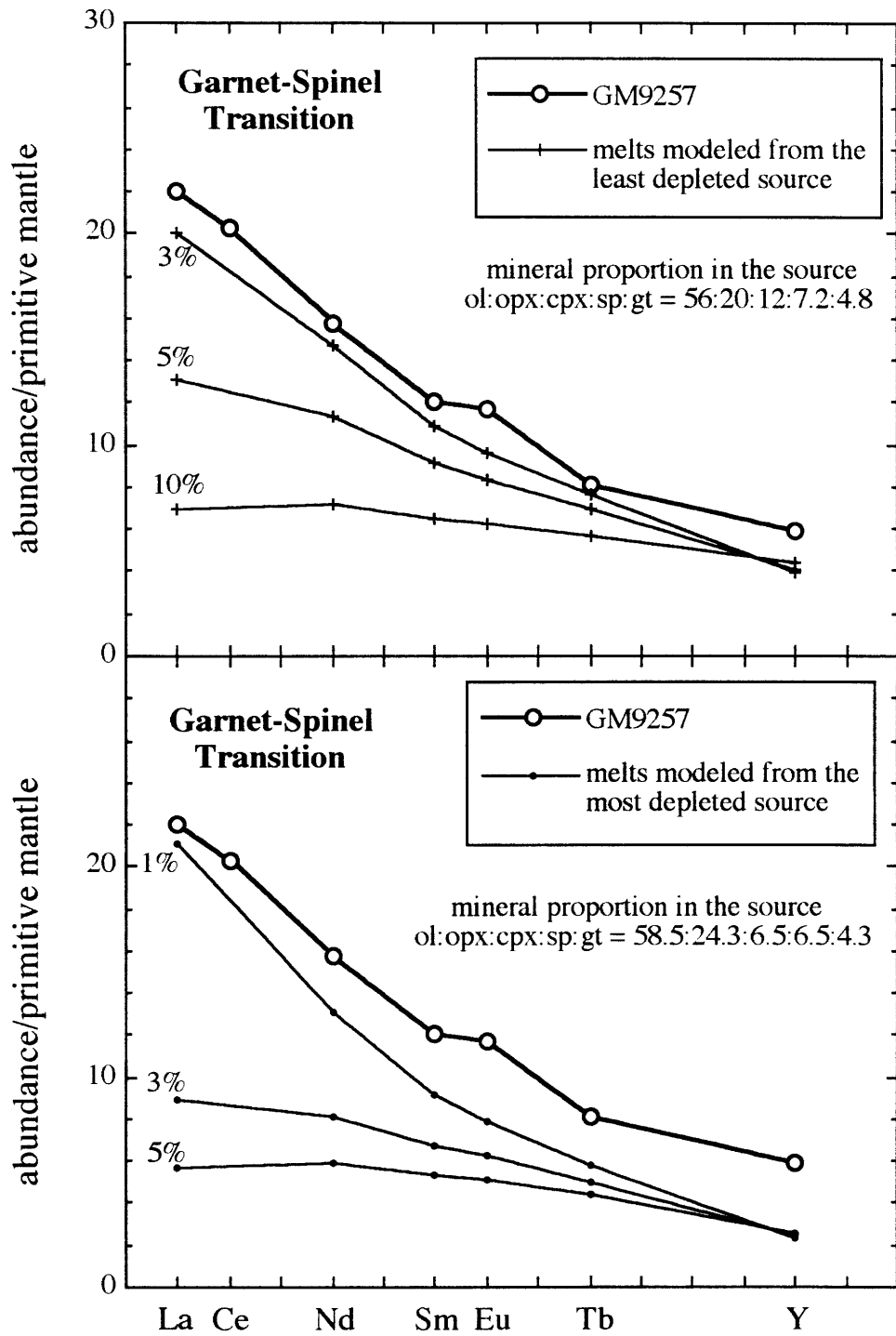


Fig. 21a

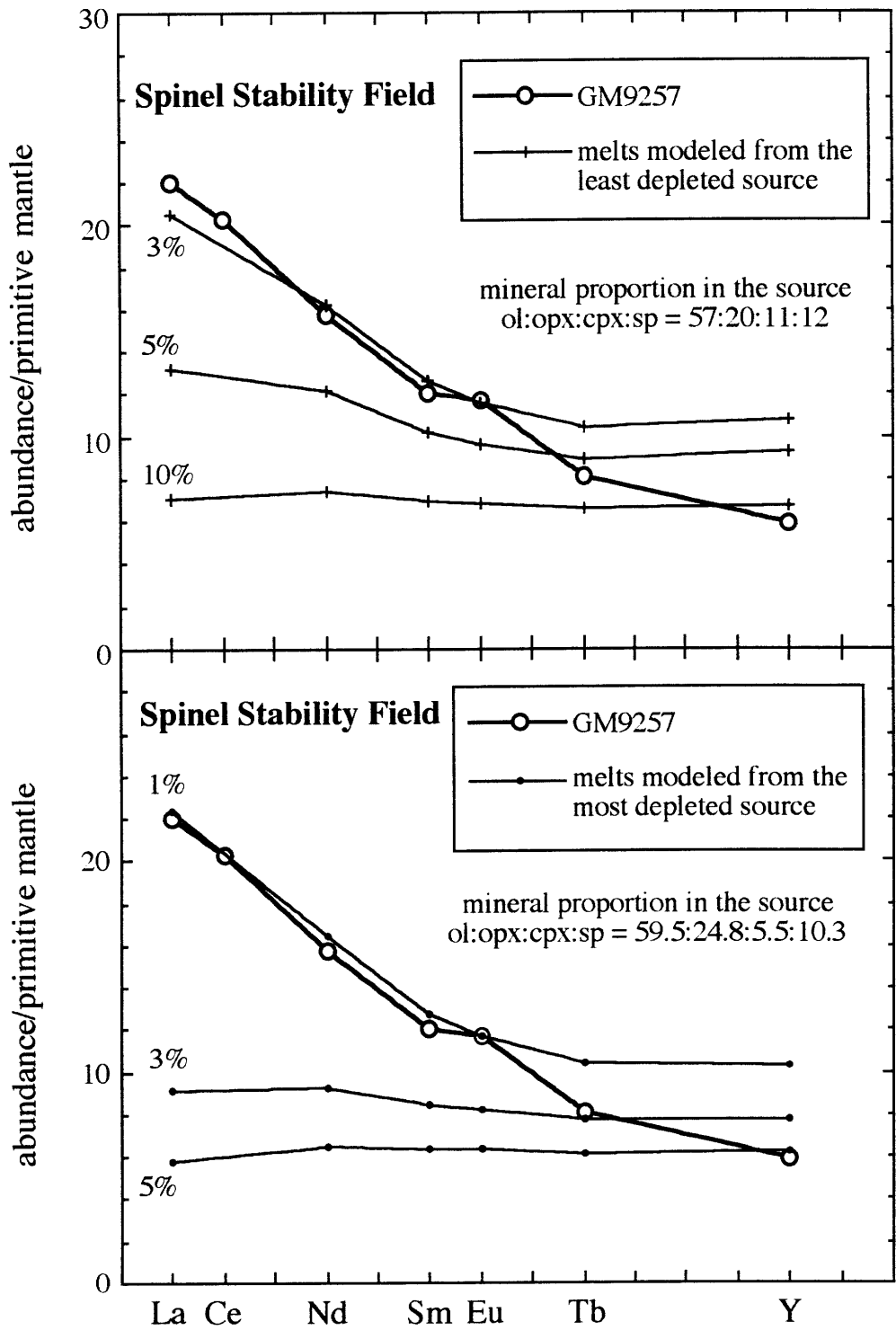


Fig. 21b

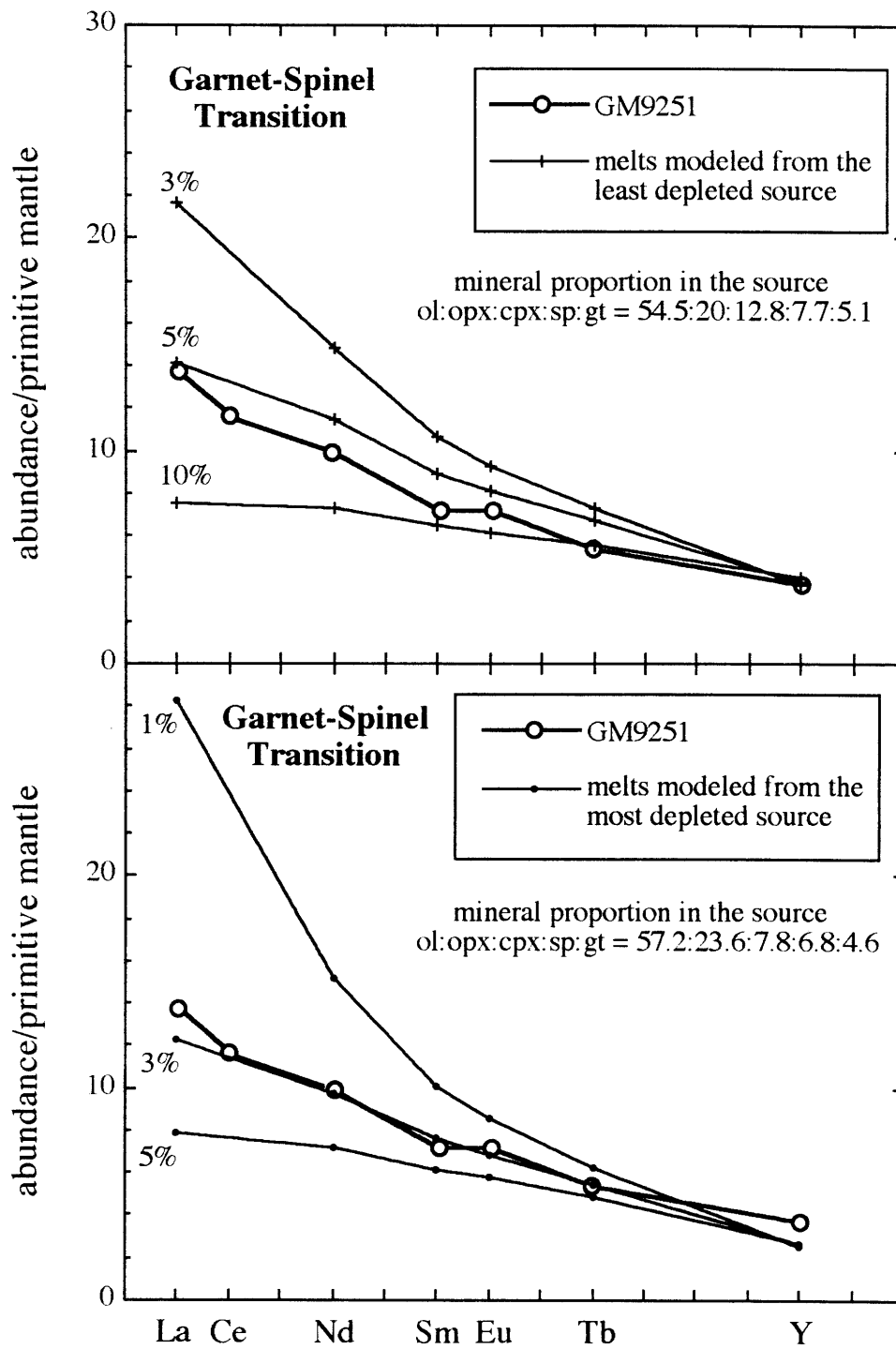


Fig. 21c

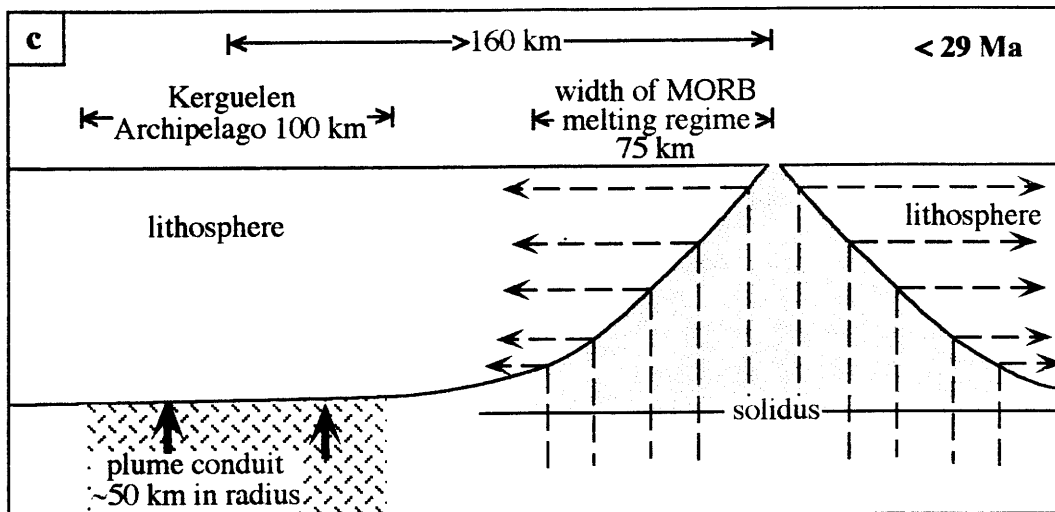
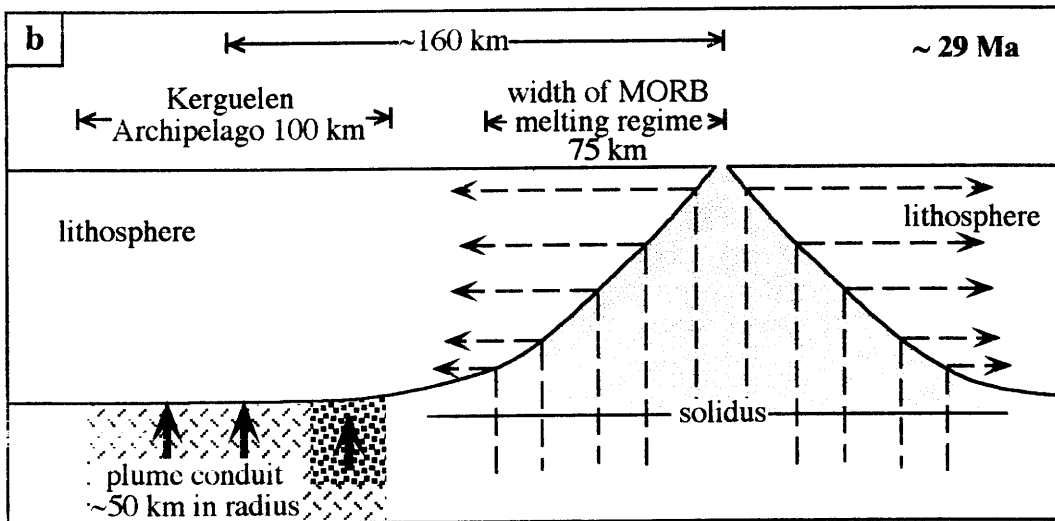
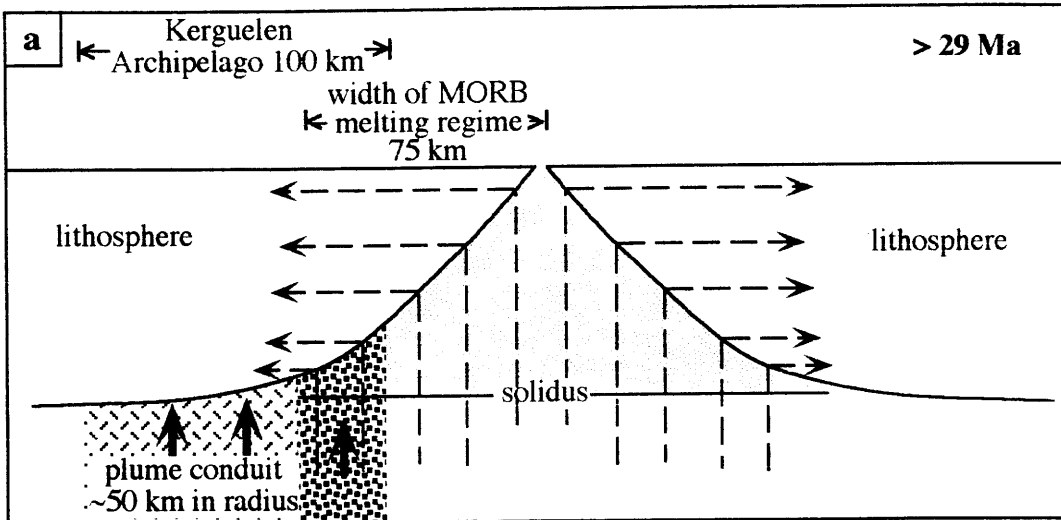


Fig. 22

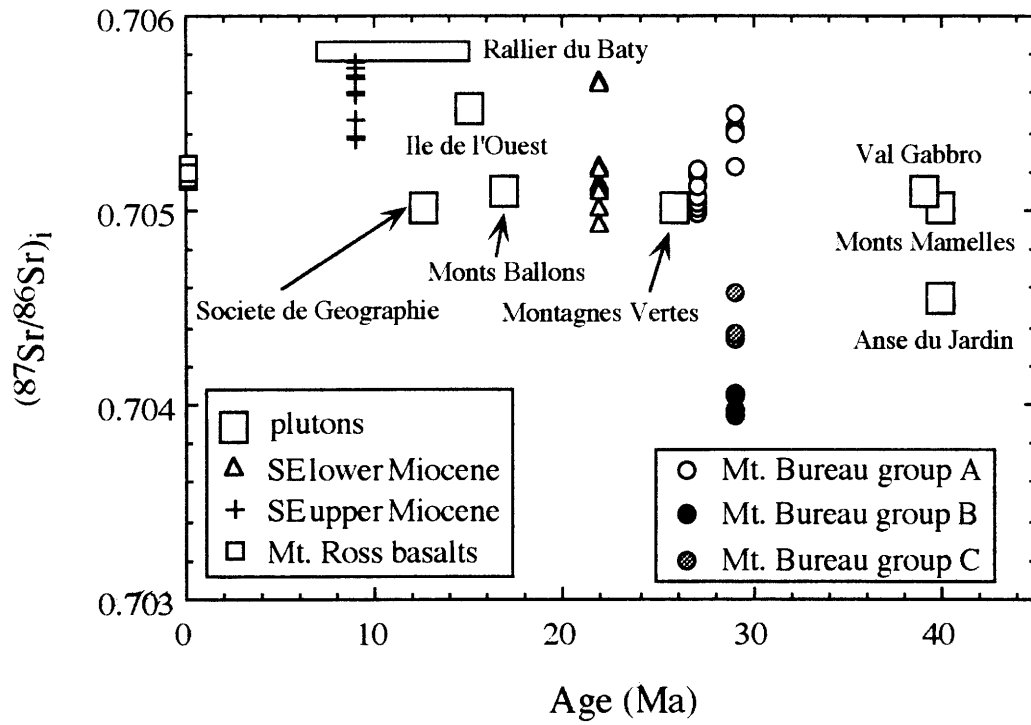


Fig. 23